The University Of Sheffield.

Biomimetic elastomeric poly(glycerol sebacate)-based scaffolds for adipose tissue engineering

Martin Frydrych

A thesis submitted in partial fulfilment of the requirements for the degree of

Doctor of Philosophy

The University of Sheffield

Faculty of Engineering

Department of Materials Science and Engineering

December 2015

Declaration

I hereby declare that this thesis is my own work and effort, and that this thesis has not been submitted to another university in full or in part for another degree or qualification. Where other sources of information have been used, they have been acknowledged. Permission has been granted from copyright holders to replicate figures or data within this thesis.

Martin Frydrych

Sheffield, December 2015

This thesis is dedicated to my parents.

Acknowledgements

I wish to express my sincere gratitude to my advisor, Dr. Biqiong Chen, for her guidance, support and many inspiring discussions throughout this research work. Her supervision has greatly sharpened my critical thinking and analytical skills. I further would like to thank all my research colleagues for their support and motivation, in particular Richard Justin and Yongzhe Piao for their generosity, hospitality and friendship. I am also thankful to the University of Sheffield, which provided me with financial support in form of a stipend.

My sincere thanks goes to the staff members and fellow researchers at the University of Sheffield. Sincerely, I am thankful to Ben Palmer, Dr. Le Ma and Dr. Peng Zeng of the Department of Materials Science and Engineering at the University of Sheffield, for their kind technical assistance throughout my research. I also gratefully acknowledge the kind support of Prof. Sheila MacNeil, Dr. Sabiniano Román and Dr. Nicola H. Green of the Department of Materials Science and Engineering at the University of Sheffield, who undertook the cell viability testing, cell imaging and analysis of variance within this thesis. Furthermore, I would like to thank Rob Hanson, Melanie Hannah, Sue Bradshaw and Dr. Oleksandr Mykhaylyk of the Department of Chemistry at the University of Sheffield, who undertook the gel permeation chromatography analysis and proton nuclear magnetic resonance spectroscopy within this thesis, and for permitting me to use their rheometry facilities.

I am thankful to Prof. Dr. Ralph Stengler and Prof. Dr.-Ing. Roland Angert of the Department of Mechanical and Plastics Engineering at the Hochschule Darmstadt - University of Applied Sciences, for their initial support and inspiration during my early stages of this journey.

A heartfelt thank you goes out to Rachel Doyle, for all her love, support and patience over the past few years. I also would like to thank my brother, Denis, for our countless discussions and for his encouragement and moral support during my research.

Finally, I would like to express my deepest gratitude to my parents: Mamo, Tato, nie ma takich słów, które mogłyby wyrazić jak bardzo jestem wdzięczny za wasze bezwarunkowe wsparcie, codzienną motywację i miłość. Wszystko to co jest byłoby niemożliwe bez Was. Dziękuję Wam z całego serca za to, że zawsze byliście i jesteście wsparciem dla moich marzeń. Obiecuję Wam z całego serca, że zrobię wszystko, abyście zawsze byli ze mnie dumni.

Abstract

In spite of recent progress in the field of adipose tissue engineering (ATE), the optimal adipose tissue scaffold still remains illusive and the tailoring of the structure and properties of tissue scaffolds according to adipose tissue were less explored or even neglected. Thus, synthetic poly(glycerol sebacate) (PGS)-based scaffolds and hydrogels which mimic the properties of adipose tissue were developed in this PhD project for potential application in ATE.

Large and porous three-dimensional PGS/poly(L-lactic acid) (PLLA) blend scaffolds with various weight ratios were successfully fabricated via a freeze-drying and a subsequent curing process, illustrating that a minor amount of PLLA can act as a structure-supporting polymer. The presence of PLLA prevented the low-viscosity pre-polymer of PGS from enclosing interconnected open-cell structure during the curing stage, thereby avoiding structural collapse of the scaffold. This novel versatile approach will simplify the fabrication of large and porous PGS-based scaffolds for soft tissue engineering.

The above PGS/PLLA blend scaffolds were optimised to achieve similar bulk mechanical properties to those of native low and high stress adapted adipose tissue. The scaffolds were fabricated by using two different organic solvents and presented suitable porous structures for cell penetration and growth for prospective applications in ATE.

The development of poly(glycerol sebacate urethane) (PGSU) scaffolds via the freeze-drying process allowed to enhance the mechanical properties, the degradation behaviour and the fabrication simplicity, in comparison to the prior fabricated PGS/PLLA blend scaffolds. The PGSU scaffolds were successfully fabricated with three different molar ratios of hexamethylene diisocyanate, without the necessity of an additional curing stage and a minor structure-supporting biopolymer. The scaffolds were stretchable, featured long-term stability

and tuneable degradation kinetics, demonstrating great potential for applications in ATE and in other fields of soft tissue engineering.

Despite the highly interesting properties, the previously applied PGS-based materials presented limited water absorption and diffusion capabilities. Therefore, novel biodegradable PGS-based polyurethane hydrogels were successfully synthesised via the pre-polymer of PGS and isocyanate-terminated poly(ethylene glycol)s with varying molecular weights. The hydrogels featured high flexibility and strechability, enhanced hydrophilicity and good biodegradability and biocompatibility, as well as thermoresponsivity. The hydrogels were evaluated for potential applications in ATE and other fields of soft tissue engineering. Additionally, its implementation for drug delivery, thermal actuation and ultralow power generation applications has been examined.

Overall, PGS-based scaffolds and hydrogels present great potential in ATE and will further advance this field of research.

Contents

List of figures

List of schemes

List of tables

List of abbreviations

^{1}H NMR	Proton nuclear magnetic resonance spectroscopy
2D	Two-dimensional
3D	Three-dimensional
ADSC	Adipose-derived stem cell
ASTM	American Society for Testing and Materials
ATE	Adipose tissue engineering
ATR	Attenuated total reflection mode
BAT	Brown adipose tissue
BDSC	Bone marrow-derived stem cell
$CDCl_3$	Chloroform
DMEM	Dulbecco's modified Eagle's medium
DMC	Dimethyl carbonate
DMF	Dimethylformamide
DPX	Dibutyl phthalate xylene
DSC	Differential scanning calorimetry
ECM	Extracellular matrix
FCS	Fetal calf serum
FDA	United States Food and Drug Administration
FIB	Fibroblasts
FTIR	Fourier transform infrared spectroscopy
GPC	Gel permeation chromatography
HA	Hydroxyapatite
HDI	Hexamethylene diisocyanate
LM	Laser micro-ablation

MDI	4,4’-diphenylmethylene diisocyanate
NCO	Isocyanate
OCT	Optimal cutting temperature compound
P3HB	Poly(3-hydroxbutyrate)
PANI	Polyaniline
PBS	Phosphate buffer saline
PBS-DLA	Poly(butylene succinate-butylene dilinoleate)
PBT	Poly(butylene terephthalate)
PC	Poly(carbonate)
PCL	Poly(ε-caprolactone)
PDI	Polydispersity index
PDLA	Poly(D-lactic acid)
PEG	Poly(ethylene gycol)
PEG-400	PEG with the a $\bar{M}_n$ of 400 g mol^{-1}
PEG-1000	PEG with the a $\bar{M}_n$ of 950-1050 g mol^{-1}
PEG-1450	PEG with the a $\bar{M}_n$ of 1305-1595 g mol^{-1}
PEGDA	Poly(ethylene glycol) diacrylate
PEGT	Poly(ethylene glycol) terephthalate
PET	Poly(ethylene terephthalate)
PEU	Polyester-based polyurethane
PEU-400	Polyester-based polyurethane, synthesised with PEG-400
PEU-1000	Polyester-based polyurethane, synthesised with PEG-1000
PEU-1450	Polyester-based polyurethane, synthesised with PEG-1450
PGA	Poly(glycolic acid)
PGS	Poly(glycerol sebacate)

PGSCA	Poly(glycerol sebacate citric acid)
PGSGA	Poly(glycerol sebacate glycolic acid)
PGSLA	Poly(glycerol sebacate lactic acid)
PGSU	Poly(glycerol sebacate urethane)
PGS-Acr	Poly(glycerol sebacate) acrylate
PGS-Cin	Poly(glycerol sebacate) cinnamate
PGS-co-PLLA	Poly(glycerol-sebacate)-co-poly(L-lactic acid)
PGS-co-PCL	Poly(glycerol sebacate)-co-poly(ε-caprolactone)
PGS-co-PEG	Poly(glycerol sebacate)-co-poly(ethylene glycol)
PGS-co-PEG-MAc	Poly(glycerol sebacate)-co-poly(ethylene glycol) methacrylate
PGS-Fur	Poly(glycerol sebacate) fumarate
Phalloidin-FITC	Phalloidin-fluorescein isothiocyanate
PHBV	Poly(3-hydroxybutyrate-co-3-hydroxyvalerate)
PLA	Poly(lactic acid)
PLDLLA	Poly(L-lactide-co-D,L-lacitide)
PLLA	Poly(L-lactic acid)
PLGA	Poly(lactic-co-glycolic acid)
PNIPAM	Poly(N-isopropylacrylamide)
PP	Poly(propylene)
PTFE	Poly(tetrafluoroethylene)
PU	Polyurethane
Pre-400	NCO-terminated PEG-400
Pre-1000	NCO-terminated PEG-1000
Pre-1450	NCO-terminated PEG-1450
Pre-PGS	Poly(glycerol sebacate) pre-polymer

PVA	Poly(vinyl alcohol)
SD	Standard deviation
SFF	Solid free-form
SEM	Scanning electron microscopy
SVF	Stromal vascular fraction
Tin(II)	Tin(II) 2-ethylhexanoate
THF	Tetrahydrofuran
Trypsin-EDTA	Trypsin-ethylenediaminetetraacetic acid
UTS	Ultimate tensile strength
UV	Ultraviolet
UV-Vis	Ultraviolet-Visible light
WAT	White adipose tissue

List of symbols

α	Deformation ratio
A	Ampere, frequently prefixed with m for milli-
°C	Degree Celsius
χ	Flory–Huggins parameter
e_0	Input strain-energy density of the loading curve
e_d	Dissipated energy
e_r	Retraction strain-energy density of the unloading curve
E_c	Young's modulus of solid or porous material (compressive)
E_s	Young's modulus of solid material (tensile)
E_t	Young's modulus of porous material (tensile)
E_t/ρ_f	Specific Young's modulus
ε_c	Compressive collapse strain of solid or porous material
ε_{sb}	Elongation at break of solid material (tensile)
$\varepsilon_{t\sigma max}$	Elongation at ultimate tensile strength of porous material (tensile)
g	Gram, frequently prefixed with µ for micro-, m for milli-, M for mega-
G'	Storage modulus
G''	Loss modulus
h	Hours
Hz	Hertz, frequently prefixed with M for mega-
h_r	Hysteresis loss ratio
IU	International unit
lm	Luminous flux
L	Litre, frequently prefixed with m for milli-

m	meter, frequently prefixed with n for nano-, µ for micro-, m for milli-, c for centi-
min	Minute
mol	Mole, frequently prefixed with m for milli-
$\bar{M}_n$	Number average molecular weight
$\bar{M}_w$	Weight average molecular weight
n_{eff}	Effective crosslink density
n_{mech}	Crosslink density, evaluated by mechanical measurements
n_{swell}	Crosslink density, evaluated by swelling measurements
N	Newton
p	Significance
P_f	Porosity of scaffold
Pa	Pascal, frequently prefixed with m for milli-, M for mega-, G for giga-
Pixel	Picture element
ϕ_2	Polymer volume ratio in the swollen state
ϕ_0	Polymer volume ratio in the relaxed state
φ_{PGS}	Volume ratio of PGS
φ_{PLLA}	Volume ratio of PLLA
Q_∞	Weight swelling degree at equilibrium
rpm	Revolutions per minute
R	Universal gas constant
ρ_f	Density of porous scaffold
$\rho_{f-matrix}$	Theoretical density of the solid matrix that constructs scaffolds
$\rho_{heptane}$	Density of heptane
ρ_{PGS}	Density of PGS

ρ_{PGSU}	Density of PGSU
ρ_{PLLA}	Density of PLLA
ρ_r	Relative density
ρ_{THF}	Density of THF
s	Second, frequently prefixed with µ for micro-,
σ_{smax}	Ultimate tensile strength of solid material (tensile)
σ_{tmax}	Ultimate tensile strength of porous material (tensile)
σ_{tmax}/ρ_f	Specific tensile strength
σ_c	Compressive stress of solid or porous material
$\sigma_{c50\%}$	Compressive stress at 50% strain of solid or porous material
$\sigma_{c75\%}$	Compressive stress at 75% strain of solid or porous material
T	Absolute temperature
T_c	Crystallisation temperature
T_g	Glass transition temperature
T_m	Melting temperature
U	Unit
U_{sb}	Energy at break of solid material (tensile)
v/v	Percentage volume for volume
vol%	Volume percentage
V	Volt, frequently prefixed with k for kilo-
V_m	Molar volume
υ_{dry}	Polymer volume fraction in the dry state
$\upsilon_{relaxed}$	Polymer volume fraction in the relaxed state
$\upsilon_{swollen}$	Polymer volume fraction in the swollen state
υ_∞	Polymer volume fraction at equilibrium

w/v	Percentage weight for volume
wt%	Weight percentage
w_{PGS}	Weight fraction of PGS
w_{PLLA}	Weight fraction of PLLA
W	Watt, frequently prefixed with m for milli-
W_0	Weight before incubation
W_{air}	Weight in air
W_{day}	Weight at the given incubation day
W_{dry}	Weight at dry state
$W_{heptane}$	Weight in n-heptane
W_{loss}	Weight loss
W_∞	Weight at equilibrium

List of publications

The following journal papers are based on the research work from this thesis:

- M. Frydrych and B. Chen, "Large three-dimensional poly(glycerol sebacate)-based scaffolds – a freeze-drying preparation approach", *J. Mater. Chem. B,* 2013, **1**, 6650–6661.
- M. Frydrych, S. Román, S. MacNeil, and B. Chen, "Biomimetic poly(glycerol sebacate)/poly(L-lactic acid) blend scaffolds for adipose tissue engineering", *Acta Biomater.*, 2015, **18**, 40–49.
- M. Frydrych, S. Román, Nicola H. Green, S. MacNeil, and B. Chen, "Thermoresponsive, stretchable, biodegradable and biocompatible poly(glycerol sebacate)-based polyurethane hydrogels", *Polym. Chem.*, 2015, **6**, 7974–7987.
- M. Frydrych and B. Chen, "Structure and properties of stretchable and biodegradable poly(glycerol sebacate urethane) scaffolds", In preparation.

The following journal paper is relevant to this thesis:

- T. Wu[†], M. Frydrych[†], K. O'Kelly, B. Chen, "Poly(glycerol sebacate urethane)–cellulose nanocomposites with water-active shape-memory effects" *Biomacromolecules,* 2014, **15**, 2663–2671. [†]These two authors contributed to the work equally.

Chapter 1. Introduction

Tissue engineering is an extensively evolving field of research which combines the fundamental principles of biomaterials and biochemical engineering with cell biology to develop complex artificial tissues and organs, addressing the current clinical limitations in using either autologous or allogeneic grafts in traditional implantation approaches [1,2]. Numerous tissue engineering strategies have been developed during the last decades with promising results in a wide variety of tissue engineering applications, with significant market potential in the healthcare sector [3,4].

Adipose tissue engineering (ATE) aims to restore soft tissue defects, and studies have shown that the regeneration of adipose tissue is possible via engineered natural or synthetic tissue substitutes *in vitro* and *in vivo*, offering potential alternatives to current clinical treatment options [5,6]. With respect to synthetic engineered substitutes, common biodegradable and biocompatible synthetic polymers with inappropriate physical properties were primarily used with limited attempts to adopt the structure and properties of adipose tissue [5–9]. Unfortunately, most of the biodegradable and biocompatible synthetic polymers available today do not provide satisfactory performance in soft tissue applications, due to their high stiffness, plastic deformation and mechanical failure when exposed to cyclic loads, thus, restraining their clinical use [10,11]. Research studies demonstrated that mechanically appropriate scaffolds are beneficial in terms of mechanical signal transmission and stimulation which can be beneficial for cell differentiation and proliferation [12,13]. Therefore, the optimal adipose tissue substitute remains illusive and the research for new biodegradable polymer scaffolds is needed.

Synthetic biodegradable and biocompatible elastomers are a relatively new class of polymers and have recently gained much attention in the field of soft tissue engineering [14,15]. Synthetic bioelastomers feature attractive elastomeric properties and can withstand

highly dynamic mechanical environments *in vitro* and *in vivo* [14,15]. Thus, the developments of functionally compliant and mechanically flexible scaffolds from synthetic bioelastomers are highly interesting for soft tissue engineering applications where non-elastomeric synthetic biodegradable polymers are currently mainly used [14,15].

Among the new class of emerging synthetic biodegradable and biocompatible elastomers, poly(glycerol sebacate) (PGS) has gained most attention in recent years [16,17]. PGS showed great potential for a variety of biomedical applications and featured tailorable mechanical properties to match specific tissue requirements [16,17]. It demonstrated good *in vitro* and *in vivo* biocompatibility and is characterised with relatively linear degradation kinetics, low swelling properties and good retention of mechanical strength relative to the mass loss [16,17]. PGS is synthesised via a polycondensation reaction of glycerol and sebacic acid, forming a meltable and soluble pre-polymer which is subsequently cured to create a covalently crosslinked network [16,17]. However, in contrast to other synthetic biopolymers, PGS reveals a set of limitations and various challenges in manufacturing large three-dimensional (3D) scaffolds, overall constraining the full potential and adoption of PGS in a broader field of soft tissue engineering applications.

The overall aim of this research is to design and develop biomimetic tissue scaffolds based on PGS with similar bulk mechanical properties to those of adipose tissue and with appropriate porous structures suitable for cell penetration and growth for potential application in ATE. There are four objectives associated with this research, which are outlined below:

- To develop a novel fabrication strategy to create large and porous 3D PGS-based scaffolds, by applying the freeze-drying technique, with enhancements in terms of fabrication simplicity, flexibility and efficiency, in comparison to previous fabrication methods.

- To engineer large PGS-based scaffolds for ATE with similar bulk mechanical properties to those of adipose tissue, and investigate the porous structure, the mechanical properties, the degradation behaviour and the biocompatibility of the biomimetic scaffolds.
- To create large PGS copolymer scaffolds for ATE with similar bulk mechanical properties to those of adipose tissue, with enhancements in terms of soft and flexible mechanical properties, tuneable degradation behaviour as well as fabrication simplicity.
- To develop novel PGS copolymer hydrogels for ATE with enhanced hydrophilic properties, and investigate the mechanical properties, the degradation behaviour and the biocompatibility.

The novel fabrication and synthesis approach of elastomeric PGS-based scaffolds and hydrogels are expected to help advancing ATE and other fields of soft tissue engineering.

Chapter 2. Literature review

2.1 Tissue engineering

Tissue engineering is an interdisciplinary field which unites the principles of engineering and life sciences [18]. The main objective of tissue engineering is the regeneration of damaged tissues or organs through the use of artificial substitutes in structure and function, thus eliminating the need for patients to obtain tissue or organ transplants, either autologous or from designated donors. The transplantation of tissue and organ is besieged with medical and ethical concerns [19–22], such as the rising ageing population and the growing shortage in donor organ availability [23,24]. Thus, new state-of-the-art technologies and tissue engineering strategies are urgently needed to eliminate these concerns [18,25].

Tissue engineering strategies are derived from three basic components, which involves the combination of cells, signals and scaffold, otherwise known as the tissue engineering triad [26]. The cells must express stable genotype and appropriate phenotype in order to regenerate the tissue and its specific functions, which can encompass autologous cells from the host tissue or various stem cell sources [26,27]. The signalling system should direct the growth and differentiation of cells via chemical or physical stimuli, involving growth factors and cytokines, or bioreactors [28], while the scaffold acts as a framework for cell migration and tissue growth [29]. The scaffold matrix should degrade gradually upon implantation and be replaced by the cell secreted extracellular matrix (ECM). In fact, each of these basic tissue engineering components can be used individually or in combination to restore or regenerate functional tissues [30].

Two fundamental fabrication strategies were developed for engineering fully functional tissues and organs, the so-called bottom-up and top-down approaches [31,32]. Each of the approaches has its own strength and weakness and is suitable for different tissue engineering

applications [31]. The bottom-up approach uses different fabrication techniques to create modular micro-tissues, which can be assembled into larger scales of tissues with specific and complex structural features [31]. It aims to create more biomimetic engineered tissues by mimicking the physiological microstructural functions of native tissue [31]. The modular micro-tissues can be fabricated via cell aggregation, cell sheeting, cell-laden microfabrication and direct three-dimensional cell printing [33–36]. The engineered micro-tissues can be subsequently assembled into larger tissues with specific architectural features via random packing, stacking of layers or directed assembly [35,37,38]. Hence, the use of the different fabrication and assemble techniques on a microscale, allows one to guide tissue growth and morphogenesis on a cellular level.

The top-down approach is the most commonly used strategy for tissue engineering [32], in which cells are seeded on scaffold constructs, resulting in the formation of new tissue. The cells adhere, proliferate and regenerate new ECM within the scaffold [30], frequently assisted via perfusion, growth factors and/or mechanical stimulation. In this approach, a highly porous scaffold structure is needed to accommodate the seeded cells to support their growth and tissue regeneration in 3D. An ideal scaffold must fulfil many requirements to be considered for tissue engineering applications [2,39]. The scaffold material must be biocompatible and should feature bioactivity to promote cell adhesion, differentiation and proliferation [2,39]. The biodegradability and the mechanical properties of the scaffold are two further important characteristics and often depend on the application [2,39]. Ideally, the scaffold should be made from a material with a controllable biodegradation profile which closely matches the regeneration profile of the desired native tissue, while the biodegradation products should not induce any adverse response [40]. The mechanical properties of the scaffold should also match the anatomical site of implantation and possess sufficient mechanical integrity to support tissue growth, particularly during the early stages [2,41]. In addition, the scaffold

should be easily fabricated into a variety of shapes and sizes, and possess highly inter-connected 3D porous structures with appropriate pore sizes, porosities and large surface areas [2,39]. The void space within the scaffold is not only essential for cell migration and tissue growth, but also for the diffusion of nutrients and waste products [2,39,41].

2.2 Adipose tissue engineering

2.2.1 Introduction to adipose tissue engineering

ATE aims to regenerate soft tissue defects caused by complex traumas, oncologic resections and congenital abnormalities, as well as confronting the current clinical limitation of autologous adipose tissue transplantation [5,6]. Soft tissue defects can lead to cosmetic abnormalities, functional impairments and affect the patient's emotional and psychological well-being [6]. In 2014, approximately 5.8 million reconstructive procedures were performed in the United States of America, with 4.4 million cases related with tumour removal [42].

Current conventional soft tissue reconstruction strategies primarily involve autologous adipose tissue transplantation, including autologous composite tissue flaps which contain two or more tissue elements, or commercially available synthetic implants or fillers [5,43]. The transfer of large autologous tissues remains the gold standard for soft tissue reconstruction, however, this technique requires complex surgical procedures with unpredictable clinical outcome, due to the absorption and subsequent volume loss of the transplanted adipose tissues with 40-60% graft volume reduction [6]. In particular the lack of sufficient revascularisation limits the long-term tissue viability and is one of the main reasons for tissue resorption [6,44,45]. Studies showed that the transplantation of small volumes of autologous adipose tissue can succeed through diffusion, however, the transplantation of small tissue volumes is clinically irrelevant for most soft tissue defects [6,46,47]. The application of synthetic implants and fillers are associated with immune response and rejection, along with migration

and resorption issues, and consequent failure in host tissue integration [7,43]. In addition, because of the large volumes of specific adipose tissue depots in humans, current clinical requirements seek engineered constructs of considerable size in the order of several cubic centimetres which is still unfulfilled in ATE [8]. Despite recent successful achievements and progress in the field of adipose tissue reconstruction [48,49], new techniques and materials are needed.

ATE aims to address these challenges and shows the potential to facilitate large volume soft tissue augmentation, enabling the development of synthetic tissue constructs which can imitate adipose tissue, both structurally and functionally [5]. Thus, the development of new ATE strategies is essential for the soft tissue restoration [50].

2.2.2 Physiology and cellular components of adipose tissue

Adipose tissue, commonly known as fat, is distributed throughout the human body and forms a specialised connective soft tissue [51]. Adipose tissue can be differentiated between two major types in humans [51]: brown adipose tissue (BAT) and white adipose tissue (WAT). The basic functions of both adipose tissue types are the insulation and cushion of the body, as well as the main storage sites for energy in form of triglycerides [51]. BAT, which provides a high vascularity, is mainly found in infants and responsible for the heat generation in the early stage at birth and decreases during the body ageing, while WAT content gradually increases [52,53]. WAT, shown in Figure 2.1, is the most prominent form of the adipose tissue, which not only serves as the main energy reservoir, but is also associated with metabolic functions and is involved in various pathological syndromes [54,55]. Even though WAT is not as highly vascularised as BAT, it features a sufficiently vascularised network, in which all adipocytes are in contact with at least one capillary, supporting active metabolism and allowing a continuous growth of the tissue [56,57]. Beside the extensive system of blood vessels, it also contains a network of lymph nodes and nerves, which are supported by the ECM structure.

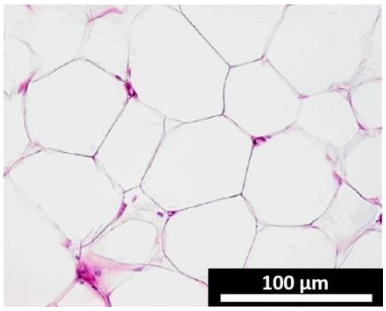

Figure 2.1: Light micrograph of human WAT, stained with haematoxylin and eosin. Adapted from Cinti *et al.* [58] with permission from Elsevier, copyright 2005.

WAT can be categorised by depot and location and can be found in areas all over the body: subcutaneous (cranial, facial, abdominal, gluteal and extremity), intra-abdominal (omental, retroperitoneal, visceral) and other sites (retro-orbital, periarticular regions, bone marrow, intramuscular, pericardial), within which the subcutaneous and intra-abdominal depots form the main compartments for WAT storage [59]. In an adult organism, WAT undergoes a continuous process of remodelling and is the only tissue that can significantly change its mass [60]. The normal weight percentage of WAT mass in adult humans, in respect to the total body weight, are between the values of 9-18% in males and 14-28% in females, while athletes reach low values of 2-3% whereas extremely obese individuals have high values of 60-70% [61].

The predominant cellular components of adipose tissue are adipocytes, also known as lipocytes or fat cells, which are composed of lipidic fluid (60-85 wt%), water (5-30 wt%) and protein (2-3 wt%) [51]. The lipidic fluid consists of 90-99% triglycerides, free fatty acids, diglycerides, cholesterol phospholipids, as well as cholesterol ester and monoglycerides [51]. Adipocytes contain a large and centrally located lipid droplet, surrounded by cytoplasm and a peripheral located nucleus, while the cells themselves are characterised by spherical or polyhedral shapes with diameters in the rage of 80-180 µm (depending on the degree of obesity) [62,63]. The size and number of adipocytes can influence the mass and volume of

adipose tissue [51]. Fully differentiated adipocytes do not proliferate but can increase or decrease in size, primarily through the accumulation of lipid fluid within the cells, which depends on the energy intake and expenditure [64]. The development of new adipocytes involves the proliferation of preadipocytes, which can differentiate into mature adipocytes for adipose tissue renewal or expansion [50].

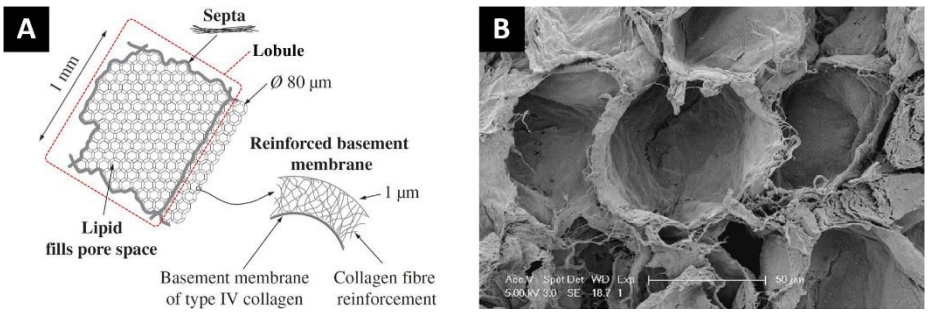

Figure 2.2: (A) Schematic of a lobule (fat cell cluster) of adipose tissue. (B) Scanning electron microscopic (SEM) images of the reinforced basement membrane of porcine adipose tissue. Adapted and modified from Comley *et al.* [65] with permission from Elsevier, copyright 2010.

As seen in Figure 2.2 (A, B), adipocytes are organised in lobules (fat cell clusters) and enclosed within ECM structures, the so-called reinforced basement membrane and interlobular septa, predominately composed of collagen types I, III, IV, V and VI [66]. Both inter-penetrating structures form a complex 3D network in which the reinforced basement membrane creates a 3D closed-cell structure, where the cavities are filled by adipocytes, while the interlobular septa interact as a reinforcement base by establishing a 3D open-cell structure throughout the basement membrane [62]. Studies indicated that the reinforced basement membrane has a thickness of around ~1 µm, while the interlobular septa consists of long fibrous bundles of several millimetres in length and diameters of up to 30 µm [65,67]. In addition to adipocytes and preadipocytes, other cell types such as fibroblasts, endothelial cells, various immune cells and stem cells are present in adipose tissue. However, the cellular composition of adipose tissue depends on its type, depot, and anatomical location [68,69].

2.2.3 Mechanical properties of adipose tissue

Adipose tissue is a viscoelastic soft tissue which is physiologically exposed to large deformations that are associated with body weight loads and weight-bearing [12,70,71]. From the mechanical point of view, adipose tissue can be considered as a closed-cell foam with cavities of fluid-filled adipocytes [72]. As discussed in Section 2.2.2, the adipocytes are enclosed within a 3D collagen network that is based on the reinforced basement membrane and the fibrous interlobular septa, which form an inter-penetrating closed- and open-cell foam [62,65], respectively. Although majority of the adipose tissue volume consists of the adipocytes lipid content [64], research studies demonstrated that the lipid droplets can be idealised as an incompressible inviscid fluid and yields a negligible contribution to the modulus of adipose tissue [62,65]. With this respect, porcine lipid exhibited a viscosity in the range of 37-61 mPa s, depending on the test temperature [65]. The mechanical properties of adipose tissue are therefore mainly dictated by the reinforced basement membrane, while the low volume fraction of the interlobular septa provides a less dominant contribution [62,65]. However, recent studies showed that the alignment of the fibrous interlobular septa causes mechanical anisotropy in adipose tissue [73].

The mechanical properties of adipose tissue were determined via tension tests [72,74], compression tests [62,72,75,76], indentation tests [77,78] and via elastography [79,80]. Adipose tissue showed in general a nonlinear dependency upon strain rate [65,72]. Adipose tissue exhibits under tension and compression a nonlinear stress versus strain response at large strain levels, while at low strain levels the response is linear [65,67,72]. At strains greater than 25-30%, adipose tissue 'locks up' and the stress level increases rapidly [65,67,81]. Also, the mechanical investigation under tension indicated higher risks of adipose tissue tearing at strains greater than 30%, although large strains do occur *in vivo* [12,70,71,73]. In normal human physiology, e.g. during normal sitting or lying, adipose tissue is exposed to

large physiological deformations [12,70,71,82]. For instance, a sitting posture induces peak tensile, compressive and shear strains of ~30%, ~45% and ~40% on the anatomical site related adipose tissues, while a lying posture induces approximately half these loads on the same anatomical locations [12,70,71,82].

Research studies indicated that the mechanical properties of adipose tissue depend on the anatomical site and function [76], similar to the structure-function relationships in other human tissues [83]. For instance, Alkhouli *et al.* [73] compared the mechanical properties of human subcutaneous and omental adipose tissues, which have different physiological functions, demonstrating that subcutaneous adipose tissue features greater expansion and recovery capabilities from mechanical deformation than omental adipose tissue. Other studies concerning the analysis of adipose tissue from human abdomen [76,84], breast [76–78,85] and heel pads [76,80,86] demonstrated similar structure-function relationships. Studies determined that low stress adapted adipose tissue from abdomen and breast features a Young's modulus in the range of 0.0003-0.003 MPa [76,84] and 0.003-0.024 MPa [76–78,85], while high stress adapted adipose tissue samples from the heel pads obtained results in the range of 0.024-0.18 MPa [76,80,86]. Hence, adipose tissue from the heel pad is exposed to intense mechanical loads, while the adipose tissue from abdomen and breast do not ordinarily bear high loads [76].

Rheological shear experiments on adipose tissue revealed that the linear regime is only valid for very small strains up to 0.1%, in which the storage and loss modulus showed a frequency and temperature dependent behaviour [67,87]. In addition, animal subcutaneous and orbital adipose tissue were characterised with an elastic and viscous shear moduli in the range of 0.0003-0.0009 MPa and 0.0001-0.0005 MPa [81,88], while adipose tissue from animal kidneys featured greater elastic and viscous shear moduli of 0.003-0.005 MPa and 0.001-0.003 MPa [88], respectively. Dynamic tests showed that adipose tissue becomes less

firm and diverge with increasing forces, strains and frequencies, as well as poor form recoverability after induced deformations [84].

2.2.4 Cell sources for adipose tissue engineering

Cell sources for ATE must satisfy several critical characteristics and should ideally be autologous or non-immunogenic, be readily available and obtainable via minimally invasive procedures [8]. Most ATE strategies involved the utilisation of preadipocyte cell lines or stem cells, either embryonic or adult [5,7,8,50]. The transplantation of mature adipocytes is limited, due to their fragile nature and susceptibility to ischemic cell death, resulting in poor volume retention abilities [7,8,89]. Fully differentiated adipocytes do not proliferate, restraining their growth and regeneration potential in the site of tissue damage [7,50]. Thus, the transplantation of large adipose tissue volumes have been demonstrated to be inadequate in terms of tissue regeneration and volume stability, due to the insufficient angiogenesis [90].

Preadipocyte cell lines from autologous, allogeneic or xenogeneic origin were utilised in ATE applications, analysing their potential in various two-dimensional (2D) and 3D culture environments for adipogenic differentiation and formation of adipose tissue [7,8]. Preadipocytes can be expanded in culture, are mechanically stable and are acquirable from biopsies or liposuction aspirates [50,91,92]. However, experimental studies in ATE primarily use 3T3-L1 cells as preadipocyte surrogates, which are not considered to be suitable for clinical applications because of their aneuploid status and xenogeneic origin [7,8].

The application of embryonic or adult stem cell sources for ATE has been dominated in the recent years and many studies have demonstrated that these cells possess the capability of adipogenic differentiation, and presented the formation of adipose tissue both *in vitro* and *in vivo* [5,7,8,50]. Stem cells are unspecialised cells which are capable of dividing and renewing themselves for long periods, and can differentiate into a wide variety of other specialised cell types [8,50]. Embryonic stem cells appear to be an appropriate cell source for

soft tissue reconstructions, however, only limited quantities of ATE related studies have been performed with these types of cells, because of ethical concerns and legal constraints [5,8,50]. With this respect, most cell-based approaches in ATE used adult stem cells, derived from bone marrow or adipose tissue [5,7,8,50]. Both bone marrow-derived stem cells (BDSCs) and adipose-derived stem cells (ADSCs) have been successfully employed in ATE and yielded similar good outcomes in the context of adipose tissue formation, when cultured with the appropriate lineage specific stimuli [5,50].

BDSCs are multipotent cells, capable of differentiating into lineages of multiple cell types and are obtainable via bone marrow aspiration or biopsy procedures [8]. However, extensive *in vitro* culture expansion of BDSCs are necessary, due to the relatively low yield of stem cells derived from bone marrow [93,94], while the differentiation capacity of BDCSs tends to decline with increasing time and passage in culture [95]. In addition, the harvesting procedures are relatively inconvenient and painful for the autologous or allogeneic donors [93,94].

ADSCs are a strong alternative cell source for ATE and easily obtainable via liposuction or abdominoplasty from the stromal vascular fraction (SVF) of adipose tissue [50,69]. ADCSs are also multipotent cells, available in abundance and expendable quantities, and are easier to harvest than BDSCs [96,97]. In addition, when the differentiation capacities of both stem cell types are directly compared, ADSCs presented a more efficient differentiation towards adipocytes, whereas BDSCs differentiated better into osteocytes and chondrocytes [98]. However, the yield, differentiation and growth characteristics of ADSCs depend on various factors, such as sex, age and health status of the donor, in addition to the used anatomic site and isolation method [97,99]. Nevertheless, ADSCs demonstrated to be a highly promising cell source for ATE and future clinical research studies and therapies.

2.2.5 Current adipose tissue engineering strategies

Several ATE strategies have been investigated to engineer adipose tissue [50], as listed in Table 2.1. The traditional cell-based scaffold guided tissue regeneration method is the most common strategy [8,50], which is based on porous implantable substitutes from various natural and synthetic materials [5,9,50]. Further ATE strategies include the utilisation of cell-seeded microspheres or cell-encapsulated hydrogels [100–108], the acellular approach of *de novo* adipogenesis [109–119], as well as the fragmented omentum based-tissue regeneration method [110].

Table 2.1: Current ATE strategies. Adapted and updated from Gomillion *et al.* [50] with permission from Elsevier, copyright 2006.

ATE strategy	Advantages	Limitations	References
Scaffold guided tissue regeneration	Shape definition; Shape maintenance	Surgical procedures necessary; Volume reduction of implants over time if biodegradable materials are used	[5,9,50]
Injectable cell-seeded microspheres or cell-encapsulated hydrogels	Avoidance of surgical procedures; Filling of irregularly shaped defect sites	Control over shape and dimension of the newly developed adipose tissue is limited; Volume reduction of implants over time if biodegradable materials are used	[100–108]
De novo adipogenesis	Avoidance of cell harvesting; Avoidance of *in vitro* culture processes; Immunological compatibility	Surgical procedures necessary if non-injectable materials are used; Volume reduction of implants over time if biodegradable materials are used	[109–119]
Fragmented omentum based-tissue regeneration	Native ECM; Highly vascularised	Surgical procedures necessary; Tissue availability; Graft volume reduction	[110]

Scaffold guided tissue regeneration

The scaffold guided tissue redevelopment strategy utilises 3D porous scaffolds to mimic the target tissue environment and to provide a support structure for cell ingrowth and proliferation [5,50]. The *in vivo* implantation of appropriate cell-seeded scaffolds into the patient defect site would provide the creation of new tissue, while the scaffold material degrades and gets absorbed over time. This process is generally applied for the cell-based regeneration approach

in ATE, regardless of the scaffold material [50]. In this context, engineered scaffolds for adipose tissue substitutes should meet critical criteria such as host compatibility (minimal to no immune response of host and appropriate degradation characteristics), bioactivity (cell adhesion and proliferation, cell-cell contact and cell migration along with the incorporation of an efficient vascular supply), sustainability (long-term viability) as well as a high porosity with suitable pore interconnectivity and matching the mechanical properties of adipose tissue [5,50]. Ideal biodegradable polymeric materials for ATE should feature degradation times of minimum 180 days to support the complete adipose tissue development *in vivo* [120,121].

Injectable cell-seeded microspheres or cell-encapsulated hydrogels

The use of injectable cell-seeded microspheres or cell-encapsulated hydrogels enables the direct treatment of the patient defect site via syringe injections [100–108,122]. Anchorage-dependent cells, like preadipocytes, adipocytes and stem cells [50,123], need an attachable matrix for cell differentiation and proliferation, which the injectable carrier systems allow. Various injectable cell carriers based on synthetic and natural biocompatible and biodegradable materials were developed, which overall presented attractive properties in terms of low infection risk, minimal scarring and reduced treatment costs, due to the avoidance of complex surgeries [8,122]. A further advantage of injectable cell carriers is the possibility to fill irregularly shaped defect sites [8,122]. However, the control over shape and dimension of the newly developed adipose tissue is limited [8,122]. The volume reduction of implanted cell carriers is unavoidable due to the material resorption over time, and subsequent injections to the defect site will be required in order to restore the original volume [50,122].

De novo adipogenesis

The *de novo* adipogenesis tissue strategy is based on the *in vivo* implantation of acellular tissue engineered replacements, which contain growth factors and stimulate the migration of

preadipocyte cells to the implant site [109–119]. The cells subsequently differentiate and proliferate into adipocytes to form connected adipose tissue [50]. Different growth factors were used and tested, amongst which particular isoforms of fibroblast growth factors (FGF) were involved. These factors demonstrated good adipogenesis and angiogenesis stimulation and the acceleration of cell differentiation [109–116]. Techniques such as the injection of hydrogels or microsphere systems, as well as the implantation of scaffold constructs within the defect site were used for the *de novo* adipogenesis strategy. The advantage of these techniques is the avoidance of complications associated with cell harvesting and immunological compatibility, as well as the necessity of cost- and time-intensive *in vitro* culture processes [124].

Fragmented omentum based-tissue regeneration

Another ATE strategy for adipose tissue regeneration is the utilisation of fragmented omentum tissue from the donor site of the patient [110]. The omentum is a highly vascularised membrane and includes a great amount of adipose tissue. It covers and supports various organs in the abdomen, while a distinction is made between the lesser and greater omentum, which are located above the stomach and below the small intestine, respectively [110]. Masuda *et al.* [110] demonstrated that the *in vivo* implantation of fragmented omentum tissue with preadipocytes has the capability to form adipose tissue.

2.2.6 Polymers for adipose tissue engineering

2.2.6.1 Natural polymers

Natural polymers are derived from the native ECM or created by biological systems [125]. Various natural polymers have been used for ATE, demonstrating good biodegradability and high biocompatibility in conjunction with good adipogenesis support [5,7,8]. The most common natural polymers utilised for ATE applications are collagen [106,116,126–137],

hyaluronan [43,102,138–145] and matrigel [109,111–113,117,119,130,146–152], which will be further discussed. Other natural polymers which demonstrate potential for adipose tissue replacements include alginate [153–156], fibrin [157–161], gelatin [109,112,116,129,162,163] and silk [127,164–166], as well as adipose-derived ECM [146,167,168] and decellurised human placenta [43,66,138,139]. These natural polymers have been utilised in many forms, including scaffolds, fibres, hydrogels and microspheres [5–9,122]. Although varying degrees of success have been reported by using natural polymers in ATE, this thesis will primarily focus on the application of synthetic polymers. Reviews of natural polymers utilised in ATE have been previously reported [5–9,122] and Table 2.2 presents a summary.

Table 2.2: Natural materials used in ATE. Adapted and updated from Choi *et al.* [5] with permission from Mary Ann Liebert, copyright 2010.

Natural materials	Advantages	Limitations	References
Collagen	Component of native ECM	Fast degradation rates; Toxic crosslinking reagents	[106,107,116,126–137]
Hyaluronan	Favourable mechanical properties	Minimal adipose tissue formation	[43,102,138–145]
Matrigel	Favourable mechanical properties; Supports adipogenesis	Tumour-derived xenogeneic origin	[109,111–113,117,119, 130,146–152]
Alginate	Favourable mechanical properties	Minimal adipose tissue formation; Fast degradation rates;	[108,153–156]
Fibrin	Favourable mechanical properties; Supports adipogenesis	Fast degradation rates	[157–161]
Gelatin	Supports adipogenesis	Fast degradation rates; Toxic crosslinking reagents	[109,112,116,129,162, 163]
Silk	Favourable mechanical properties; Supports adipogenesis; Slow degradation rates	Processability	[127,164–166]
Adipose-derived ECM	Native ECM	Material availability; Isolation and preparation procedure	[146,167,168]
Decellurised human placenta	Native ECM	Material availability; Isolation and preparation procedure	[43,66,138,139]

Collagen

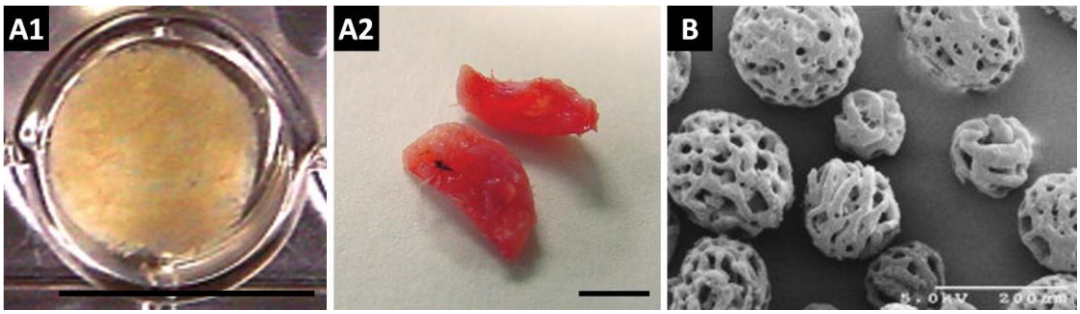

Figure 2.3: Collagen implants in ATE. (A1) Preadipocyte-seeded collagen gel specimen containing short collagen fibres. (A2) Oil Red O stained preadipocyte-seeded collagen gels after 21 days *in vitro* culture, implying the development of lipids (scale bar: (A1) 10 mm; (A2) 5 mm). Adapted from Gentleman *et al.* [132] with permission from Mary Ann Liebert, copyright 2006. (B) Porous collagenous microspheres with diameters ranging from of 100-380 µm, adapted from Rubin *et al.* [106] with permission from Wolters Kluwer Health, copyright 2007.

Collagen is a widely used natural polymer in tissue engineering applications, owing to its similarity in composition to the ECM, and to its low immunogenicity and cytotoxicity [169–171]. In ATE, crosslinked and non-crosslinked collagen substitutes were used [116,132,134], as seen in Figure 2.3 (A1-2, B), which demonstrated adipogenesis support and the development of new adipose tissue *in vivo* [116,129]. Non-crosslinked collagen features in general faster degradation rates *in vivo* [127], while crosslinked collagen exhibits slower degradation rates *in vivo* [131,137], along with enhanced mechanical properties [116,134]. Slower degradation rates and enhanced *in vivo* stability are desired in ATE, however, substitutes with rigid mechanical properties may result in a comfort deficit for the patient [6]. In addition, mainly chemical crosslinking methods were used, involving toxic reagents [116,134].

Hyaluronan

Hyaluronan, also known as hyaluronic acid, is a ubiquitous component in the ECM and plays an important role in terms of cell motility, differentiation and adhesion, as well as in other processes, e.g. wound healing processes and cancer metastasis [172–174]. Hyaluronan is in it natural state highly soluble, poses fast degradation rates and features overall low mechanical properties with compressive Young's modulus, E_c, values of below 0.0001 MPa [175,176], owing to its high viscosity [172–174]. The utilisation of different crosslinking or esterification methods results in an insoluble polymer, characterised with degradation rates of 56 days *in vivo* [139]. In ATE, various hyaluronan based substitutes were implanted *in vivo*, as seen in Figure 2.4 (A, B, C), in which neovascularised structures were observed but relatively weak adipogenic differentiation [144,177].

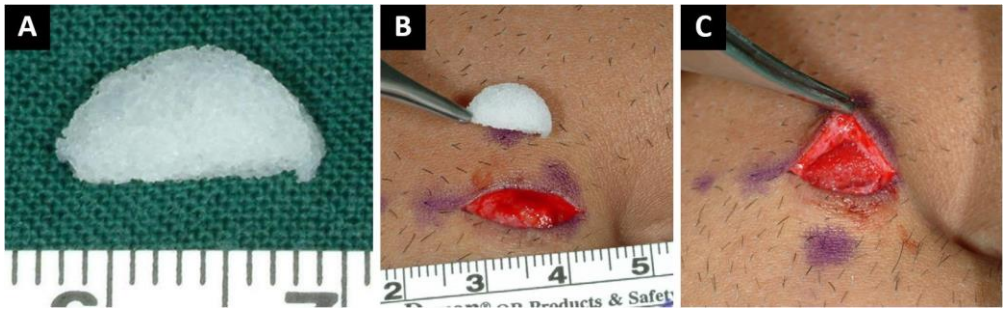

Figure 2.4: Hyaluronic acid-based implants in ATE. (A) Hyaluronic acid-based scaffolds were seeded with preadipocyte and (B, C) implanted *in vivo* (human model) in the subumbilical area in a subcutaneous pocket, adapted from Stillaert *et al.* [144] with permission from Elsevier, copyright 2008.

Matrigel

Matrigel is an ECM-derived biomaterial, based from the Engelbreth-Holm-Swarm mouse sarcoma and contains a range of proteins, including collagen IV, laminin and various growth factors which can promote differentiation and proliferation of various cell lines [178]. Thus, matrigel mimics the complex extracellular environment of many soft tissues and has been extensively used to study cellular responses within 3D environments [130,146]. Matrigel

exhibits high malleability and is characterised with a low E_c in the range of 0.0001-0.0007 MPa [179–182], along with degradation rates of over 42 days *in vivo* [116,147,183]. However, matrigel has only limited potential for clinical applications, due to its tumour-derived xenogeneic origin and its likely immunogenicity [116]. In ATE, matrigel has shown to support adipogenesis from various cell sources and the extensive formation of adipose tissue [7,177], in particular with additional growth factors [109,112,117].

In general, natural polymers have many advantages especially in terms of biocompatibility and adipogenesis support, as well as favourable mechanical properties. However, many natural polymers are limited in supply, reproducibility and application capabilities, due to their fast degradation rates *in vivo*. Further concerns involve the possibility of immunogenic reactions and infection *in vivo* when animal-derived natural polymers are used.

2.2.6.2 Synthetic polymers

Synthetic biocompatible and biodegradable polymers provide a significant advancement in respect to the ability to design tissue scaffolds with predictable and reproducible mechanical, chemical and biodegradation properties [184]. In ATE, considerable work has been performed using polymers such as poly(lactic acid) (PLA) [127,185,186], poly(glycolic acid) (PGA) [121,137,158,162,187] and the copolymer poly(lactic-co-glycolic acid) (PLGA) [91,104,105,118,119,188–194], which are among the most commonly used synthetic polymers in tissue engineering [2,10,39]. Further, synthetic biodegradable materials which showed potential for adipose tissue replacements include hydrogels and polymers formed from varying compositions of poly(ε-caprolactone) (PCL) [120,195], poly(ethylene glycol) (PEG) [84,196–202], poly(ethylene glycol)terephthalate/poly(butylene terephthalate) (PEGT/PBT) [197] and biodegradable polyurethane (PU) [195,203]. Non-degradable synthetic materials such as polycarbonate (PC) [118,119], poly(ethylene terephthalate) (PET)

[204], polypropylene (PP) [128,162], fluoropolymers [205,206] and silicones [117,119] were also investigated for ATE, as listed in Table 2.3.

Table 2.3: Synthetic materials used in ATE. Adapted and updated from Choi *et al.* [5] with permission from Mary Ann Liebert, copyright 2010.

Synthetic materials	Advantages	Limitations	References
Poly(lactic acid)	Biodegradable; Supports adipogenesis; Tailorable	Hydrophobic; Stiff / inflexible	[127,185,186]
Poly(glycolic acid)	Biodegradable; Supports adipogenesis; Tailorable	Fast degradation rates; Hydrophobic; Stiff / inflexible	[121,137,158,162,187]
Poly(lactic-co-glycolic acid)	Biodegradable; Tailorable	Hydrophobic; Stiff / inflexible	[91,104,105,118,119,188–194]
Poly(ε-caprolactone)	Biodegradable; Tailorable	Hydrophobic; Inflexible	[120,195]
Poly(ethylene glycol)[a]	Hydrophilic; Supports adipogenesis; Soft/flexible; Tailorable	Non-biodegradable	[84,196–202]
Poly(ethylene glycol) Terephthalate/poly(butylene terephthalate)	Biodegradable; Hydrophilic; Soft/flexible; Tailorable; Supports adipose tissue formation	Slow degradation rate; Incomplete degradation *in vivo*	[197]
Biodegradable polyurethane	Biodegradable; Flexible; Tailorable	Hydrophobic	[195,203]
Polycarbonate	Shape maintenance	Non-biodegradable; Hydrophobic; Stiff / inflexible	[118,119]
Poly(ethylene terephthalate)	Shape maintenance; Supports adipose tissue formation	Non-biodegradable; Hydrophobic; Stiff / inflexible	[204]
Polypropylene	Shape maintenance	Non-biodegradable; Hydrophobic; Stiff/inflexible	[128,162]
Fluoropolymers	Shape maintenance	Non-biodegradable; Hydrophobic; Stiff / inflexible	[205,206]
Silicones	Shape maintenance	Non-biodegradable; Hydrophobic	[117,119]

[a] Acrylated PEG-based hydrogels were mainly utilised in ATE.

Poly(lactic acid)

PLA is an aliphatic polyester derived from lactic acid monomers and has been used for a wide variety of tissue engineering applications, due to its good biocompatibility and biodegradability [207,208]. It possesses adjustable physicochemical properties, is highly hydrophobic, and is characterised with long degradation times via bulk erosion [207,208]. PLA is a stiff polymer and features a tensile Young's modulus, E_s, ultimate tensile strength, σ_{smax}, and strain at break, ε_{sb}, in the range of 1.57-4.18 GPa, 34.5-67.2 MPa and 2.43-8.57% [209], respectively. Furthermore, PLA has stereoisomers [210], such as poly(L-lactic acid) (PLLA) and poly(D-Lactic acid) (PDLA).

With respect to ATE, Mauney *et al.* [127] investigated the *in vitro* and *in vivo* (athymic nude mouse model) response of human BDSCs and ADSCs on woven PLA meshes for up to 28 days. Cell differentiation into adipocytes was assessed in both *in vitro* and *in vivo*, while the woven PLA meshes degraded completely *in vivo* within the test period. However, silk or collagen scaffolds presented quantitatively higher cell differentiation performances under the same cell culture conditions. In addition, Chaubey *et al.* [186] examined the response of mouse BDSCs on patterned and plain PLLA film surfaces for up to 36 days *in vitro*, demonstrating that the cells fully differentiated into adipocytes, with greater lipid accumulation on the plain PLLA film surfaces.

Poly(glycolic acid)

PGA is an aliphatic polyester derived from glycolic acid monomers, features good biocompatible and biodegradable properties and has been studied for numerous tissue engineering applications [207,208]. It is a highly crystalline polymer and more hydrophilic than PLA, thus it is more easily degradable via bulk erosion. PGA has alterable physicochemical properties and features a E_s, σ_{smax} and ε_{sb} in the ranges of 6.08-7.18 GPa, 60.8-71.8 MPa and 4.61-18.9% [209], respectively.

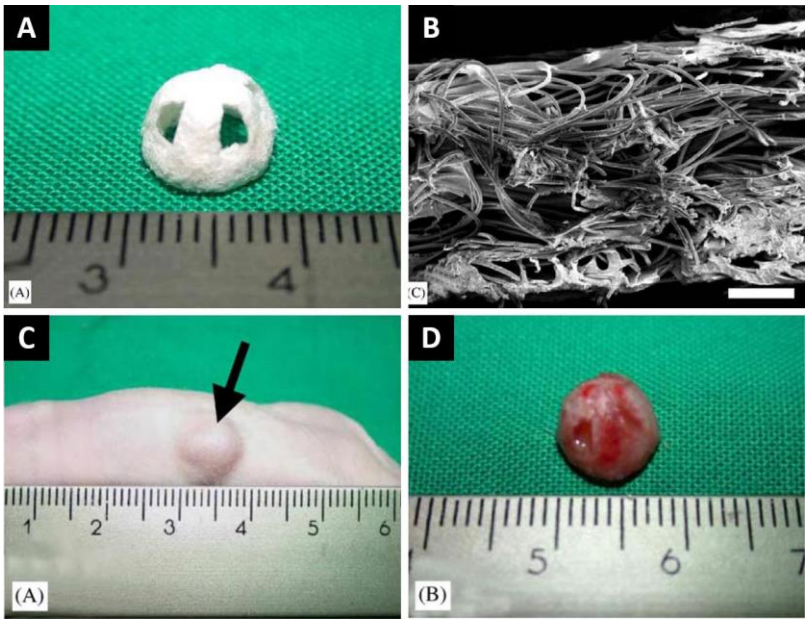

Figure 2.5: PGA scaffolds for ATE. (A) Dome-shaped PGA fibre-based matrix reinforced with PLLA. (B) SEM micrographs of the cross-section of the PGA fibre-based matrix (scale bar: 200 µm). (C) Implanted PGA-based scaffold into the subcutaneous pocket of athymic nude mouse. The arrow indicates the implantation sites. (D) Implant after 42 days *in vivo* implantation. Adapted from Cho *et al.* [158] with permission from Elsevier, copyright 2005.

With regard to ATE, Fischbach *et al.* [187] and Weiser *et al.* [121] analysed the *in vitro* and *in vivo* (athymic nude mouse model) response of murine 3T3-L1 preadipocytes on non-woven PGA meshes for up to 35 or 168 days. The non-woven PGA meshes were characterised with fibre diameters and porosities of 12-14 µm and 96%, respectively, and degraded *in vivo* within 84 days. The studies illustrated that the *in vitro* cell differentiation prior to *in vivo* implantation facilitated favourable formations of vascularised fat pads. As presented in Figure 2.5 (A, B, C, D), Cho *et al.* [158] developed hollow dome-shaped PGA fibre-based matrices reinforced with PLLA as mechanical support structures, which were tested for up to 42 days *in vivo* (athymic nude mouse model). The support structures exhibited a compression modulus of ~11.9 MPa, after 42 days *in vitro* incubation. In addition, the support structures withstood the *in vivo* compressive loads and did not biodegrade *in vivo*

within the test period. Human preadipocytes with fibrin gel containing FGF were injected into the hollow support structures and had the capacity to differentiate into adipocytes.

Poly(lactic-co-glycolic acid)

PLGA is an aliphatic copolymer, composed of lactic and glycolic acid, which has been extensively researched for various tissue engineering applications, owing to its biocompatibility and biodegradability [208]. PLGA combines the attractive properties of both, PLA and PGA, which thus possesses changeable physicochemical properties, while featuring a E_s, σ_{smax} and ε_{sb} in the ranges of 1.25-2.86 GPa, 41.7-55.6 MPa and 2.3-9.5% [209], respectively.

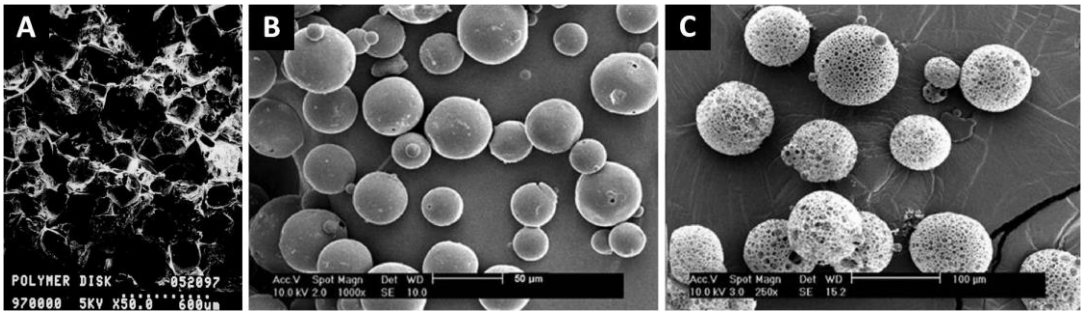

Figure 2.6: PLGA scaffolds and microspheres in ATE. (A) SEM micrograph of the microstructure of PLGA scaffolds, characterised with pore sizes of 135-633 µm and porosity of 90% (scale bar: 600 µm), adapted from Patrick *et al.* [91] with permission from Mary Ann Liebert, copyright 2008. SEM micrographs of (B) non-porous and (C) porous PLGA microspheres, adapted from Chung *et al.* [193] with permission from Mary Ann Liebert, copyright 2009.

In respect to ATE, PLGA was used in the form of porous scaffolds and microspheres [91,104,105,118,119,188–194]. Patrick *et al.* [91,190] investigated the response of rat preadipocyte on PLGA scaffolds for up to 365 days *in vivo* (Sprague-Dawley or Lewis rat model). As seen in Figure 2.6 (A), the PLGA scaffolds were fabricated via the solvent casting/particulate leaching technique and characterised with pore sizes and porosities in the range of 135-633 µm and ~90%, respectively, and biodegraded *in vivo* completely after

152 days. Cell-seeded PLGA scaffolds presented the formation of new adipose tissue after 14 days of transplantation, it peaked at ~62 days and decreased dramatically thereafter. In addition, the formation of *de novo* adipose was also observed within *in vivo* implanted acellular PLGA scaffolds, but it featured less favourable outcomes. In a different study, Neubauer *et al.* [189] analysed the response of rat BDSCs in the presence and absence of FGF within PLGA scaffolds for up to 28 days *in vitro*. The PLGA scaffolds were fabricated via a porogen leaching technique and characterise with pore sizes of 100-300 μm. Cell differentiation and the accumulation of lipid droplets were significantly enhanced in the presence of FGF. Also, Morgan *at el.* [191] analysed the response of human BDSCs on hollow PLGA fibre and PLGA fibre-alginate/chitosan scaffolds with for up to 56 days *in vivo* (MF-1 nu/nu immunodeficient mice model). The scaffolds showed signs of disintegration after 56 days implantation, but demonstrated the ability of cell differentiation and adipose tissue formation. In different studies, Dolderer *et al.* [118] and Cronin *et al.* [119] used acellular PLGA scaffolds as filler materials in hollow chamber implants, demonstrating the formation of *de novo* adipose tissue *in vivo* within 42 days implantation (Sprague-Dawley rat or wild-type mice model).

Choi *et al.* [104] analysed the response of attached rabbit BDSCs on injectable PLGA microspheres for up to 14 days *in vivo* (athymic nude mouse model). The PLGA microspheres were fabricated via an emulsification technique and were characterised with sizes in the range of 100-250 μm. Adipogenically induced cells differentiated fully into adipocytes and generated adipose tissue. In addition, Choi *et al.* [105] examined the response of subcutaneously injected ADSCs, PLGA microspheres and ADSC attached PLGA microspheres for up to 56 days *in vivo* (athymic nude mouse model), respectively. Newly formed adipose tissue was only observed at the site of injection with cell-free PLGA microspheres and ADSC attached PLGA microspheres, while the latter performed the best.

Choi *et al.* [192] also investigated the effects of the diameter of PLGA microspheres on the adipogenic differentiation of attached rabbit BDSCs for up to 28 days *in vivo* (athymic nude mouse model), concluding that the optimal microsphere size for adipogenesis was 100-150 µm. In a further study, Kang *et al.* [188] developed porous PLGA microspheres for ATE, which were characterised with diameters and pore sizes of ~372 µm and ~36 µm, respectively. The *in vivo* analysis of the porous PLGA microspheres permitted cell adhesion, proliferation and differentiation of human ADSCs. Chung *at el.* [193] investigated the response of murine 3T3-L1 preadipocytes on injectable nonporous and porous PLGA microspheres for up to 28 days *in vivo* (athymic nude mouse model). As seen in Figure 2.6 (B, C), both microsphere types featured sizes of ~50 µm, while the porous microspheres were characterised with sizes and porosities of ~5 µm and ~90%, respectively. *In vivo* results demonstrated that the porous PLGA microspheres provided the most favourable cell environment and showed the formation of adipose tissue.

Poly(ε-caprolactone)

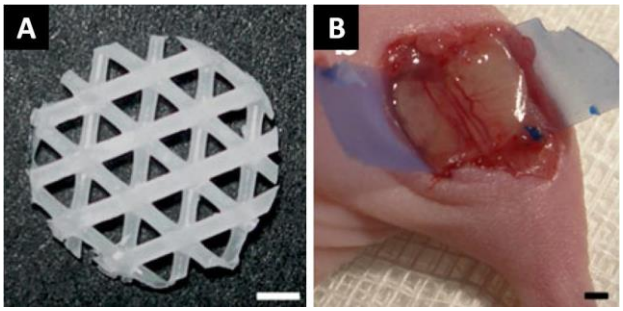

Figure 2.7: PCL scaffolds in ATE. (A) PCL scaffold with stacked-fibre architecture were fabricated via the fused deposition modeling method, characterised with a porosity of 58%. (B) PCL scaffold after 28 days *in vivo* (nude mouse model) implantation in the femoral region (scale bar: (A, B) 1 mm). Adapted from Wiggenhauser *et al.* [120] with permission from Springer, copyright 2011.

PCL is a biodegradable and biocompatible aliphatic polyester and has been studied extensively for tissue engineering applications [207,208]. PCL features intrinsic hydrophobic properties and can degrade over a period of 2-4 years, depending on its molecular weight and degree of crystallinity [211]. In addition, PCL possesses E_s, σ_{smax} and ε_{sb} values in the range of 250-430 MPa, 14-57 MPa and 50-900% [212,213], respectively.

In the context of ATE, Kang *et al.* [195] analysed the *in vitro* response of murine embryonic stem cells on 3D nanofibrous PCL scaffolds. The 3D nanofibrous PCL scaffolds were fabricated via electrospinning and characterised with a scaffold thickness, fibre diameter, pore size and porosity of ~200 µm, ~0.69 µm, ~30 µm and ~88%, respectively, and presented no changes in structural integrity within 21 days *in vitro* culture. The murine embryonic stem cells migrated to a scaffold depth of ~40 µm and differentiated into mature adipocytes within 14 days. Also, the expression of adipocyte related genes were more prominent in the 3D culture environment, compared to conventional 2D culture conditions, while the use of adipogenic differentiation medium enhanced the adipocyte differentiation in general. Wiggenhauser *et al.* [120] investigated the response of human ADSCs on PCL scaffolds for up to 28 days *in vitro* and *in vivo* (athymic nude mouse model), as illustrated in Figure 2.7. The PCL scaffold with stacked-fibre architecture were fabricated via a fused deposition modelling technique and featured an E_c, porosity and pore size of 17.5 MPa, 58% and 0.42 mm, respectively. *In vivo*, the ADSCs differentiated into adipocytes and the formation of adipose tissue was observed throughout the scaffold.

Poly(ethylene glycol)

PEG is a hydrophilic, biocompatible and non-biodegradable polymer, which has been extensively used for synthesising crosslinked hydrogels for numerous tissue engineering applications [214]. Crosslinked PEG-based hydrogels are swellable in aqueous environments

and feature viscoelastic properties similar to soft tissues, while the physicochemical properties are highly versatile and flexible, depending on the selected polymerisation conditions [214].

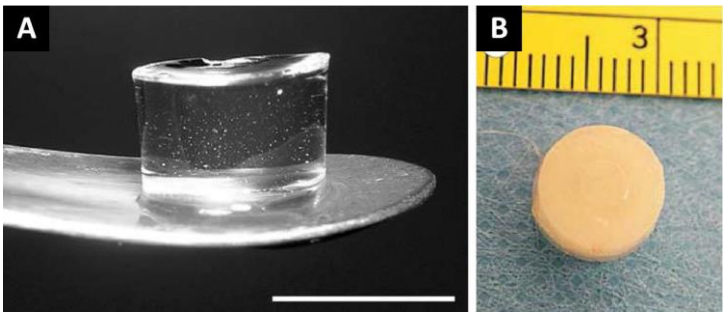

Figure 2.8: Poly(ethylene glycol) diacrylated (PEGDA) hydrogels for ATE. (A) Pristine PEGDA hydrogel (scale bar: 5 mm), adapted from Patel *et al.* [201] with permission from Mary Ann Liebert, copyright 2005. (B) PEGDA engineered construct with encapsulated human BDSCs, adapted from Alhadlaq *et al.* [196] with permission from Mary Ann Liebert, copyright 2005.

With respect to ATE, significant work has been performed on cell-encapsulated photopolymerisable PEGDA hydrogels [84,196,199–202], as seen in Figure 2.8 (A, B). The PEGDA hydrogels featured a high water content, slow degradation rates and high volume retention after *in vitro* and *in vivo* evaluations, along with no cytotoxic induced effects [215]. Patel *et al.* [84] investigated the rheological properties of PEGDA hydrogels, indicating superior properties compared to human adipose tissue, because the tested PEGDA hydrogels were able to recover up to 78% of their original height after 15% deformation, while adipose tissue failed under the same test conditions. Stacey *et al.* [202] analysed the *in vitro* response of encapsulated human preadipocytes within PEGDA hydrogels, which were characterised with an E_s in the range of 0.002-0.04 MPa, under 2D and 3D culture conditions for up to 16 days. Preadipocytes which were treated with adipogenic differentiation medium presented enhanced adipogenic differentiation under 3D culture conditions, as well as under coculture conditions with adipocytes [202]. Similar results were found via the encapsulation of embryonic [200] and adult stem cells [196] [199], demonstrating that these cells are capable

of differentiating within the PEGDA hydrogels toward an adipogenic lineage. Furthermore, Patel *et al.* [201] demonstrated that the cell viability, adhesion and proliferation performance of PEGDA hydrogels can be enhanced through the incorporation of specific peptide sequences. In a different study, Brandl *et al.* [198] evaluated the *in vitro* response of encapsulated murine 3T3-L1 preadipocytes in modified biodegradable and non-biodegradable branched PEG-amines for up to 42 days. The biodegradable branched PEG-amines were modified with enzyme-sensitive peptides and crosslinked with branched PEG-succinimidyl propionates (under the omission of free-radical initiators), while alanine-modified PEG-amines were used as non-biodegradable hydrogels. The biodegradable branched PEG-amines degraded completely under enzyme-containing conditions within 10-19 days *in vitro*. Fully differentiated adipocytes and the formation of adipose tissue were evident in all hydrogels, while the non-biodegradable branched PEG-amines presented less favourable tissue formation and higher degrees of isolated adipocytes.

Poly(ethylene glycol) terephthalate/poly(butylene terephthalate) block copolymer

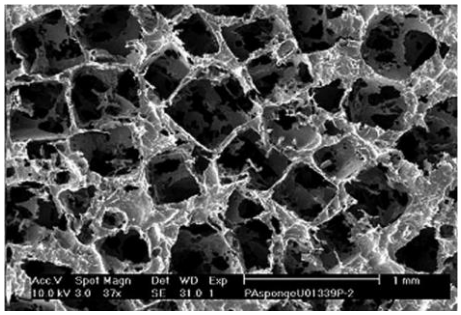

Figure 2.9: PEGT/PBT scaffolds in ATE. SEM micrographs of compression moulded and salt leached (salt grains of sizes in rang of 500-600 μm) PEGT/PBT scaffolds, adapted from Lamme *et al.* [197] with permission from SAGE Publications, copyright 2008.

PEGT/PBT is a block copolymer composed of altering hydrophilic PEGT and hydrophobic PBT soft/hard segments [216–218]. PEGT/PBT implants presented suitable biocompatibility and biodegradability in various biomedical applications, with no initiation of adverse

effects on the surrounding tissue [216–218]. The swelling, degradability and mechanical properties of PEGT/PBT block copolymers are tailorable and depend on the copolymer composition [197].

In ATE, Lamme *et al.* [197] investigated the implantation of porous degradable PEGT/PBT copolymer implants with different compositions for up to 360 days *in vivo* (Göttinger mini-pig model), as illustrated in Figure 2.9. Implants with various polymer ratios were fabricated via the compression moulding/leaching technique and possessed porosities and pore sizes of 76-82% and 500-600 µm, respectively. Histological observation showed unevenly distributed cell clusters on the implant surfaces. Hydrophobic PEGT/PBT copolymer implants with a higher ratio of PEGT displayed overall lower degrees of foreign body reaction, generated greater quantities of connective tissue and presented slower degradation related changes in molecular weight, compared to hydrophilic PEGT/PBT copolymer implants with a higher ratio of PBT.

Polyurethane

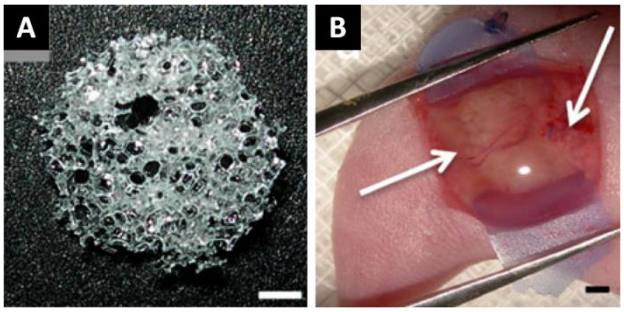

Figure 2.10: PU scaffolds in ATE. (A) PU scaffold characterised with a porosity of 93%. (B) PU scaffold after 28 days *in vivo* (nude mouse model) implantation in the femoral region, encapsulated by abundant fibrous tissue (white arrows) (scale bar: (A, B) 1 mm). Adapted from Wiggenhauser *et al.* [120] with permission from Springer, copyright 2011.

PUs are among the most versatile polymeric materials and have been used in numerous medical applications [219,220]. They are synthesised commonly from a wide variety of di- or

polyisocyanate and polyols, offering the flexibility of tailoring their physicochemical properties to match specific requirements [219,220]. PUs can be designed to have a broad range of mechanical properties, good biocompatible and biodegradable characteristics, as well as hydrophilic properties, which makes them a promising alternative to the classical synthetic biopolymers and their copolymers [219,220].

Wiggenhauser *et al.* [120] analysed the response of human ADSCs on biodegradable PCL-based PU scaffolds for up to 28 days *in vitro* and *in vivo* (athymic nude mouse model), as illustrated in Figure 2.10. PU scaffolds were fabricated via mould casting and methylal as a forming agent and featured an E_c, porosity and pore size of 0.0135 MPa, 93% and 0.56 mm, respectively. Adipose tissue formation was observed *in vivo* throughout the PCL-based PU scaffold. Gugerell *et al.* [203] investigated the response of human ADSCs on electrospun and biodegradable poly(ε-caprolactone-co-urethane-co-urea) and poly[(L-lactide-co-ε-caprolactone)-co-(L-lysine ethyl ester diisocyanate)-block-oligo(ethylene glycol)-urethane] non-woven meshes for up to 21 days *in vitro*. The electrospun PU meshes were composed of fibres with a diameter of 0.5-1.3 µm, high porosities and good and mechanical flexibilities. *In vitro* results demonstrated that the seeded ADSCs were able to adhere, proliferate and differentiate into the adipogenic lineage on both PU meshes.

Polycarbonate

PC is a hydrophobic thermoplastic polymer, biologically inert and features an E_s, σ_{smax} and ε_{sb} in the range of 2.1-2.4 GPa, 60-121 MPa and 65-150% [221–223], and mainly used for medical devices and engineering applications [224].

In ATE, Dolderer *et al.* [118] and Cronin *et al.* [119] investigated the use of hollow dome-shaped PC housings as a support structure for the *de novo* adipose tissue formation for up to 42 days *in vivo* (Sprague-Dawley rat or wild-type mice model), as illustrated in Figure 2.11 (A, B, C). The PC chambers were accompanied with vascularised pedicled fat

pads (containing veins and arteries for vascular supply) and filled with matrigel or PLGA scaffolds, which were capable of inducing cell migration and angiogenesis.

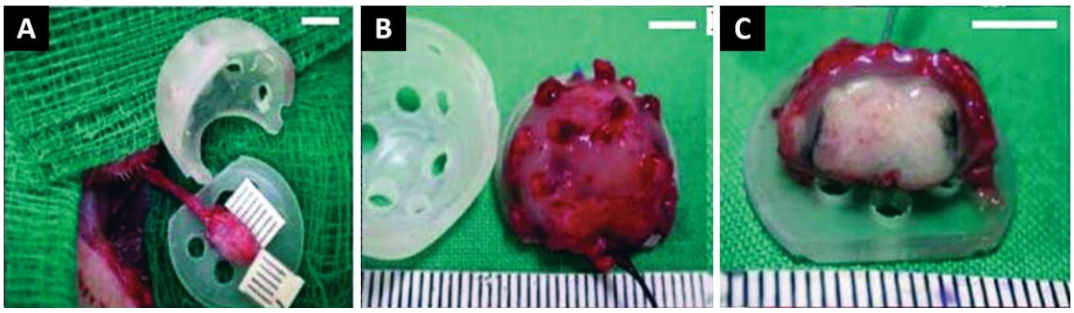

Figure 2.11: PC constructs in ATE. (A) Dome-shaped PC housing with included pedicled fat flap. (B) Harvest tissue out of the PC housing chamber after 42 days. (C) Cross section of the harvest tissue, showing fat tissue surrounded by a capsule (scale bars: (A, B, C) 5 mm). Adapted from Dolderer *et al.* [118] with permission from Mary Ann Liebert, copyright 2007.

Poly(ethylene terephthalate)

PET is a non-biodegradable polyester which features good biocompatibility properties and was used for a variety of biomedical long-term implants, such as for abdominal hernia, rhinoplasty and ligament reconstruction applications, particularly in the form of surgical meshes [225,226]. PET has hydrophobic properties and is characterised with E_s, σ_{smax} and ε_{sb} values in the range of 2.7-4.1 GPa, 50-70 MPa and 30-300 % [223], respectively.

In regard to ATE, Kang *et al.* [204] investigated the *in vitro* response of seeded murine 3T3-L1 preadipocytes on non-biodegradable 3D fibrous PET meshes. The non-woven PET meshes were characterised with fibre diameters of ~20 µm and a porosity of ~87%, while the surface of the fibres were chemically treated to enhance the hydrophilicity and biocompatibility. The preadipocytes differentiated into mature adipocytes within 14 days after induction of adipogenic differentiation medium. Fully differentiated adipocytes secreted higher degrees of leptin on the 3D fibrous PET meshes, compared to conventional 2D culture conditions.

Polypropylene

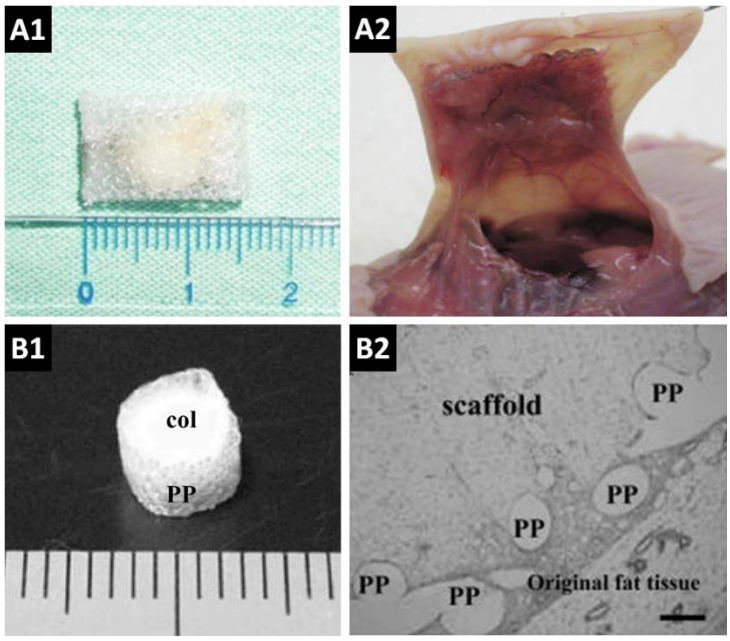

Figure 2.12: PP meshes in ATE. (A1) PP mesh framework with gelatin sponges and PGA meshes in the core. (A2) Engineered adipose tissue implant after 180 days *in vivo* (nude mouse model) implantation. Adapted from Lin *et al.* [162] with permission from Mary Ann Liebert, copyright 2008. (B1) PP mesh framework with a collagen sponge core. (B2) Histological section of the implantation site (scale bar: 200 µm). Adapted from Hiraoka *et al.* [128] with permission from Mary Ann Liebert, copyright 2006.

PP is a non-degradable, hydrophobic thermoplastic and used in a variety of medical applications, due to its cost-effectiveness and inertness in terms of biological and chemical interactions [224], and characterised with an E_s, σ_{smax} and ε_{sb} in the range of 1.1-1.5 GPa, 30-40 MPa and 100-600% [223], respectively. PP in the form of woven surgical meshes are widely used to repair hernias and other abdominal defects [162,227], owing to their good dimensional stability and the relatively simple suturation onto the defect site.

With the respect of ATE, Lin *et al.* [162] developed implantable scaffold constructs based on a PP mesh framework, while gelatin sponges and PGA meshes constructed the core material, as illustrated in Figure 2.12 (A1-2). Human ADSCs were seeded into the scaffold core and implanted for up to 270 days *in vivo* (athymic nude mouse model). The scaffolds

harvested at day 180 presented large numbers of fully differentiated adipocytes and newly formed adipose tissue. The gelatin sponges and PGA meshes resorbed completely, while the PP meshes maintained the scaffold framework. No inflammatory reaction was observed, however, at day 270 the implanted scaffolds were lost due to skin erosion. As seen in Figure 2.12 (B1-2), Hiraoka *et al.* [128] also developed implantable scaffold constructs based on a PP mesh framework and a collagen sponge core, along with gelatin microspheres containing different amounts of growth factors. The scaffold constructs were implanted with or without preadipocytes for up to 42 days *in vivo* (rat model). The cell-seeded scaffold constructs presented fully differentiated adipocytes, while the cell-free scaffold constructs indicated the *de novo* formation of adipose tissue.

Fluoropolymers

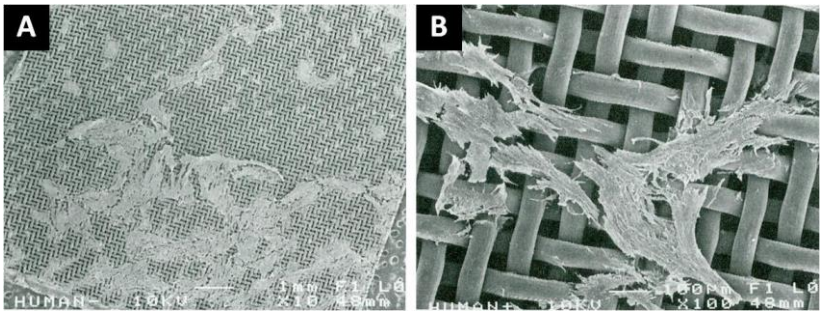

Figure 2.13: PTFE meshes in ATE. SEM micrographs of fibronectin-coated PTFE meshes with seeded human preadipocyte, at (A) low and (B) high magnification. Adapted from Kral *et al.* [206] with permission from Wolters Kluwer Health, copyright 1999.

Poly(tetrafluoroethylene) (PTFE) is highly hydrophobic, biologically and chemically inert polymer, and has been used in form of surgical meshes in numerous biomedical applications [228,229]. PTFE is characterised with an E_s, σ_{smax} and ε_{sb} in the range of 400-550 MPA, 14-35 MPa and 200-400% [223].

With respect to ATE, Kral *et al.* [206] analysed the *in vitro* response of human preadipocytes on non-biodegradable PTFE meshes, as shown in Figure 2.13 (A, B), which

featured pore sizes of 52 µm and fibre coatings of collagen, albumin or fibronectin. Uncoated PTFE meshes demonstrated poor cell attachment characteristics, while the fibronectin-coated PTFE meshes obtained the highest cell seeding efficiency. Over a period of 3 days the human preadipocytes proliferated and differentiated into adipocytes on the fibronectin-coated PTFE meshes. In a different study, Calvijo-Alvarez *et al.* [205] investigated the *in vitro* and *in vivo* (athymic nude mouse model) response of human ADSCs on porous scaffolds with pore sizes of 10-55 µm and 100-180 µm, based on commercially available none-degradable fluoropolymers. Fibronectin-coated fluoropolymers scaffolds presented most favourable cell attachment and proliferation characteristics, both *in vitro* and *in vivo* over a period of up to 30 days, respectively.

Silicones

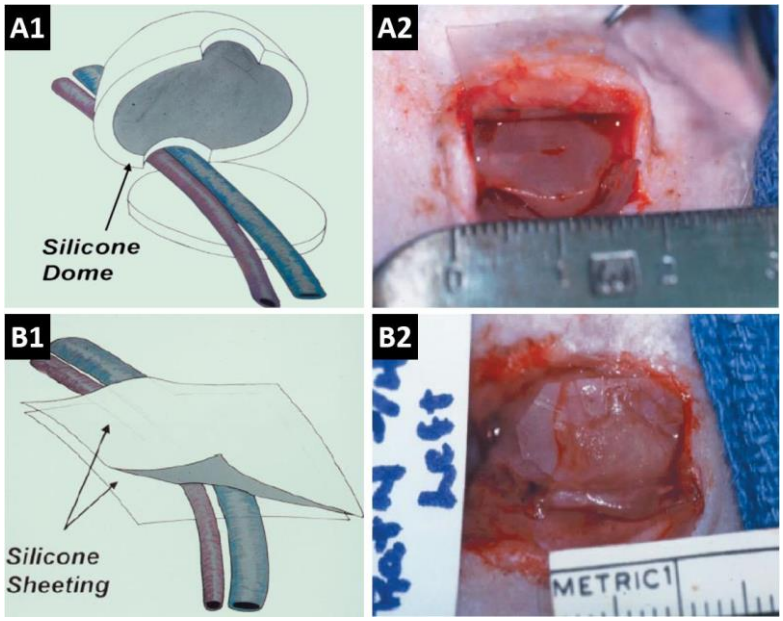

Figure 2.14: Silicone constructs in ATE. Schematic of (A1) dome-shaped silicone housing and (B1) flat silicone sheets with included vascular pedicle. Fat growth in (A2) the dome-shaped silicone housing and in (B2) the flat silicone sheets. Adapted from Walton *et al.* [117] with permission from John Wiley and Sons, copyright 2004.

Silicones exhibit a wide variety of physicochemical properties and are considered as non-degradable elastomers, characterised with biological and chemical inertness [230,231]. However, research studies showed that silicone implants can be associated to capsular fibrosis formation, carcinogenesis and autoimmune diseases [232].

As shown in Figure 2.14 (A1-2, B1-2), Walton *et al.* [117] developed implantable hollow non-degradable silicone dome and sheet constructs, which were filled with matrigel and FGF. The support constructs were connected to their own pedicled blood supply and lead to the formation of *de novo* adipose tissue via the *in vivo* (rat model) migration of preadipocytes. The silicone constructs protected the developing tissue against mechanical loads and allowed to control the shape and dimension of the adipose tissue ingrowth within 140 days. Fully differentiated adipocytes, as well as the *de novo* formation of adipose tissue were confirmed. In a different study, Cronin *et al.* [119] used silicone tubes and chambers as a support structure for the *de novo* adipose tissue formation.

Overall, the applied synthetic biodegradable and non-biodegradable polymers in ATE demonstrated the ability to support cell differentiation, cell proliferation and the formation of new adipose tissue *in vitro* and *in vivo*. In some cases combined approaches of natural and synthetic polymers were performed, in particular to improve the performance of the synthetic polymer implants in terms of cell attachment and biocompatibility [128,162,206]. However, this raises concerns with respect to immunogenic reactions and infection *in vivo* when animal-derived natural polymers are used, as stated in Section 2.2.6.1. Also, the development of synthetic polymer scaffolds with similar mechanical properties to those of native human adipose tissue was less explored, with the exception of research studies based on PEGDA hydrogels and PU scaffolds [84,120,196,198–202]. Therefore, most synthetic biodegradable and non-biodegradable polymers used in ATE were characterised with unsuitable mechanical properties compared to native human adipose tissue [76–78,80,84–86]. The engineered

implants based on these types of synthetic polymers are more prone to plastic deformations under external loads, feature stiffer bulk properties and lack of flexibility and strechability, which consequently will decrease the comfort of the patient after implantation [6]. Implants which featured a hollow chamber for tissue grow and served as a mechanical support structure demonstrated to be useful for the development of volume-stable adipose tissue [117–119,158]. However, it is questionable if this technique is clinically applicable, in particular if synthetic non-biodegradable polymers are used, due to the necessity of an additional surgery for implant removal [8].

2.3 Poly(glycerol sebacate)

2.3.1 Introduction to poly(glycerol sebacate)

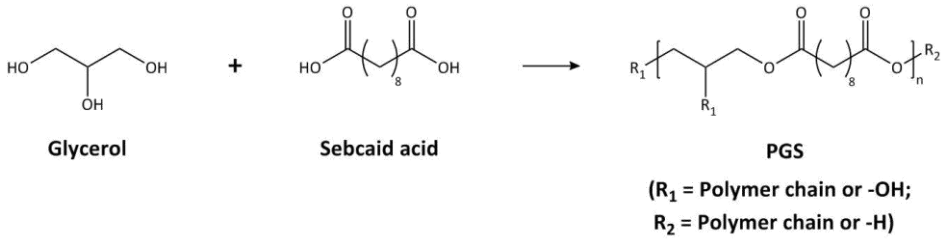

Scheme 2.1: Reaction scheme and chemical structure of PGS.

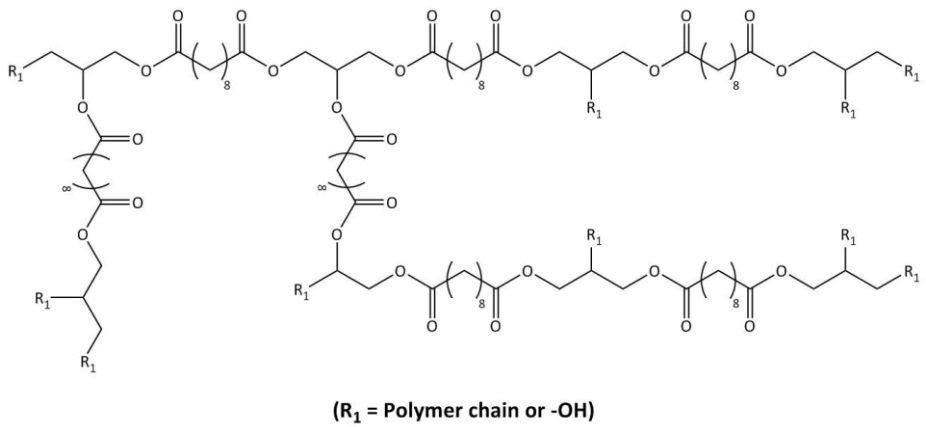

Scheme 2.2: Crosslinking scheme between PGS chains with a low degree of crosslinking, adapted from Li *et al.* [14] with permission from The Royal Society of Chemistry, copyright 2012.

PGS is a recently developed biocompatible and biodegradable elastomer whose mechanical properties can be tailored to match specific soft tissue requirements [16,17]. In respect to its soft tissue applications, PGS has been successfully approached in the fields of nerve [233], cardiac [234–237], retinal [238,239], vascular [240,241], cartilage [242] and bone [243] tissue engineering. Due to its positive attributes, PGS has been further explored in various biomedical applications, such as drug delivery devices [244], tissue adhesives and sealants [245–247], as well as coating materials [248–250], highlighting its versatility in many different applications.

PGS is a polycondensed polyester, derived from glycerol and sebacic acid monomers, in which both tri- and two-functional monomers form a 3D network of randomly crosslinked coils during the polymer synthesis [16]. The conventional PGS synthesis is proceeded in two steps with an equimolar mixture of glycerol and sebacic acid, in which first a highly viscous pre-polymer is synthesised, while in the second step the pre-polymer is further polymerised to a covalently crosslinked polymer, as illustrated in Schemes 2.1 and 2.2. This method represents the current gold standard in PGS synthesis which allows one to prepare the PGS pre-polymer (pre-PGS) first into various shapes by melting it at high temperatures or by dissolving it in organic solvents, before the crosslinking process is performed [16,17]. Both polycondensation steps are executed under harsh process conditions (noble gas or vacuum environment, temperature range of 110-165 °C) [237,251,252] and long reaction times (time range of 24-114 hours) [237,251,252]. The crosslinking of PGS *in vivo,* as well as the incorporation of temperature sensitive molecules with the conventional PGS synthesis method is therefore not possible [253]. Aydin *et al.* [254] presented recently the option to accelerate the synthesis reaction of PGS via a microwave-assisted pre-polymerisation, significantly reducing the reaction times. The properties of PGS can be modified simply by either changing the parameters of the molar ratio between glycerol and sebacic acid [242] or by altering the

time and/or temperature [237,251,252] in one or both of the pre-polymer synthesis and crosslinking processes [251,252].

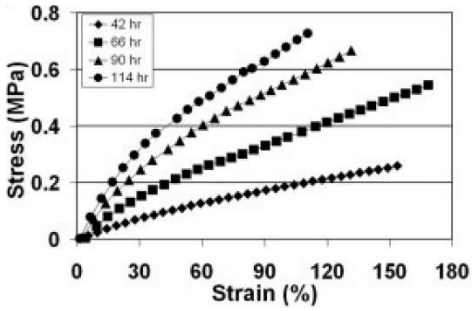

Figure 2.15: Stress-strain curves for PGS as a function of curing time (42-114 h), adapted from Pomerantseva *et al.* [251] with permission from John Wiley and Sons, copyright 2008.

PGS exhibits a non-linear stress-strain behaviour under quasi-static tensile tests, which is typical for elastomers [16]. The mechanical properties of PGS depend on the crosslink density of the covalently crosslinked 3D network [16,251], while the hydrogen bonding interaction between the hydroxyl groups contribute to the elastomeric nature of PGS [16]. The virtue of PGS is the capability to tailor its mechanical properties, which overall depend on the processing conditions and alters the crosslinking density [16,251]. Previous studies demonstrated that an increase in the molar ratio of glycerol to sebacid acid lead to decreased stiffness [242], while longer times and/or higher temperatures increased the Young's modulus and *vice versa* [237,251,252], as seen in Figure 2.15. With this respect, the mechanical properties of PGS were characterised with an E_s, σ_{smax} and ε_{sb} in the range of 0.05-2.12 MPa, 0.23-0.79 MPa and 69-448%, respectively [16,237,251,255–257]. Furthermore, PGS presented stable mechanical properties under cyclic load [256], demonstrating high flexibility and good recovery characteristics in mechanically dynamic environments. As typical for an elastomer, PGS is characterised by a low glass transition temperature between -30 °C and -40 °C, thus, it remains flexible over a wide temperature range [252]. The ability to undergo large reversible deformations compared to conventional polyester-based polymers, such as

PLA, PGA, PCL and their copolymers, which undergo plastic deformation and failure when exposed to long-term cyclic loads [10,11,258], makes PGS particularly interesting for soft tissue engineering applications [16,17].

PGS undergoes relatively linear degradation kinetics under various *in vitro* [251,259] and *in vivo* [251,260] conditions, indicating that the degradation mechanism is based on surface erosion and prone to the hydrolytic cleavage of ester groups [251]. The surface degradation mechanism of PGS leads to a preservation of geometry, low swelling properties and retention of mechanical strength relative to the mass loss [237,238,260]. Compared to *in vitro* degradation conditions, PGS presents enhanced *in vivo* degradation kinetics [16], demonstrating accelerated degradation rates under enzymatic environments. With this respect, PGS exhibited complete *in vivo* degradation within 60 days, while under the same time period PGS was characterised with an *in vitro* degradation of only 18% weight loss [16]. In addition, the degradation kinetics of PGS are tuneable and dependant on the crosslinking density, in which a higher crosslinking density decreases the water diffusion in the chain network and decelerates the degradation kinetics [259,261].

PGS demonstrated good *in vitro* and *in vivo* biocompatibility with no cytotoxic effects, enhanced hemocompatibility and minimal inflammatory responses to implants in various soft tissue engineering applications [16,233,237,239,251,259,260,262,263]. The biocompatibility of PGS originates from both monomers, glycerol and sebacic acid. Glycerol is one of the basic components in lipids, while sebacic acid is a natural metabolic intermediate of various fatty acids [16]. Both monomers are nontoxic, endogenous to the human metabolism and have been approved in medical applications by the United States Food and Drug Administration (FDA) [16]. The omission of a catalyst or other additives during the pristine PGS synthesis avoids further possible toxic effects and chemical by-products of degradation in biomedical applications [17]. However, research studies showed that localised acidic environments,

caused by non-crosslinked pre-PGS or by acidic degradation products of PGS, can result in cytotoxic effects if not removed [256,259]. Compared to conventional polyester-based polymers, PGS exhibited overall similar or superior *in vitro* or *in vivo* biocompatibility characteristics [16]. Wang *et al.* [16] investigated the *in vitro* cell response of mouse embryonic fibroblast cells on PGS and PLGA reference surfaces, observing a higher cell adhesion and cell growth rate on the PGS specimens, as well as the development of normal cell morphologies with no cluster formation. Further *in vitro* biocompatibility studies involving arterial smooth muscle cells [264] and Schwann cells [233] presented similar results, in which PGS performed with favourable cell metabolic activity, attachment, proliferation and apoptosis in comparison to PLGA. The minimal inflammatory responses of PGS during *in vivo* tests in rats were similar to or lower than PLGA and presented in addition reduced fibrous capsule formation [16]. Also, the surface erosion mechanism of PGS and its gradual resorption affected tissue responses positively, while the bulk degradation mechanism of PLGA resulted in spiked inflammatory responses, due to the late rapid mass loss [233]. Overall, the *in vitro* and *in vivo* performance of PGS is adaptable and dependent on various factors, such as the porosity and permeability [238,265], surface energy and hydrophilicity [266], contact guidance and surface morphology [267], as well as on the degradation products [256,259].

2.3.2 Scaffold manufacturing strategies for PGS

Various fabrication methods have been developed to fabricate biocompatible and biodegradable polymeric materials into porous three-dimensional scaffolds [2,39]. In contrast to other biomaterials including natural and synthetic polymers, PGS reveals a set of limitations and various challenges in manufacturing large 3D scaffolds [17]. This is due to the harsh curing conditions of PGS, including high curing temperatures, long curing times and a vacuum environment as previously described [237,251,252]. In addition, the viscosity of

pre-PGS decreases significantly at high temperatures and liquefies, unable to maintain any 3D structure by itself [268]. As listed in Table 2.4, several processing methods have been utilised or developed to engineer porous and pristine PGS scaffolds, such as micromoulding/lamination [238,239,265,267,269–271], laser micro-ablation (LM)/lamination [234,255,272,273], solid freeform (SFF) fabrication method [242], blend [266,268,274–281] and coaxial core/shell [268,278,282–286] electrospinning, as well as the combined salt-leaching and salt-fusion method [235,236,287–289]. Despite specific advantages of using these technologies, the efficient fabrication of large 3D scaffolds based on PGS is still infeasible.

Table 2.4: Scaffold manufacturing strategies for pristine PGS

Manufacturing strategy	Advantages	Limitations	References
Micromoulding/ lamination	Freedom to design complex 2D geometries; High resolution	Sophisticated fabrication method; Multi-layered scaffold design; Relatively fragile scaffolds; Low-throughput; Expensive	[238,239,265,267,269–271]
Laser micro-ablation/ lamination	Freedom to design complex 2D geometries; High resolution	Sophisticated fabrication method; Multi-layered scaffold design; Relatively fragile scaffolds; Low-throughput; Expensive	[234,255,272,273]
Solid freeform fabrication	Freedom to design complex 3D geometries; No use of organic solvents	Sophisticated fabrication method; Usage of sacrificing mould technique; Low resolution; Low-throughput; Expensive	[242]
Electrospinning with polymer blend	Facile fabrication method; High porosity; Low cost	Low pore size; High fibre pack density; Low porosity; Limited thickness; Low-throughput	[266,268,274–281]
Coaxial electrospinning	High porosity; Low cost	Sophisticated fabrication method; Low pore size; High fibre pack density; Low porosity; Limited thickness; Low-throughput	[268,278,282–286]
Salt-leaching and salt-fusion	Facile fabrication method; High porosity; Low cost	Pore shape and interpore opening; Dense surface skin layers; Residual salt particles; Leaching process necessary	[235,236,287–289]

Micromoulding / lamination

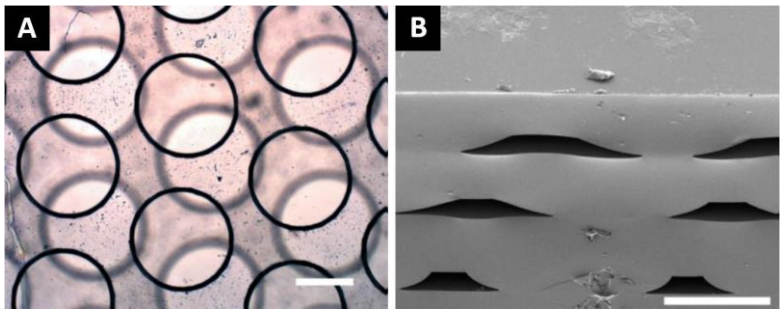

Figure 2.16: PGS scaffold fabricated via the micromoulding fabrication technique and physically bonded through heat. (A) Bright-field optical micrograph of a stacked two-layered PGS scaffold. (B) SEM micrograph of a stacked three-layered PGS scaffold (scale bar: (A, B) 200 µm). Adapted from Bettinger *et al.* [265] with permission from John Wiley and Sons, copyright 2005.

The microelectromechanical systems [269] and the replica moulding [238,239,265,267] techniques were used to manufacture photolithography patterned moulds for PGS crosslinking of individual sheets, whereas multi-layered PGS sheets were engineered via lamination and additional physically bonding steps [265,269]. Machining-based moulding methods were also utilised to fabricate simple patterned moulds [270,271]. Crosslinked PGS sheets with a thickness of 45-1000 µm were fabricated on pre-treated silicone, replica-moulded poly(dimethylsiloxane) and machined ceramic micromoulds, characterised with feature resolutions down to 30 µm [238,239,265,269–271]. Prior to the PGS curing process, the micromoulds were plasma oxidised to create hydrophilic surfaces and spin-coated with sucrose, enabling a damage-free delamination of the crosslinked PGS sheets after incubating in distilled water for 1-16 days [238,239,265,269–271]. As seen in Figure 2.16 (A, B), multi-layered PGS sheets were fabricated via sheet stacking and heat treatments lead to the formation of new ester linkages between the sheets (chemically crosslinked), owing to the free hydroxyl and acid groups [265,269]. The pores and struts of each layer were off-set, allowing to create porous 3D scaffold with interconnected pores. Still, only two- or

three-layered PGS scaffolds were constructed and analysed via micromoulding techniques [265,269]. The thickness of each layer has to be considered in order to permit mass transport of oxygen through the material [265]. With respect to achievable bond strength between the bonded PGS sheets, only qualitative data were provided, whereas quantitative data are still missing which are crucial for dynamic applications. Also, the heat treatment for the layer bonding enhanced the stiffness of PGS, thus increasing the difficulty to target specific mechanical properties [265,269].

Laser micro-ablation / lamination

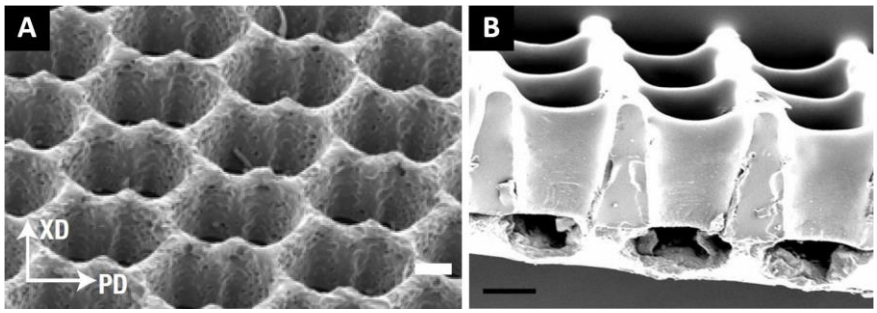

Figure 2.17: PGS scaffold fabricated via the laser micro-ablation technique and physically bonded through heat. (A) SEM micrograph of an accordion-like honeycomb PGS scaffold layer. (B) SEM micrograph of a stacked two-layered PGS scaffold (scale bar: (A, B) 100 µm). Adapted from Englemayr *et al.* [255] with permission from Nature Publishing Group, copyright 2008.

The LM technique enabled the ablation of highly accurate micropatterns on individual PGS sheets, whereas the construction of laminated multi-layered PGS sheets were accomplished via additional physical bonding steps [234,255,272], as seen in Figure 2.17 (A, B). Crosslinked PGS sheets with a thickness of 250-500 µm were fabricated on sucrose spin-coated moulds and microstructure geometries shaped via excimer or solid-state Nd-YAG lasers [234,255]. Feature resolutions of down to 50 µm were realisable and characterised with a slight top-to-bottom taper, which is typically for laser drilling [255,273].

Completed PGS sheets were damage-free delaminated after incubating in distilled water for one day [234,255]. Multi-layered PGS sheets were fabricated via sheet stacking and physically bonded through heat or oxygen-plasma treatments under compression, resulting in a close bonding interface between the layers [234,255]. The pores and struts of each layer were off-set, allowing to create 3D scaffold constructs. However, the LM technique exhibits overall similar difficulties as the micromoulding techniques discussed earlier. In addition, the thickness of some PGS sheets were limited to permit mass transport of oxygen through the material [265,290,291], resulting in only delicate 2D sheets or small-sized 3D layered scaffolds [234,255].

Solid freeform fabrication

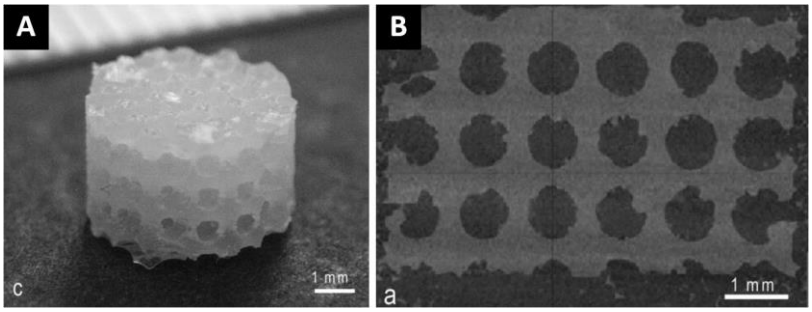

Figure 2.18: PGS scaffold fabricated via the solid free-form technique. (A) Side view picture of the PGS scaffold specimen. (B) X-ray micro-computed tomography picture of the scaffolds microstructure (scale bar: (A, B) 1 mm). Adapted from Kemppainen *et al.* [242] with permission from John Wiley and Sons, copyright 2010.

An alternative technique for the fabrication of PGS scaffolds is the utilisation of sacrificial 3D hydroxyapatite moulds, which can sustain the harsh curing conditions of PGS [242]. Curable hydroxyapatite slurry was poured into positive wax moulds, which were created via the SFF fabrication method. The inverse 3D hydroxyapatite moulds were then embedded into melted pre-PGS, followed by curing pre-PGS and dissolving the hydroxyapatite with a rapid decalcifying agent, resulting in 3D PGS scaffolds. The fabricated PGS scaffolds were

characterised by a large average pore size of ~1 mm and a low porosity of 48%, demonstrating the poor porosity due to a low 3D printing resolution [242], as seen in Figure 2.18 (A, B). The SFF fabrication approach presented overall a low-throughput of 3D PGS scaffolds, however, no organic solvents were used during the fabrication process.

Electrospinning

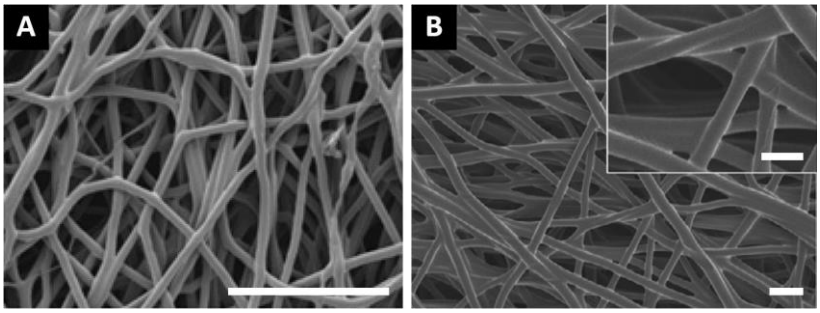

Figure 2.19: PGS-based nanofibrous scaffolds fabricated via blend electrospinning. (A) SEM micrograph of electrospun pre-PGS/PCL fibres (scale bar: 100 µm), adapted from Sant *et al.* [274] with permission from Elsevier, copyright 2013. (B) SEM micrograph of electrospun and thermally crosslinked PGS/PVA fibres (scale bar: 10 µm; scale bar inset: 5 µm), adapted from Jeffries *et al.* [277] with permission from Elsevier, copyright 2015.

The formation of pristine PGS nanofibres is challenging, however, non-woven meshes of randomly deposited PGS-based nanofibres were fabricated using polymer blends [266,268,274–281] or via coaxial core/shell [268,278,282–286] electrospinning, as shown in Figure 2.19 (A, B) and 2.20 (A, B). The blend electrospinning process was performed using blended solutions of pre-PGS and natural or synthetic biopolymers as carrier materials, such as gelatin [276], poly(vinyl alcohol) (PVA) [277], PCL [266,274,275,281], PLLA [268,278], poly(butylene succinate-butylene dilinoleate) (PBS-DLA) [280], poly(L-lactide-co-D,L-lacitide) (PLDLLA) and poly(3-hydroxybutyrate-co-3-hydroxyvalerate) (PHBV) [279]. The addition of a carrier material into the pre-PGS solution is required to increase the viscosity to suitable values for the electrospinning process [268]. Pre-PGS itself cannot be electrospun to

form stable nanofibres, because of its low molecular weight and consequently low solution viscosity [268,275]. The thermal curing process of pristine formed pre-PGS nanofibers is also not feasible [268], due to the low melting point (5-8 °C) [248,292] of pre-PGS and the high curing temperatures (110-165 °C) [237,251,252] which are required for crosslinking. With this respect, no crosslinking processes were conducted on fibrous pre-PGS/PCL [266,274,275,281], pre-PGS/PBS-DLA [280] and pre-PGS/PLDLLA/PHBV blends [279]. Pre-PGS was thermally crosslinked in fibrous pre-PGS/PVA [277] and pre-PGS/PLLA [268,278] blends, while the fibrous pre-PGS/gelatin blends [276] were crosslinked via the immersion in an ethanol solution containing N,N-(3-dimethylaminopropyl)-N′-ethyl-carbodiimide hydrochloride and N-hydroxysuccinimide as crosslinking agents. The electrospinning process enabled the production of fibrous PGS-based blends with average fibre diameters in the range of 0.3-8.3 µm [266,275,277], with randomly dispersed or aligned fibre formations, large specific surface areas and small pore sizes.

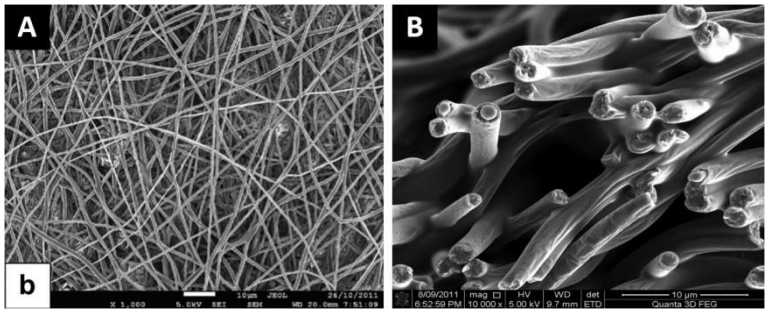

Figure 2.20: PGS-based nanofibrous scaffolds fabricated via coaxial electrospinning. SEM micrograph of electrospun and crosslinked PGS/PLLA core/shell fibres: (A) Top view, (B) cross section (scale bar: (A, B) 10 µm). Adapted from Xu *et al.* [278] with permission from Elsevier under the Creative Commons Attribution License 2013.

The coaxial core/shell electrospinning process was used to produce core/shell nanofibres, containing pre-PGS or PGS as a core and natural or synthetic biopolymers as a protective or removable shell, using materials such as gelatin [283], collagen [284], fibrinogen [285], PVA [286] or PLLA [268,278,282]. The use of a natural biopolymer as the shell material allowed

to create core/shell nanofibres, where the PGS core was accountable for the mechanical properties, whereas the shell material provided additional functional properties, such as improved cell attachment and proliferation capability [283–285]. The shell materials based on natural biopolymers were crossslinked via glutaraldehyde vapour, to enhance their performance under physiological conditions [283,284]. The thermal crosslinking of the pre-PGS core was restricted within natural biopolymers, due to the polymers limited thermal long-term stability. In contrast, the application of a synthetic biopolymer as the shell material allowed subsequent thermal crosslinking treatments on the fibrous pre-PGS-based core/shell formations [268,278,282,286]. PVA and PLLA maintained the tube shape during the harsh curing condition of pre-PGS, and were removable via an organic solvent or aqueous washing treatments, after the PGS core was crosslinked [268,282,286]. In general, the coaxial core/shell electrospinning process produced PGS-based core/shell meshes with average fibre diameters in the range of 0.4-10.0 µm, which were characterised by random fibre formations and non-uniform pore structures [268,278,282,283]. Compared to the electrospinning process with a polymer blend, the coaxial core/shell electrospinning process presented overall a more complex fabrication set-up and poor adjustability of the scaffold properties, due to the limited ratio control between the two electrospun polymers [277]. Both the polymer blend and coaxial core/shell electrospinning processes, can fabricate fibrous meshes with large specific surface areas, however, these are mainly characterised by small pore sizes and low porosities within the electrospun scaffolds [266,268,277,282]. A tight fibre density is a common problem in electrospun scaffolds and known to limit cell infiltration [277,293,294]. Further drawbacks are the low rates of generating large masses of fibres as well as the incidence of charge build-up at the collector, preventing the production of thick scaffolds [295–297]. Also, the removal of the carrier or shell polymer from the nanofibrous PGS-based scaffolds was only possible to a limited extent [277].

The application of photocrosslinkable PGS is an alternative approach to electrospinning PGS, which avoids additional curing steps [298,299].

Salt-leaching and salt-fusion

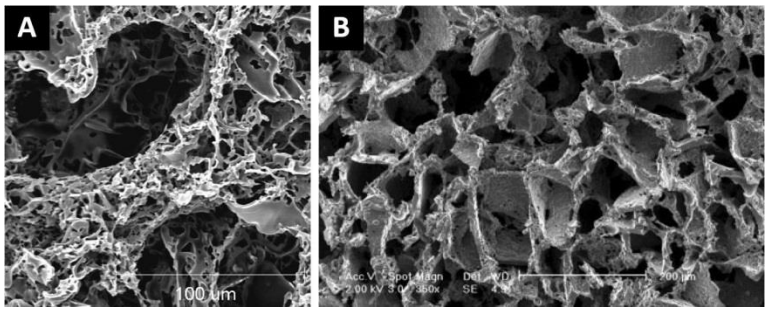

Figure 2.21: PGS scaffold fabricated via the salt-leaching and salt-fusion technique. (A) SEM micrograph of the cross section of crosslinked PGS scaffold (scale bar: 100 µm), adapted from Gao *et al.* [288] with permission from Mary Ann Liebert, copyright 2006. (B) SEM micrograph of the cross section of crosslinked PGS scaffold (scale bar: 200 µm), adapted from Radisic *et al.* [236] with permission from John Wiley and Sons, copyright 2007.

A less complex scaffold processing technology is the combined salt-leaching and salt-fusion technique, as seen in Figure 2.21 (A, B), which was successfully applied to create interconnected porous PGS circular scaffolds as well as tubular scaffolds with an average pore size in the range of 20-300 µm and a porosity of 75-95% [235,236,287–289]. While the porosity and pore size are adjustable, other important parameters such as pore shape and interpore opening are only poorly modifiable [300]. Other drawbacks of this technique include the possibility of dense surface skin layers and the remaining residual salt particles. Furthermore, only relatively thin scaffolds (thickness in the range of 1-5 mm) [235,236,287–289] were prepared, and some of these scaffolds were further modified with the laser microablation method to integrate an array of parallel channels (accurate diameter dimension of 250 µm) to improve the scaffold perfusion [235,287].

The creation of PGS scaffolds involved the utilisation of various sophisticated technologies [17], primarily characterised by a low-throughput of small-sized scaffolds with unsuitable porous structures or porosities, constraining the full potential and adoption of PGS in a broader field of soft tissue engineering applications.

2.3.3 Modification of PGS

Various PGS-based copolymeric systems [246,247,253,292,298,299,301–312], blends [266,268,274–279] and composites [243,256,257,259,313–317] were developed to improve the applications of PGS, by incorporating different functionalities and tailoring its physicochemical properties for specific tissue engineering applications. With this respect, most research studies aimed to either improve the processability of PGS, or modify the mechanical properties, biocompatibility, bioactivity, degradation behaviour or its hydration properties.

Functionalisation of PGS

The functionalisation or copolymerisation of PGS or pre-PGS with other chemical entities can yield physicochemical property enhancements, increase its range of applicability and enhance its processing capabilities. With this respect, photopolymerisation is an alternative processing approach to from a crosslinked elastomeric network from PGS, overcoming the limitation of the thermal curing process [246,247,253,298,299,301–303]. Nijst *et al.* [253] demonstrate the synthesis of photocrosslinkable poly(glycerol sebacate) acrylate (PGS-Acr), by reacting pre-PGS with acrylic chloride under mild conditions and short UV exposure times. The physicochemical properties of the PGS-Acr elastomers were adjustable, by varying the degree of acrylation during the PGS-Acr synthesis. The PGS-Acr elastomers were characterised with E_s, σ_{smax} and ε_{sb} values in the range of 0.05-1.38 MPa, 0.05-0.50 MPa and 42-189% [253], respectively, which increased linearly with the degree of acylation. The elastomers exhibited

in vitro degradation rates of 10% in 49 days under enzyme-free conditions and enhanced weight losses under enzyme-containing conditions [253], while PGS-Acr exhibited *in vivo* degradation rates of 3-12% in 7 days [246]. PGS-Acr presented good biocompatibility but indicated the tendency of enhanced inflammatory response *in vivo* with an increased degree of acrylation [298]. Bodakhe *et al.* [318] synthesised photocrosslinkable poly(glycerol sebacate) fumarate (PGS-Fur), by reacting pre-PGS with different ratios of fumaryl chloride under mild conditions and short UV exposure times. The physical and mechanical properties of the PGS-Fur depended on the degree of fumarylation and were characterised with E_s and ε_{sb} values in the range of 0.5-1.0 MPa and 37-80%, respectively. The elastomers presented good *in vitro* and *in vivo* biocompatibility and exhibited *in vitro* degradation rates of up to 8% in 45 days under enzyme-free conditions, while PGS-Fur exhibited enhanced *in vivo* degradation rates of up to 60% in 45 days. Zhu *et al.* [303] prepared photocrosslinkable poly(glycerol sebacate) cinnamate (PGS-Cin) elastomers, by functionalising pre-PGS with pendant cinnamate groups under mild condition and without photoinitiators. The PGS-Cin elastomers required long UV exposure times and featured relatively high sol contents between 31-49% after the photocrosslinking process. Depending on the cinnamate moieties, PGS-Cin elastomers exhibited E_s, σ_{smax} and ε_{sb} values of 0.05-0.15 MPa, ~0.03-0.07 MPa and 80-140%, respectively. The elastomers were characterised with weight losses in the range of between ~20-50% after 90 days in enzyme-free *in vitro* degradation tests, and possessed good biocompatibility properties.

The incorporation of alpha hydroxy acid monomers or low molecular polyester into PGS is a different and simple method to alter its physicochemical properties. Liu *et al.* [309] synthesised poly(glycerol sebacate citric acid) (PGSCA) elastomers by using various molar ratios of citric acid and curing times to crosslink with pre-PGS. The addition of citric acid increased the crosslinking density, the mechanical properties and the hydrophilicity of the

elastomer. The PGSCA elastomers were characterised with E_s, σ_{smax} and ε_{sb} values of 0.6-6.9 MPa, 0.6-2.7 MPa and 33-170%, respectively, and presented *in vitro* degradation rates of ~9-32% in 28 days under enzyme-free conditions [307–309]. However, pure PGSCA elastomers presented a certain cytotoxicity, due to the high degree of acidic degradation products [307,309], which was counteracted through the incorporation of composite materials [307,309]. Sun *et al.* [306] analysed the degradation behaviour of poly(glycerol sebacate lactic acid) (PGSLA) elastomers, which were synthesised with different ratios of lactic acid. *In vitro* degradation tests indicated characteristics of surface and bulk erosion [305,306], while the PGSLA elastomers exhibited *in vitro* degradation rates of ~20-40% in 80 days under enzyme-free conditions [305]. The PGSLA elastomers featured E_s values of 2.94-21 MPa and presented suitable biocompatibility [305,306]. Similarly, Cheng *et al.* [311] synthesised a series of poly(glycerol-sebacate)-co-poly(L-lactic acid) (PGS-co-PLLA) branched copolymers via the ring opening copolymerisation of low molecular weight L-lactide with pre-PGS. PGS-co-PLLA presented overall improved hydrophilicity and favourable inflammatory responses *in vivo*, compared to low molecular weight PLLA and PGS/PLLA blends. Sun *et al.* [304] investigated the biodegradability and mechanical properties of poly(glycerol sebacate glycolic acid) (PGSGA) elastomers, which were produced with various molar ratios of glycolic acid, while the synthesis reaction was conducted with all constituent monomers simultaneously. The PGSGA elastomers were characterised with E_s values of ~2.5-12.5 MPa, which dropped with higher degrees of glycolic acid. The elastomers were characterised with *in vitro* degradation rates of ~30-75% in 65 days under enzyme-free conditions, while the PGSGA elastomers degraded *in vivo* completely after 60 days. Aydin *et al.* [319] reported the synthesis of poly(glycerol sebacate)-co-poly(ε-caprolactone) (PGS-co-PCL) via a two-stage, catalyst-assisted terpolymerisation reaction. PGS-co-PCL elastomers were flexible and presented good biocompatibility, but

characterised with poor cell-adhesion properties *in vitro*. The usage of a supercritical carbon dioxide fluid-assisted foaming method failed to create stable and porous structures with the elastomer, however, PGS-co-PCL presented self-healing behaviours through the relaxation of the random chain network and the formation of new hydrogen bonds.

The incorporation of hydrophilic polyols into the PGS is another route to alter its physicochemical properties, enhancing its hydration characteristics but with limited water uptake capacity. Patel *et al.* [310] developed poly(glycerol sebacate)-co-poly(ethylene glycol) (PGS-co-PEG) copolymers with different molar ratios of glycerol to PEG. The elastomers were synthesised via the polycondensation of sebacic acid and PEG, followed by the addition of glycerol. The incorporation of PEG increased the hydrophilic characteristics of the PGS-co-PEG elastomers and affected their physicochemical properties, such as its mechanical properties, along with their swelling and degradation behaviour. Hydrated PGS-co-PEG elastomers were characterised with E_s, σ_{smax} and ε_{sb} values of 0.01-1.5 MPa, 0.01-0.3 MPa and ~25-190%, and featured *in vitro* degradation rates of between 15-81% after 21 days under enzyme-free conditions. The PGS-co-PEG elastomers presented good cyclic mechanical properties and good biocompatibility properties. Wu *et al.* [302] developed photocrosslinkable hydrogels based on methacrylated poly(glycerol sebacate)-co-poly(ethylene glycol) (PGS-co-PEG-MAc) copolymers. The sebacic acid and PEG were polycondensed to a pre-polymer, followed by the addition of glycerol to synthesise the copolymer, and then methacrylated. The physicochemical properties of the PGS-co-PEG-MAc hydrogels were controllable by altering the degree of methacrylation. The hydrogels were characterised with *in vitro* degradation rates of between 13%-87% after 25 days under enzyme-free conditions, along with good biocompatibility properties. Recently, Ye *et al.* [292] developed supramolecular hydrogels via PGS-based copolymers through the atom transfer radical polymerisation method. Briefly, brominated PGS macroinitiators were

copolymerised with poly(ethylene glycol) methyl ether methacrylate and threaded with α-cyclodextrin, creating the supramolecular hydrogel system. The hydrogel system featured injectable properties, as well as a tuneable and a low upper critical solution temperature of less than 90 ºC, in addition to rapid gelation and rapid self-healing properties.

The use of isocyanate-based crosslinkers to create PGS-based urethane is a different approach to overcome the long and harsh process conditions of pristine PGS. Pereira *et al.* [312] developed highly tuneable PGS-based urethane with hexamethylene diisocyanate (HDI), which will be more specifically discussed in Chapter 5. Li *et al.* [320] synthesised PGS-based urethane with low molar ratios of 4,4'-diphenylmethylene diisocyanate (MDI), via the additional use of a thermal crosslinking step. The PGS-based urethane exhibited E_s, σ_{smax} and ε_{sb} values in the ranges of 0.3-1.6 MPa, 0.9-1.7 MPa and 240-270%, respectively. The elastomers were characterised with *in vitro* degradation rates of between ~15%-23% after 21 days under enzyme-free conditions. However, the application of MDI as a crosslinking agent is limited due to its high cytotoxicity [320,321].

PGS-based blends

The blending of PGS with different biopolymers is a versatile method of combining two or more polymers with different physical properties in a single system [322]. However, the development of PGS-based blends was mainly applied in association with the electrospinning process, as discussed in Section 2.3.3. PGS-based blends were fabricated with natural and synthetic biopolymers, such as gelatin [276], PCL [266,275], PVA [277], PLLA [278], PBS-DLA [281,323], poly(3-hydroxbutyrate) (P3HB) [324], PHBV [279] and PLDLLA [279], as well as polyaniline (PANI) [325].

Kharaziha *et al.* [276] engineered fibrous pre-PGS/gelatin blend scaffolds containing 33 wt% and 66 wt% of pre-PGS. The pre-PGS/gelatin blends were crosslinked via the crosslinking agents N-(3-dimethylaminopropyl)-N'-ethylcarbodiimide and

N-hydroxysuccinimide, which lead to the formation of amide bonds between the carboxyl and amine groups of both polymers [276]. The fibrous pre-PGS/gelatin blend scaffolds with 66 wt% of pre-PGS presented lower stiffness and strength, but enhanced elongation at break compared to pristine gelatin scaffolds, which was attributed to the plasticising effects of pre-PGS [276].

Sant *et al.* [266] developed electrospun pre-PGS/PCL blend scaffolds which contained 66 wt%, 75 wt% and 83 wt% of pre-PGS. Compared to the pristine electrospun PCL scaffold, the pre-PGS/PCL scaffolds exhibited superior hydrophilicity and biocompatibility, due to the high degree of non-bonded hydroxyl groups on the pre-PGS backbone chain [266]. The pre-PGS/PCL scaffolds with 66 wt% and 75 wt% of pre-PGS exhibited decreased stiffness and elongation compared to PCL, while higher pre-PGS concentrations enhanced the stiffness and strength of the fibrous scaffolds, owing to the increase in electrospun fibre diameter [266].

Jeffris *et al.* [277] manufactured fibrous PGS/PVA blend scaffolds containing 55 wt% of PGS. PVA was used solely as a soluble carrier material and was removed by washing in water, after the PGS was thermally crosslinked. However, the fibrous PGS scaffolds were still comprised of residual PVA, after performed washing procedures [277]. The residual PVA in the fibrous PGS scaffolds were attributed to material encapsulation, or PVA was thermally crosslinked with PGS, due to the condensation reaction between the carboxyl groups of PGS and the hydroxyl groups of PVA [277].

Kenar *et al.* [279] fabricated fibrous pre-PGS/PLDLLA/PHBV blend scaffold with 2 wt% of pre-PGS, as well as macroporous pre-PGS/PLDLLA scaffold with 4 wt% of pre-PGS, without any crosslinking process applied.

Tallawi *et al.* [281,323] investigated fibrous pre-PGS/PBS-DLA blend scaffolds and films with 30 wt%, 40 wt%, 50 wt%, 60 wt% and 70 wt% of pre-PGS. The mechanical properties, the hydrophobicity increased with higher weight ratios of PBS-DLA in the blend, while the

degradation rate decreased. In addition, the pre-PGS/PBS-DLA blends presented also good biocompatibility *in vitro*, however, the blends with a higher ratio of pre-PGS presented a lower cell viability, due to the higher acidity.

Xu *et al.* [278] prepared PGS/PLLA blend films containing 80 wt%, 90 wt% and 95 wt% of PGS. The films were created via solution casting and were thermally crosslinked. All PGS/PLLA film blends presented similar mechanical properties to pristine PGS, but they featured enhanced elongation at break.

Roether *et al.* [324] developed PGS/P3HB blend films with 87.5 wt% and 90 wt% of PGS via solvent casting and thermal crosslinking. The addition of P3HB improved the mechanical properties and the hydrophilicity of the blends, but increased the *in vitro* degradation rates. The incorporation of titanium dioxide nanoparticles of 1 vol% and 2 vol% was also investigated, affecting the morphology, hydrophilicity, mechanical and chemical properties of the PGS/P3HB blends.

Qazi *et al.* [325] developed electrically conductive PGS/PANI blends with 10-30 vol% of PANI content, created via solution casting and thermal crosslinking. The electrical conductivity and the mechanical properties of the blends improved with increasing PANI content. The PGS/PANI blends featured mechanical properties with E_s, σ_{smax} and ε_{sb} values in the ranges of 2.4-6.3 MPa, 1.9-9.2 MPa and 20-31%, respectively. The conductivity of the PGS/PANI blends was preserved for at least 100 h and presented *in vitro* degradation rates of up to 7.72% in enzyme-free PBS solution. The PGS/PANI blends presented good biocompatibility and possessed an attractive pH buffering effect compared to pure PGS.

PGS-based composites

The creation of PGS-based composites is a simple and effective method to improve the physicochemical properties of PGS. Nano- or micro-sized inorganic or organic fillers, such as Bioglass® [256,259,313], nanohydroxyapatite [314], silica glass [243,317], cellulose [315],

titanium dioxide [324], halloysite nanotubes [257], and carbon nanotubes [316] have been added into the matrix of PGS to incorporate different functionalities and to tailor its properties for specific tissue engineering applications. For instance, the incorporation of cellulose into PGS presented enhanced tensile strength and modulus, due to the strong bonding between the hydroxyl groups of PGS and cellulose as well as the high strength and modulus of cellulose, along with tuneable biodegradation and hydrophilicity characteristics [315]. Also, Wu *et al.* [326] developed poly(glycerol sebacate urethane)-cellulose nanocomposites which demonstrated water-active shape-memory effects and mechanically adaptive functions, due to the reversible formation and disruption of a cellulose percolation network in the polymer matrix. The addition of Bioglass® into PGS resulted in reinforced mechanical properties, along with improved biocompatibility, attributed to the decrease of acidic degradation products of PGS [256,259,313]. Gaharwar *et al.* [316] developed covalent crosslinked PGS/carbon nanotubes composites which significantly increased in mechanical stiffness with no compromised effects on its elastomeric properties. Overall, the development of PGS-based composites presented to be an effective and cost-efficient strategy to enhance the physicochemical properties of PGS, while maintaining the desired compliance of biomaterials required for soft tissue engineering.

2.4 Principle of freeze-drying

Freeze-drying, also known as lyophilisation, is a common method for producing porous scaffolds from natural and synthetic polymers [327–330]. It is a special drying process in which the solvent of an appropriate polymer/solvent solution crystallises at a temperature below its freezing point and then directly sublimes from solid phase into vapour phase by reducing the surrounding pressure. Thus, the crystallised solvent acts as a template for the pores and the polymer remains in its dry state after solvent sublimation, yielding a porous structure.

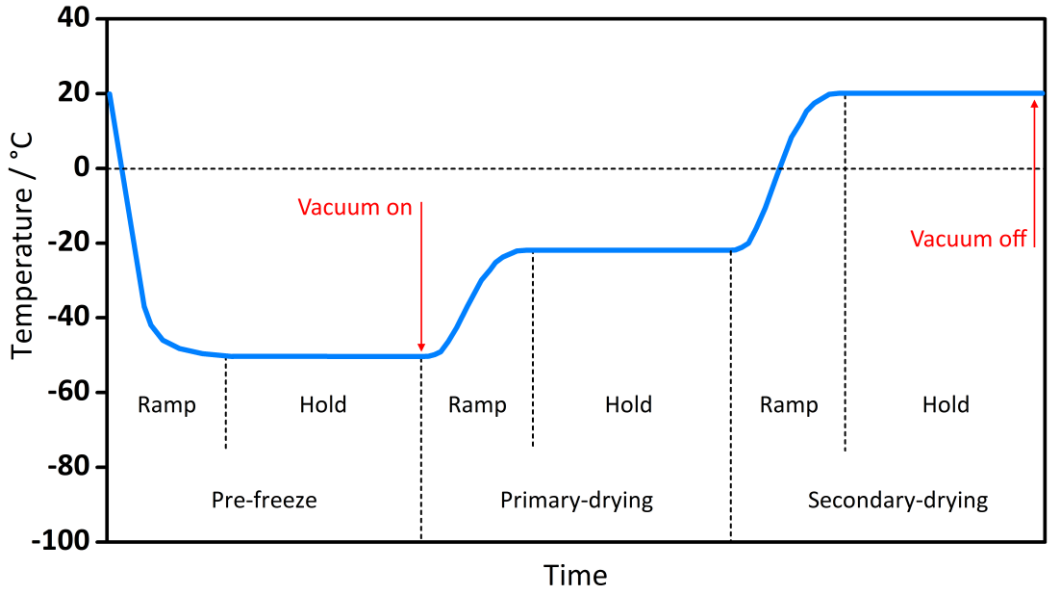

Figure 2.22: Diagram of a typical three stage program during a freeze-drying process, adapted from Labconco Corporation [331].

The freeze-drying process consists of three stages [332,333], as seen in Figure 2.22. In the first stage, the so-called pre-freeze stage, the polymer/solvent solution crystallises to create a solid matrix while holding the temperature constant for equilibration. The second stage, the so called primary-drying stage, involves the sublimation of the crystallised solvent by reducing the pressure of the environment by a vacuum, which also takes place at low temperatures. The difference between the vapour pressure of the crystallised solvent and the environment pressure provides the driving force for sublimation. The primary-drying stage is completed when all crystallised solvent sublimates. At this stage, it is still possible that some bound solvent is remaining in the product which can be removed by desorption at higher temperatures. Therefore, in the last stage, the so-called secondary-drying stage, the environment temperature is raised to ambient or higher temperatures and held until the polymer material is equilibrated at the desired temperature.

The porous structure and properties of the scaffolds such as pore size, porosity, interpore connectivity, pore shape, pore wall morphology and mechanical properties can be modified

via the alteration of the process conditions, or by adjusting the polymer/solvent solution [329,330,334]. For instance, the differences in the pore size and inner scaffold structure reflect the differences in heat transfer rates during the solvent crystallisation process at low temperatures. Higher freezing rates produce a large number of small sized solvent crystals and therefore the formation of many nuclei of solvent crystals, resulting in a structure of smaller-sized pores. In contrast, lower freezing rates lead to larger porous structure due to the fact that larger solvent crystals occur [335]. In addition, studies have shown that it is possible to influence the growing direction of solvent crystals by controlling the heat transfer direction [329,330].

2.5 Summary of the literature review

Various ATE strategies, cell sources, materials and types of cell carriers have been investigated to engineer adipose tissue *in vitro* and *in vivo*. Despite promising approaches, the optimal adipose tissue scaffolds from either natural or synthetic materials remain illusive and engineered scaffolds that mimic structure and properties of adipose tissue are not yet readily available. The utilisation of synthetic materials combined with adult stem cells presented potential to generate adipose tissue, however, the current synthetic scaffolds do not provide satisfactory performance in ATE, due to their high stiffness, plastic deformation and failure when exposed to dynamic loads. With this respect, adipose tissue is exposed to large deformations and engineered scaffolds for ATE need to be flexible and withstand physiologically induced deformations, hence, the mechanical properties of engineered scaffolds cannot be ignored when regenerative therapies are being developed, indicating a strong need for developing tissue scaffolds from other synthetic biomaterials [82].

PGS demonstrated to be a highly versatile synthetic biodegradable and biocompatible elastomer, which was specifically designed to imitate the mechanical behaviour of soft tissues. PGS features several benefits compared to common synthetic biopolymers, such as

tailorable physicochemical properties and superior performance in dynamic mechanical environments, overall demonstrating high potential in ATE. Recent developments in terms of PGS-based copolymers, blends or composites presented further performance improvements with respect to the bioelastomers processability, biocompatibility, bioactivity, degradation behaviour, mechanical properties or hydration properties, overall indicating high modifiability for specific requirements. However, PGS reveals various processing limitations and challenges, due to its harsh curing conditions including long periods of curing time, high curing temperatures and a mandatory vacuum environment. In addition, pre-PGS melts at its curing temperature and is unable to maintain its structure, making it challenging to fabricate 3D structures. With this respect, current fabrication strategies for manufacturing large-volume 3D PGS-based scaffolds are limited, which constrains the full potential and adoption of PGS in a broader field of biomedical applications. Thus, the development of novel fabrication technologies or strategies is essential for the design of PGS-based scaffolds with biomimetic structures and properties for prospective tissue engineering applications.

Chapter 3. Large three-dimensional poly(glycerol sebacate)-based scaffolds - A freeze-drying preparation approach

3.1 Introduction

As discussed in Chapter 2, various sophisticated technologies such as micromoulding/lamination [238,239,265,267,269–271], laser micro-ablation/lamination [234,255,272,273], solid freeform fabrication method [242], blend [266,268,274–281] and coaxial core/shell [268,278,282–286] electrospinning, as well as the combined salt-leaching and salt-fusion method [235,236,287–289] were utilised to create PGS scaffolds. Despite their specific advantages, these technologies led to a primarily low throughput of small-sized scaffolds with unsuitable porous structures or porosities, constraining the full potential and adoption of PGS in a broader field of soft tissue engineering applications. The focus of this chapter is, therefore, the development of a novel fabrication strategy which will enable an efficient preparation of large 3D porous PGS-based scaffolds.

The novel fabrication strategy will employ a minor structure-supporting biopolymer and create large 3D porous PGS-based scaffolds containing the additional biopolymer via a freeze-drying and a subsequent curing process. Biocompatible and biodegradable PLLA was chosen as the structure-supporting polymer because of its high melting point, which will prevent the low-viscosity pre-PGS from enclosing the porous structures during the curing stage and therefore avoiding structural collapse and maintaining 3D structures.

This will allow one to overcome several constraints of pure PGS in terms of the scaffold design and fabrication possibilities. The variation of the PGS/PLLA blends in respect to the composition and concentration will enable the creation of scaffolds with the desired physical

properties, such as high porosities and interconnected open-cell structures, as well as softer and more ductile scaffolds resulting from the higher PGS ratios.

The PGS/PLLA blend scaffold samples were created using different ratios of PGS and PLLA material along with the solvent 1,4-dioxane, via the combined processes of freeze-drying and curing. The microstructure characteristics of the fabricated scaffolds were analysed by SEM after each processing step, as well as analysing the effects of varying the ratios of the material compositions and concentrations on the scaffold morphology. The mechanical properties were examined by quasi-static tensile tests, and the *in vitro* degradation kinetics of the scaffolds assessed in enzyme-free and enzyme-containing PBS solution. The structure and properties of the pre-PGS, the crosslinked PGS film and pristine PLLA scaffold were also investigated.

3.2 Experimental section

3.2.1 Materials

Sebacic acid, glycerol, tetrahydrofuran (THF), 1,4-dioxane, phosphate buffered saline (PBS) tablets, ethanol and lipase enzyme from porcine pancreas (54 U mg^{-1}), were purchased from Sigma-Aldrich. PLLA (NatureWorks 4043D; Number average molecular weight, $\bar{M}_n$ = 130,000 g mol^{-1}) was from Cargill Dow LLC.

3.2.2 Preparation of pre-PGS

Pre-PGS was synthesised by using an established method in the literature [16,288]. Briefly, a three-neck flask, loaded with a 1:1 molar mixture of sebacic acid and glycerol, was attached to a Dean-Stark trap with a condenser and a nitrogen bubbler. The mixture was reacted at 120 °C for 72 h under a low-flow nitrogen environment and at constant stirring. The resulting highly viscous pre-PGS was cooled and stored in a closed glass container at room temperature until further use.

3.2.3 Preparation of PGS films

Pre-PGS was dissolved in THF and cast into a non-sticky Teflon-coated metal mould (purchased from a local store). The cast pre-PGS samples were dried under room temperature for 24 h and then cured under vacuum at 150 °C for 24 h. Cured PGS films were stored at room temperature before further examinations were carried out.

3.2.4 Preparation of PLLA and PGS/PLLA blend scaffolds

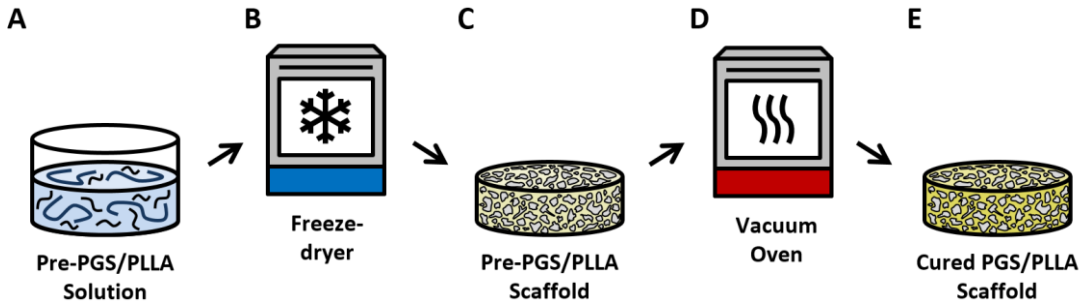

Scheme 3.1: Fabrication steps to obtain cured PGS/PLLA blend scaffolds. The first processing stage is comprised by (A) the solution preparation (dissolution of pre-PGS and PLLA in 1,4-dioxane) and (B) the lyophilisation process (crystallisation of the solvent below its triple point and subsequent sublimation due to low pressure), which produce (C) porous pre-PGS/PLLA scaffolds. The second processing stage involves (D) the curing of the porous pre-PGS/PLLA scaffolds in a vacuum oven at high temperature (crosslinking of pre-PGS), resulting in (E) porous cured PGS/PLLA blend scaffolds.

Cured PGS/PLLA blend scaffolds were prepared in a two-step process, as illustrated in Scheme 3.1. The first step includes the solution preparation, in which various pre-PGS/PLLA weight ratios (in g g^{-1} = 0:2, 1:2, 2:2, 2:3, 2:1, 2.5:1, 3:1, 3.5:1 and 4:1) were dissolved in 40 mL 1,4-dioxane (freezing point: 10-12 °C). All solutions were prepared separately in closed glass containers and stirred for 48 h at 50 °C. The solutions were then cast into a non-sticky Teflon-coated metal baking tray (six cylindrical cavities with a diameter of 60 mm purchased from a local store) and placed in a Labconco FreeZone Triad freeze-dryer for lyophilisation. All solutions were cooled to -40 °C and kept at the temperature for

5 h, allowing the solutions to freeze completely. The frozen solutions were then heated to 10 °C (heating rate of 1 °C min^{-1}) for primary-drying under vacuum for 10 h. In the secondary-drying stage, the temperature was raised to 40 °C (heating rate of 5 °C min^{-1}), held for 10 h, and then lowered to 20 °C (cooling rate of 1 °C min^{-1}) and held for further 10 h to maximize the removal of the solvent. All the as-fabricated pre-PGS/PLLA scaffolds were cut into halves; one half was directly used for analysis, while the other half was utilised for the second processing stage. The second processing stage involved the curing process of all pre-PGS/PLLA scaffolds in a vacuum oven for 24 h at 150 °C, in order to crosslink the pre-PGS. For the purpose of comparison, one type of pristine PLLA scaffolds was created, under the same fabrication scheme as described above. All fabricated scaffolds were stored at room temperature until further use.

3.2.5 Characterisation and testing of pre-PGS and PGS films

Fourier transform infrared spectroscopy (FTIR) was executed by using a Perkin Elmer Spectrum One NTS analyser under attenuated total reflection (ATR) mode (ATR crystal: diamond). Pre-PGS and cured PGS were analysed in the mid-infrared region of 4000-550 cm^{-1} and recorded with a resolution of 1 cm^{-1}.

The density, ρ_{PGS}, of cured PGS film (n = 5) was determined by weight and volume measurements. A Mettler Toledo AB204-S balance was used for weight measurements, while the film volumes were determined by calliper measurements. Samples were dried in a vacuum oven for 24 h at 37 °C, prior to measurements.

Quasi-static tensile tests of cured PGS film were performed on a Zwick Z005 testing machine. Punched-out ‘‘dog bone’’ shaped specimens (n = 5; width: 2.6 mm, gauge length: 20 mm, thickness: 1.74 ± 0.17 mm) were tested at a strain rate of 50 mm min^{-1} using a 100 N load cell till fracture (ASTM D412). All tests were performed at room temperature.

The crosslink density, n_{mech}, of the cured PGS film was evaluated by mechanical measurements and calculated based on the theory of rubber elasticity, which is related to the ideal gas law and given by Equation 3.1 [16,336],

$$n_{mech} = \frac{E_s}{3RT} \tag{3.1}$$

where E_s is the Young's modulus of the solid film, R the universal gas constant, and T the absolute temperature during the tensile tests. With this respect, the crosslink density is expressed in moles of elastically effective network chains per unit volume, and depends on the average molecular weight of the polymer chain segments between two adjacent crosslinks [16,336].

Residual monomer analysis was performed by examining the weight difference of cured PGS samples before and after 24 h ethanol extraction, identifying the leaching quantity of unreacted monomers and oligomers.

3.2.6 Characterisation and testing of PLLA and PGS/PLLA blend scaffolds

The microstructures of all scaffolds were examined by SEM on a Tescan Mira XMU and a FEI Inspect F50. The samples were placed on an aluminium stub and coated with gold (approx. 35 nm thickness) by using a High Resolution Polatron Sputter Coater before SEM observations at 5 kV (pristine PLLA, pre-PGS/PLLA and cured PGS/PLLA scaffolds) or 10 kV (PGS films) were executed. Scanning electron micrographs were taken from the scaffold cross-sections and the average pore sizes of all scaffolds were evaluated by using ImageJ software (n = 600). Only fully defined pores were considered for the geometrical measurements.

The scaffold densities (n = 5), ρ_f, were determined by weight and volume measurements. A Mettler Toledo AB204-S balance was used for weight measurements, while the scaffold volumes were determined by calliper measurements. Samples were dried in a vacuum oven

for 24 h at 37 °C, prior to measurements. The theoretical densities of the solid matrix, $\rho_{f-matrix}$, used in the formation of the PGS/PLLA scaffolds with different weight ratios were calculated according to Equation 3.2,

$$\rho_{f-matrix} = \frac{(w_{PGS} + w_{PLLA})}{(w_{PGS}/\rho_{PGS} + w_{PLLA}/\rho_{PLLA})} \tag{3.2}$$

where w_{PGS} and w_{PLLA} are the weight fractions of PGS and PLLA in the scaffold material (note that $w_{PGS} + w_{PLLA} = 1$), while ρ_{PLLA} is the density of pristine PLLA (1.22 Mg m^{-3}) (note that ρ_{PGS} was determined in Section 3.3.1) [337]. The volume ratio of PGS, φ_{PGS}, was calculated by Equation 3.3, and the volume ratio of PLLA, φ_{PLLA}, is equal to $1 - \varphi_{PGS}$,

$$\varphi_{PGS} = \frac{(w_{PGS}/\rho_{PGS})}{(w_{PGS}/\rho_{PGS} + w_{PLLA}/\rho_{PLLA})} \tag{3.3}$$

The relative density, ρ_r, and the porosity, P_f, of all scaffolds were calculated by Equation 3.4 and 3.5,

$$\rho_r = \frac{\rho_f}{\rho_{f-matrix}} \tag{3.4}$$

$$P_f = (1 - \rho_r) \times 100\% \tag{3.5}$$

respectively.

Quasi-static tensile tests were performed on a Hounsfield H100KS testing machine. As Scheme 3.2 illustrates, scaffold tensile test samples (n = 5; width: 5.92 ± 0.11 mm (y-axis), gauge length: 15 mm (x-axis), thickness: 3.23 ± 0.11 mm (z-axis)) were cut from the centre cross section of each scaffold and tested in the longitudinal direction. Each end of a tensile test strip was glued with adhesive to home-built sample end holders, allowing the fixation onto the tensile grip without damaging the scaffold sample. A 10 N load cell was used and a strain rate of 5 mm min^{-1} was executed till fracture.

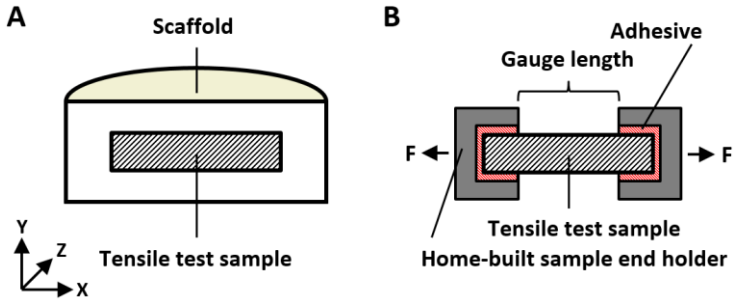

Scheme 3.2: (A) Scaffold tensile test samples were cut out from the centre cross-section of each individual scaffold type. (B) Each tensile test sample was tested in the longitudinal direction and glued with epoxy resin onto home-built sample end holders, allowing a damage-free fixture onto tensile test grips.

3.2.7 *In vitro* degradation tests

In vitro degradation studies were performed on cured PGS film (n = 3; diameter: 3.5 mm, thickness: 1.57 ± 0.18 mm mm), as well as on PLLA scaffold and PGS/PLLA (weight ratios 2.5:1 and 3:1) scaffolds (n = 3; width: 3.83 ± 0.41 mm, length: 5.41 ± 0.81 mm, thickness: 2.91 ± 0.22 mm). All samples were first subjected to a sterilisation procedure, before degradation studies were performed. Briefly, all specimens were saturated in a 70% v/v ethanol-water solution and shaked in a Stuart SI500 shaking incubator (15 min, 100 rpm) to extract the unreacted pre-polymer and monomers, and were then washed with copious amounts of distilled water. This cleaning procedure was performed three times in series, while at the end all specimens were dried in a vacuum oven at 37 °C until constant weight was obtained. For the enzymatic degradation tests, specimens were saturated in a PBS solution (30 mL, pH = 7.4) containing 110 U L^{-1} lipase enzyme, noting that serum lipase in healthy adults is in the range of 30-190 U L^{-1} [338]. Specimens were placed in a Stuart SI500 shaker incubator at 37 °C and 100 rpm. The enzyme containing solutions were changed every day to guarantee enzymatic activity. The pH value of the degradation medium was monitored after each solution change. After 1, 3, 7, 11, 15, 19, 23, 27 and 31 days of incubation, the specimens were removed from the vials, washed with distilled water and dried in an vacuum

oven at 37 °C, until constant weight was obtained. The percentage of weight loss, W_{loss}, was calculated by Equation 3.6,

$$W_{loss} = \frac{W_0 - W_{day}}{W_0} \times 100\% \quad (3.6)$$

where W_0 and W_{day} are the initial weight before incubation and the weight measured on the day of the incubation. Control studies were performed on all sample types in enzyme-free PBS solutions, under the same test conditions. SEM analysis was performed after 31 days of *in vitro* degradation on a Camscan S2 at 5 kV on gold coated cured PGS film, as well as PLLA and PGS/PLLA scaffold specimens.

3.2.8 Statistical analysis

All measurements were reported as mean ± standard deviation (SD) with a confidence level of 95%. Differences were statistically tested against a null hypothesis of no difference between samples using a two-sample *t*-test (two-tailed) with equal variance not assumed (significance = $p < 0.05$).

3.3 Results and discussion

3.3.1 Characterisation of pre-PGS and cured PGS film

Pre-PGS and cured PGS film samples were successfully fabricated. Pre-PGS was characterised by a white/yellowish colour, high viscosity and extreme adhesive properties. Cured PGS films were transparent and characterised by a light yellow colour, high elasticity and low adhesive qualities.

FTIR spectra of pre-PGS and cured PGS, which was treated at 150 °C for 24 h, are illustrated in Figure 3.1 (A, B). With respect to the spectrum of pre-PGS, the broad peak at 3442 cm^{-1} is attributed to hydrogen bonded hydroxyl groups (O-H) [339], while the intense peaks at 2926 cm^{-1} and 2852 cm^{-1} are associated to the stretching vibration of alkane groups

[252,339]. The sharp absorption peaks at 1732 cm^{-1} and 1166 cm^{-1} are attributed to the formation of ester bonds C=O and C-O, respectively [252,339]. Peaks at around 1400 cm^{-1} are related to carboxylic acid O-H bend, and the distinct peaks in the range of 1300-1200 cm^{-1} as well as at 1097 cm^{-1} and 1048 cm^{-1} belong to the stretch vibration bands of C-O [17].

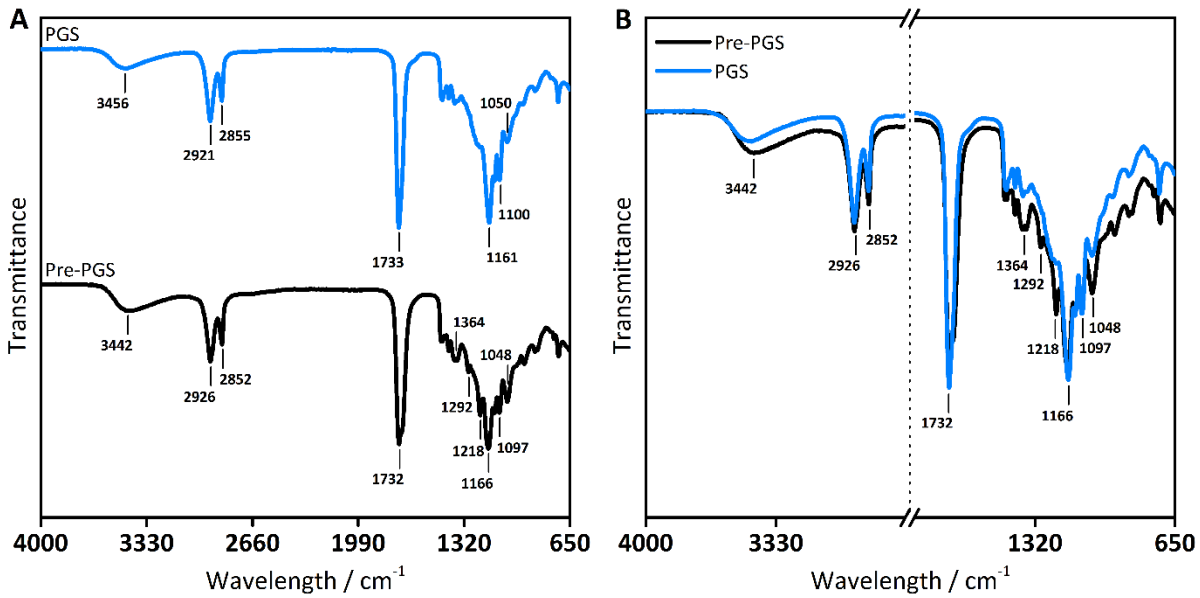

Figure 3.1: (A) Vertically shifted and (B) overlapped FTIR spectra of pre-PGS and cured PGS (24 h at 150 °C).

FTIR spectrum of the cured PGS sample is characterised by the same distinct bands as the pre-PGS. Due to the curing process, the broad absorption peaks of hydroxyl groups at around 3456 cm^{-1} decreased, while the absorption peaks of the ester bonds at around 1733 cm^{-1} and 1161 cm^{-1} increased. In addition, the distinct peaks at around 1400-1200 cm^{-1} became weaker or disappeared, the band at 1100 cm^{-1} increased and the peak at 1050 cm^{-1} decreased. The obtained results are in accordance with previous studies, overall indicating an increase in the degree of crosslinking [244,252,256,339].

Representative tensile stress-strain curve of cured PGS film (24 h at 150 °C) is illustrated in Figure 3.2, which featured a tensile Young's modulus, E_s, ultimate tensile strength, σ_{smax}, strain at break, ε_{sb}, and energy at break, U_{sb}, of 0.89 ± 0.17 MPa, 0.38 ± 0.03 MPa, 49.56 ±

5.60% and 0.11 ± 0.01 MJ m^{-3}, respectively. The mechanical properties of PLLA were determined in a previous research study, with a E_s, σ_{smax}, ε_{sb} and U_{sb} of 1.56 ± 0.03 GPa, 41.4 ± 1.6 MPa, 3.2 ± 0.3% and 0.79 ± 0.42 MJ m^{-3}, respectively [337]. The results demonstrate an immense discrepancy between the mechanical properties of PGS and PLLA, in which PGS features softness and flexibility suggesting it is more appropriate for soft tissue engineering applications [16]. The density of the cured PGS was measured as 1.13 ± 0.01 Mg m^{-3}, which again is in agreement with previous research studies [237,251].

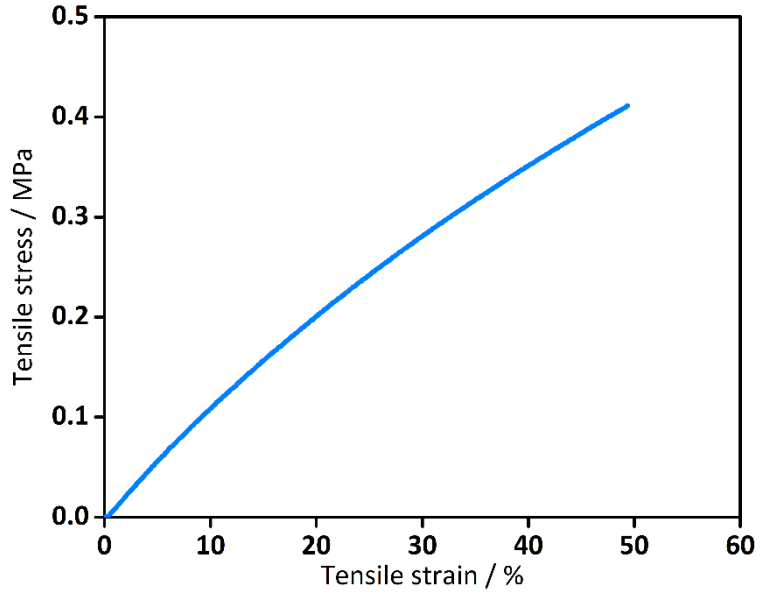

Figure 3.2: Representative tensile stress-strain curve of cured PGS film (24 h at 150 °C).

The n_{mech} of the cured PGS sample was calculated by using Equation 3.1 as 120.39 ± 22.49 mol m^{-3}, while the residual analysis presented a weight change of 6.25 ± 0.28% after 24 h ethanol extraction. The surface of the cured PGS samples was analysed after the ethanol extraction, indicating that strong swelling might promote surface microcracking (Figure 3.S1, Appendix A). All results demonstrate that the curing process of pre-PGS resulted in a highly crosslinked polymer.

3.3.2 Microstructures of PLLA and PGS/PLLA blend scaffolds

The pristine freeze-dried PLLA scaffold was characterised by a homogenous scaffold structure and white colour (Figure 3.S2, Appendix A). It presented a ladder-type and oval shaped open-cell microstructure, as seen in Figure 3.3 (A), which is commonly found for the freeze-drying process [340]. PLLA scaffolds were subjected to the same curing process as for PGS (24 h at 150 °C), and the results showed no major modification with respect to pore size and open-cell microstructure, as presented in Figure 3.4 (A). The mean pore size decreased after the curing stage by 13.7% to 70.1 µm, as listed in Table 3.1. The results demonstrate that PLLA can withstand the harsh curing condition of PGS due to its high melting temperature, and is a promising material for realizing the freeze-drying fabrication strategy for cured PGS/PLLA scaffolds.

Table 3.1: Pore sizes of PLLA and PGS/PLLA blend scaffolds, before and after the curing process

Solution conc.[a] / g mL^{-1}	PGS : PLLA weight ratio / g g^{-1}	PGS : PLLA volume ratio, φ_{PGS}: φ_{PLLA}	Pore size, non-cured / µm	Pore size, cured / µm	Pore size difference before & after curing / %
0.050	0 : 2	0 : 100	81.2 ± 3.2	70.1 ± 2.4	-13.7
0.075	1 : 2	35 : 65	78.5 ± 4.2	59.9 ± 2.3	-23.7
0.100	2 : 2	52 : 48	82.8 ± 4.5	55.2 ± 4.2	-33.4
0.125	2 : 3	42 : 58	54.8 ± 1.9	40.0 ± 0.8	-26.9
0.075	2 : 1	68 : 32	85.9 ± 3.7	83.5 ± 4.2	-2.7
0.088	2.5 : 1	73 : 27	104.1 ± 6.4	92.6 ± 2.8	-11.1
0.100	3 : 1	76 : 24	93.7 ± 6.8	89.8 ± 3.5	-4.2
0.113	3.5 : 1	79 : 21	88.2 ± 5.9	82.2 ± 3.1	-6.8
0.125	4 : 1	81 : 19	81.7 ± 5.9	73.5 ± 3.4	-10.0

[a] Concentration.

Pre-PGS/PLLA blend scaffolds with different weight ratios were produced via the freeze-drying process, characterised by a homogenous scaffold structure and a

white/yellowish colour, as demonstrated in Figure 3.5 (A1-2). Each of the scaffolds was approximately 6 cm in diameter and over 1 cm in thickness. The surface of the pre-PGS/PLLA samples exhibited minor adhesive properties, due to the presence of pre-PGS. All freeze-dried pre-PGS/PLLA scaffolds were characterised by highly interconnected open-cell microstructure, as seen in Figure 3.3 (B-I) The structure analysis showed in general, that both polymers were well distributed throughout the scaffold matrix, indicating that both components can coexist in a hybrid system. All samples were analysed from three perspectives, evaluating how the material composition and solution concentration affect the pore size and microstructure of the pre-PGS/PLLA scaffolds. The scaffolds (listed in Table 3.1) were classified into groups which featured (I) a fixed PLLA and a varied PGS concentration in the initial freeze-drying solution (pre-PGS/PLLA scaffolds with weight ratios of 1:2 and 2:2, as well as 2:1, 2.5:1, 3:1, 3.5:1 and 4:1), (II) a fixed PGS and a varied PLLA concentration (pre-PGS/PLLA scaffolds with weight ratios of 2:1, 2:2 and 2:3) and (III) pre-PGS/PLLA scaffolds with a fixed total material concentration (pre-PGS/PLLA scaffolds with weight ratios of 1:2 vs. 2:1, 2:2 vs. 3:1 and 2:3 vs. 4:1).

The examination of pre-PGS/PLLA scaffolds which featured a fixed PLLA and a varied PGS concentration (Figure 3.3 (B, C, E-I)) showed that a higher weight ratio of pre-PGS had the tendency to form non-uniform and irregularly shaped cell structures (Figure 3.3 (E-I)), due to the presence of a higher amount of viscous and malleable pre-PGS under the secondary-drying stage (holding the samples at 40 °C for 10 h). In addition, at lower pre-PGS ratios (1:2 vs. 2:2, 2:1 vs. 2.5:1) the average pore size increased with increasing pre-PGS content. For instance, pre-PGS/PLLA scaffold with a weight ratio of 1:2 gave a lower pore size than that with a weight ratio of 2:2, and the scaffold with a weight ratio of 2:1 had a smaller pore size than that with a ratio of 2.5:1. In contrast, at higher pre-PGS ratios (3:1, 3.5:1 and 4:1) the average pore size decreased with increasing pre-PGS ratio, presumably due

the higher material concentration and the high content of viscous pre-PGS under the secondary-drying stage. The pre-PGS/PLLA scaffold with a weight ratio of 2.5:1 exhibited the highest average pore size of 92.6 μm, which also represents a peak point within the characterised pre-PGS/PLLA scaffolds with weight ratios of 2:1, 2.5:1, 3:1, 3.5:1 and 4:1.

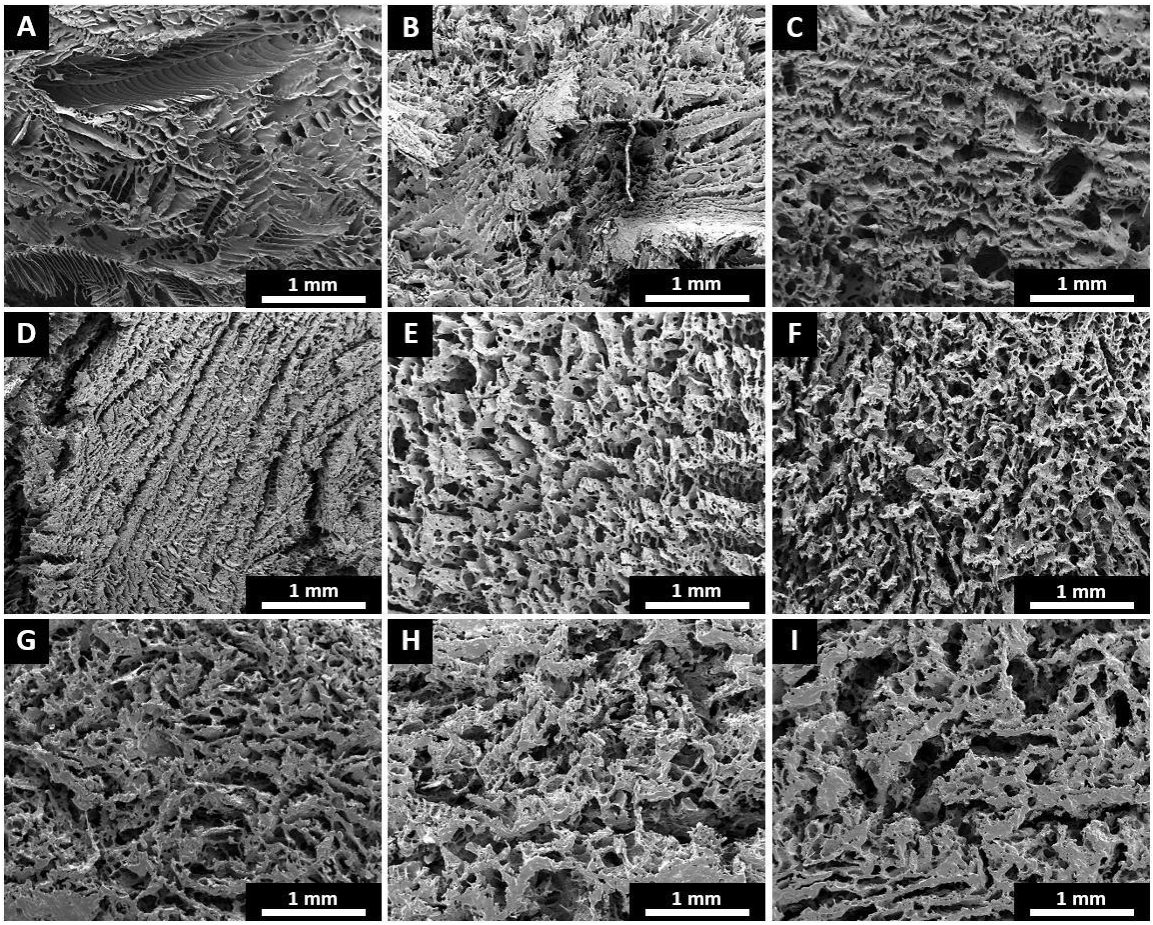

Figure 3.3: SEM micrographs of (A) pristine PLLA, and pre-PGS/PLLA blend scaffolds with weight ratios of (B) 1:2, (C) 2:2, (D) 2:3, (E) 2:1, (F) 2.5:1, (G) 3:1, (H) 3.5:1 and (I) 4:1, presenting the highly interconnected pore structure after the freeze-drying stage.

By analysing pre-PGS/PLLA scaffolds with a fixed PGS and a varied PLLA concentration, results demonstrated that an increase of the PLLA weight ratio reduced the pore size in the scaffolds (Table 3.1). For instance, pre-PGS/PLLA scaffold with a weight ratio of 2:1 featured an average pore size of 85.9 μm, which decreased to 40.0 μm for the pre-PGS/PLLA scaffold with a weight ratio of 2:3. This change in pore size is attributable to the higher

material concentration. The material concentration influences the pore size, in which an increased material amount gives rise to a higher polymer volume in the solution and therefore smaller pore dimensions. The evaluation of the cell structures illustrated that a higher weight ratio of solid PLLA tended to form uniform circular and regular cell structure, characterised with rougher and thicker cell-walls, while a higher weight ratio of pre-PGS caused thinner and smoother cell-wall structures, as seen in Figure 3.6.

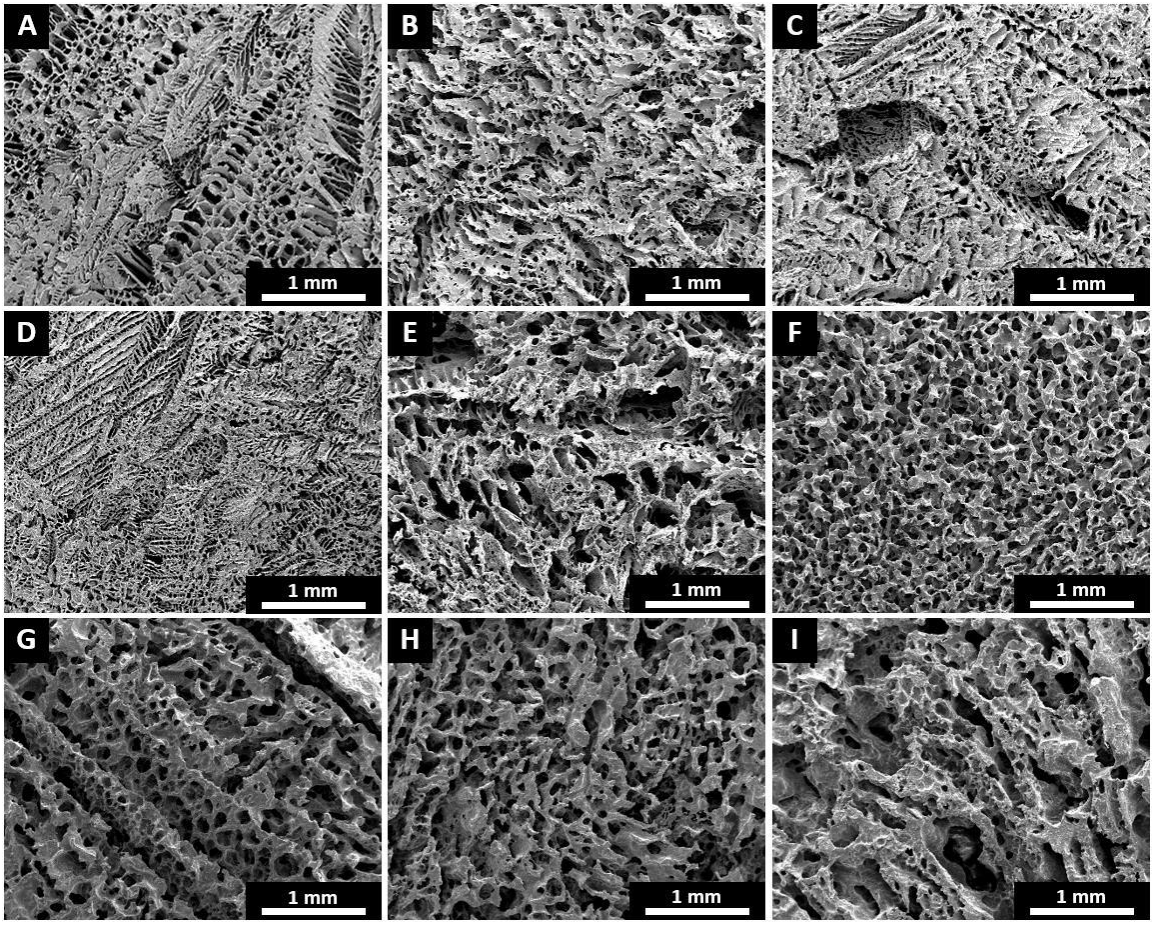

Figure 3.4: SEM micrographs of (A) pristine PLLA and PGS/PLLA blend scaffolds with weight ratios of (B) 1:2, (C) 2:2, (D) 2:3, (E) 2:1, (F) 2.5:1, (G) 3:1, (G) 3.5:1 and (I) 4:1, demonstrating the final microstructure after the curing stage.

The comparison of pre-PGS/PLLA scaffolds with a fixed total material content indicated that the weight ratio of pre-PGS to PLLA influenced the pore size and structure even when the material concentration was fixed. Results indicated clearly, that the pre-PGS/PLLA

scaffolds with a higher pre-PGS weight ratio accomplished larger pore sizes than their corresponding scaffolds with a higher PLLA weight ratio. For example, the pre-PGS/PLLA scaffold with a weight ratio of 4:1 achieved 83% bigger average pore size than the pre-PGS/PLLA scaffold with a weight ratio of 2:3, and the pre-PGS/PLLA scaffold with a weight ratio of 2:1 achieved 39% bigger pore size than the pre-PGS/PLLA scaffold with a weight ratio of 1:2. It is interesting to note, that pre-PGS is characterised by a lower density (namely a higher volume per equal weight) compared to PLLA, being 1.13 Mg m^{-3} vs. 1.22 Mg m^{-3}. Thus, freeze-dried pre-PGS/PLLA scaffolds with a higher pre-PGS weight ratio should have obtained smaller pore sizes owing to the higher polymer volume content in the solution. The discrepancy from this assumption to the actual results can be explained by two main effects from the pre-freezing and the secondary-drying stages. First, both polymers featured significantly different molecular weights and glass transition temperatures, T_g. PLLA was characterised by a higher number average molecular weight ($\overline{M}_n$= 130,000 g mol^{-1}) and a T_g of 54.2 °C [337], while non-crosslinked pre-PGS features generally a lower number average molecular weight value (below $\overline{M}_n$ = 30,000 g mol^{-1}) [253,257,308] and a T_g in the range of -40 °C to -30 °C [252]. Briefly, during the pre-freezing stage of the lyophilisation process (from room temperature to -40 °C), the polymer solution became gradually frozen, and crystals of the 1,4-dioxane solvent developed, with increasing freezing time. Owing to the high T_g value of PLLA, the polymer chains of PLLA were immobilised and harder to be pushed around by the growing 1,4-dioxane crystals. In contrast, pre-PGS polymer chains were more flexible and easier to shift in the polymer-rich phase, thus, facilitating the growth of the solvent crystals and leading to a big pore size. Second, during the secondary-drying stage (in particular when holding the samples at 40 °C for 10 h), pre-PGS became viscous, which could move and affect the cell structure and pore size. As expected, scaffolds which were produced with lower material concentrations (pre-PGS/PLLA scaffolds with a weight ratio of

1:2 and 2:1), achieved greater pore sizes than scaffolds with higher material concentrations (pre-PGS/PLLA scaffolds with a weight ratio of 2:3 and 4:1), again indicating that the material concentration influences the pore size.

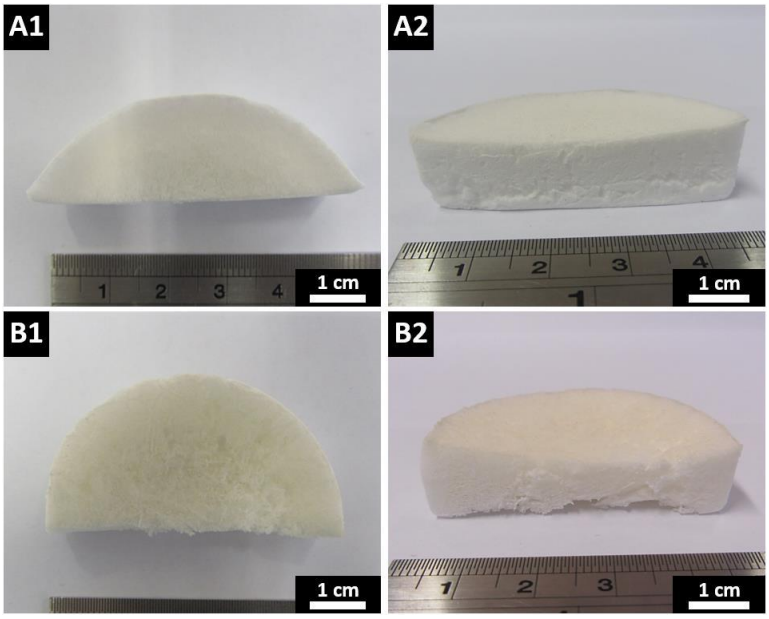

Figure 3.5: Top and side views of pre-PGS/PLLA blend scaffold samples with a weight ratio of 2:1, (A1-2) before and (B1-2) after curing.

Freeze-dried pre-PGS/PLLA blend scaffolds were successfully cured at 150 °C for 24 h, in which most scaffolds showed no external physical change, as presented in Figure 3.5 (B1-2). As seen in Figure 3.4 (B-I), all cured PGS/PLLA scaffolds were characterised by a highly interconnected open-cell structure, demonstrating that PLLA can act as a base support structure, preventing the melted low-viscosity pre-PGS from enclosing the existing open-cell structure, as well as from complete structural scaffold collapse during the curing stage. While the cell microstructure of all scaffolds was not affected by the curing process, the analysis indicated the tendency of a modest drop in the pore size, as presented in Table 3.1. The change in pore size was due to the pre-PGS, which melted and gained flowability during the curing process. Nevertheless, cured PGS/PLLA scaffolds which featured a higher weight ratio of PGS (PGS/PLLA scaffolds with weight ratios of 2:1, 2.5:1, 3:1, 3.5:1 and 4:1) showed only

a minimal pore size drop in the range of 2.7-11.1%, demonstrating good scaffold structure stability. Bigger changes were found in the cell-wall properties of the PGS/PLLA scaffolds, in which the cell-wall surfaces exhibited rougher features after curing, as illustrated in Figure 3.7. The increases in surface roughness can be beneficial for cell differentiation, influencing the cell adhesion and viability as various research studies presented [341,342].

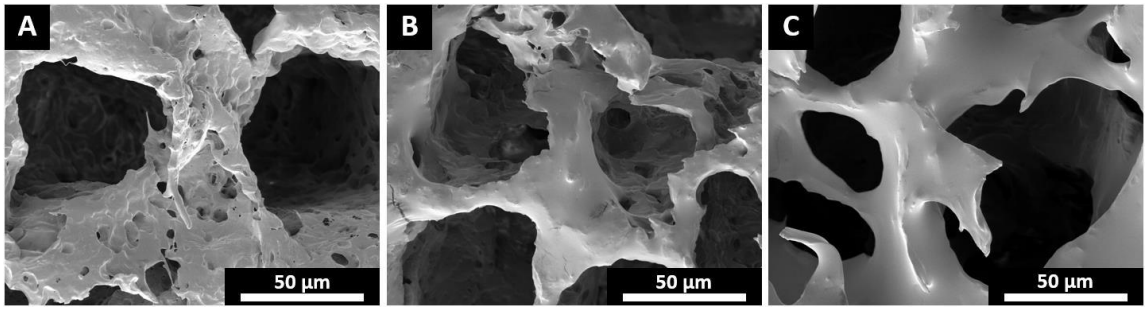

Figure 3.6: SEM micrographs of non-cured pre-PGS/PLLA blend scaffolds with weight ratios of (A) 2:3, (B) 2:2 and (C) 2:1, indicating a change of surface roughness due to different material compositions.

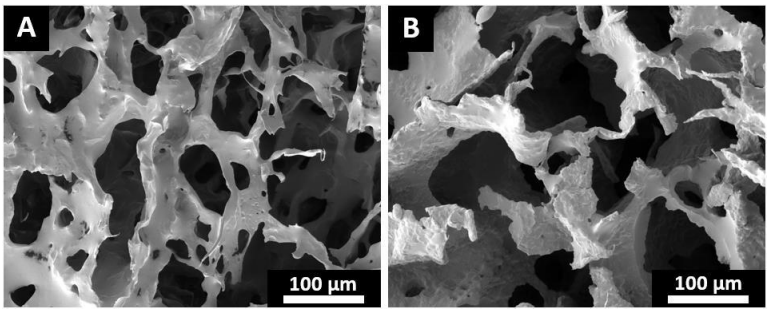

Figure 3.7: SEM micrographs present the change of the cell wall surface roughness after the curing process. Pre-PGS/PLLA blend scaffold with a weight ratio of 2:1, (A) before and (B) after curing.

In most instances, cured PGS/PLLA scaffolds with a high PGS ratio showed no indication of external physical change (Figure 3.S3-4, Appendix A), with the exception of the scaffolds with weight ratios of 3.5:1 and 4:1 (Figure 3.S5-6, Appendix A). The sample with a PGS/PLLA weight ratio of 3.5:1 presented a drop of structure height in the middle of the scaffold sample, while the scaffold with a weight ratio of 4:1 exhibited an overall reduction in

sample height. This suggests that a high amount of the pre-PGS, without sufficient PLLA supporting matrix, would melt and collapse during the curing process. However, the fabrication of PGS/PLLA samples with an increased PGS weight ratio of up to 3:1 was possible, demonstrating good microstructure characteristics and a minimum PLLA volume percentage in the scaffold of only 24%.

The SEM investigation illustrates that the freeze-drying fabrication approach in the presence of a structure-supporting polymer is a promising strategy for creating large PGS based open-cell interconnected scaffolds for soft tissue engineering applications. Cured PGS/PLLA scaffolds with the weight ratios of 2.5:1 and 3:1 presented the highest average pore sizes among the measurement range, namely 89.8-92.6 μm. The material composition and freeze-drying parameters (e.g. the cooling rate, the freezing temperature, and the total freezing time) can be altered to increase the pore size, which will be beneficial for potential cell growth and cell penetration. For instance, by decreasing the concentration of the pre-PGS/polymer in the solution or by reducing the cooling rate, bigger pore sizes can be achieved. The open-cell structure of the scaffolds can be altered to unidirectional pores by controlling the heat transfer direction in order to fabricate biomimetic scaffolds with different porous structures for different applications, e.g. interconnected open-cell structures for adipose or lung tissue engineering [5,343] and aligned laminar pores for cardiac or nerve tissue engineering [258,344].

3.3.3 Physical and mechanical properties of PLLA and PGS/PLLA blend scaffolds

The $\rho_{f-matrix}$, the ρ_f and the ρ_r of the neat PLLA and all cured PGS/PLLA scaffolds are listed in Table 3.2. The results illustrate that the densities and porosities depend on the material concentration, and the weight ratio of PGS to PLLA, and are affected by the presence of viscous pre-PGS during the curing process. For instance, the pristine PLLA scaffold (weight ratio of 0:2) with the lowest material concentration featured the lowest scaffold

density with 0.085 Mg m^{-3} and the highest porosity of 93%. PGS/PLLA scaffolds with the highest material amounts (weight ratios of 2:3 and 4:1) featured the highest scaffold densities of 0.188 Mg m^{-3} and 0.218 Mg m^{-3}, corresponding to the lowest porosities of 84% and 81%, respectively. Due to the same solvent volume applied for each scaffold sample, the results demonstrate that the use of a greater material amount increases the scaffold density and reduces the porosity. The ratio of PGS to PLLA also affected the final scaffold density and porosity, in which higher PGS ratios presented the tendency of lower scaffold densities and greater porosities. For example, the PGS/PLLA scaffold with a weight ratio of 2:1 featured a 14% lower scaffold density and a 2% increased porosity compared to the PGS/PLLA scaffold with a weight ratio of 1:2. However, when the PGS ratio in the scaffold was too high, the scaffold structure collapsed or changed during the curing stage due to the high amount of viscous pre-PGS as previously discussed, causing high scaffold densities and low porosities, as explicitly shown by the results for the PGS/PLLA scaffold with a weight ratio of 4:1.

Table 3.2: Densities and porosities of PLLA and cured PGS/PLLA scaffolds.

PGS : PLLA weight ratio[a] / g g^{-1}	Solid density[b] $\rho_{f-matrix}$ / Mg m^{-3}	Scaffold density[c], ρ_f / Mg m^{-3}	Relative density, ρ_r	Porosity, P_f / %
0:2	1.220	0.085 ± 0.002	0.070	93
1:2	1.188	0.152 ± 0.005	0.128	87
2:2	1.173	0.175 ± 0.009	0.149	85
2:3	1.182	0.188 ± 0.040	0.159	84
2:1	1.158	0.131 ± 0.003	0.113	89
2.5:1	1.154	0.138 ± 0.004	0.114	88
3:1	1.151	0.178 ± 0.032	0.149	85
3.5:1	1.149	0.171 ± 0.015	0.149	85
4:1	1.147	0.218 ± 0.017	0.190	81

[a] Solvent volume: 40 mL; [b] Calculated by Equation 3.2; [c] Scaffold density was determined by measuring the weight and volume of each scaffold type.

Table 3.3: Mechanical properties of PLLA and cured PGS/PLLA scaffolds

PGS : PLLA weight ratio[a] / g g^{-1}	Young's modulus, E_t / MPa	Ultimate tensile strength, σ_{tmax} / MPa	Elongation at σ_{tmax}, $\varepsilon_{t\sigma max}$ / %
0:2	2.20 ± 0.34	0.18 ± 0.06	9.34 ± 3.13
1:2	3.62 ± 1.08	0.11 ± 0.04	3.98 ± 1.17
2:2	6.31 ± 0.64	0.13 ± 0.03	2.95 ± 0.43
2:3	8.56 ± 1.36	0.28 ± 0.07	4.70 ± 0.83
2:1	1.05 ± 0.21	0.03 ± 0.01	5.48 ± 0.79
2.5:1	1.01 ± 0.17	0.08 ± 0.01	15.66 ± 3.35
3:1	0.36 ± 0.27	0.03 ± 0.01	12.88 ± 3.71
3.5:1	0.83 ± 0.24	0.05 ± 0.01	8.73 ± 1.51
4:1	2.66 ± 0.53	0.18 ± 0.04	13.35 ± 2.21

[a] Solvent volume: 40 mL.

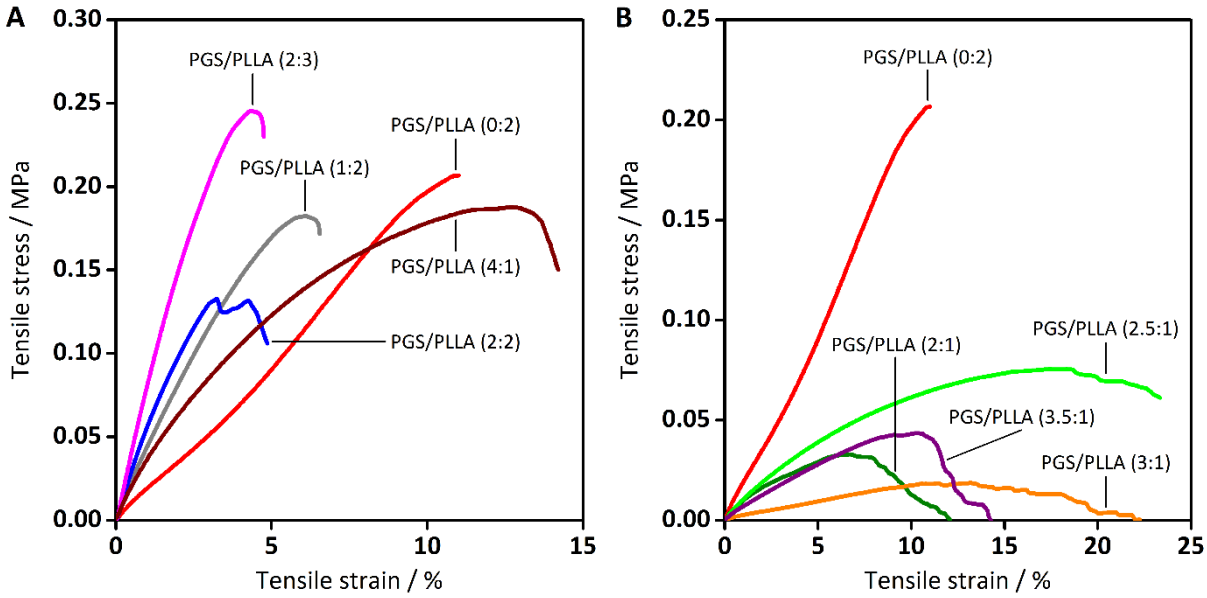

Figure 3.8: Representative tensile strength-strain curves of PLLA and cured PGS/PLLA blend scaffolds with various weight ratios: (A) PGS/PLLA blend scaffolds with high stiffness, (B) PGS/PLLA blend scaffolds with low stiffness. The E_t of the PLLA scaffold (weight ratio of 0:2) served as a baseline in both cases (see Table 3.3).

Table 3.3 lists the values for the tensile Young's modulus, E_t, the ultimate tensile strength, σ_{tmax}, and the elongation at ultimate tensile strength, $\varepsilon_{t\sigma max}$, of all cured scaffolds.

Representative tensile stress-strain curves for these scaffolds are depicted in Figure 3.8. Results show that soft and elastomeric PGS/PLLA scaffolds for soft tissue engineering applications are producible. As previously arranged, all scaffolds were classified in three groups which featured (I) a fixed PLLA and a varied PGS concentration, (II) a fixed total PGS and a varied PLLA concentration and (III) PGS/PLLA scaffolds with a fixed material content.

The analysis of cured PGS/PLLA scaffolds which featured a fixed PLLA and a varied PGS concentration demonstrated the general tendency that a higher ratio of PGS improved the ductility of the elastomeric scaffold (depending on the material concentration). For instance, cured PGS/PLLA scaffolds with weight ratios of 2:1, 2.5:1 and 3:1 showed improvements in realising soft and elastomeric scaffolds at higher ratios, in which the PGS/PLLA scaffold with a weight ratio of 2.5:1 achieved the highest $\varepsilon_{t\sigma max}$ value of 15.66%, while the PGS/PLLA scaffold with a weight ratio of 3:1 featured the lowest E_t and σ_{tmax} results of 0.36 MPa and 0.03 MPa, respectively, as well as a high $\varepsilon_{t\sigma max}$ of 12.88%. In contrast, a further increase of the PGS ratio to 3.5:1 or 4:1 led to an enhancement of the E_t and σ_{tmax}, which can be accounted for by the reduced pore size and porosities because of the collapse of the scaffolds as previously discussed. The pristine PLLA scaffold (weight ratio of 0:2) presented an E_t, σ_{tmax} and $\varepsilon_{t\sigma max}$ of 2.20 MPa, 0.18 MPa and 9.34%, respectively, demonstrating statistically stiffer scaffolds in comparison to PGS/PLLA scaffolds with weight ratios of 2:1, 2.5:1 and 3:1 and 3.5:1. Also, cured PGS/PLLA scaffolds with weight ratios of 1:2 and 2:2 presented statistically lower $\varepsilon_{t\sigma max}$ values, owing to their relatively high PLLA contents.

By examining the cured PGS/PLLA scaffolds with a fixed PGS and a varied PLLA concentration, results illustrated that an increase of the PLLA weight ratio enhanced the tensile strength and modulus of the scaffold. Among all the scaffold types (ratios of 2:1, 2:2 and 2:3), the cured PGS/PLLA scaffold with a weight ratio of 2:3 obtained the highest E_t and

σ_{tmax} results with statistical significance of 8.6 MPa and 0.3 MPa, respectively, whereas PGS/PLLA scaffolds with lower PLLA concentrations exhibited higher $\varepsilon_{t\sigma max}$ (<5.48%), and statistical significant lower E_t and σ_{tmax} values. The results show that these scaffolds with relatively high PLLA ratios are unsuitable for creating soft and elastomeric soft tissue substitutes.

The evaluation of the cured PGS/PLLA scaffolds with a fixed material content indicated again that a higher content of PGS offered a softer and more ductile scaffold. The PGS/PLLA scaffold with a weight ratio of 2:1 presented statistically significant lower E_t and σ_{tmax} values, in contrast to the PGS/PLLA scaffold with a weight ratio of 1:2. The PGS/PLLA scaffold with a weight ratio of 2:2 versus 3:1 and with a ratio of 2:3 versus 4:1 presented a significant difference in E_t, σ_{tmax} and $\varepsilon_{t\sigma max}$, respectively.

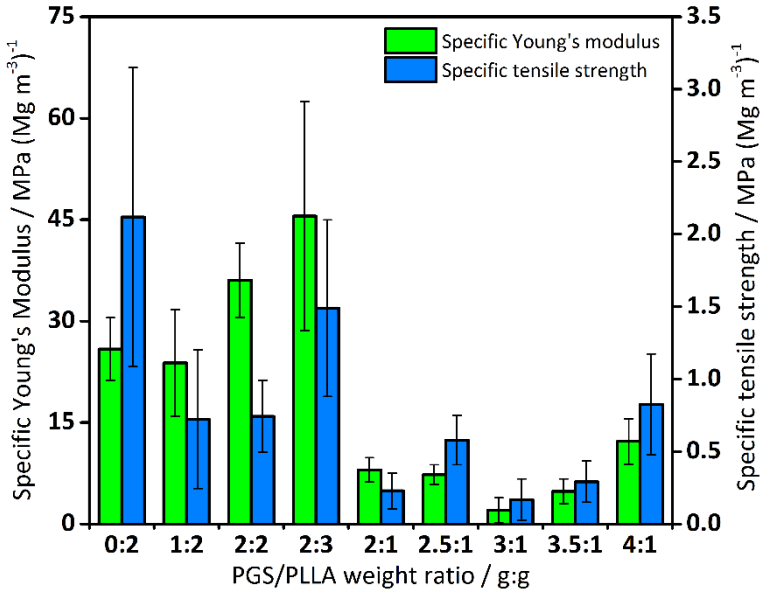

Figure 3.9: Specific Young's modulus and specific tensile strength for PLLA and cured PGS/PLLA blend scaffolds with different weight ratios.

It should be noted that the mechanical properties of the polymer blend scaffolds are also dependent on the porosity of the scaffold and the total material concentration in the freeze-drying solution. As illustrated in Figure 3.9, the elimination of the contribution from

the porosity or relative density, namely specific Young's modulus, E_t/ρ_f, and specific tensile strength, σ_{tmax}/ρ_f, of the scaffolds, demonstrated similar trends to those presented in Table 3.3 with the exception of the pristine PLLA. By comparing PGS/PLLA scaffolds produced with different concentrations, e.g. 3 g / 40 mL (PGS/PLLA weight ratio of 1:2 and 2:1), 4 g / 40 mL (PGS/PLLA weight ratio of 2:2 and 3:1) and 5 g / 40 mL (PGS/PLLA weight ratio of 2:3), there is no clear trend in the mechanical properties due to the variations in the ratio of PGS to PLLA which affects the mechanical properties significantly as previously discussed. Nevertheless, when the ratio of PGS to PLLA is relatively close, an increase in the material concentration generally resulted in a higher specific strength and higher specific stiffness. All these results suggest that suitable PGS/PLLA scaffolds for soft tissue engineering applications should be fabricated with low material concentrations and high ratios of PGS to PLLA.

The mechanical results as well as the porous structures illustrate that the freeze-drying fabrication strategy of PGS/polymer blend scaffolds has the potential to achieve ductile and highly porous scaffolds for soft tissue engineering applications. In this work, cured PGS/PLLA scaffolds with weight ratios of 2.5:1 and 3:1 presented the most promising mechanical results, in which both scaffold types accomplished a E_t of 0.36-1.01 MPa, a σ_{tmax} of 0.03-0.08 MPa and a $\varepsilon_{t\sigma max}$ of 13-16%. Also, the porous structures of both scaffold types featured a pore size and porosity in the range of 89.8-92.6 μm and 85-88%, respectively. The PGS/PLLA scaffolds are softer and more flexible compared to the pristine PLLA scaffold. Thus, these two PGS/PLLA scaffolds were selected for subsequent biodegradation studies.

3.3.4 *In vitro* degradation

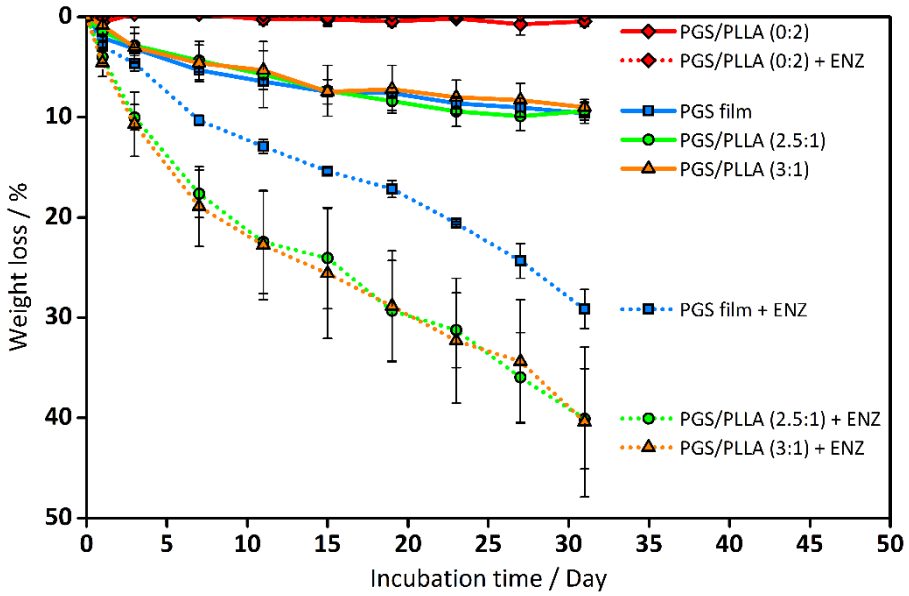

Figure 3.10: Percentage of weight loss of PGS film, PLLA and PGS/PLLA scaffolds, incubated in enzyme-free or enzyme-containing PBS solutions in a shaker incubator for up to 31 days at 37 °C.

Figure 3.10 presents the *in vitro* degradation behaviour of cured PGS film, PLLA scaffold and PGS/PLLA scaffolds with weight ratios of 2.5:1 and 3:1 in enzyme-free PBS solution and in lipase enzyme-induced PBS solution for up to 31 days. The PGS film specimens underwent a weight loss of 9.6% in the enzyme-free PBS solution in 31 days, while in the enzyme-containing PBS solution it exhibited with statistical significance an enhanced weight loss, being 29.1% within the same period of time. Due to the high weight loss, the enzymatically degraded PGS specimens presented a visible loss of volume (Figure 3.S7, Appendix A). The SEM analysis of the non-enzymatically tested PGS specimens presented smooth surface finishes, whereas the enzymatically tested PGS specimens were characterised by various degrees of surface imperfection, such as rough features with pits and craters, as seen in Figure 3.11. These results are in accordance with previous studies and demonstrate that the lipase enzyme catalyses the hydrolysis of the ester bonds in the PGS polymer

[244,251,259,345], resulting in a faster degradation process. The PLLA scaffold specimens presented insignificant weight losses of below 0.5% in 31 days in the PBS solutions with and without the presence of lipase enzyme. PLLA is a semi-crystalline polymer and is in general known as a long-term biodegradable polymer. No changes of the specimen sizes and shapes were detected (Figure 3.S8, Appendix A), and correspondingly SEM investigation displayed no explicit morphological changes after both *in vitro* degradation tests, as seen in Figure 3.12. The results indicate that the degradation of the PLLA scaffold via hydrolysis or enzyme-catalysed hydrolysis is minimal during the test period, which is in agreement with previous degradation studies [346–348].

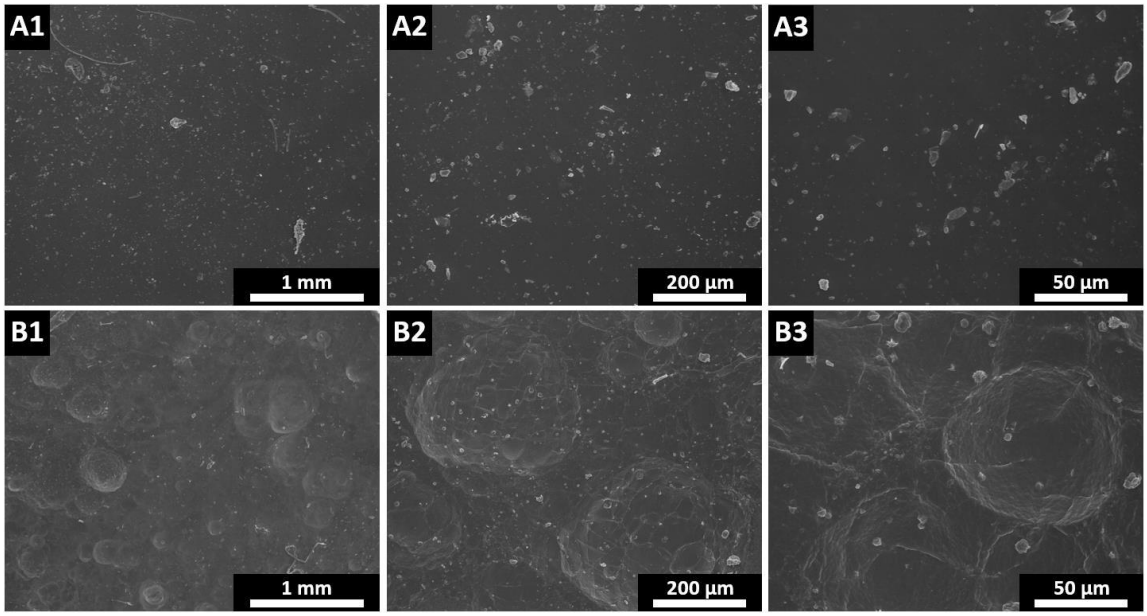

Figure 3.11: SEM micrographs of cured PGS film (24 h at 150 °C) after 31 days incubation at 37 ˚C in (A1-3) enzyme-free and (B1-3) in enzyme-containing PBS solution (note that visual differences are minor).

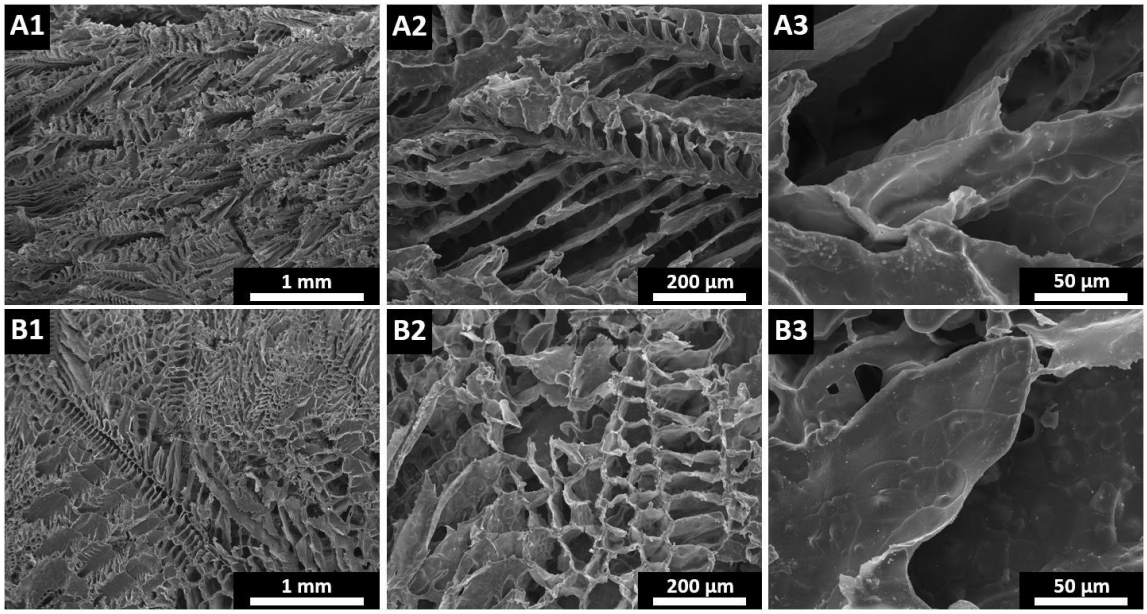

Figure 3.12: SEM micrographs of PLLA scaffolds after 31 days incubation at 37 ˚C in (A1-3) enzyme-free and (B1-3) in enzyme-containing PBS solution (note that visual differences are minor).

In contrast, the degradation of both types of PGS/PLLA scaffolds was with statistical significance faster, and the results showed relatively linear weight losses during the test period. The PGS/PLLA scaffolds with weight ratios of 2.5:1 and 3:1 obtained in the enzyme-free PBS solution similar degradation rates of 9.4% and 9.0% respectively in 31 days, and showed only minor shape modifications of the specimens (Figure 3.S9-10, Appendix A). In the enzyme-containing PBS solution, the specimens showed with statistical significance enhanced degradation rates of 40.1% and 40.4%, respectively, with visible shape changes (Figure 3.S9-10, Appendix A). The SEM investigation of both PGS/PLLA specimens presented no major changes in respect to the original open-cell scaffold microstructure; however, the analysis of the cell-wall and strut surface morphology demonstrated explicit signs of surface degradation, characterised by rough features, craters and pits, as seen in Figure 3.13 and 3.14. It is postulated that the large surface areas of the PGS/PLLA scaffolds have contributed to the high degradation rates, and that PGS is the main polymer that has

degraded, due to the slow degradation rate of PLLA. With respect to the pH values of the degradation media, no changes were measured during the test periods.

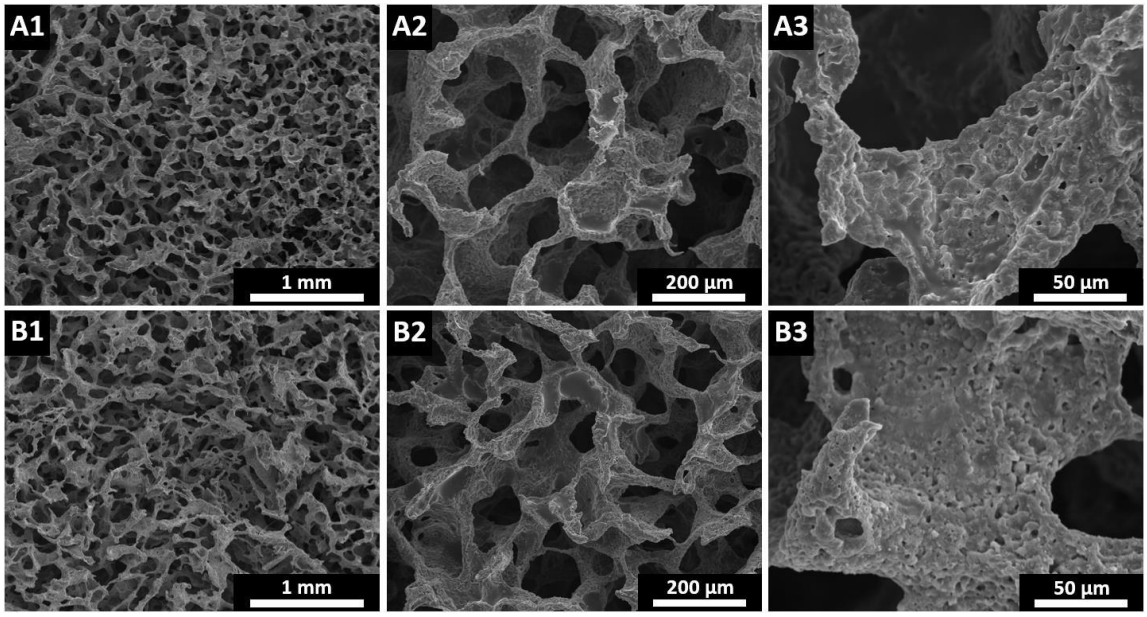

Figure 3.13: SEM micrographs of PGS/PLLA scaffolds with a weight ratio of 2.5:1 after 31 days incubation at 37 ˚C in (A1-3) enzyme-free and (B1-3) in enzyme-containing PBS solution (note that visual differences are minor).

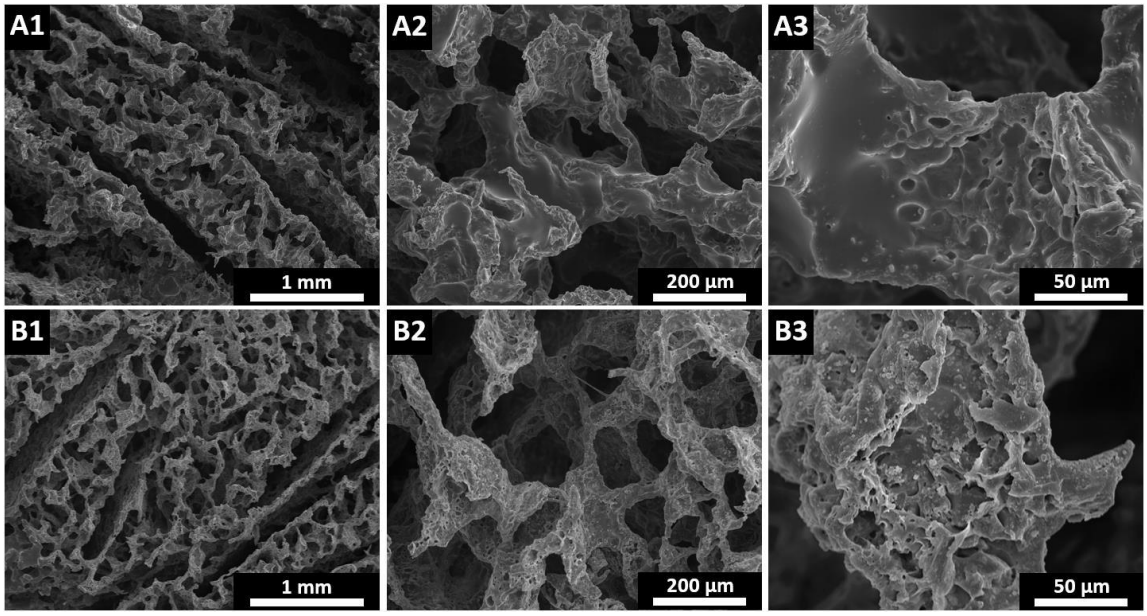

Figure 3.14: SEM micrographs of PGS/PLLA scaffolds with a weight ratio of 3:1 after 31 days incubation at 37 ˚C in (A1-3) enzyme-free and (B1-3) in enzyme-containing PBS solution (note that visual differences are minor).

Overall, the freeze-drying fabrication strategy, with the use of a structure-supporting biopolymer, presented in this work permits the creation of interesting PGS-based scaffolds for soft tissue engineering. It also gives plenty of opportunities to optimise the porous structures and mechanical properties of the resulting scaffolds according to the targeted soft tissue environment. For instance, pre-PGS/PLLA scaffolds could be cured at a lower temperature after the freeze-drying stage, resulting in a PGS with a lower crosslink density [237,242,252], thus creating cured PGS/PLLA scaffolds with lower Young's modulus, strength and superior ductility. Furthermore, the pore size, porosity, pore shape and pore orientation can be tailored by adjusting the material concentration in the solution, material ratio, freezing rate, mould material and geometry, as well as heat transfer direction [349], which can also lead to the optimisation of the mechanical properties of the scaffolds. PLLA can be changed to another structural-supporting polymer that has a high melting point (above the curing temperature of pre-PGS) to modify the structure and properties of the scaffolds. Regarding the usage of organic solvents and the possible residual solvent within the scaffolds, numerous studies demonstrated that scaffolds could be repeatedly washed and immersed in distilled water, PBS or ethanol for a prolonged period of time, to remove the residual solvent, without indication of negative cell toxicity [350,351].

After the cured PGS/PLLA blend scaffolds had been fabricated, attempts were made to remove PLLA by leaching in order to create pure PGS scaffolds. Organic solvents such as 1,4-dioxane and chloroform were used to dissolve the high molecular PLLA. Within the solvent, the PGS/PLLA scaffolds swelled and the integrity of the scaffold structure decreased tremendously. Shaking movements for improving the PLLA leaching process broke the swollen scaffolds apart. When the swollen scaffolds were removed from the solvent, they collapsed and/or felt apart, unable to maintain their porous scaffold structure. Further work by

using an alternative polymer and different material compositions is currently ongoing in order to create pure PGS scaffold by using the freeze-drying approach.

Nevertheless, the biocompatible PGS/PLLA scaffolds reported herein are still promising materials for soft tissue applications. The addition of a second polymer, such as PLLA, can achieve large elastomeric scaffolds with high porosities, suitable cell sizes and interconnected porous structure. It could also be a viable option for applications where the degradation of PGS is considered to be too fast. The *in vitro* degradation results shown above demonstrate that PGS poses a significantly faster degradation rate compared to PLLA. Previous *in vivo* degradation studies showed similar results; PGS degraded completely in 60 days *in vivo* [16,237], while it took at least 4 years to degrade PLLA completely *in vivo* [352]. PLLA could improve the structure integrity of the PGS-based scaffolds during degradation and act as a mechanical support for a longer term.

3.4 Conclusions

Large 3D porous PGS/PLLA blend scaffolds with varying PGS/PLLA ratios were successfully fabricated via a freeze-drying and a subsequent curing process. Results demonstrated that the presence of a minor second polymer such as PLLA can act as a base support structure during the curing stage, preventing the low-viscosity pre-PGS from enclosing the existing open-cell structure as well as the scaffolds from structure collapse. The cured PGS/PLLA scaffolds were characterised by a highly interconnected open-cell structures, in which the material concentration and the combination of PGS and PLLA influenced the final pore size, cell structure, porosity as well as the mechanical properties of the scaffolds. The scaffolds which featured a higher PGS to PLLA ratio accomplished more favourable cell microstructures and better elastomeric properties. In respect to the mechanical properties of pristine cured PGS film, results presented a Young's modulus, tensile strength and elongation at break of 0.89 MPa, 0.38 MPa and 49.6%, respectively, indicating a high

crosslink density and superior ductility compared to PLLA. Cured PGS/PLLA scaffolds with weight ratios of 2.5:1 and 3:1 presented the most promising results for soft tissue scaffolds. Both scaffold types featured a low PLLA volume ratio, high porosity and pore size in the ranges of 24-27%, 85-88% and 89.8-92.6 μm, as well as a Young's modulus, ultimate tensile strength and an elongation at ultimate tensile strength in the range of 0.36-1.01 MPa, 0.03-0.08 MPa and 12.88-15.66%, respectively. *In vitro* degradation tests demonstrated the same results for both types of PGS/PLLA scaffolds, with weight losses of 40% and 9% in 31 days in PBS solutions with and without the presence of lipase enzyme, respectively, and both with good scaffold microstructure retention.

The freeze-dried PGS-based scaffolds have great potential to be further developed for uses in soft tissue engineering. In comparison with other PGS scaffold fabrication strategies, this freeze-drying method is less complex, and able to produce large 3D interconnected porous scaffolds with high porosities and pore sizes at ease, whilst offering opportunities for further optimisations of the structure, mechanical and biological properties. In addition, the fabrication strategy can be extended to other combinations of synthetic curable bioelastomers and structure-supporting biopolymers, on the condition that (I) both biopolymers (the pre-polymer and the structure-supporting polymer) are soluble in the same solvent (or a mixed solvent) and (II) the structure-supporting biopolymer can sustain the harsh curing condition of the bioelastomer.

Chapter 4. Biomimetic poly(glycerol sebacate) / poly(L-lactic acid) blend scaffolds for adipose tissue engineering

4.1 Introduction

The scaffold fabrication strategy described in Chapter 3 presents great potential to achieve flexible and highly porous PGS-based scaffolds for various soft tissue engineering applications. The freeze-drying and subsequent curing process of PGS/PLLA blends allows one to overcome significant constraints of pure PGS in terms of scaffold production and design flexibility, therefore improving the overall efficiency of the fabricating large-sized PGS-based scaffolds. The simple modification of the material composition of the polymer blend and/or the processing parameters, is expected to create porous scaffold constructs with the desired mechanical and biological properties, ideal for soft tissue substitutes.

The focus of this chapter is based on the fabrication of large 3D PGS/PLLA blend scaffolds with similar bulk mechanical properties to those of native adipose tissue (see Section 2.2.3), as well as suitable porous structures for cell penetration and growth for prospective application in ATE. As described in Section 2.2.6, most synthetic scaffold constructs are composed of conventional polyester-based polymers which were found to be rigid and therefore unable to mimic the micro and macroscopic mechanical properties of adipose tissue, as well as other surrounding soft tissues [5,353,354]. In normal human physiology, e.g. during normal sitting or lying, the adipose tissue is exposed to large deformations, thus, the scaffolds for ATE need to be flexible and withstand physiologically induced deformations [12,70]. As stated in Section 2.2.3, a sitting posture induces peak

tensile, compressive and shear strains of ~30%, ~45% and ~40% on the anatomical site related adipose tissues, while a lying posture induces approximately half these loads on the same anatomical locations [12,70,71,82]. Hence, the mechanical properties of the engineered scaffolds for ATE cannot be ignored when regenerative medicine-based treatments are being developed [12,70,71,82].

The PLLA and PGS/PLLA blend scaffold samples were created using either 1,4-dioxane or dimethyl carbonate (DMC) as the solvent via a modified freeze-drying and a subsequent curing process. DMC is a ‘‘green’’ solvent and is characterised with low volatility and non-toxicity, as well as biodegradability [351]. The microstructure characteristics of the fabricated PLLA and PGS/PLLA scaffolds were analysed by SEM, the mechanical properties were evaluated by quasi-static tensile and compressive tests, and the hydrophilicity was investigated by water absorption tests. *In vitro* degradation tests were executed in enzyme-free and enzyme-containing PBS solution to assess the degradation kinetics of the scaffolds. *In vitro* cell tests with cultured ADSCs were performed to evaluate the performance of the scaffolds in terms of cell proliferation, cell penetration and extracellular matrix production. The structure and properties of the pre-PGS and crosslinked PGS film were also investigated.

4.2 Experimental section

4.2.1 Materials

The materials for this chapter are those used in Chapters 3, with the following additions: DMC, toluene, trypsin-ethylenediaminetetraacetic acid (trypsin-EDTA), fungizone, glutamine, paraformaldehyde, peracetic acid, Sirius red stain (Direct Red 80), sodium hydroxide and methanol were acquired from Sigma-Aldrich. Fetal calf serum (FCS), penicillin-streptomycin, Harris haematoxylin and eosin were purchased from Gibco. Isopropanol, xylene, dibutyl phthalate xylene (DPX) mounting medium and Tissue-Tek®

4583 optimal cutting temperature (OCT) compound were acquired from Fisher Scientific. Collagenase type A was obtained from Roche Diagnostics GmbH. Dulbecco's modified Eagle's medium (DMEM) was purchased from Advanced Protein Products.

4.2.2 Preparation of pre-PGS

Pre-PGS was synthesised as described in Chapter 3.

4.2.3 Preparation of PGS films

Cured PGS film was produced via a solvent-free process. Briefly, pristine pre-PGS was melted on a hotplate at 80 °C and equally distributed into a non-sticky Teflon-coated metal mould (purchased from a local store). The viscous pre-PGS film was further degassed in a vacuum oven at 80 °C, until a void-free film was accomplished. In the last step, the pre-PGS film sample was crosslinked under vacuum at 120 °C for 36 h, cooled down to room temperature and slowly peeled off from the mould surface. Cured PGS films were stored at room temperature before further examinations were carried out.

4.2.4 Preparation of PLLA and PGS/PLLA blend scaffolds

Table 4.1: Material compositions of the PLLA and pre-PGS/PLLA blended solutions for freeze-drying.

Sample code	Polymer(s)	Weight ratio of pre-PGS to PLLA / g g^{-1}	Solvent	Solvent quantity / mL
PLLA-D	PLLA	0:1.75	1,4-dioxane	40
PGS/PLLA-D	Pre-PGS/PLLA	1.25:0.5	1,4-dioxane	40
PLLA-DMC	PLLA	0:1.75	Dimethyl carbonate	40
PGS/PLLA-DMC	Pre-PGS/PLLA	1.25:0.5	Dimethyl carbonate	40

PLLA and PGS/PLLA scaffolds were prepared in a modified two-step process, based on the previous method in Chapter 3. Briefly, the first step included the PLLA and pre-PGS/PLLA solution preparation with 1,4-dioxane (freezing point: 10-12 °C) or DMC (freezing point:

2-4 °C) for the freeze-drying procedure, as listed in Table 4.1. For the preparation of the PLLA solution, PLLA was dissolved for 24 h at 60 °C in 1,4-dioxane or at 80 °C in DMC, respectively, and then cooled down to room temperature under continuous stirring until further use. The pre-PGS/PLLA solutions were prepared by dissolving first PLLA under the same conditions as described previously, while pre-PGS was added to the cooled solutions and dissolved under stirring, three hours before the freeze-drying process. All the solutions were produced separately in closed glass containers. The solutions were then cast into a non-sticky Teflon-coated metal baking tray (six cylindrical cavities with a diameter of 60 mm purchased from a local store) and placed in a Labconco FreeZone Triad freeze-dryer for lyophilisation. All solutions were cooled during the freezing stage to -30 °C and kept at the temperature for 5 h, allowing the solution to freeze completely (note that the holding temperature during the primary drying stage was modified as compared to Chapter 3, allowing to accelerate the scaffold fabrication process). During the primary drying stage the solutions were heated to -5 °C (heating rate of 1 °C min^{-1}) and sublimated for 10 h under vacuum (note that the holding temperature during the secondary-drying stage was modified as compared to Chapter 3, allowing to create scaffolds by using either 1,4-dioxane or DMC as the solvent via equal fabrication parameters). In the secondary drying stage, the temperature was raised to 40 °C (heating rate of 5 °C min^{-1}), held for 5 h, and then lowered to 20 °C (cooling rate of 1 °C min^{-1}) and held for a further 5 h (note that the holding times during the secondary-drying stage were reduced as compared to Chapter 3, allowing to accelerate the scaffold fabrication process). The second step involved the curing process of the pre-PGS/PLLA scaffolds in a vacuum oven for 36 h at 120 °C, in order to crosslink the pre-PGS into PGS, while the PLLA scaffolds passed through the same curing process for comparison reasons (note that the time and temperature were modified during the curing process as compared to Chapter 3, allowing to create soft and elastomeric PGS/PLLA

scaffolds). All specimens were subjected to a cleaning procedure prior to tests (24 h ethanol saturation and drying in a vacuum oven at 37 °C until constant weight was obtained) to remove unreacted pre-polymer and monomers from the scaffolds. The nomenclature of all scaffold specimens is listed in Table 4.1, under the column "Sample code".

4.2.5 Characterisation and testing of pre-PGS and PGS films

The number average molecular weight, $\bar{M}_n$, the weight average molecular weight, $\bar{M}_w$, and the polydispersity index (PDI) of the pre-PGS were analysed by gel permeation chromatography (GPC) using THF as eluent at a flow rate of 1.0 mL min^{-1} with 1 x PLGel 10 lm Guard and 3 x PLGel 10 lm Mixed B as columns. A Gilson 307 pump and an Erma ERC-7512 refractive index detector were utilised for the GPC measurements, while polystyrene standard samples were used for calibration. FTIR characterisation on pre-PGS and cured PGS films were performed as described in Chapter 3.

The density, ρ_{PGS}, of cured PGS film was measured by using a AccuPycII 1340 helium pycnometer. Samples were dried in a vacuum oven for 24 h at 37 °C, prior to density measurements.

Quasi-static tensile tests of cured PGS film were performed on a Hounsfield H100KS testing machine. Punched-out ''dog bone'' shaped PGS film specimens (n = 7; width: 2.6 mm, gauge length: 20 mm, thickness: 0.83 ± 0.09 mm) were tested at a strain rate of 50 mm min^{-1} using a 10 N load cell till fracture (ASTM D412). All tests were performed at room temperature.

The crosslink density, n_{mech}, of the cured PGS film was assessed as described in Chapter 3, as well as via swelling measurements [257,259]. For the evaluation of the crosslink density, n_{swell}, specimens (n = 5; diameter: 6 mm and thickness: 0.61 ± 0.13 mm) were swollen in THF until the samples reached the state of equilibrium. n_{swell} was

calculated by the Flory-Rehner expression for an ideal tri-functional affine network, given by Equation 4.1 [257,259],

$$n_{swell} = \frac{ln(1 - v_\infty) + v_\infty + \chi\, v_\infty^2}{V_m\left(\frac{2}{3}v_\infty - v_\infty^{\frac{1}{3}}\right)} \tag{4.1}$$

where v_∞ is the volume fraction of polymer in the swollen weight at equilibrium, V_m is the molar volume of THF solvent, χ is the Flory-Huggins parameter and determined as 0.52 for PGS [259]. v_∞ and the weight swelling degree at equilibrium, Q_∞, were calculated by Equation 4.2 and 4.3 [257,259],

$$v_\infty = \left[1 + (Q_\infty)\left(\frac{\rho_{THF}}{\rho_{PGS}}\right)\right]^{-1} \tag{4.2}$$

$$Q_\infty = \frac{W_\infty - W_{dry}}{W_{dry}} \times 100\% \tag{4.3}$$

where W_∞ and W_{dry} are the weights of the polymer at equilibrium and at dry state, while ρ_{THF} is the density of THF (0.89 Mg m^{-3}).

Residual monomer analysis was performed as described in Chapter 3.

4.2.6 Characterisation and testing of PLLA and PGS/PLLA blend scaffolds

The microstructures of all scaffolds were analysed by SEM on a Camscan S2 and FEI Inspect F50. Cubic samples cut from the centre of the scaffolds were placed on an aluminium stub and coated with gold for 3 min at 15 mA by using an Emscope SC500 Sputter Coater before SEM observations at 5 kV were executed. The average pore sizes (n = 350) of all scaffolds were evaluated by using ImageJ software. Only fully defined pores were considered for geometrical measurements.

The procedures for measuring the scaffold densities, ρ_f, the theoretical densities of the solid matrix, $\rho_{f-matrix}$, the volume ratio of PGS, φ_{PGS}, the volume ratio of PLLA, φ_{PLLA}, as well as the porosity, P_f, of all PLLA and PGS/PLLA scaffolds (n = 5) were obtained as described in Chapter 3.

Quasi-static tensile and compression tests were performed on a Hounsfield H100KS testing machine. Scaffold tensile test samples (n = 8; width: 5.95 ± 0.17 mm (y-axis), gauge length: 15 mm (x-axis), thickness: 3.52 ± 0.14 mm (z-axis)) were prepared as described in Chapter 3. Tensile tests (ASTM D412) were performed at a tensile strain rate of 50 mm min^{-1} till fracture by using a 10 N load cell. Cylindrical scaffold samples for quasi-static (n = 8; diameter: 12 mm, thickness: 5.3 ± 0.9 mm (y-axis)) compression tests were punched-out from the centre cross section of the scaffolds. Compression tests (ASTM C365-05) were performed at a strain rate of 1 mm min^{-1} up to a strain of 75%, using a 10 N load cell for PGS/PLLA samples, and a 1 kN load cell for PLLA samples. All tests were performed at room temperature.

Hydrophilicity of all the scaffolds was analysed by dropping 0.04 mL of blue-dyed PBS solution on the cross-section surface of scaffold samples and observing the absorption behaviour for up to 1 h.

4.2.7 *In vitro* degradation tests

In vitro degradation tests in enzyme-free and enzyme-containing PBS solution were performed on PLLA and PGS/PLLA scaffolds (n = 3; width: 5.78 ± 0.22 mm, length: 6.48 ± 0.21 mm and thickness: 3.72 ± 0.17 mm) for up to 31 days at 37 °C, as described in Chapter 3. SEM analysis was performed after 31 days *in vitro* degradation on a Camscan S2 at 5 kV on gold coated PLLA and PGS/PLLA scaffold specimens.

4.2.8 *In vitro* cell culture experiments

Human subcutaneous fat tissue from abdominoplasties (biopsies were used on an anonymous basis, under a Human Tissue Authority research tissue bank licence: 08/H1308/39) was selected as the ADSC source and processed as previously stated [355]. Mechanical and enzymatic (collagenase type A) digestion was followed by several washes, and the SVF was cultured in DMEM culture medium (supplemented with 10% FCS, 1% penicillin–streptomycin, 1% glutamine and 0.25% fungizone). Cells were subcultured to passage 6 for their use in all experiments.

For sample preparation, PLLA-D and PGS/PLLA-D scaffolds (n = 3; diameter: 16 mm, thickness: 5 mm) were placed in a 24-well plate (well with the same diameter as sample) and each specimen was sterilised in 2 mL of 1% peracetic acid in PBS for 24 h. Then, scaffolds were washed 3 times with PBS and dried overnight in an incubator under ultraviolet (UV)-light (37 °C, 5% CO2). After trypsinisation, cells were seeded with 1 mL of DMEM onto the scaffold surface (8.5 x 10^5 cells/sample) and allowed to attach for 2 h in a laminar flow culture hood. One millilitre of DMEM was then added to each sample, and subsequently the culture medium was changed 3 times per week for up to 21 days. Cell-free scaffolds were included as controls in DMEM medium.

For histology, samples (after 21 days culture in DMEM) were embedded with OCT compound and frozen in liquid nitrogen. Scaffold cross-sections (10 µm thickness) were cut with a Leica CM300 cryostat and placed on frosted slides. The sample-carrying slides were then soaked in deionised water (2 min) to remove the OCT, stained with Harris haematoxylin (8 min), and afterwards washed with running tap water (5 min) and stained with eosin (3 min). After another wash with tap water (1 min), samples were dehydrated in 70% alcohol (1 min), followed with the immersion in 100% alcohol (1 min). Finally, the slides were cleaned twice in xylene (1 min each), and mounted with a coverslip by using a DPX mounting

medium. An MOTIC DMB optical microscope was used for taking images. Nonstained cross-sections, as well as the cell-seeding surfaces were analysed by SEM with a Camscan S2 at 5 kV. Samples were fixed in 3.7% formaldehyde and were processed as described in the literature [355].

For the evaluation of the total collagen production by cells on the scaffolds (after 21 days culture in DMEM), Sirius red staining was assessed and processed as described in the literature [355]. Briefly, after the excess stain was washed off, samples were dried and weighed. Then, the stain was eluted and the absorbance was read at 490 nm in a Bio-TEK plate reader spectrophotometer. Data analysis involved calculating absorbance of stain per gram of dry construct. Control measurements were performed on cell-free scaffolds for comparison purpose, under the same test conditions.

4.2.9 Statistics

All measurements were reported as mean ± SD with a confidence level of 95%. Statistical analysis was performed as described in Chapter 3.

4.3 Results and discussion

4.3.1 Characterisation of pre-PGS and cured PGS films

GPC analysis of the pre-PGS determined an $\bar{M}_n$, $\bar{M}_w$ and PDI of 1248 g mol^{-1}, 8192 g mol^{-1} and 6.6, respectively. As seen in Figure 4.1 (A,B) , the FTIR spectrum of the pre-PGS presented a broad absorption peak of hydroxyl groups at 3443 cm^{-1} and sharp peaks at 2926 cm^{-1} and 2853 cm^{-1}, which belong to the stretch vibration of methyl and alkane groups [252,339]. The distinct peak at 1732 cm^{-1} is associated to the formation of ester bonds, while the bands around 1291-1048 cm^{-1} belong to the stretch vibration bands of carboxyl bonds [17,252,339]. The curing process of pre-PGS at 120 °C for 36 h resulted in a reduction of the broad absorption peak of hydroxyl groups at 3456 cm^{-1} and a red shift. The distinct peaks

attributed to the ester bonds at 1731-1097 cm^{-1} increased their intensity, while the band at 1049 cm^{-1} decreased, indicating an increase in the crosslink degree of cured PGS [252,259,339].

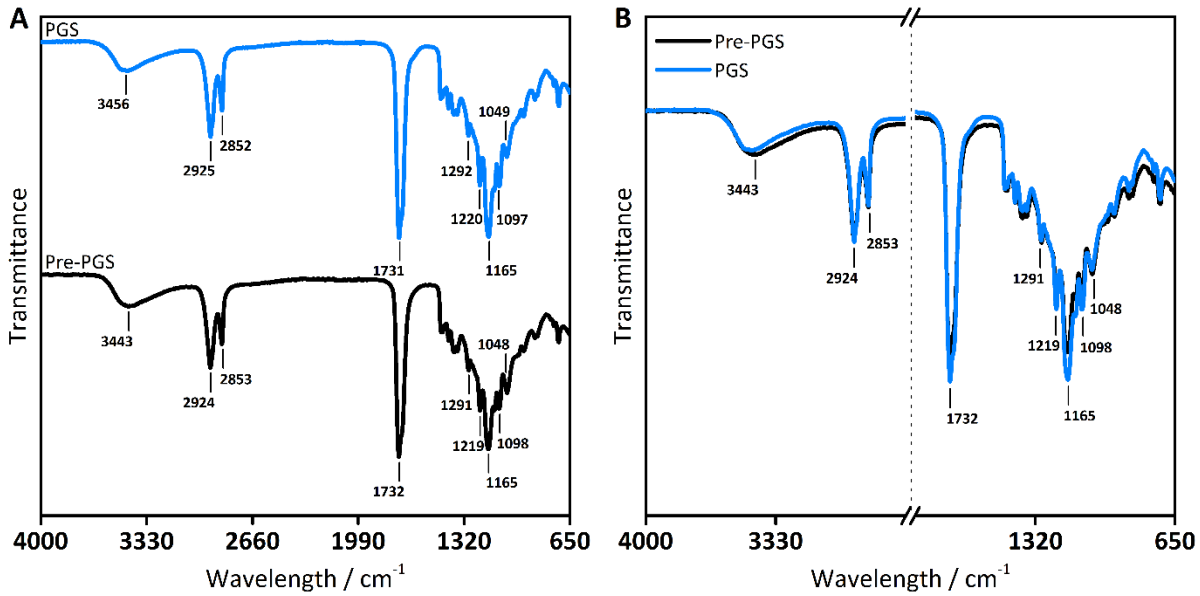

Figure 4.1: (A) Vertically shifted and (B) overlapped FTIR spectra of pre-PGS and cured PGS (36 h at 120 °C).

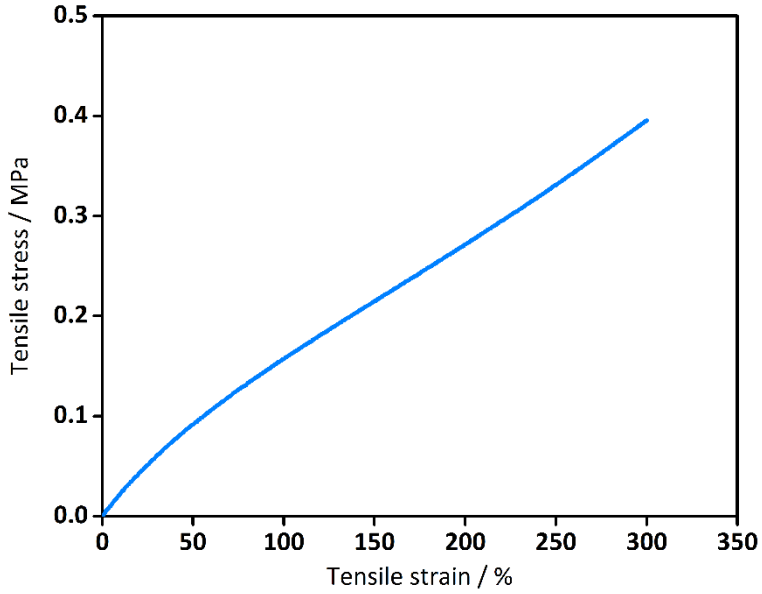

Figure 4.2: Representative tensile stress-strain curve of cured PGS film (36 h at 120 °C).

The Q_∞ of the cured PGS film in THF was measured as 708.8 ± 70.8%, giving a n_{swell} as 24.6 ± 7.4 mol m^{-3}. The tensile Young's modulus, E_s, was determined as 0.22 ± 0.02 MPa, leading to a n_{mech} of 29.8 ± 2.3 mol m^{-3}. Both, values of the crosslink density are in accordance with earlier studies [251], and indicated a low crosslink density. Correspondingly, the residual analysis presented a high weight change of 24.8 ± 6.2% after 24 h ethanol extraction, confirming the existence of a relatively high amount of non-crosslinked monomers and pre-PGS oligomers [251]. In comparison, the cured PGS film (24 h at 150 °C) of Chapter 3 has in average a four times higher n_{mech} and a four times lower residual amount (see Section 3.3.1). The density of the cured PGS was measured as 1.1397 ± 0.0014 Mg m^{-3}.

Due to the low crosslink density, the cured PGS presented soft and highly flexible properties, as seen in the representative tensile stress-strain curve in Figure 4.2. PGS exhibited a ultimate tensile strength, σ_{smax}, strain at break, ε_{sb}, and energy at break, U_{sb}, of 0.39 ± 0.04 MPa, 302.57 ± 25.71% and 0.64 ± 0.10 MJ m^{-3}, respectively, which are similar to previous published results for PGS with similar crosslink densities [251], but more ductile than the PGS at a higher crosslink density [356]. In comparison, the cured PGS film (24 h at 150 °C) of Chapter 3 exhibited in average a four times higher E_s and a six times lower ε_{sb} (see Section 3.3.1), indicating that the curing parameter have a significant effect on the materials final physicochemical properties.

4.3.2 Microstructure of PLLA and PGS/PLLA blend scaffolds

PLLA and PGS/PLLA scaffolds were fabricated via the freeze-drying process and the subsequent curing process at 120 °C for 36 h. The final PLLA-D and PLLA-DMC scaffolds were characterised by a white colour, whereas PGS/PLLA-D and PGS/PLLA-DMC scaffolds showed a light yellowish colour, as seen in Figure 4.3 (A1, B1) and 4.4 (A1, B1). Except for the PGS/PLLA-DMC scaffold, all the other samples were approximately 6 cm in diameter and over 1 cm in thickness. The PGS/PLLA-DMC scaffold

shrank and caused a smaller specimen diameter and height. All the scaffolds were characterised by a highly interconnected open-pore microstructure, as presented in Figure 4.3 (A2-3, B2-3) and 4.4 (A2-3, B2-3). SEM analysis implies that the microstructure characteristics of the scaffolds vary with the solvent and the polymer composition.

Both PLLA and pre-PGS demonstrated good solubility in 1,4-dioxane, resulting in relatively uniform scaffold microstructure characteristics after the freeze-drying and curing process, similar to the findings in Chapter 3. The PLLA-D scaffold samples were characterised by a ladder-type and oval shaped open-pore microstructure, as seen in Figure 4.3 (A2-3), and featured an average pore size of 74.3 ± 4.3 µm. This type of microstructure is commonly found in freeze-dried PLLA scaffolds with 1,4-dioxane as the solvent [259]. In comparison, the PGS/PLLA-D scaffold presented randomly distributed and highly interconnected open-pore structures with a high average pore size of 141.2 ± 6.4 µm, as illustrated in Figure 4.3 (B2-3).

Pre-PGS presented good solubility in DMC, while PLLA demonstrated a rather low solubility. As shown in Figure 4.4 (A2-3), the PLLA-DMC scaffold samples showed vertically large flaky-like aligned pores, with thin and highly porous walls. The scaffold was very weak and brittle, and so it was not further analysed. Due to the poor solubility of PLLA in DMC, it is assumed that the inhomogeneous polymer solution prevented the formation of a continuous structure-supporting foundation for the scaffold during freeze-drying [357]. In contrast, the microstructure of the PGS/PLLA-DMC scaffold was characterised by interconnected, elongated and orientated open-pores with thicker pore struts and an average pore size of 108.6 ± 5.4 µm, as seen in Figure 4.4 (B2-3). The thick pore struts indicate a relatively poor polymer dispersion, which could lead to the shrinking of the PGS/PLLA-DMC scaffold samples after the curing process.

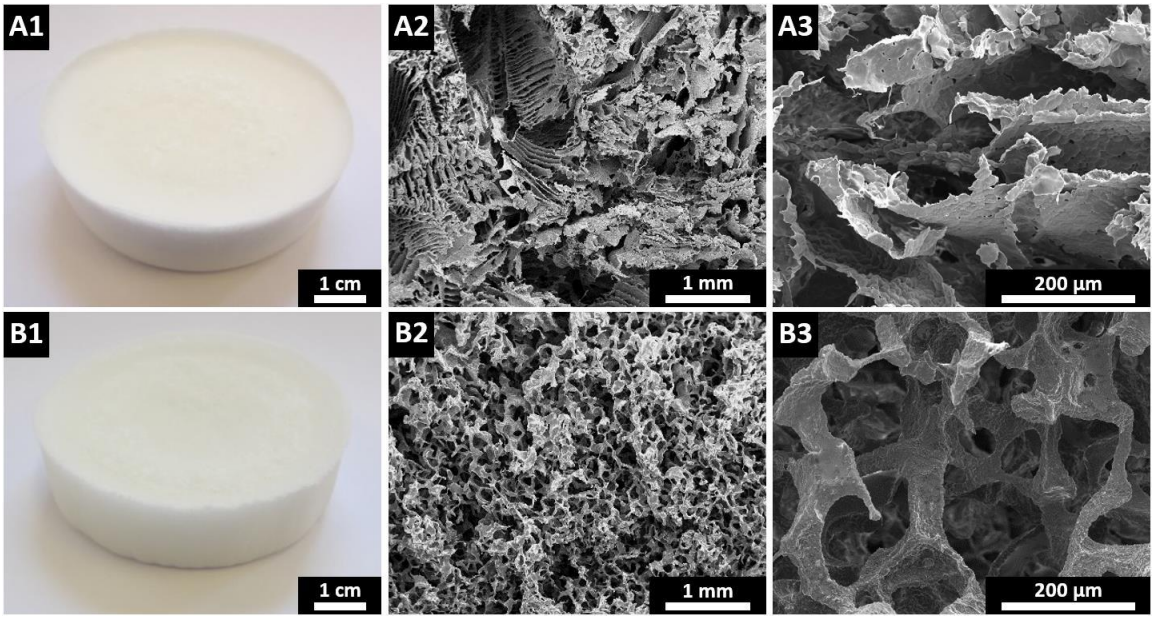

Figure 4.3: Pictures and SEM micrographs of (A1-3) PLLA-D and (B1-3) PGS/PLLA-D scaffold samples after freeze-drying and curing, showing their microstructures.

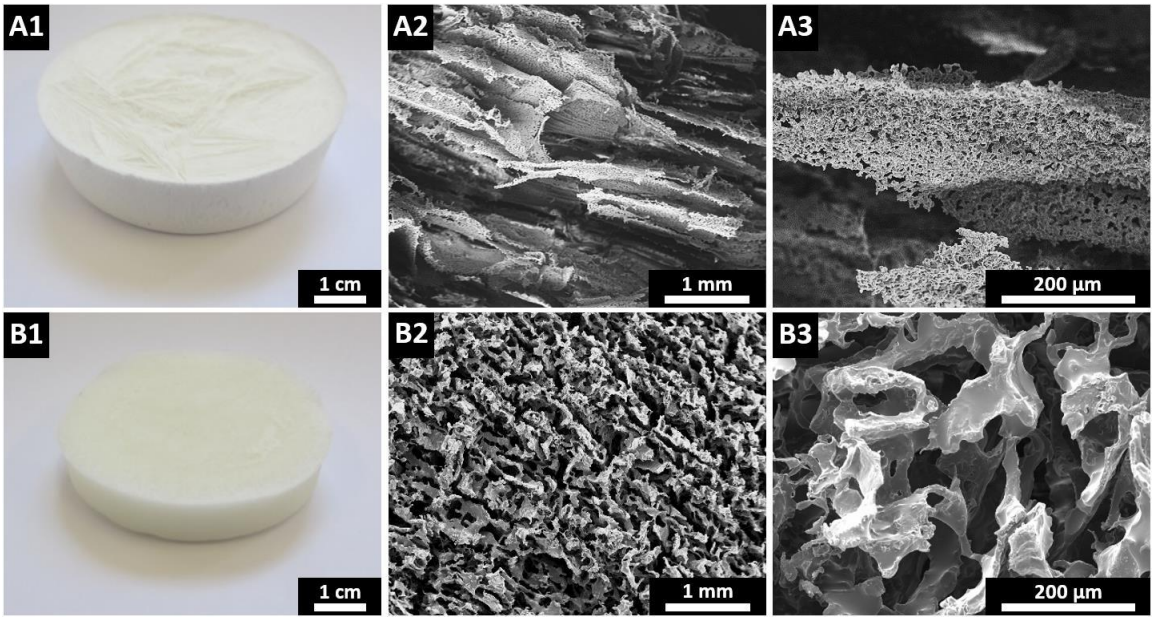

Figure 4.4: Pictures and SEM micrographs of (A1-3) PLLA-DMC and (B1-3) PGS/PLLA-DMC scaffold samples after freeze-drying and curing, showing their microstructures.

Compared to the PLLA-D scaffold, the PGS/PLLA-D and PGS/PLLA-DMC scaffold samples had larger pore sizes of 90% and 46%, respectively, as well as wider pore size distributions (Figure 4.S1, Appendix B). The increases in pore size can be attributed to the

non-crosslinked pre-PGS polymer and its low glass transition temperature, T_g, and low $\bar{M}_n$, as previously discussed in Chapter 3 [356]. Briefly, the pre-PGS features a T_g in the range of -40 °C to -30 °C [252] and a $\bar{M}_n$ of 1248 g mol^{-1}, while the PLLA polymer is characterised with a T_g of 54.2 °C and a $\bar{M}_n$ of 130,000 g mol^{-1} [337]. Thus, pre-PGS molecular chains were more flexible and easier to move during the pre-freeze and holding stages of the freeze-drying process, whereas the growth of the solvent crystals might have been restrained by the glassy PLLA polymer chains [356]. In addition, the PGS/PLLA-D and PGS/PLLA-DMC scaffolds featured overall larger pore sizes then the PGS/PLLA scaffolds of Chapter 3, due to a lower total material content in the initial freeze-drying solution.

4.3.3 Physical and mechanical properties of PLLA and PGS/PLLA scaffolds

Table 4.2: Pore size, volume ratios, densities and porosities of PLLA and PGS/PLLA scaffolds.

Sample code	Pore size / µm	PGS:PLLA volume ratio, φ_{PGS}: φ_{PLLA}	Solid density, $\rho_{f-matrix}$ / Mg m^{-3}	Scaffold density[a], ρ_f / Mg m^{-3}	Porosity, P_f / %
PLLA-D	74.29 ± 4.28	0:100	1.22	0.088 ± 0.008	93
PGS/PLLA-D	141.21 ± 6.40	73:27	1.16	0.091 ± 0.001	92
PGS/PLLA-DMC	108.55 ± 5.37	73:27	1.16	0.106 ± 0.009	91

[a] Scaffold density was determined by measuring the weight and volume of each scaffold type.

Table 4.3: Tensile and compression properties of PLLA and PGS/PLLA scaffolds.

Sample code	Tensile			Compression			
	Young's modulus, E_t / MPa	UTS[a], σ_{tmax} / MPa	Elong.[b] at σ_{tmax}, $\varepsilon_{t\sigma max}$ / %	Young's modulus, E_c / MPa	Comp.[c] collapse stress, σ_c /MPa	Comp.[c] stress at 50% strain, $\sigma_{c50\%}$ / MPa	Comp.[c] collapse strain, ε_c / %
PLLA-D	2.23 ± 0.53	0.12 ± 0.027	7.82 ± 1.07	4.67 ± 1.02	0.44 ± 0.11	1.23 ± 0.05	9.16 ± 1.11
PGS/PLLA-D[d]	0.030 ± 0.005	0.007 ± 0.001	26.17 ± 3.15	0.014 ± 0.006	N/A	0.019 ± 0.004	N/A
PGS/PLLA-DMC[d]	0.031 ± 0.008	0.007 ± 0.001	23.55 ± 2.40	0.006 ± 0.001	N/A	0.007 ± 0.003	N/A

[a] Ultimate tensile strength; [b] Elongation; [c] Compressive; [d] PGS/PLLA-D and PGS/PLLA-DMC scaffolds did not collapse during compression tests.

The pore sizes, the PGS:PLLA volume ratio, the $\rho_{f-matrix}$, the ρ_f and the P_f of the PLLA and PGS/PLLA scaffolds are listed in Table 4.2. All scaffolds had a high porosity in the range of 91-93%. The results also showed that the use of 1,4-dioxane or DMC as a solvent slightly affected the density and porosity of the scaffold, due to the different polymer solubility characteristics and polymer compositions.

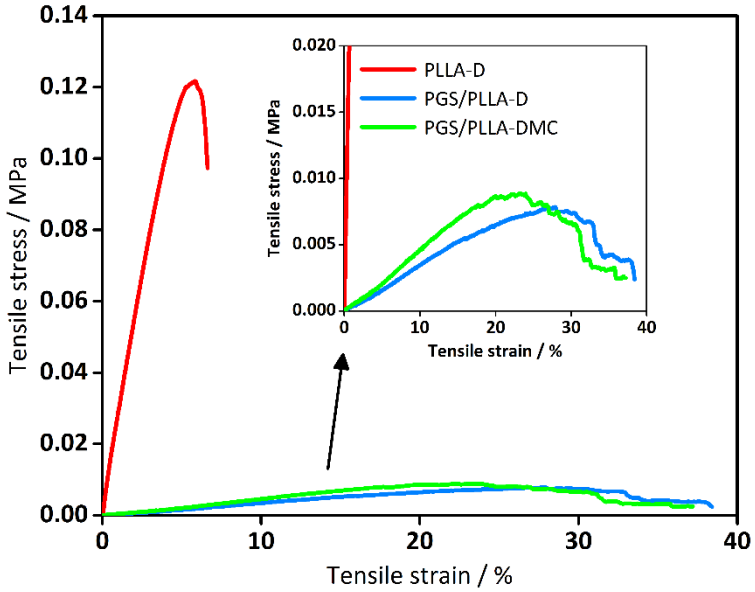

Figure 4.5: Representative tensile stress-strain curves of the polymer scaffolds. PGS/PLLA-D and PGS/PLLA-DMC scaffolds are softer and more resilient than the PLLA-D scaffold with statistical significance ($p < 0.05$). The insets show the stress-strain curves at a smaller scale of Y-axis and highlight the results of both PGS/PLLA scaffolds.

Figure 4.5 illustrates representative tensile stress-strain curves of the PLLA and PGS/PLLA scaffolds. The tensile Young's modulus, E_t, the ultimate tensile strength, σ_{tmax}, and the elongation at ultimate tensile strength, $\varepsilon_{t\sigma max}$, were obtained, as listed in Table 4.3. The tensile testing results demonstrated with statistical significance ($p < 0.05$) that the PGS/PLLA-D and PGS/PLLA-DMC scaffolds are softer and more flexible compared to the PLLA-D scaffold. The PLLA-D scaffold presented at the same material concentration a 70 times higher E_t, a 16 times higher σ_{tmax} and an approximately twice lower $\varepsilon_{t\sigma max}$ than

both PGS-based scaffolds. Compared to the PGS/PLLA scaffolds with weight ratios of 2.5:1 and 3:1 of Chapter 3, the PGS/PLLA-D and PGS/PLLA-DMC scaffolds have in average a ~12-34 times lower E_t and a ~two times higher $\varepsilon_{t\sigma max}$ (see Section 3.3.3), overall demonstrating favourable mechanical properties.

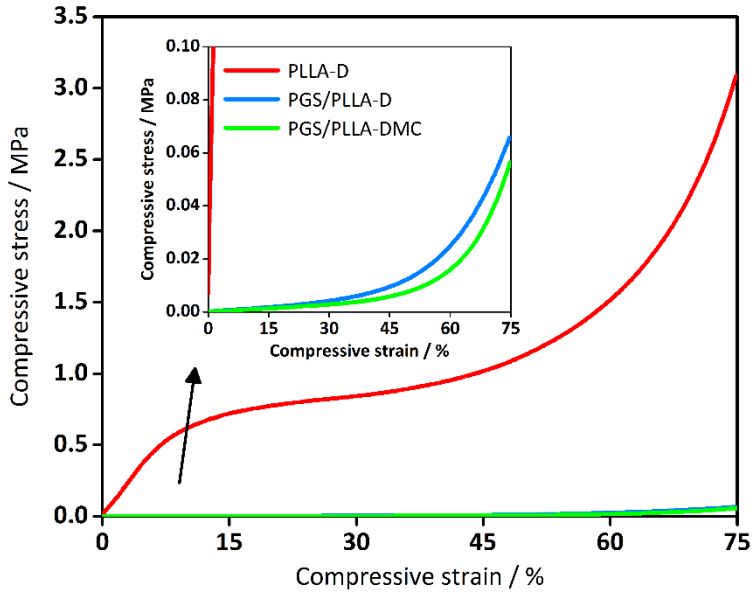

Figure 4.6: Representative compressive stress-strain curves of the polymer scaffolds. PGS/PLLA scaffolds are significantly softer than the PLLA-D scaffold ($p < 0.05$) and also do not collapse during the tests. The insets show the stress-strain curves at a smaller scale of Y-axis and highlight the results of both PGS/PLLA scaffolds.

Figure 4.6 shows representative compressive stress-strain curves of all the scaffolds. The compressive Young's modulus, E_c, the compressive collapse stress, σ_c, the compressive collapse stress at 50% strain, $\sigma_{c50\%}$, and compressive collapse strain, ε_c, were obtained, as listed in Table 4.3 (Figure 4.S2, Appendix B). The results presented highly flexible PGS/PLLA-D and PGS/PLLA-DMC scaffolds, characterised with only a linear elastic and a densification regime, while the stiffer PLLA-D scaffold featured in addition a collapse plateau regime [358]. Both PGS-based scaffolds withstood high compression and presented full shape recovery after the release of load, while the PLLA-D scaffold was not capable to recover because of the collapse of the scaffold during testing, as seen in Figure 4.7. The PLLA-D

scaffold exhibited a 466 times greater E_c, presenting significantly higher stiffness compared to both PGS-based scaffolds ($p < 0.05$). The overall softness and flexibility characteristics of both PGS-based scaffolds can be attributed to the high volume ratio of the elastomeric PGS in the scaffold and its related low crosslink density.

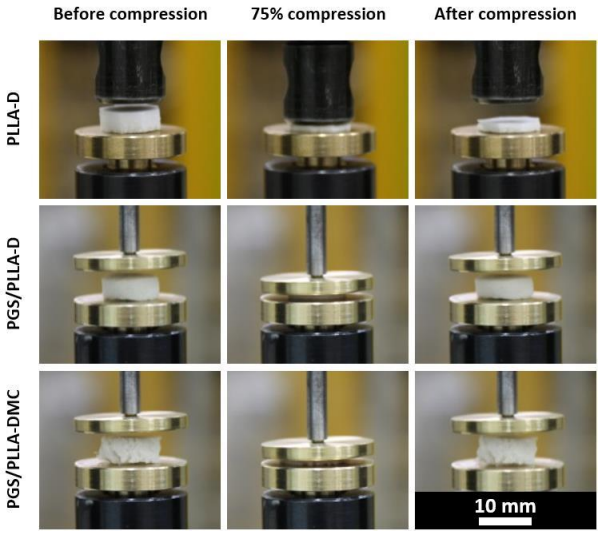

Figure 4.7: Compressive behaviour of all PLLA-D, PGS/PLLA-D and PGS/PLLA-DMC scaffolds after 75% strain compression.

Figure 4.8 illustrates the wetting behaviour of all the scaffolds by dropping a blue-dyed PBS solution on the scaffold surface. The PGS/PLLA-D and PGS/PLLA-DMC scaffolds featured hydrophilic characteristics with an accelerated uptake of fluid (complete soaking < 30 s), whereas the PLLA-D scaffold presented hydrophobic characteristics which prevented fluid absorption within 1 h. The hydrophilic characteristics of both PGS-based scaffolds can be attributed to non-bonded hydroxyl groups on the PGS polymer backbone (due to the low crosslink density), while the hydrophobic properties of the PLLA scaffolds are ascribed to the pendant methyl group on the alpha carbon [359]. The wettability results are in accordance with previous studies [242,266], which demonstrated that the addition of non-crosslinked pre-PGS or PGS itself with a low crosslink density can improve the hydrophilicity of scaffold constructs.

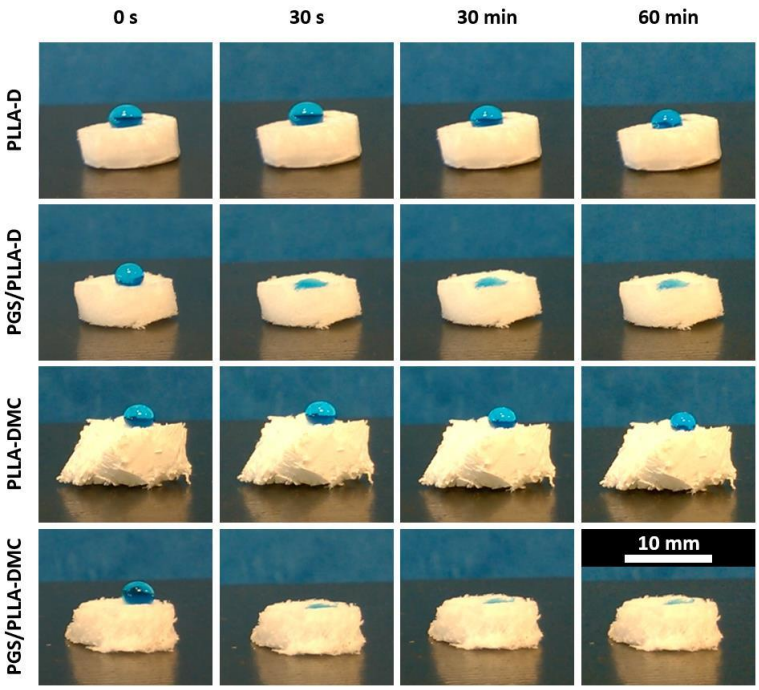

Figure 4.8: Wettability of PLLA-D, PGS/PLLA-D and PGS/PLLA-DMC scaffold samples (drop size: 0.04 mL; blue-dyed PBS). PGS-based scaffolds presented hydrophilic properties with good wetting behaviour, while the PLLA-D scaffold showed hydrophobic characteristics.

4.3.4 *In vitro* degradation

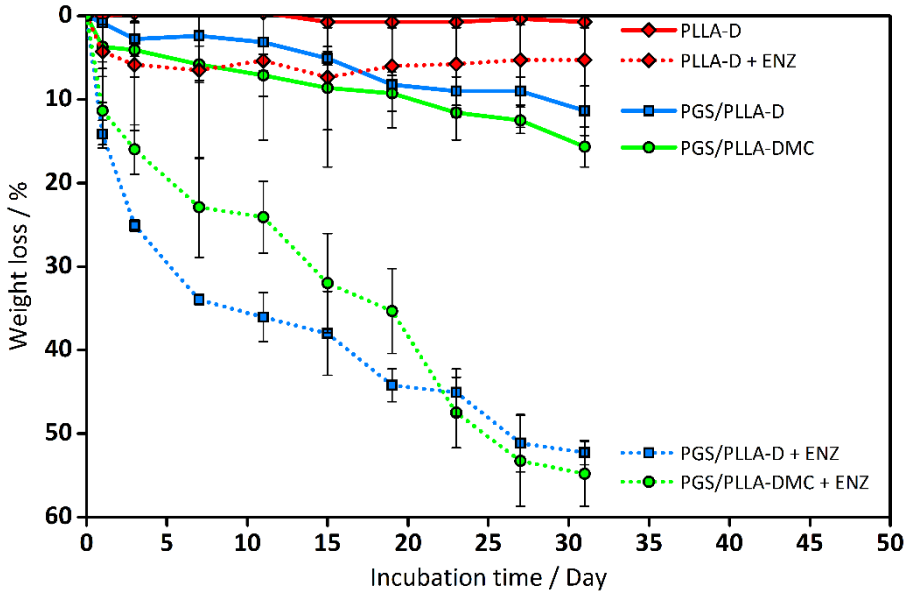

Figure 4.9: Percentage of weight loss of PLLA-D, PGS/PLLA-D and PGS/PLLA-DMC scaffolds, incubated in enzyme-free or enzyme-containing PBS solutions in a shaker incubator for up to 31 days at 37 °C.

Figure 4.9 presents the *in vitro* degradation performance of PLLA-D, PGS/PLLA-D and PGS/PLLA-DMC scaffolds in enzyme-free and lipase enzyme-containing PBS solution for up to 31 days. The PLLA-D scaffold samples presented a stable horizontal trend with only minor weight losses of 1% and 5% in the enzyme-free and enzyme-included PBS solutions, respectively, similar to the findings in Chapter 3. PLLA-D scaffold samples demonstrated no morphological changes as seen in Figure 4.10 (A1-2) and 4.11 (A1-2). PLLA is in general characterised by bulk degradation and known as a long-term biodegradable polymer due to its hydrophobic characteristics, in which the hydrolysis or enzyme-catalysed hydrolysis is minimal [346,347,356]. The degradation characteristics of both PGS-based scaffolds showed a steady and linear decline. In the enzyme-free PBS solution the PGS/PLLA-D and PGS/PLLA-DMC specimens obtained similar degradation rates of 11% and 16% in 31 days, while in the enzymatic PBS solution the specimens exhibited statistically significant enhanced degradation rates of 55% and 54% in the same time period, respectively. As seen in Figure 4.10 (B1-2, C1-2) and 4.11 (B1-2, C1-2), the PGS/PLLA-D and PGS/PLLA-DMC specimens showed no major changes in the scaffold microstructure, compared to untreated samples. The pore-wall surface morphology demonstrated signs of surface degradation, characterised by rough features, craters and pits. The enzymatically tested PGS/PLLA-D and PGS/PLLA-DMC specimens showed a higher degree of degradation effects, indicating the catalysed hydrolysis of the ester bonds due to the lipase enzyme [345]. PGS primarily degrades by surface degradation [260], as supported by the comparison of the *in vitro* degradation behaviour of pristine PLLA and PGS film tests (Figure 4.S3-4, Appendix B). The large surface area of the PGS/PLLA scaffolds, the hydrophilic characteristics, as well as the low crosslink density of PGS contributed to the high degradation rates, similar to the results reported in previous PGS degradation studies [259,356]. With this respect, the cured PGS films and PGS/PLLA scaffolds of Chapter 3 exhibited slower degradation kinetics under the

same test conditions, indicating that the degradation rate of PGS-based scaffold constructs is tuneable and depends on the crosslink density and available surface area.

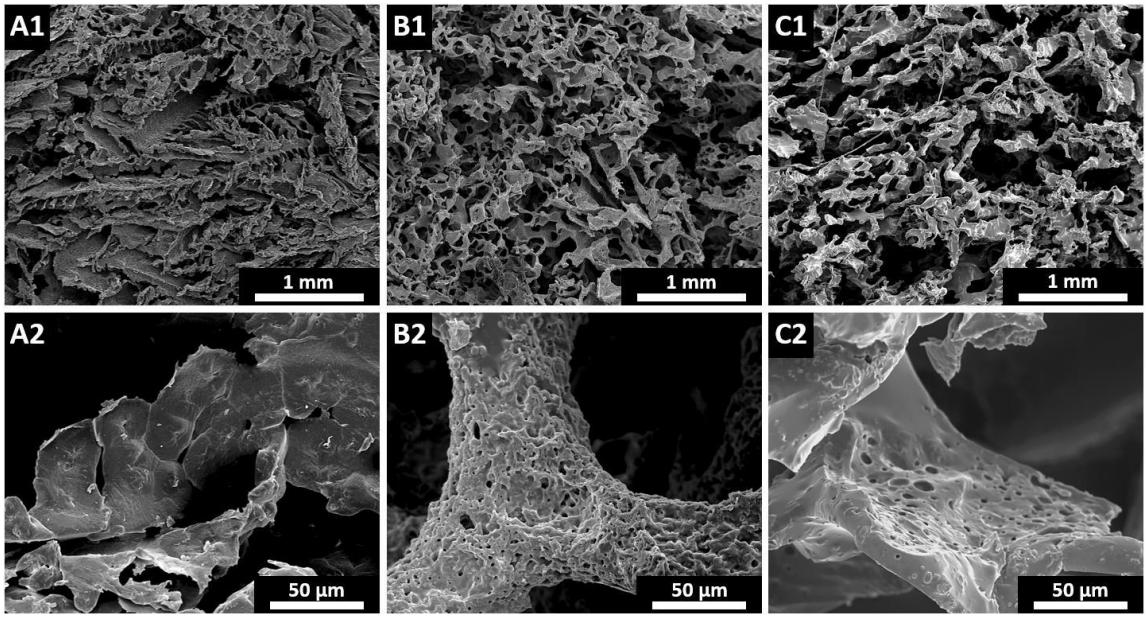

Figure 4.10: SEM micrographs of (A1-2) PLLA-D, (B1-2) PGS/PLLA-D and (C1-2) PGS/PLLA-DMC scaffold after 31 days at 37 ˚C in enzyme-free PBS solution (note that visual differences are minor).

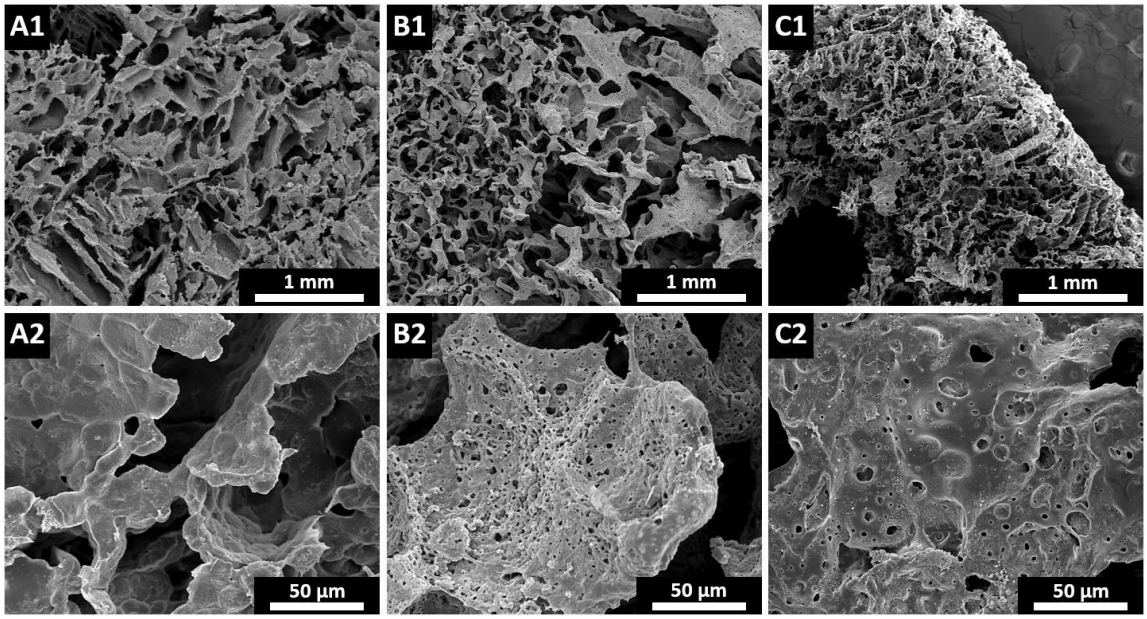

Figure 4.11: SEM micrographs of (A1-2) PLLA-D, (B1-2) PGS/PLLA-D and (C1-2) PGS/PLLA-DMC scaffold after 31 days at 37 ˚C in enzyme-containing PBS solution (note that visual differences are minor).

4.3.5 Cell penetration and tissue growth

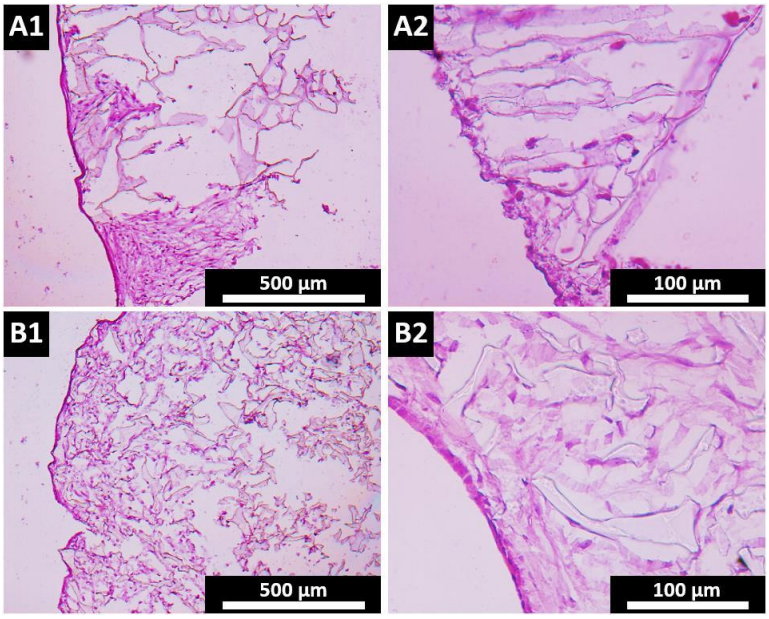

Figure 4.12: Histological analysis via optical microscopy of ADSC-seeded (A1-2) PLLA-D and (B1-2) PGS/PLLA-D scaffold samples after 21 days culture in DMEM, stained with haematoxylin and eosin.

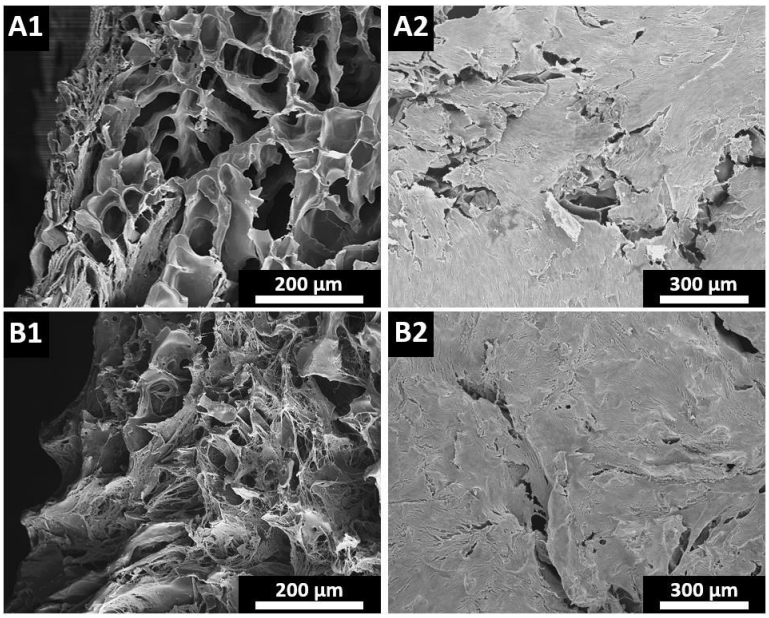

Figure 4.13: Histological analysis via SEM of ADSC-seeded (A1-2) PLLA-D and (B1-2) PGS/PLLA-D scaffold samples after 21 days culture in DMEM. SEM micrographs of (A1, B1) the cross-sectional surface and (A2, B2) the top surface of the cell-seeded scaffolds.

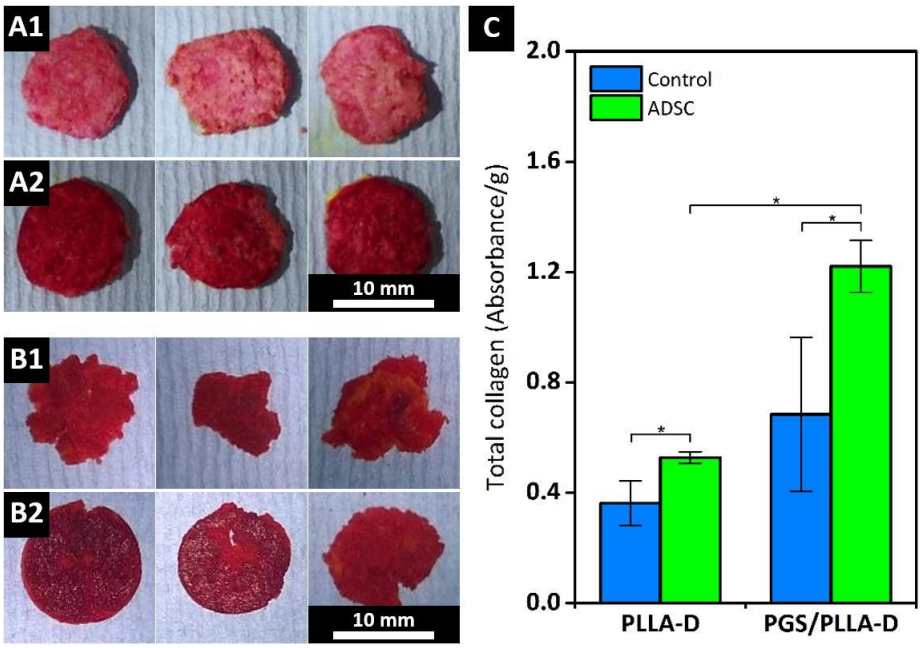

Figure 4.14: Evaluation of the extracellular matrix deposition of ADSCs in PLLA-D and PGS/PLLA-D scaffolds by Sirius red staining after 21 days culture in DMEM. Visualised Sirius red staining of (A1) cell free PLLA-D control samples and (A2) ADSC-seeded PLLA-D samples, as well as (B1) cell free PGS/PLLA-D control samples and (B2) ADSC-seeded PGS/PLLA-D samples. (C) Total collagen amounts determined from Sirius red staining shown as mean ± SD (n = 3; * = $p < 0.05$).

Figure 4.12 and 4.13 shows the histological analysis of ADSC-seeded PLLA-D and PGS/PLLA-D scaffold samples after 21 days culture in DMEM, demonstrating qualitatively the distribution of ADSCs in both scaffolds after the test period. Cells were successfully attached to both types of scaffold and were not removed after washes or medium changes. All the scaffolds had a dense layer of cells and ECM at the cell-seeding surface, as seen in Figure 4.12 (A1-2, B1-2). The inspection of the cross-sectional surfaces of the scaffolds showed deeper cell penetration and ECM growth within the PGS/PLLA-D scaffold than the PLLA-D scaffold. This was verified by SEM analysis which demonstrated the formation of abundant fibrous tissue in the deep layers of PGS/PLLA-D scaffold, in comparison to negligible tissue growth into the 3D structure of the PLLA-D scaffold, as seen in Figure 4.13 (A1-2). The improved cell penetration and tissue growth within the PGS/PLLA-D

scaffold can be attributed to their hydrophilicity and larger pore sizes, overall enhancing the absorption and diffusion of cell culture medium and allowing cells to attach onto and penetrate into the scaffold as well as to proliferate. As depicted in a previous study [266], the addition of partially crosslinked pre-PGS (with a high quantity of free hydroxyl groups) can significantly improve cell attachment, spreading and proliferation in hydrophobic PCL scaffolds, improving the cytocompatibility characteristics. In addition, the use of 1,4-dioxane for the scaffold fabrication in this study showed no negative toxicological effects. While no cell tests were performed with PGS/PLLA-DMC scaffolds, it is assumed that these scaffolds will achieve similar results as the tested PGS/PLLA-D specimens.

Figure 4.14 (A1-2, B1-2) shows collagen accumulation in the control and ADSC-seeded PLLA-D and PGS/PLLA scaffold samples visualised by Sirius red staining. The control and ADSC-seeded PLLA-D scaffold samples (Figure 4.14 (A1-2)) had small differences in the sample size and shape, while the ADSC-seeded PGS/PLLA-D scaffold samples (Figure 4.14 (B1-2)) exhibited a much more distinctive difference from their control samples, with the former showing markedly enhanced maintenance of their original scaffold shape. These initially suggest that new ECM has been formed within the cell-seeded PGS/PLLA-D scaffolds which improved the structural integrity of the scaffold during the *in vitro* cell culture. The histological comparison of the cell-free and the ADCS-seeded PGS/PLLA-D scaffold samples showed a high density of structural integrated cells and ECM in the latter (Figure 4.S5-6, Appendix B). Previous studies have shown that a cell-produced ECM network can help retain or even exceed the initial mechanical properties of PGS-based scaffold constructs which compensates for the degradation related gradual decrease in the mechanical properties, thus, improving structural integrity [271,274]. As presented in Figure 4.14 (C), the collagen produced during the test period was significantly ($p < 0.05$) higher for both ADSC-seeded scaffold types compared to their respective controls without

cells. Further, the comparison between both ADSC-seeded scaffold types showed that ADSCs produced significantly ($p < 0.05$) more collagen per sample in PGS/PLLA-D than in PLLA-D specimens. Overall, the *in vitro* cell test results provide strong evidence that the PGS/PLLA-D scaffolds are suitable for the culture of ADSCs.

The results presented here demonstrate that large 3D and flexible PGS/PLLA scaffolds, with similar bulk mechanical properties to those of native adipose tissue and porous structures suitable for cell penetration and growth, can be prepared by the freeze-drying fabrication strategy from Chapter 3 [356]. With respect to the bulk mechanical properties, both PGS/PLLA scaffolds exhibited comparable stiffness to high stress and low stress adapted adipose tissue from heel pad and breast [127]. The stiffness of the PLLA-D scaffold was significantly higher, confirming that the polymer is too rigid to mimic the mechanical properties of native adipose tissue. The PGS/PLLA scaffolds also showed excellent shape recovery after release of the compressive load, in contrast to the collapse and plastic deformation of the PLLA scaffold during testing. Due to the consistence of the obtained mechanical properties with the native anatomical site, implantation of the PGS/PLLA scaffolds may reduce the inflammatory response of native surrounding tissue and improve the patient comfort compared to rigid scaffold implants [6].

The *in vitro* degradation study of these soft and flexible PGS/PLLA scaffolds showed fast degradation kinetics, which could be too fast for scaffolds to support the growth of target tissue or organs. Further characterisation *in vivo* is needed to demonstrate if these scaffolds would be useful for clinical ATE applications. Previous *in vivo* degradation studies of pure PGS showed complete degradation in 60 days, whereas PLLA degraded fully *in vivo* within 4 years [16,237,352]. If the present PGS/PLLA scaffolds degrade too fast in *vivo*, the chemical structure of PGS in the scaffolds may be modified by changing the crosslink mechanism and introducing more stable urethane groups [312,326]. Future work may also

include the investigation of the *in vitro* and *in vivo* tissue growth behaviour of cell-seeded scaffolds by varying the cell number and cell seeding method (such as constant perfusion of cells using a bioreactor) as well as studying cell behaviour on the scaffolds under mechanical stimulation (e.g., tensile strains or hydrostatic pressure) [12,82]. To ensure future successful clinical applications, it would be advantageous to seed freshly isolated SVF, without *in vitro* selection or expansion processes. SVF can develop into a diversity of cell types, and previous studies indicated that adipose tissue can be regenerated by seeding freshly isolated and uncultured SVF on fibrin hydrogels [360], porous 3D collagen matrix and gelatin sponge scaffolds [136].

Vascularisation is a critical aspect in tissue engineering and a key factor governing the survival of adipose tissue in engineered scaffolds [291,361] in particular in large-volume scaffolds. The highly interconnected open-pore structure with large pore sizes and hydrophilic characteristics of the PGS/PLLA scaffolds is expected to be advantageous in tissue vascularisation. However, vasculogenesis (i.e. the de novo formation of micro-vascular networks) and angiogenesis (i.e. the formation of micro-vascular networks based on existing adjacent vascular trees) in these scaffolds needs to be critically examined *in vivo* to further establish the potential of the scaffolds in the clinical reconstruction of large-volume adipose tissues. Of relevance to this, the application of SVF and growth factors to autologous fat transplants [362], as well as in fibrin hydrogels [360], has been found to promote neovascularisation, demonstrating high potential for SVF to mediate vasculogenesis and adipogenesis for ATE.

4.4 Conclusions

Large and flexible 3D porous PGS/PLLA scaffolds were fabricated with either 1,4-dioxane or DMC as the solvent, by a freeze-drying and a subsequent curing process. The PGS/PLLA scaffolds with a weight ratio of 1.25:0.5 were characterised with highly interconnected open-

pore structures, as well as high porosities and pore sizes in the range of 91-92% and 109-141 μm, respectively. The microstructure characteristics of the scaffolds varied with the solvent in use. The PGS/PLLA scaffold produced with 1,4-dioxane was characterised with favourable, relatively uniform and large pores, while scaffolds produced with DMC presented a more vertically aligned pore structure with thick pore walls and struts. Both PGS/PLLA scaffold types showed a tensile Young's modulus, ultimate tensile strength and elongation at ultimate tensile strength in the range of 0.030-0.032 MPa, 0.007 MPa and 23-25%, respectively. Compressive tests presented elastomeric behaviour of both PGS/PLLA scaffolds with full shape recovery capability after 75% axial strain. The bulk mechanical properties of these scaffolds matched the stiffness of native low and high stress adapted adipose tissue, attributed to the high volume ratio of 73% PGS in scaffolds which possessed a low crosslink density, a low Young's modulus, a low tensile strength and a high elongation at break.

In vitro degradation tests of both PGS/PLLA scaffolds obtained similar weight losses in 31 days of 11-16% and 54-55% in enzyme-free and enzyme-containing PBS solution, respectively. *In vitro* cell test results provided clear evidence that PGS/PLLA scaffolds are suitable for the culture of ADSCs, characterised with deep cell penetration and ECM growth, which improved the scaffold structure integrity during the test period. In contrast, the pure PLLA scaffolds prepared with the same fabrication procedure exhibited microstructures with smaller average pore sizes, hydrophobic characteristics, extremely rigid and less flexible bulk material properties, as well as less favourable scaffold cell penetration and tissue in-growth characteristics.

The results demonstrated that the freeze-dried PGS/PLLA blend scaffolds with similar mechanical properties and desirable porous structures with respect to native adipose tissue as

well as hydrophilic characteristics have great potential to be further developed in tissue scaffolds for ATE.

Chapter 5. Structure and properties of stretchable and biodegradable poly(glycerol sebacate urethane) scaffolds

5.1 Introduction

The large and highly porous developed PGS/PLLA blend scaffolds as described in Chapter 4 featured similar mechanical bulk properties to those of native adipose tissue, as well as desirable porous structures and hydrophilic characteristics, which showed great potential to be developed further in tissue scaffolds for ATE. The PGS/PLLA blend scaffolds, however, were characterised with fast degradation kinetics, which could potentially be too fast for scaffolds to support the growth of certain target tissue or organs, if highly elastomeric and porous PGS-based scaffolds are required. The harsh PGS curing conditions, which include long curing times, high curing temperatures and a mandatory vacuum environment, further limit the potential application of the fabrication strategy described in the previous two chapters.

The main objective of this chapter is the development of large flexible 3D porous poly(glycerol sebacate urethane) (PGSU) scaffolds for ATE applications. PGSU was recently designed by Pereira *et al.* [312] to overcome the limitations of pristine PGS, such as its fast degradation kinetics and its relative narrow tuneable mechanical range [312]. PGSU is a biocompatible and highly tuneable elastomer, synthesised by reacting pre-PGS with isocyanate-based crosslinkers, such as HDI, as seen in Figure 5.1. It can be synthesised rapidly under mild conditions through a solvent-based or solvent-free method, therefore avoiding the time-consuming and harsh curing conditions of pristine PGS [312,326]. The mechanical and biodegradation properties of PGSU can be easily tailored by varying the synthesis method and the molar ratio of crosslinker [312]. PGSU featured broad mechanical properties with Young's moduli, strengths and strains at break in the range of 0.71-19.7 MPa, 1.00-12.10 MPa and 78-516%, respectively [312]. The biodegradation of PGSU is dominated

by surface erosion and presented *in vivo* degradation rates of over 280 days [312]. PGSU specimens presented no significant signs of inflammatory responses *in vivo* and the presence of sol content had no effect on its biocompatibility profile [312]. Previous studies on PGSU were mainly focused on their physical and chemical structures, mechanical properties and biocompatibility, while studies on large 3D PGSU scaffolds were limited [312,326].

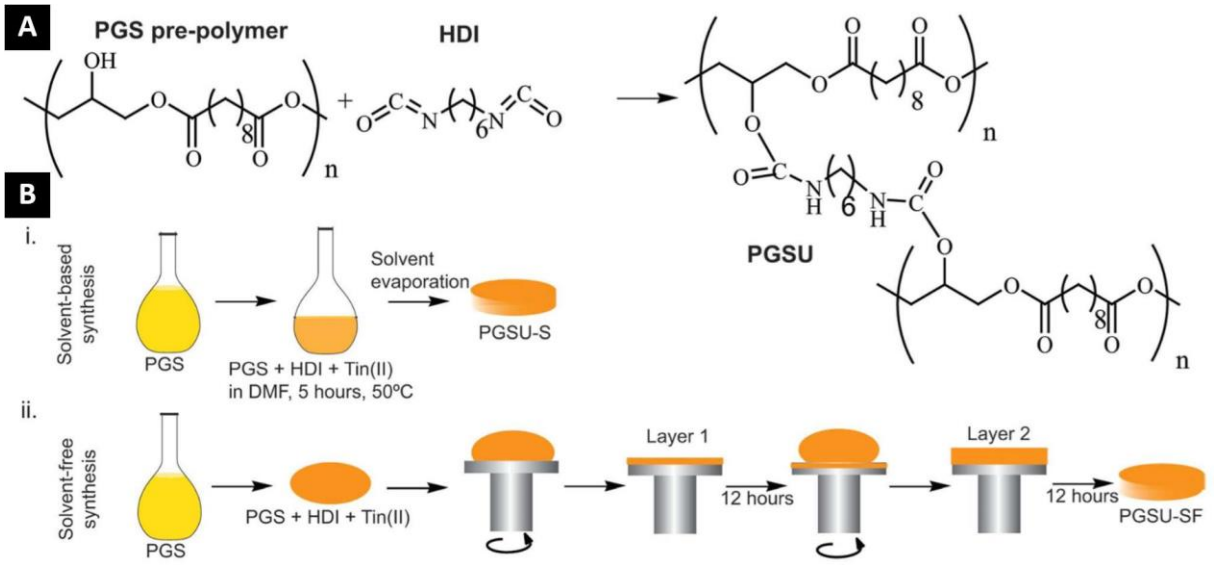

Figure 5.1: (A) Reaction and chemical structure of PGSU. (B) PGSU synthesis under (i) solvent-based and (ii) solvent-free conditions. Adapted from Pereira *et al.* [312] with permission from John Wiley and Sons, copyright 2012.

Flexible and large 3D porous PGSU scaffolds with three different low molar ratios of HDI were fabricated via a freeze-drying process. 1,4-dioxane was used as the solvent for the fabrication of PGSU scaffold. The morphology of the PGSU scaffolds was analysed by SEM. The hydrophilic characteristics and water absorption of the scaffolds were investigated and evaluated. The mechanical properties were measured in dry and hydrated state during quasi-static and cyclic tensile and compression tests, along with rheometry measurements. *In vitro* degradation studies up to 112 days were performed in enzyme-free and enzyme-containing PBS solutions. The chemical structure and physical characteristics of pre-PGS and PGSU films were also evaluated.

5.2 Experimental section

5.2.1 Materials

The materials for this chapter are those used in Chapters 3 and 4, with the following additions: HDI, Tin(II) 2-ethylhexanoate (Tin(II)), dimethylformamide (DMF), acetone, chloroform, were purchased from Sigma-Aldrich.

5.2.2 Preparation of pre-PGS

Pre-PGS was synthesised as described in Chapter 3.

5.2.3 Preparation of PGSU films and Scaffolds

Table 5.1: Material compositions of the PGSU solutions for freeze-drying.

Sample code	Molar ratio of glycerol to HDI / mol mol^{-1}	Weight ratio of pre-PGS to HDI / g g^{-1}	Solvent	Solvent quantity / mL
PGSU-1:0.4	1:0.4	1.42 : 0.33	1,4-dioxane	50
PGSU-1:0.5	1:0.5	1.36 : 0.39	1,4-dioxane	50
PGSU-1:0.6	1:0.6	1.30 : 0.45	1,4-dioxane	50

PGSU specimens with three different low molar ratios of glycerol to HDI (glycerol:HDI = 1:0.4; 1:0.5, 1:0.6) were synthesised on the basis of a previously reported solvent-based method [312]. These low molar ratios of glycerol to HDI were chosen to guarantee soft and flexible properties [312]. The nomenclature of the synthesised specimens is presented as PGSU-X, where "X" represents the molar ratio of glycerol to HDI: PGSU-1:0.4, PGSU-1:0.5 and PGSU-1:0.6. Briefly, pre-PGS was dissolved in 1,4-dioxane under the presence of the catalyst Tin(II) (0.05% w/v) and heated to 55 °C under constant stirring in a sealed flask. HDI was then added drop wise to the solution, nitrogen purged into the reaction flask, sealed and held at 55 °C for 5 h. For the preparation of PGSU films, the solution was cast onto a Teflon dish and left for 2 days in a fume cardboard at room temperature, and then kept for

2 days in a vacuum oven at 37 °C to evaporate any residual solvent and allow for further crosslinking [312,326].

For the preparation of PGSU scaffolds, the solutions were cast into a non-sticky Teflon-coated metal baking tray (six cylindrical cavities with a diameter of 60 mm purchased from a local store) and placed in a Labconco FreeZone Triad freeze-dryer for lyophilisation. With this respect, the PGSU scaffolds were prepared with a fixed total material concentration, as listed in Table 5.1, and fabricated via a modified freeze-drying procedure, based on the previous methods in Chapter 3 and 4. Hence, the solutions were cooled to -30 °C during the freezing stage and held for 5 h, allowing the complete freezing of the solutions. In the primary drying stage the frozen solutions were heated to -5 °C (heating rate of 1 °C min^{-1}) and sublimated for 24 h under vacuum. For the secondary drying stage the temperature was raised to room temperature (heating rate of 1 °C min^{-1}) and held for further 5 h. The as-prepared specimens were left for 2 days in a fume cupboard at room temperature, and then kept for 2 days in a vacuum oven at 37 °C to evaporate any residual solvent and to cure it further [312,326]. All PGSU films and scaffolds underwent a cleaning procedure prior to tests (24 h saturation in ethanol at 21 °C; vacuum oven drying at 37 °C for 24 h) and were stored in a standard 50% relative humidity at 21 °C until further use.

5.2.4 Characterisation and testing of pre-PGS and PGSU films

The number average molecular weight, $\bar{M}_n$, the weight average molecular weight, $\bar{M}_w$, and the PDI of the pre-PGS were obtained by GPC as described in Chapter 3. FTIR characterisation on pre-PGS and PGSU films was the same as per Chapter 3.

The densities, ρ_{PGSU}, of PGSU films were measured by using a AccuPycII 1340 helium pycnometer. Samples were dried in a vacuum oven for 24 h at 37 °C, prior to density measurements.

The solubility of PGSU film specimens were evaluated by 24 h solvent saturation in dimethylformamide, 1,4-dioxane, acetone, dimethyl carbonate, toluene, chloroform and ethanol at 21 °C. The sol content of non-cleaned PGSU film specimens (n = 5) was measured by determining the weight difference before and after 24 h ethanol saturation at 21 °C. The swelling properties of the dried PGSU specimens (n = 9) were analysed in PBS solution (24 h saturation at 37 °C) and ethanol (24 h saturation at 21 °C), in which the weight swelling ratio was determined by dividing the weight gained during the fluid saturation by the weight of the initial sample.

Quasi-static tensile tests of dry and hydrated PGSU films (hydrated PGSU films had been immersed in PBS solution for 24 h at 37 °C and were immediately removed from the solution for the tests) were performed on a Hounsfield H100KS testing machine. Punched-out PGSU film specimens (n = 5; "dog bone" shaped; width: 2.6 mm, gauge length: 20 mm, thickness: 0.4 ± 0.05 mm) were tested at a strain rate of 50 mm min^{-1} using a 10 N load cell till fracture (ASTM D412). All the tests were performed at room temperature.

The crosslink density, n_{mech}, of the PGSU films was evaluated as described in Chapter 3.

5.2.5 Characterisation and testing of PGSU scaffolds

The microstructures of as-prepared and cleaned PGSU scaffolds was examined by SEM on a Camscan S2, as described in Chapter 3. The average pore sizes (n = 450) of all scaffolds were evaluated by using ImageJ software. Only fully defined pores were considered for geometrical measurements.

The procedures for measuring the scaffold densities, ρ_f, the relative density, ρ_r, and the porosity, P_f, of all PGSU scaffolds (n = 8) were the same as per Chapter 3.

Quasi-static and cyclic tensile and compression tests of dry and hydrated PGSU scaffolds (hydrated PGSU scaffolds had been immersed in PBS solution for 24 h at 37 °C and were immediately removed from the solution for the tests) were performed on a Hounsfield

H100KS testing machine with a 10 N load cell. Scaffold tensile test samples for quasi-static (n = 10; width: 5.14 ± 0.70 mm (y-axis), gauge length: 15 mm (x-axis), thickness: 3.04 ± 0.71 mm (z-axis)) and cyclic (n = 3; width: 5.60 ± 0.78 mm (y-axis), gauge length: 15 mm (x-axis), thickness: 3.66 ± 0.82 mm (z-axis)) tests were prepared as described in Chapter 3. Tensile tests (ASTM D412) were performed at a tensile strain rate of 50 mm min^{-1} till fracture, while the cyclic tensile tests were stretched to 20% strain during 20 cycles, at the same tensile strain rate. Cylindrical scaffold samples for quasi-static (n = 10; diameter: 10 mm, thickness: 4.13 ± 0.94 mm (y-axis)) and cyclic (n = 3; diameter: 10 mm, thickness: 5.99 ± 0.35 mm (y-axis)) compression tests were punched-out from the centre cross section of the scaffolds. Compression tests (ASTM C365-05) were performed at a strain rate of 5 mm min^{-1} up to a strain of 75%, while cyclic compression tests were compressed to 50% strain during 20 cycles, at the same strain rate. The hysteresis, or dissipated energy, e_d, was determined by evaluating the area between the loading and unloading curves during cyclic tensile or compression tests, and a hysteresis loss ratio, h_r, was defined by Equation 5.1 [363],

$$h_r = \frac{e_0 - e_r}{e_0} = \frac{e_d}{e_0} \tag{5.1}$$

where e_0 and e_r are the input and retraction strain-energy densities of the loading and unloading curves, respectively. All the tests were performed at room temperature.

Rheological measurements on hydrated (after 24 h saturation in PBS solution at 37 °C) PGSU scaffold specimens were executed on an Anton Paar Physica MCR 301 rheometer. Dynamic frequency sweep measurements were performed at 25 °C, over a frequency range of 0.1 to 10 Hz under a fixed strain of 0.1% (in the linear viscoelastic region; pre-determined by dynamic strain sweep tests), by using a stainless-steel-plate geometry (diameter: 12 mm) and

a fixed gap of 1 mm between the two parallel plates. Punched-out cylindrical samples (diameter: 12 mm, thickness: 1 mm) from the centre cross section of the scaffolds were used.

The water absorption behaviour within PGSU scaffolds (n = 9) was evaluated by calculating the weight difference between initial dry and soaked specimens, after 24 h saturation in PBS solution at 37 °C. The specimens were carefully wiped with filter paper to remove excess water on their surface, prior to weight measurements.

5.2.6 *In vitro* degradation tests

In vitro degradation tests in enzyme-free and enzyme-containing PBS solution were performed on punched-out PGSU scaffolds (n = 3; diameter: 6 mm; thickness: 2.58 ± 0.12 mm) for up to 112 days at 37 °C, as described in Chapter 3. SEM analysis was performed after 34 days *in vitro* degradation on a Camscan S2 at 5 kV on gold coated PGSU scaffold specimens.

5.2.7 Statistics

All measurements were reported as mean ± SD with a confidence level of 95%. Statistical analysis was performed as described in Chapter 3.

5.3 Results and Discussion

5.3.1 Characterisation of pre-PGS and PGSU Films

The pre-PGS utilised for the solvent-based PGSU synthesis was characterised by GPC with a $\bar{M}_n$, $\bar{M}_w$ and PDI of 1549 g mol^{-1}, 10522 g mol^{-1} and 6.8, respectively. As seen in Figure 5.2 (A-B), the FTIR spectrum of pre-PGS shows the stretching vibration of -OH at 3443 cm^{-1}, C-H_2 at 2926 cm^{-1} and 2854 cm^{-1}, C=O and C-O at 1732 cm^{-1} and 1160 cm^{-1}, respectively [17,252,339]. In comparison, the PGSUs were characterised with the stretching vibration of -OH and -NH at 3362 cm^{-1}, C-H_2 at 2926 cm^{-1} and 2854 cm^{-1}, C=O and C-O at 1720 cm^{-1}, the

bending vibration of amide I, II and III at 1646 cm^{-1}, 1532 cm^{-1} and 1238 cm^{-1}, and stretching vibration of C=O and C-O at 1160 cm^{-1}, respectively [312,326]. The amide groups are attributed to the formation of urethane, the reaction product of HDI and hydroxyl groups [312,326]. The crosslinking of pre-PGS and HDI resulted in peak shifts to lower wavenumbers (e.g. 3362 cm^{-1} and 1720 cm^{-1}), also indicating the establishment of urethane linkages and an increase in hydrogen bonding strength [312,326]. In addition, the PGSU elastomers with higher molar ratios of glycerol to HDI presented stronger amide-based absorption peaks, demonstrating a higher degree of urethane groups. The results confirm the successful formation of urethane linkages between pre-PGS and HDI to form PGSU, as previously reported [312,326]. The characteristic isocyanate group band at 2270 cm^{-1} was absent in all the PGSUs, implying the complete reaction of the isocyanate groups [312,326].

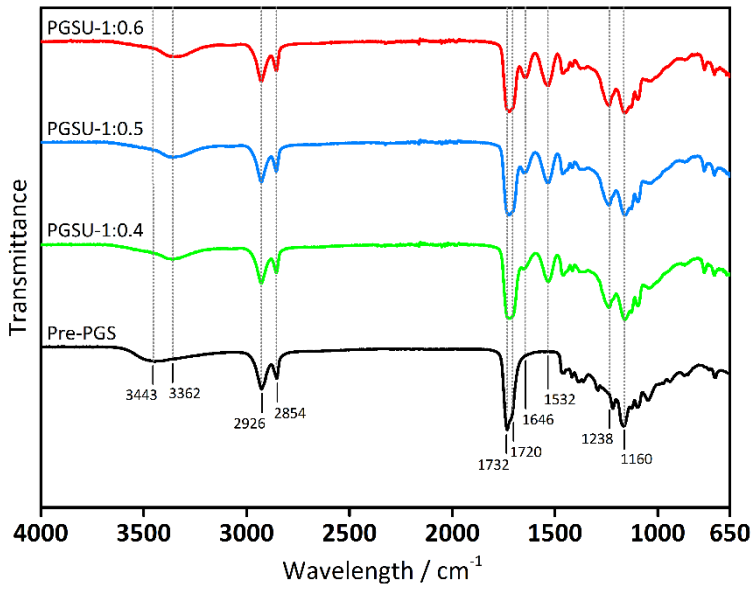

Figure 5.2: FTIR spectra of pre-PGS and PGSU derivatives in the range of 4000-650 cm^{-1}. The spectra were shifted vertically for clarity.

All of the PGSUs were insoluble in various organic solvents (ethanol, acetone, 1,4-dioxane, DMF, DMC, toluene, chloroform), confirming the formation of a covalently crosslinked network. They are, however, swellable in these solvents. For instance,

PGSU-1:0.4, PGSU-1:0.5 and PGSU-1:0.6 specimens presented relatively high mass swelling ratios in ethanol (after 24 h saturation at 21 °C) of 88.2 ± 5.6%, 67.9 ± 1.3% and 55.9 ± 5.7%, while these specimens presented only low mass swelling ratios in aqueous PBS solution (24 h saturation at 37 °C) of 4.9 ± 0.9%, 4.0 ± 0.8% and 2.7 ± 0.9%, respectively. The PGSU elastomers with higher molar ratios of glycerol to HDI showed in general lower degrees of mass swelling ratios, which can be linked to a presumably higher crosslink density, while the overall low mass swelling ratios in PBS solution can be attributed to the primarily hydrophobic nature of the elastomer [312]. In respect to the residual analysis of non-cleaned PGSU-1:0.4, PGSU-1:0.5 and PGSU-1:0.6 specimens (after 24 h ethanol extraction), mass losses of 15.9 ± 2.0%, 5.4 ± 0.9% and 2.0 ± 1.0% were measured, indicating the existence of unreacted monomers, oligomers, and pre-polymers [326]. The PGSU specimens had a similar ρ_{PGSU} of 1.164 ± 0.004 Mg m^{-3} to the value previously reported (1.15 Mg m^{-3}) [326].

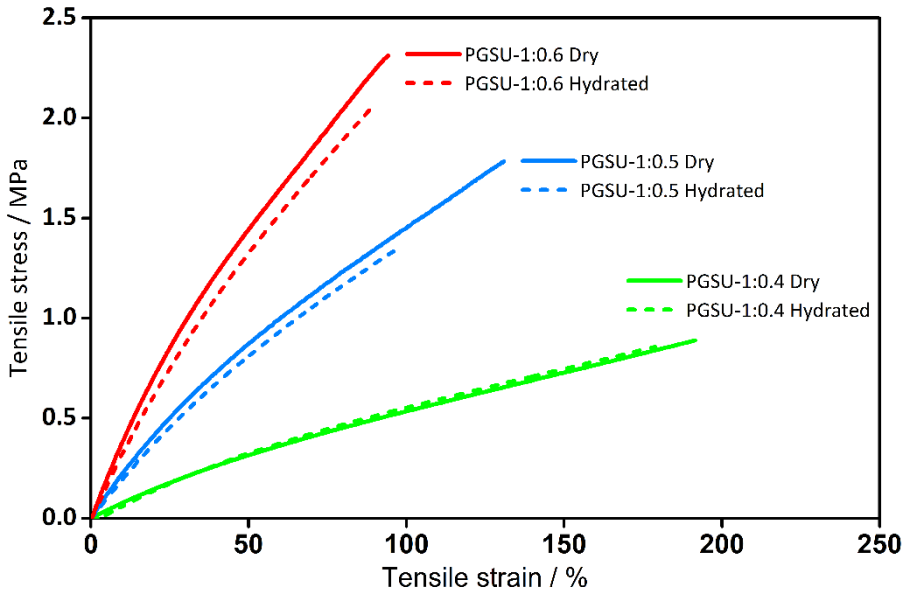

Figure 5.3: Representative quasi-static tensile stress-strain curves of dry and hydrated PGSU films.

Table 5.2: Quasi-static tensile properties of dry and hydrated PGSU films.

	Sample code	Young's modulus, E_s / MPa	Ultimate tensile strength, σ_{smax} / MPa	Elongation at break, ε_{sb} / %
Cleaned / dry	PGSU-1:0.4	0.84 ± 0.03	0.93 ± 0.07	198.6 ± 1.0
	PGSU-1:0.5	2.11 ± 0.11	1.55 ± 0.07	125.2 ± 17.6
	PGSU-1:0.6	3.98 ± 0.62	2.24 ± 0.45	91.6 ± 3.8
Cleaned / hydrated[a]	PGSU-1:0.4	0.84 ± 0.01	0.91 ± 0.04	186.4 ± 4.5
	PGSU-1:0.5	2.11 ± 0.03	1.44 ± 0.10	98.0 ± 4.1
	PGSU-1:0.6	3.51 ± 0.01	2.07 ± 0.12	90.8 ± 5.5

[a] 24 h saturation in PBS at 37 °C.

As shown in Figure 5.3, all the PGSUs were characterised with soft and highly flexible properties, which can be mainly ascribed to the urethane crosslinks [312,364,365]. The tensile Young's modulus, E_s, the ultimate tensile strength, σ_{smax}, and the strain at break, ε_{sb}, were obtained for dry and hydrated PGSUs, as listed in Table 5.2. The tensile testing results of the cleaned and dry PGSUs demonstrated significant difference in terms of E_s, σ_{smax} and ε_{sb}. The mechanical properties of the cleaned and hydrated PGSUs presented also difference among themselves, with only one exception (the ε_{sb} results of the hydrated PGSU-1:0.5 and PGSU-1:0.6 specimens exhibited no statistical difference). So, in general the alteration of the HDI crosslinker ratio changed the PGSUs mechanical characteristics significantly. The PGSU-1:0.4 specimens presented the softest and most flexible properties with an E_s, σ_{smax} and ε_{sb} in the range of 0.84 MPa, 0.91-0.93 MPa and 186-199%, while the PGSU-1:0.5 and PGSU-1:0.6 specimens exhibited stiffer mechanical characteristics with an E_s, σ_{smax} and ε_{sb} in the range of 2.11-3.98 MPa, 1.44-2.24 MPa and 98-125%, respectively, both in dry and hydrated states. The direct comparison of dry and hydrated PGSU counterparts demonstrated similar results, due to their hydrophobicity as previously stated. Still, the hydrated PGSU specimens presented the tendency of decreased σ_{smax} and ε_{sb} results compared to their dry equivalents. It is assumed that the absorbed water molecules may interfere with the hydrogen

bonding of urethane N-H groups and urethane or ester C=O carbonyl groups, which also contributes to the mechanical performance of PUs [364–366]. In comparison to the cured PGS film (26 h at 120 °C) of Chapter 4, the PGSU films have in average a ~4-18 times higher E_s and a ~2-3 times lower ε_{sb} (see Section 4.3.1), due to the strong urethane linkages which affects the materials final physicochemical properties significantly.

All the PGSUs presented statistically significant difference in n_{mech}, which were calculated for dry PGSU-1:0.4, PGSU-1:0.5 and PGSU-1:0.6 as 113.4 ± 6.9 mol m^{-3}, 285.6 ± 14.9 mol m^{-3} and 539.1 ± 84.4 mol m^{-3}, respectively. The n_{mech} results correlate to the prior discussed FTIR and swelling results. With this respect, previous studies demonstrated that minor differences in the molar ratio of HDI had substantial effects on the physicochemical properties of PGSU [312].

5.3.2 Microstructures of PGSU scaffolds

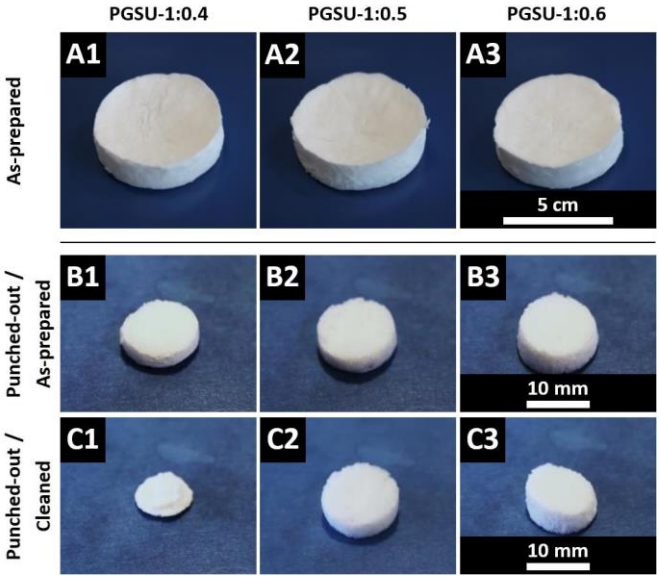

Figure 5.4: As-prepared scaffolds of (A1) PGSU-1:0.4, (A2) PGSU-1:0.5 and (A3) PGSU-1:0.6, directly after freeze-drying. Punched-out scaffold specimens of (B1, C1) PGSU-1:0.4, (B2, C2) PGSU-1:0.5 and (B3, C3) PGSU-1:0.6, in as-prepared and cleaned state.

PGSU scaffolds with three different molar ratios of HDI to glycerol and a fixed material concentration of 1.75 g per 50 ml were fabricated by freeze-drying. All as-prepared PGSU scaffolds were characterised by a white colour and dimensions of approximately 6 cm in diameter and over 1 cm in thickness, as demonstrated in Figure 5.4 (A1-3). These results demonstrate that the immediate freeze-drying of the PGSU pre-polymer/solvent polymerisation medium can lead to stable three-dimensional PGSU scaffold constructs. The surfaces of the PGSU samples revealed minor adhesive properties, due to the low crosslink density and/or due to the presence of unreacted oligomers or pre-polymer, indicating the necessity of additional cleaning procedures. As seen in Figure 5.4 (B1-3, C1-3), the execution of cleaning procedures (24 h saturation in ethanol at 21 °C) on all the as-prepared PGSU scaffolds affected their physical shape and presented the tendency of specimen shrinkage, with the strongest effect on the PGSU-1:0.4 specimens. Thus, the scaffold microstructures of dry as-prepared and cleaned PGSU scaffolds were examined by SEM, analysing the impact of the cleaning procedure on the pore sizes and structures of the scaffolds.

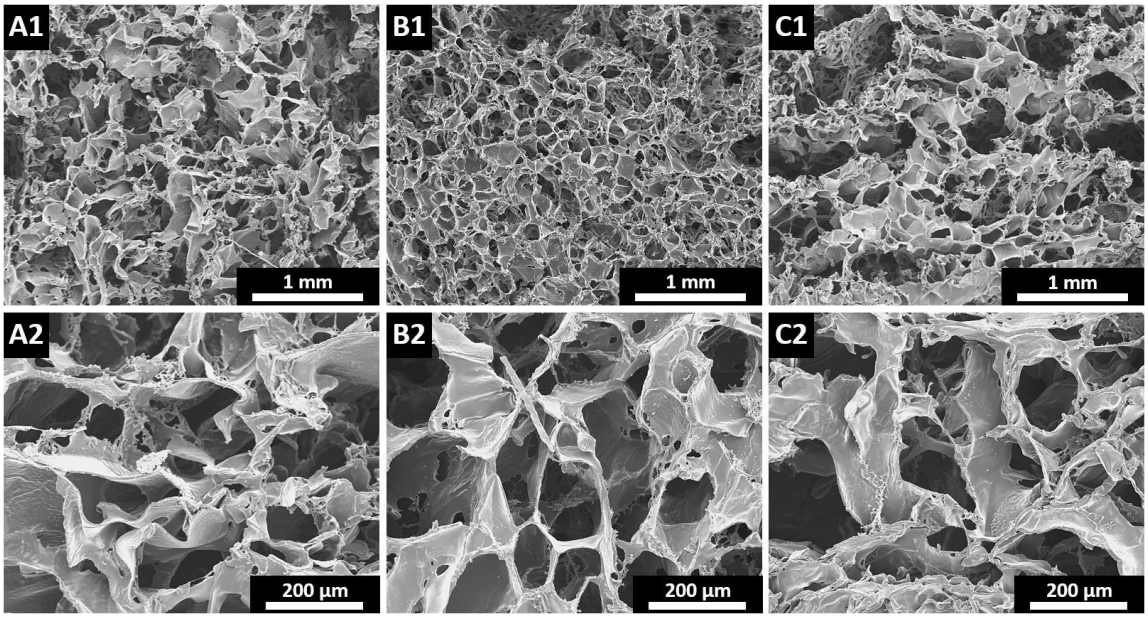

Figure 5.5: SEM micrographs of as-prepared (A1-2) PGSU-1:0.4, (B1-2) PGSU-1:0.5 and (C1-2) PGSU-1:0.6 scaffold microstructures.

All the as-prepared PGSU scaffolds showed randomly distributed and highly interconnected open-pore structures, illustrating relatively good distribution of the solid PGSU throughout the scaffold, as presented in Figure 5.5 (A1-2, B1-2, C1-2). The pores of the scaffold were characterised with non-uniform shapes, which are commonly found in freeze-dried PGS-based scaffolds with 1,4-dioxane as the solvent [356,367]. The as-prepared PGSU-1:0.4, PGSU-1:0.5 and PGSU-1:0.6 scaffolds featured broad pore size distributions (Figure 5.S1, Appendix C), in which the PGSU-1:0.4, PGSU-1:0.5 and PGSU-1:0.6 scaffolds presented similar pore sizes of 93 ± 4 µm, 102 ± 3 µm and 112 ± 4 µm, respectively. The variation of the HDI crosslinker ratio changes the average pore size of the PGSU scaffolds (at a fixed material concentration of the freeze-drying solution). Higher molar ratios of the HDI crosslinker lead to an increase in crosslink density, which improved the structural stability of the scaffold, due to more stable pore struts and walls in the microstructure.

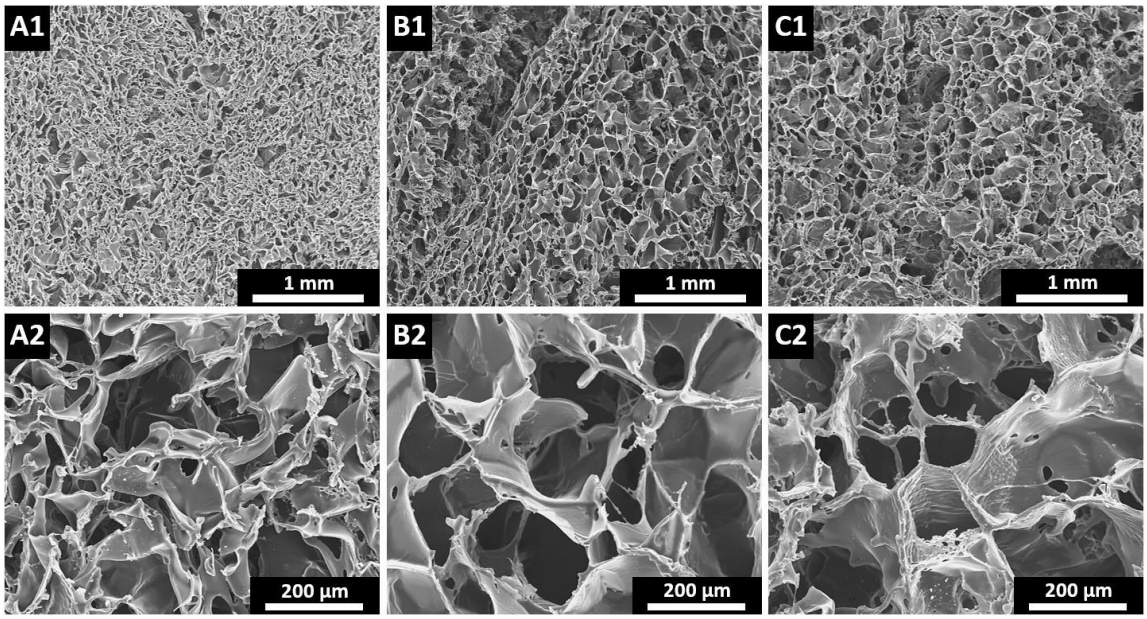

Figure 5.6: SEM micrographs of cleaned (A1-2) PGSU-1:0.4, (B1-2) PGSU-1:0.5 and (C1-2) PGSU-1:0.6 scaffold microstructures.

As shown in Figure 5.6 (A1-2, B1-2, C1-2), all the cleaned PGSU scaffolds maintained a highly interconnected open-cell structure, but presented drops in pore size. The cleaned

PGSU-1:0.4, PGSU-1:0.5 and PGSU-1:0.6 scaffolds featured a narrow pore size distribution and average pore sizes of 55 ± 1 µm, 74 ± 2 µm and 72 ± 4 µm, demonstrating a statistically significant pore size drop of 41.2%, 27.4% and 35.9%, compared to the as-prepared counter parts, respectively. The pore size drop resulted in more compact microstructures, in particular for the cleaned PGSU-1:0.4 scaffold specimens, as seen in Figure 5.6 (A1-2). The open-pore structure of the cleaned PGSU-1:0.4 scaffold specimens were characterised with less defined pore shapes and struts, while the cleaned PGSU-1:0.5 and PGSU-1:0.6 scaffolds featured larger and better preserved pore shapes. The overall drop in pore sizes can be linked to the cleaning procedure, owing to the self-loaded deformation of the ethanol swollen PGSU matrix, as well as due to the sol content removal. Thus, the self-supporting microstructures of the PGSU scaffolds collapsed due to the high mass swelling ratio in ethanol. The PGSU-1:0.5 and PGSU-1:0.6 specimens featured a higher crosslink density and were less swellable, contributing to greater scaffold structure stability. Previous studies also showed that cleaning or sterilisation treatments affected the physical properties of polymer scaffolds, resulting in changed pore sizes and scaffold dimensions [368–370]. In addition, the cleaned PGSU scaffolds featured smaller pore sizes than the PGS/PLLA scaffolds of Chapter 4, indicating room for improvements.

5.3.3 Physical and mechanical properties of PGSU scaffolds

Table 5.3: Densities and porosities of PGSU scaffolds.

Sample code	Scaffold density, ρ_f / Mg m^{-3}	Relative density, ρ_r / ρ_f / ρ_s	Porosity, P_f / %
PGSU-1:0.4	0.265 ± 0.042	0.227 ± 0.036	77.27 ± 3.60
PGSU-1:0.5	0.170 ± 0.014	0.147 ± 0.012	85.34 ± 1.23
PGSU-1:0.6	0.141 ± 0.009	0.121 ± 0.007	87.87 ± 1.28

The cleaned PGSU-1:0.5 and PGSU-1:0.6 scaffolds were characterised with relatively high porosities in the range of 85-88%, while the PGSU-1:0.4 scaffolds featured a lower porosity of 77%, as listed in Table 5.3. Overall, the porosities of the PGSU scaffolds align with the pore sizes discussed previously and presented relativly similar values to those of the PGS/PLLA scaffolds of Chapter 3 and 4.

The water absorption abilities of the PGSU scaffolds were evaluated by immersing specimens for 24 h in PBS solution at 37 °C. The PGSU-1:0.5 and PGSU-1:0.6 scaffolds presented significant differences in the water swelling degree at equilibrium, compared to the PGSU-1:0.4 specimens. The PGSU-1:0.5 and PGSU-1:0.6 scaffolds obtained similar high water absorption ratios of 970 ± 127% and 1052 ± 72%, while the PGSU-1:0.4 specimens presented a lower value of 385 ± 25%. The results imply that the water absorption ability is dependent on the scaffold porosity.

Table 5.4: Quasi-static tensile and compression properties of dry and hydrated PGSU scaffolds.

		Tensile			Compression	
	Sample code	Young's modulus, E_t / MPa	Ultimate tensile strength, σ_{tmax} / MPa	Elongation at σ_{tmax}, $\varepsilon_{t\sigma max}$ / %	Young's modulus, E_c / MPa	Comp.[a] stress at $\varepsilon_{c75\%}$, $\sigma_{c75\%}$ / MPa
Cleaned / dry	PGSU-1:0.4	0.040 ± 0.003	0.018 ± 0.004	48.9 ± 4.2	0.020 ± 0.007	0.075 ± 0.019
	PGSU-1:0.5	0.038 ± 0.013	0.016 ± 0.004	54.9 ± 3.1	0.006 ± 0.001	0.039 ± 0.007
	PGSU-1:0.6	0.030 ± 0.001	0.022 ± 0.001	81.6 ± 9.0	0.005 ± 0.001	0.032 ± 0.004
Cleaned / hydrated[b]	PGSU-1:0.4	0.029 ± 0.014	0.016 ± 0.004	51.6 ± 4.7	0.008 ± 0.001	0.043 ± 0.010
	PGSU-1:0.5	0.032 ± 0.006	0.012 ± 0.003	50.0 ± 1.3	0.004 ± 0.001	0.029 ± 0.005
	PGSU-1:0.6	0.029 ± 0.003	0.019 ± 0.003	56.8 ± 1.7	0.003 ± 0.001	0.013 ± 0.001

[a] Compressive; [b] 24 h saturation in PBS at 37 °C.

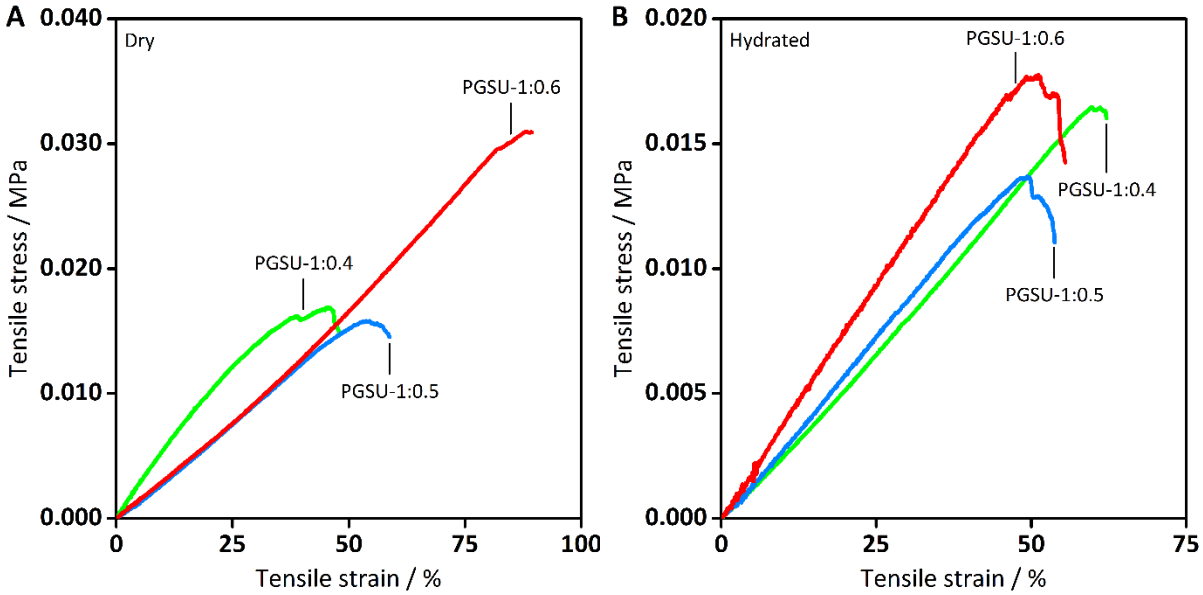

Figure 5.7: Representative quasi-static tensile stress-strain curves of (A) dry and (B) hydrated PGSU scaffolds.

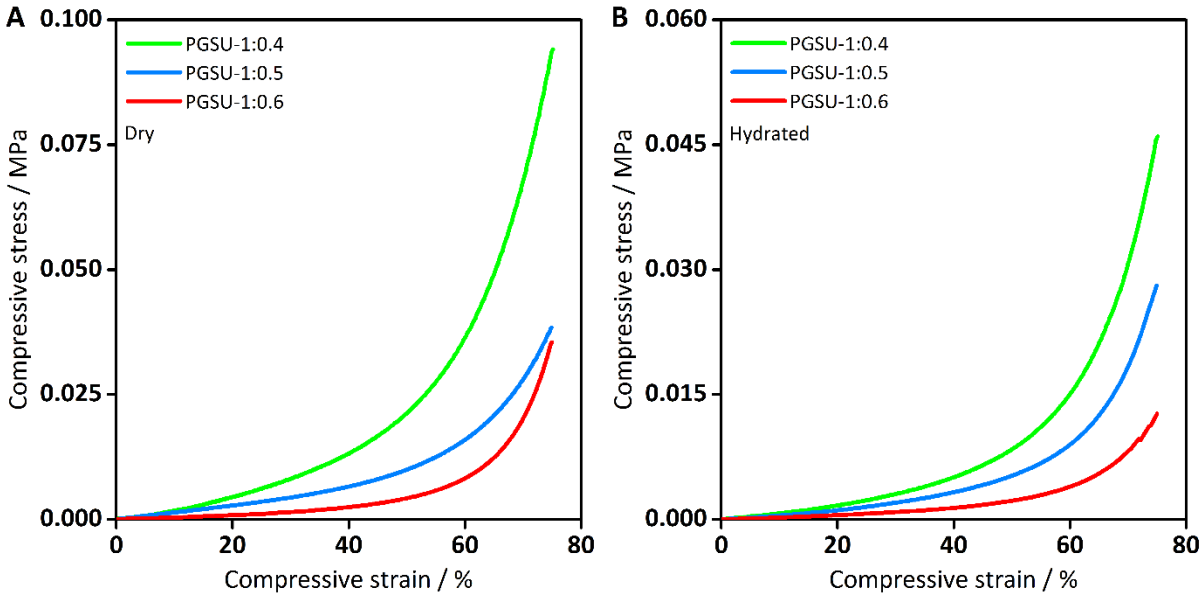

Figure 5.8: Representative quasi-static compressive stress-strain curves of (A) dry and (B) hydrated PGSU scaffolds. Compressive tests were terminated at a strain rate of 75%.

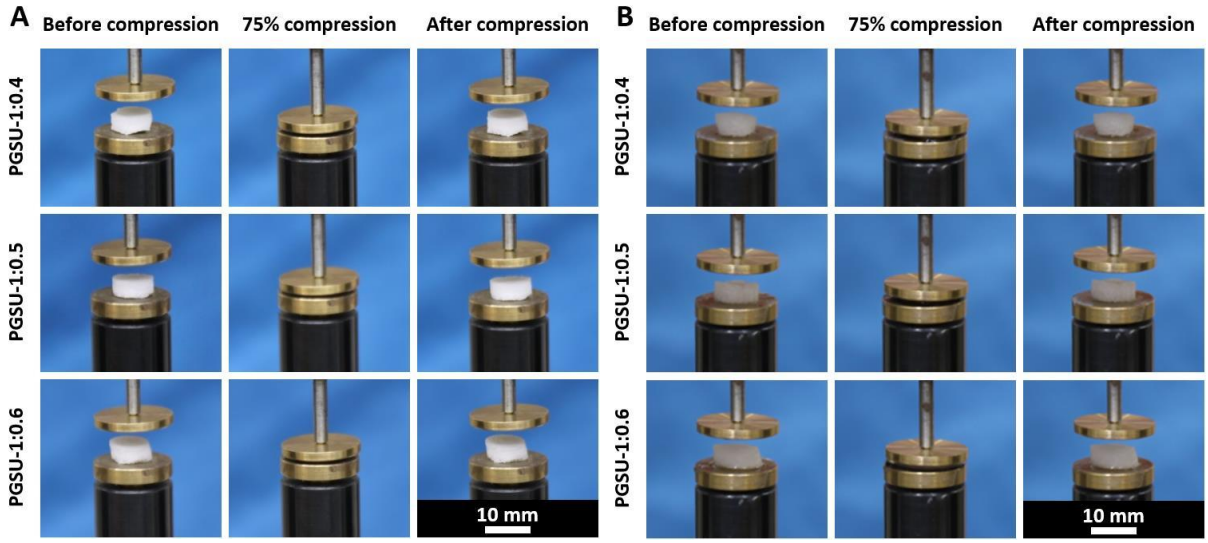

Figure 5.9: Compressive behaviour of (A) dry and (B) hydrated PGSU scaffolds, illustrating the shape restorability after released compression load.

The mechanical properties of cleaned PGSU scaffolds were determined under dry and hydrated state by quasi-static and cyclic tensile and compression tests. Representative tensile stress-strain curves of the scaffolds are presented in Figure 5.7 (A, B). The tensile Young's modulus, E_t, the ultimate tensile strength, σ_{tmax}, and the elongation at ultimate tensile strength, $\varepsilon_{t\sigma max}$, were obtained, as listed in Table 5.4. The results showed that the PGSU scaffolds, are highly flexible in dry and hydrated conditions; no yielding was observed in the testing curves before failure occurred. At cleaned and dry state, all the PGSU scaffolds presented similar E_t and σ_{tmax} results in the ranges of 0.030-0.040 MPa and 0.016-0.022 MPa, respectively, while the PGSU-1:0.6 scaffold exhibited with significant difference a high $\varepsilon_{t\sigma max}$ of 82% compared to the other two scaffolds. The physical characteristics of the PGSU-1:0.6 scaffold such as a large pore size and high porosity [371], as well as the relatively high ductility of the solid PGSU promoted the overall good $\varepsilon_{t\sigma max}$ properties. At cleaned and hydrated state, all the PGSU scaffolds obtained also similar E_t and σ_{tmax} results. The hydrated PGSU-1:0.6 scaffold exhibited a low E_t of 0.029 MPa and the highest $\varepsilon_{t\sigma max}$ of 57%, representing a significant difference to the PGSU-1:0.5 scaffold. The comparison of the

tensile properties between dry and hydrated counterparts demonstrated no difference between the PGSU-1:0.4 and PGSU-1:0.5 scaffolds, however, the hydrated PGSU-1:0.6 scaffold exhibited decreased σ_{tmax} and $\varepsilon_{t\sigma max}$ results of 13.6% and 30%, respectively. The results indicate that the mechanical properties of the PGSU scaffolds can be affected under hydrated conditions, due to the water molecules absorbed into the polymer matrix which affected the hydrogen-bonding interactions between urethane and ester linkages within the network [364–366]. Compared to the PGS/PLLA-D and PGS/PLLA-DMC scaffolds of Chapter 4, these PGSU scaffolds presented under dry and hydrated state similarly low E_t results, but have in average a ~2-3 times higher σ_{tmax} and a ~2-3 times higher $\varepsilon_{t\sigma max}$ (see Section 4.3.3).

Figure 5.8 (A, B) shows representative compressive stress-strain curves of dry and hydrated PGSU scaffolds. The compressive Young's modulus, E_c, and the compressive stress at 75% strain, $\sigma_{c75\%}$, were measured, as listed in Table 5.4. All the PGSU scaffolds withstood the high compression and presented full shape recovery after the release of load, both in dry and hydrated state, as demonstrated in Figure 5.9 (A, B). In addition, all the PGSU scaffolds were characterised with only a linear elastic and a densification regime, with no presence of a collapse plateau, indicating no structure collapse or fracture [358]. At cleaned and dry state, the PGSU-1:0.6 and PGSU-1:0.5 scaffolds showed similar E_c and $\sigma_{c75\%}$ results in the range of 0.003-0.004 MPa and 0.013-0.029 MPa, while the PGSU-1:0.4 scaffold featured significantly higher E_c and $\sigma_{c75\%}$ values of 0.020 MPa and 0.075 MPa, respectively. In this respect, the relatively dense microstructure of the PGSU-1:0.4 scaffold, characterised with small pore sizes and low porosity, resulted in stiffer scaffold constructs. At cleaned and hydrated state the PGSU scaffolds presented similar results as under dry conditions, in which the hydrated PGSU-1:0.6 scaffold obtained the lowest E_c and $\sigma_{c75\%}$ of 0.003 MPa and 0.013 MPa, respectively. The comparison of the compressive properties between dry and hydrated counterparts demonstrated no difference in E_c, however, the hydrated PGSU-1:0.4

and PGSU-1:0.6 scaffolds exhibited a decrease in $\sigma_{c75\%}$ of 43% and 59%, respectively. The results indicated the tendency that the E_c and $\sigma_{c75\%}$ values of the PGSU scaffolds were inversely related to their porosities and pore sizes. In comparison to the PGS/PLLA-D and PGS/PLLA-DMC scaffolds of Chapter 4, the PGSU scaffolds presented under dry and hydrated state similar low E_c results (see Section 4.3.3).

Cyclic tensile and compressive stress-strain curves of dry and hydrated PGSU scaffolds presented relatively minimal hysteresis loop during loading, as seen in Figure 5.10 (A, B) and Figure 5.11 (A, B). Under cyclic tensile testing, the dry PGSU-1:0.4, PGSU-1:0.5 and PGSU-1:0.6 scaffolds were characterised with a h_r of 0.17, 0.12 and 0.07, while hydrated PGSU-1:0.4, PGSU-1:0.5 and PGSU-1:0.6 scaffolds were characterised with a negligiblely low h_r of 0.07, 0.08 and 0.04 after 20 cycles of tensile loading to 20% strain, respectively. With respect to cyclic compressive testing, the dry PGSU-1:0.4, PGSU-1:0.5 and PGSU-1:0.6 scaffolds were characterised with a h_r of 0.29, 0.36 and 0.17, while the hydrated PGSU-1:0.4, PGSU-1:0.5 and PGSU-1:0.6 scaffolds were characterised with a decreased h_r of 0.20, 0.14 and 0.19 after 20 cycles of compressive loading to 50% strain, respectively. It is assumed that the expelling of water during the performed cyclic compressive tests resulted into higher h_r results [372]. Nevertheless, all PGSU scaffolds were fully recoverable after cessation of the cyclic tensile and compression loadings under dry and hydrated state. The PGSU-1:0.6 scaffold presented overall best resilience characteristics, due to the low h_r values under dry and hydrated state. With this respect, the low hysteresis properties can be attributed to the higher crosslink density of the generally light crosslinked PGSU scaffolds, which improved the load transfer efficiency of the polymer networks.

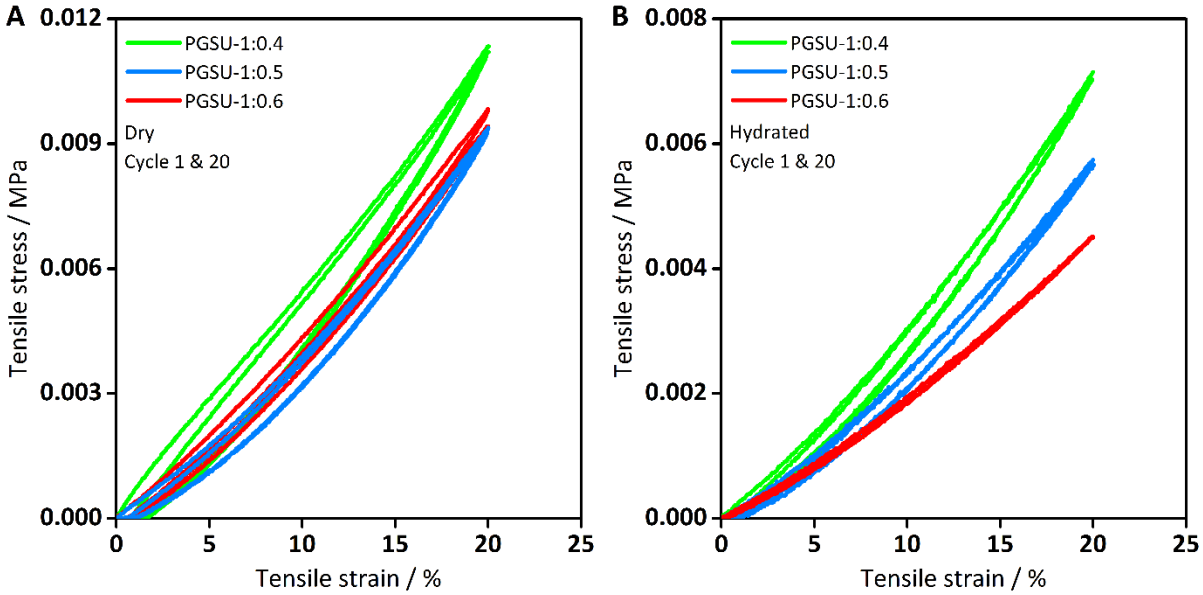

Figure 5.10: Representative cyclic tensile tress-strain curves of (A) dry and (B) hydrated PGSU scaffolds.

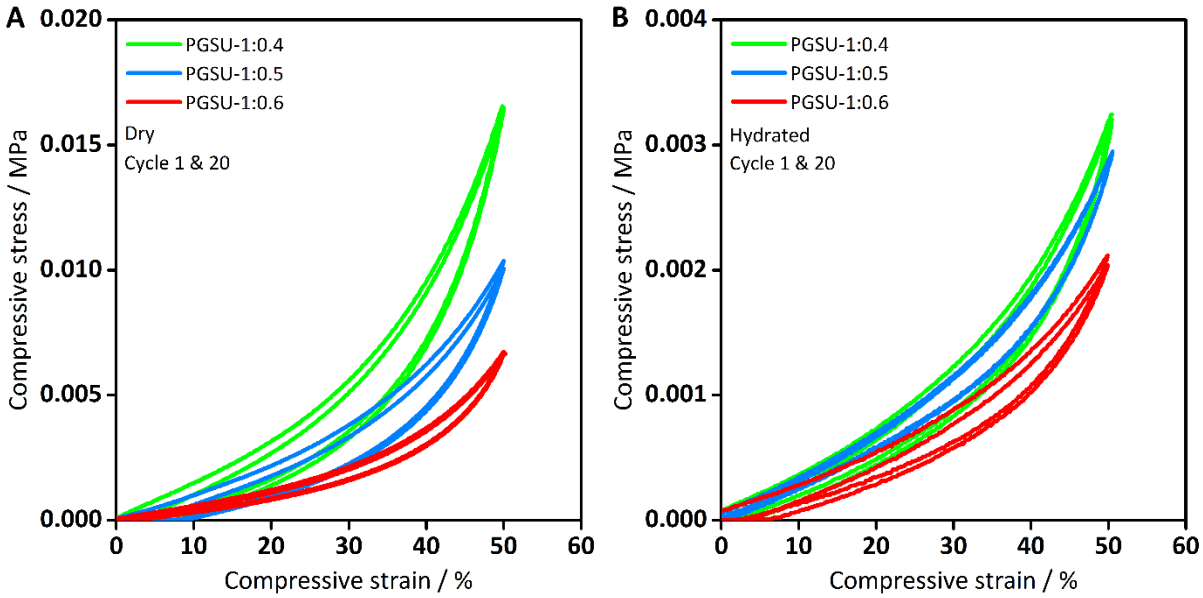

Figure 5.11: Representative cyclic compressive stress-strain curves of (A) dry and (B) hydrated PGSU scaffolds.

Rheological measurements were performed on hydrated PGSU scaffolds to assess their potential performance in dynamic and wet conditions similar to physiological environments. The storage modulus, G', and loss modulus, G'', as a function of the oscillatory frequency are

shown in Figure 5.12 (A, B). Briefly, the G' values of the PGSU scaffolds dominated the whole range of frequency and were one to two orders of magnitude higher than corresponding G'' values, suggesting that the bulk response of the hydrated PGSU scaffolds to an applied deformation is mainly elastic, while the G' and G'' values increased slightly with increasing frequency. The PGSU-1:0.4 scaffolds presented overall the highest G' and G'' values, due to the highest scaffold density, lowest porosity and lowest water absorption ability, in comparison to the PGSU-1:0.5 and PGSU-1:0.6 scaffolds which presented similar results.

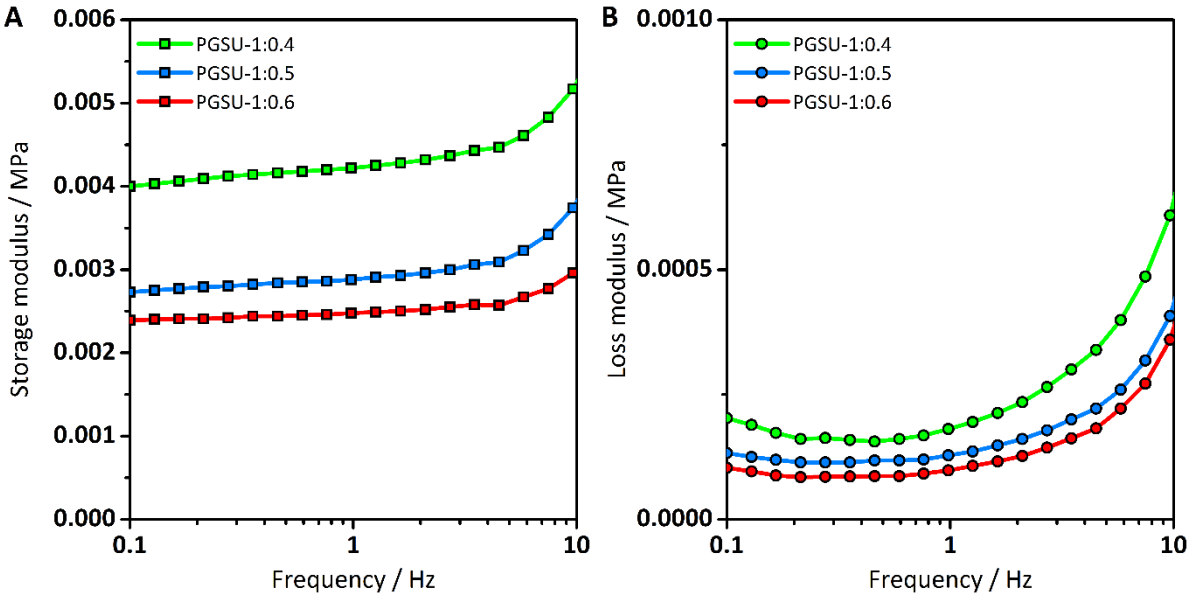

Figure 5.12: Frequency sweep data for hydrated PGSU scaffolds. The (A) storage modulus and (B) loss modulus were measured as a function of frequency under oscillatory shear at a strain of 0.1%, in the frequency range of 0.1-10 Hz at 25 °C.

Overall, the PGSU scaffolds reported here show excellent mechanical characteristics under quasi-static and cyclic tensile and compressive loads with structurally stable and stretchable properties, suitable to engineer scaffolds for a range of soft tissues, such as human cardiac muscles (Young's modulus: 0.01-0.30 MPa) [258] or high stress adapted adipose tissue (Young's modulus: 0.02-0.18 MPa) [76]. As illustrated in Figure 5.13, at the same relative density, the PGSU scaffolds show a much lower compressive modulus than other porous

scaffolds based on traditional synthetic polyesters, such as PLLA, PDLLA, PLGA and PCL. Scaffolds based on these common types of synthetic polyesters are more prone to plastic deformations under external loads, feature stiffer bulk properties and lack of flexibility and strechability. Hence, the elastomeric PGSU scaffolds mimic the bulk mechanical properties of soft tissues more closely. The high flexibility and stretchability of the scaffold constructs indicate that the PGSUs have high potential in soft tissue engineering applications for dynamic environments.

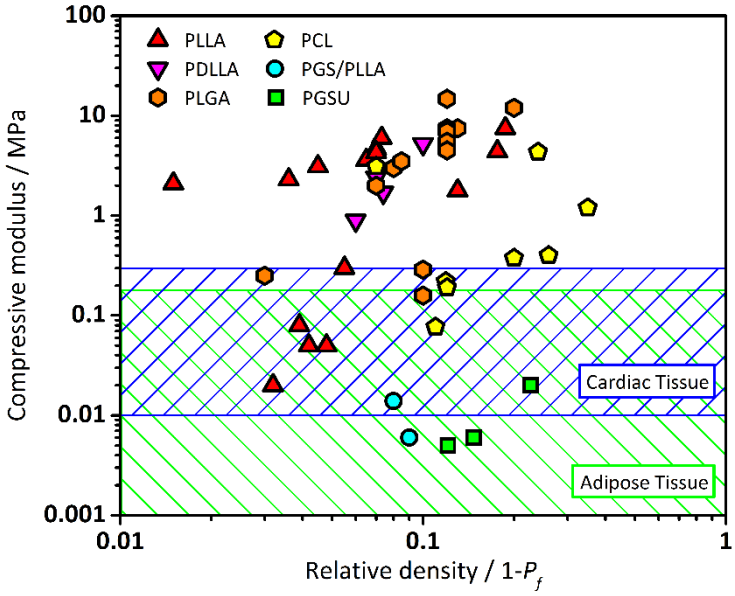

Figure 5.13: Compressive modulus of porous scaffolds as a function of relative density. Comparison of literature values of different polymer scaffolds based on traditional polyesters for tissue engineering [373–391] (Table 5.S1, Appendix C), in addition to the results from Chapter 4 (PLLA-D, PGS/PLLA-D and PGS/PLLA-DMC scaffolds) and 5 (PGSU-1:0.4, PGSU-1:0.5 and PGSU-1:0.6 scaffolds).

5.3.4 *In vitro* degradation

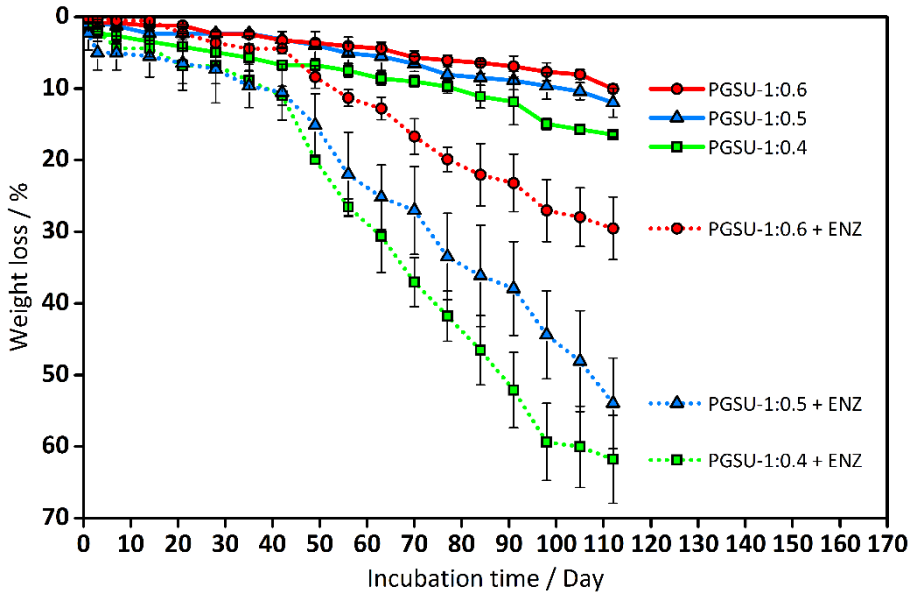

Figure 5.14: Percentage of mass loss of PGSU scaffolds, incubated with and without the presence of lipase enzyme in PBS for up to 112 days in a shaker incubator at 37 °C at 100 rpm.

The *in vitro* degradation performance of all PGSU scaffolds were analysed in enzyme-free and lipase enzyme-containing PBS solution for up to 112 days, as shown in Figure 5.14. In the enzyme-free PBS solution the PGSU-1:0.4, PGSU-1:0.5 and PGSU-1:0.6 scaffold specimens obtained degradation degrees of 16%, 12% and 10% in 112 days, while in the enzymatic PBS solution the PGSU specimens exhibited higher degradation degrees of 62%, 54% and 30% in the same time period, respectively. The PGSU scaffolds were characterised with relatively linear degradation kinetics and presented a gradual and visible loss in volume (Figure 5.S2-4, Appendix C), suggesting that the degradation mechanism is based on the surface erosion like PGS [312]. However, the microstructure (e.g. pore sizes, porosities) of the PGSU scaffolds had no direct effect on the degradation kinetics, implying that the degradation kinetics are more dependent on the number of urethane groups (increased urethane content hindered the accessibility to ester bonds, resulting in slower degradation

rates) [312]. The enzymatically tested PGSU specimens displayed quicker degradation, indicating the catalysed hydrolysis of the ester bonds of the PGS segments due to the lipase enzyme [345]. SEM examination (after 34 days *in vitro* degradation) presented smooth strut surface morphologies for the PGSU scaffolds in enzyme-free PBS solution, while in enzyme-containing PBS solution the specimens showed stronger signs of surface degradation, characterised by rough features, as seen in Figure 5.15 and 5.16. The PGSU-1:0.6 scaffold specimens presented the slowest degradation, due to their higher degree of crosslinking and urethane groups, indicating that the degradation rate of PGSU can be tuned and depend on the molar ratio of glycerol to HDI, which is in alignment with previous studies [312,326].

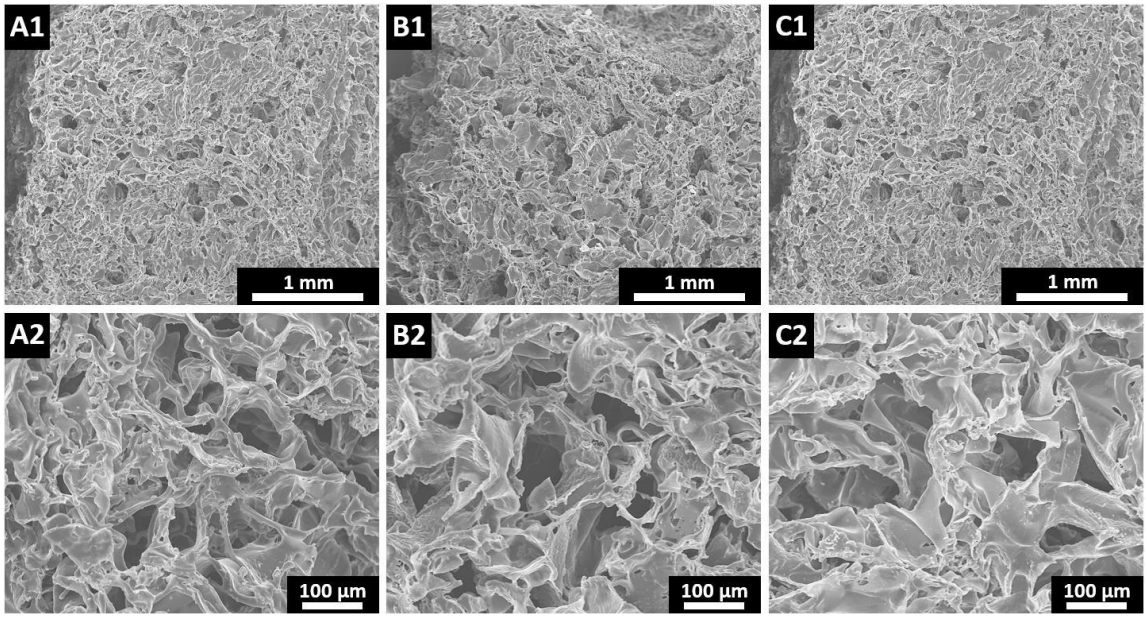

Figure 5.15: SEM micrographs of (A1-2) PGSU-1:0.4, (B1-2) PGSU-1:0.5 and (C1-2) PGSU-1:0.6 scaffold specimens after 34 days *in vitro* incubation at 37 ˚C in enzyme-free PBS solution (note that visual differences are minor).

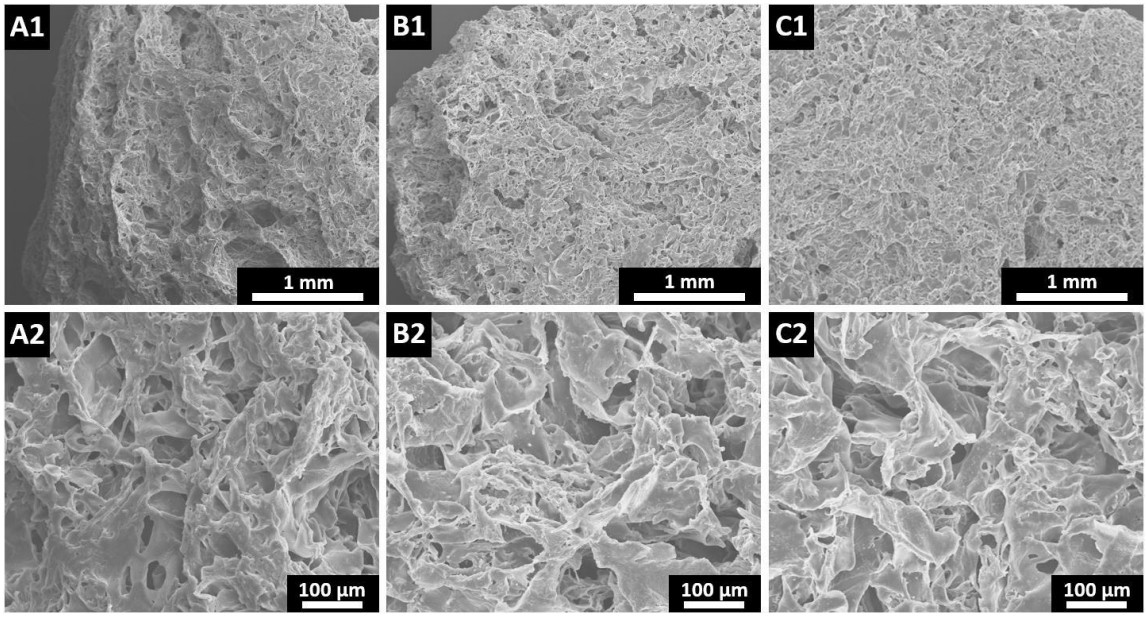

Figure 5.16: SEM micrographs of (A1-2) PGSU-1:0.4, (B1-2) PGSU-1:0.5 and (C1-2) PGSU-1:0.6 scaffold specimens after 34 days *in vitro* incubation at 37 ˚C in enzyme-containing PBS solution (note that visual differences are minor).

The *in vitro* degradation tests of the PGSU scaffolds illustrate high potential for designing tissue engineered constructs with long-term stability and tuneable degradation kinetics. Previous *in vitro* degradation studies with large and porous PGS/PLLA scaffolds from Chapter 4, containing 73 vol% PGS and characterised with porosities and pore sizes in the range of 91-92% and 109-141 µm, presented mass losses of 11-16% and 54-55% without and with the presence of lipase enzyme in 31 days, respectively. In addition, *in vivo* studies of channelled PGS scaffolds with porosities and pore sizes in the range ~95% and ~100 µm presented mass losses of up to 80% during the implantation period of 35 days [287]. In comparison, under the same *in vitro* degradation test conditions and period the PGSU scaffolds presented mass losses of 2-6% and 5-10% in the enzyme-free and enzyme-containing PBS solution, respectively, demonstrating significantly reduced degradation rates due to the urethane groups in the chemical structure [312]. Previously performed *in vivo* studies with PGSU film specimens also demonstrated long-term shape maintenance and slow

degradations rates, in which sample fragmentation was first discovered after 280 days implantation [312].

The freeze-dried PGSU scaffolds in this work presented slow degradation kinetics, microstructures with high porosities and interconnected large pores, relative good hydrophilic characteristics, as well as soft and highly stretchable mechanical properties, demonstrating great potential for soft tissue engineering applications. Compared to other fabrication strategies, the freeze-drying fabrication method is less complex and enables the production of large and porous 3D scaffold constructs with interconnected pores in a wide range of dimensions and directions, capable to fit specific cell types and tissue engineering applications [258,343,356,367,392]. With this respect, PGSU presented in previous studies good *in vitro* cytocompatibility with human mesenchymal stem cells, in which the cell proliferation and metabolic performance were equivalent compared to standard tissue culture polystyrene [312]. PGSU also presented similar *in vivo* inflammatory responses compared to PLGA material, which were characterised by mixed lymphohistiocytic infiltrates, however, no adverse reactions or complications were noted during the implantation period [312]. Due to the tunability of PGSU, scaffolds with a broad range of mechanical properties are producible to match those of the native host soft tissues. Soft tissues, e.g. fat, cardiac muscle and blood vessels, are physiologically exposed to large deformations, and exist in a mechanically dynamic environment where the loads can vary spatially and temporally [82,393,394]. For instance, in the sitting posture, physiological loads induced peak tensile, compressive and shear strains of ~30%, ~45% and ~40% on the anatomical site related fat tissues, as well as tensile, compressive and shear strains of ~75%, ~75% and 91% on the anatomical site related muscle tissues, respectively [70,71]. Traditional synthetic biodegradable polyesters, such as PLA, PGA and their copolymers, although commonly used in tissue engineering, are not stretchable, subjected to plastic deformation, prone to failure

under cyclic deformations, and ultimately causing a mismatch in compliance [258,365,395]. Thus, the mechanical properties of engineered scaffold constructs are critical for successful surgical implantation [82,365,396]. Ideal engineered soft tissue scaffold should not only be structurally stable to withstand *in vivo* mechanical stresses and deformations, but also feature certain flexibility and stretchability which can provide mechanical stimulation, while providing support to the ingrowing tissue [365,394]. Future work should examine the *in vitro* and *in vivo* tissue growth behaviour of cell-seeded scaffolds, as well as analysing the cell behaviour under mechanical stimulation.

5.4 Conclusions

Flexible and large 3D porous PGSU scaffolds with different molar ratios of HDI were produced via a freeze-drying process. Results proved that the solvent-based PGSU synthesis with a subsequent freeze-drying process can create stable and highly interconnected open-pore scaffold constructs with no structure collapse. PGSU scaffolds were characterised with non-uniform shapes and smooth pore-wall surfaces, and featured high porosities and pore sizes in the range of 77-88% and 55-74 μm, respectively. The PGSU scaffolds exhibited relatively good hydrophilic characteristics, as well as high water absorption abilities. Hydrated PGSU scaffolds obtained a Young's modulus, ultimate tensile strength and elongation at break in the range of 0.029-0.032 MPa, 0.012-0.019 MPa and 52-57%, respectively, and showed no fracture and full recoverability after 75% strain compression. In addition, hydrated PGSU scaffolds presented overall minor hysteresis loss ratio at high strain after performed cycle tensile and compression tests. Rheometer measurements indicated furthermore a primarily elastic bulk response at low strain. PGSU scaffolds were characterised with linear degradation kinetics and obtained *in vitro* degradation rates of 10-16% and 30-62% in 112 days in enzyme-free and enzyme-containing PBS solution,

respectively. Overall, the freeze-dried PGSU scaffolds have great potential to be further developed for ATE, as well as for other soft tissue engineering applications.

Chapter 6. Stretchable, biodegradable and biocompatible poly(glycerol sebacate)-based polyurethane hydrogels with thermoresponsive properties

6.1 Introduction

The large and highly porous PGSU scaffolds developed in Chapter 5 featured improved physicochemical properties over the PGS/PLLA scaffolds of Chapter 3 and 4, while also offering similar mechanical bulk properties to those of native adipose tissue, illustrating great potential to be developed further for ATE applications and other soft tissue substitutes. The PGSU scaffolds with a high ratio of HDI, however, exhibited slow degradation rates and decreased hydrophilic characteristics. Ideally, the engineered scaffolds should degrade at the same rate as cells proliferate and secret their own ECM into the scaffold constructs [2]. Also, despite the highly interesting properties, PGS and PGSU material presented limited water absorption and diffusion capabilities [16,310,312], which is in need of improvement to guarantee the effective transport of oxygen and nutrients within the deeper compartments of large-volume engineered tissue scaffolds, especially in the absence of a functional vascular system [397,398].

The main purpose of this chapter is the development of PGS-based hydrogels with enhanced and tailorable hydrophilic properties, as well as mechanical and degradation characteristics. Novel polyester-based polyurethane (PEU) hydrogels were synthesised from pre-PGS and PEGs of different molecular weights, both containing hydroxyl groups, with aliphatic HDI. Hydrogels have attractive characteristics, owing to their high water content and 3D network structure, which closely mimic the natural extracellular matrices of soft tissues [214]. It was hypothesised that the synthesis of the PEU using

(I) biodegradable pre-PGS as the main macromolecular crosslinker, (II) hydrophilic PEG as the main polyol component, and (III) hydrophobic HDI as the diisocyanate component, could theoretically create a chemically crosslinked hydrogel with the combined advantages of PGS, PEG and PU. The chemical and physical characteristics of the PEU hydrogels should potentially be tailorable by varying the molecular weight of PEG.

Stretchable, biodegradable and biocompatible PEU hydrogels, based on pre-PGS and PEGs of different molecular weights were synthesised by a solvent-based two-step method. HDI was selected due to its extensive use in synthesizing biocompatible PUs [312,399]. The structure and properties of these materials were investigated, and their potential applications for tissue engineering evaluated. The structures of the PEUs were characterised by spectroscopic and calorimetric measurements. The mechanical properties were analysed via quasi-static and cyclic tensile and compression tests, and the hydration kinetics studied. *In vitro* degradation tests were carried out in media with and without lipase, and the cell proliferation response was examined *in vitro* with human ADSCs and dermal fibroblasts (FIBs). The potential of fabricating the PEU material into different forms such as microspheres and large 3D porous scaffolds was also investigated and demonstrated. In addition, the synthesised PEU hydrogels also presented negative thermoresponsive properties, thus, the swelling behaviour under various medium temperatures were analysed, and drug delivery and temperature-induced actuation tests were performed.

6.2 Experimental section

6.2.1 Materials

The materials for this chapter are those used in Chapters 3, 4 and 5, with the addition of: PEG (with the number average molecular weight, $\bar{M}_n$, of 400 g mol^{-1} (PEG-400), 950-1050 g mol^{-1} (PEG-1000) and 1305-1595 g mol^{-1} (PEG-1450)), hexane, mineral oil, Span 80, n-heptane,

lidocaine, formaldehyde, phalloidin-fluorescein isothiocyanate (phalloidin-FITC) and resazurin were purchased from Sigma-Aldrich. Glutamine and amphotericin B were purchased from Gibco. Difco-trypsin plus was obtained from Difco Laboratories.

6.2.2 Preparation of pre-PGS

Pre-PGS was synthesised as described in Chapter 3.

6.2.3 Solvent-based Synthesis of PEUs

PEUs were synthesised by using a solvent-based two-step approach with a fixed molar ratio (glycerol : isocyanate (NCO)-terminated PEG = 1 : 0.3). Briefly, the first step involved the reaction of PEG (1 mmol; PEG-400, PEG-1000 or PEG-1450) and HDI (2 mmol) in 1,4-dioxane (20 mL) with Tin (II) (0.05% w/v) as the catalyst for 1 h at 85 °C. In the second step the NCO-terminated PEG/1,4-dioxane solution was cooled down to 55 °C, to which a pre-PGS solution (3.4 mmol pre-PGS in 20 mL 1,4-dioxane with 0.05% w/v Tin (II)) was added and reacted for 5 h. At each step the reaction flasks were purged with nitrogen and sealed. The reacted solution was poured onto a non-sticky mould and the solvent was allowed to evaporate for 2 days at room temperature and another 2 days in a vacuum oven at 40 °C, which also allowed for further crosslinking. All the specimens were subjected to a cleaning procedure (24 h ethanol saturation and drying in a vacuum oven at 37 °C) prior to tests, to remove unreacted pre-polymer and monomers. The nomenclature of the synthesised NCO-terminated PEG is presented as Pre-X, where "X" represents $\overline{M}_n$ of the utilised PEG: Pre-400, Pre-1000 and Pre-1450. In addition, the nomenclature of the synthesised PEU hydrogels is presented as PEU-X, where "X" represents $\overline{M}_n$ of the utilised PEG: PEU-400, PEU-1000 and PEU-1450.

6.2.4 Characterisation of pre-PGS

The $\bar{M}_n$, the weight average molecular weight, $\bar{M}_w$, and the PDI of pre-PGS were measured by GPC as described in Chapter 4. FTIR characterisation on pre-PGS were performed as described in Chapter 3.

6.2.5 Characterisation and testing of PEUs

Proton nuclear magnetic resonance spectroscopy (^{1}H NMR) was performed on a Bruker Avance III HD 500, and samples were recorded at 25 °C at 500 MHz, using deuterated chloroform ($CDCl_3$) as the solvent. PEUs were soaked overnight in $CDCl_3$ and the acquired ^{1}H NMR data were analysed using ACDLABS/1D NMR software. FTIR characterisation on PEU films were performed as described in Chapter 3. Raman spectroscopy was executed on a Renishaw inVia Raman spectroscope using a 514.5 nm wavelength laser. Spectra were recorded between 500-3500 cm^{-1} with a laser power of 2 mW and a spectra resolution of 0.5 cm^{-1}.

Differential Scanning Calorimetry (DSC) was carried out on a Perkin Elmer Diamond DSC, and temperature scans from -60 °C to 120 °C at 10 °C min^{-1} under a nitrogen flow rate of 20 ml min^{-1} were performed during two consecutive heating cycles. The heat capacity change in the second heating cycle was used for analysis.

The solubility of PEU film specimens was evaluated by immersing the specimens in a solvent, 1,4-dioxane, dimethylformamide, DMC, toluene, chloroform, acetone or ethanol, for 24 h at room temperature. The sol contents of non-cleaned PEU film specimens (n = 5) were calculated by determining the weight difference after 24 h ethanol saturation at room temperature.

Quasi-static tensile and compression tests were performed on dry and hydrated PEU film specimens (hydrated PEU specimens had been immersed in PBS solution for 24 h at 37 °C

and were immediately removed from the solution for the tests), while cyclic tensile and compression tests were conducted on hydrated PEUs. Briefly, quasi-static tensile tests (ASTM D412) were carried-out on a Hounsfield H100KS testing machine with a 10 N load cell, at a tensile strain rate of 50 mm min^{-1} till fracture with punched-out "dog bone" shaped specimens (n = 8; width: 2.6 mm, gauge length: 20 mm, thickness: 0.42-1.29 mm). Cyclic tensile tests (n = 3; width: 2.6 mm, gauge length: 20 mm, thickness: 0.82-1.65 mm) were performed under the same testing set-up at a tensile strain rate of 50 mm min^{-1} and stretched to 50% strain during 20 cycles. Quasi-static compression tests were executed on punched-out cylindrical specimens (n = 7; diameter: 6 mm; thickness: 1.10-3.72 mm) with a 1 kN load cell up to a strain of 75% and a strain rate of 1 mm min^{-1}. Cyclic compression tests (n = 3; diameter: 6 mm; thickness: 1.09-3.57 mm) were performed under the same testing set-up at a strain rate of 1 mm min^{-1} and compressed to 50% strain during 20 cycles. All the tests were performed at room temperature.

The effective crosslink density, n_{eff}, of the PEU hydrogels was calculated from compressive testing results (based on 24 h saturation in PBS at 37 °C) by Equation 6.1 [400,401],

$$\sigma_c = n_{eff} RT \phi_2^{1/3} \phi_0^{2/3} (\alpha - \alpha^{-2}) \tag{6.1}$$

where σ_c is the applied force per unit area of swollen hydrogel during compression, ϕ_2 is the polymer volume ratio in the swollen state, ϕ_0 is the polymer volume ratio in the gel in the relaxed state, and α is the deformation ratio ($\alpha = L/L_0 \geq 0.95$) under compression. The ϕ_2 and the ϕ_0 were calculated by Equation 6.2 and 6.3 [400,401],

$$\phi_0 = \frac{v_{dry}}{v_{relaxed}} \tag{6.2}$$

$$\phi_2 = \frac{\upsilon_{dry}}{\upsilon_{swollen}} \tag{6.3}$$

where υ_{dry}, $\upsilon_{relaxed}$ and $\upsilon_{swollen}$ are the PEU polymer volume fractions in dry, relaxed and swollen state, respectively. The polymer volume fractions of relaxed, swollen and dried PEU polymers (n = 5) were calculated by Equation 6.4 [400,401],

$$\upsilon_x = \frac{W_{air} - W_{heptane}}{\rho_{heptane}} \tag{6.4}$$

where the subscript x refers to the dry, or relaxed or swollen state, respectively. W_{air} is the weight of the corresponding PEU polymer in air at dry, relaxed (after the crosslinking process) or swollen (after 24 h saturation in PBS solution at 37 °C) state, $W_{heptane}$ is the weight of the corresponding PEU polymer in n-heptane at dry, relaxed or swollen state, and $\rho_{heptane}$ is the density of n-heptane (0.7 g ml^{-1}).

Hydration kinetics and swelling behaviour of dried PEU film specimens (n = 5) were analysed at various medium temperatures for up to 48 h. Dry specimens of initial known weight were immersed in PBS solution at constant 5 °C, 21 °C or 37 °C. At specific time intervals, swollen specimens were taken out of the medium, with excessive surface water removed and their swollen weight determined, and the tests was continued until the specimens reached the stage of equilibrium. The weight swelling ratio was determined by the difference between the weights of the swollen sample and the initial dry sample divided by the weight of the initial sample. The reversible swelling/deswelling behaviour of dried PEU film specimens (n = 5) was analysed in PBS solution at alternating temperatures of 5 °C and 50 °C, at an interval of 40 min for up to 4 h.

6.2.6 *In vitro* degradation tests

In vitro degradation tests in enzyme-free and enzyme-containing PBS solution were performed on PEU films (n = 3; thickness: 0.57 ± 0.10 mm; width: 2.5 ± 0.03 mm; length: 4.8 ± 0.02 mm) for up to 31 days, as described in Chapter 3. SEM analysis was performed after 31 days *in vitro* degradation on a Camscan S2 at 5 kV on gold coated PEU film specimens.

6.2.7 Drug encapsulation and release tests of PEUs

For the drug encapsulation, dry punched-out PEU film specimens (n = 5; diameter: 6 mm; thickness: 0.74 ± 0.18 mm) were soaked in a lidocaine solution (0.01 g mL^{-1} PBS, 10 mL) for 48 h at 5 °C. The swollen specimens were removed and dried in a vacuum oven for 24 h at 37 °C. The lidocaine-loaded samples were then immersed in PBS (10 mL) in a shaker incubator (100 rpm) at 37 °C. At several time intervals, 1 mL was removed and replaced by the same volume of fresh PBS. The cumulative drug release rate was calculated by evaluating the characteristic absorbance peak of lidocaine at 263 nm against a calibration curve of lidocaine-containing PBS solutions at known concentrations, determined via a Perkin Elmer Lambda 900 UV-Visible light spectrometer.

6.2.8 *In vitro* cell culture experiments

Skin and associated fat were obtained with informed consent from patients undergoing elective surgery for breast reductions or abdominoplasties, from tissue not required for their treatment donated for research. All donated tissues were handled on an anonymous basis, under a Human Tissue Authority research tissue bank license: 08/H1308/39. Human subcutaneous fat from discarded skin was selected as the ADSC source. Mechanical and enzymatic (collagenase type A) digestion was followed by several washes, and the SVF was cultured in DMEM (supplemented with 10% FCS, 100 IU ml^{-1} penicillin-streptomycin, 100

µg ml^{-1} glutamine and 0.625 µg ml^{-1} amphotericin B). The human ADSCs were subcultured to passage 4 for use in the experiments. Human skin biopsies were treated enzymatically (Difco-trypsin plus) to separate the dermis. FIBs were obtained after collagenase treatment (collagenase type A) from finely minced dermis and cultured in supplemented DMEM. The human skin FIBs were subcultured to passage 9, as described previously [402].

Experiments were performed in triplicate. Briefly, PEU specimens (diameter: 15 mm) were placed in a 12-well plate and sterilised with 0.1% peracetic acid in PBS overnight. Then, specimens were washed 3 times with PBS (1 h each) and dried overnight in a sterile laminar flow culture hood under UV light. The sterilised and dried specimens were soaked in DMEM overnight in an incubator (37 ºC, 5% CO_2), and fixed with a metal ring (internal diameter: 10 mm) for cell seeding. After cell trypsinisation with Trypsin-EDTA, ADSCs (5 x 10^4 cells per sample) or FIBs (5 x 10^4 cells per sample) were seeded onto the PEU specimens with DMEM (cell-free specimens were included as controls in DMEM). After 2 h incubation (37 ºC, 5% CO_2), rings and DMEM were removed and a metabolic activity assay was performed (1 ml of resazurin (5 µg mL^{-1} in PBS) was added to each well and incubated for 60 min). The absorbance at 570 nm was measured in a colorimetric plate reader (Bio-TEK). Resazurin was then removed and samples returned to culture conditions with 2 mL of DMEM. This metabolic assay was repeated on days 3, 6 and 9 and images of the well plates were taken after each incubation. After the final incubation, all samples were washed in PBS and fixed with 3.7% formaldehyde in PBS for 15 min. After 3 PBS washes, the samples were incubated in 2 mL phalloidin-FITC (diluted 1:500 in PBS) for 30 min. After 3 further PBS washes, images (512x512 pixels) were obtained using a Zeiss LSM 510Meta inverted confocal microscope and WN-Achroplan 40x 0.75 NA objective, with a 12.8 µs pixel dwell time. FITC was excited using a 488 nm laser and emission detected between 500 and 550 nm.

6.2.9 Water temperature activated force generation measurements

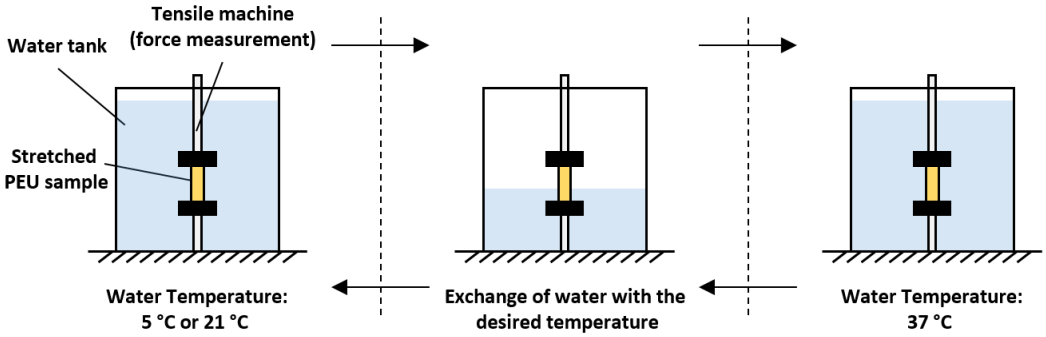

Scheme 6.1: Schematic illustration of the water-temperature activated force generation measurements.

Water temperature activated force generation was evaluated on PBS saturated (at 21 °C for 48 h) and stretched (constant strain = 40 %) PEU-1450 strip samples (n = 2; thickness: ~1.45 mm; width: 8 mm; gauge length: 20 mm), as illustrated in Scheme 6.1. During the testing period water temperature was alternated between 21 °C and 37 °C, or 5 °C and 37 °C, with an interval of 10 min for up to 70 min. This was accomplished by exchanging the same volume of water (of the desired temperature) rapidly. The force was measured with a 10 N load cell on a Hounsfield H100KS mechanical testing machine.

6.2.10 Water temperature responsive cantilever tests

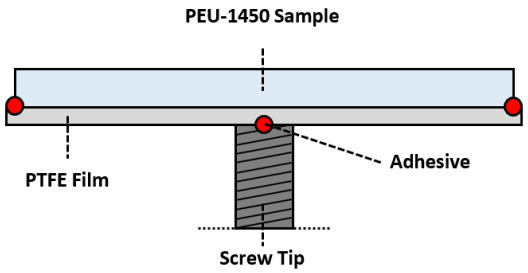

Scheme 6.2: Schematic illustration of the cantilever stripe test setup.

A two-layer cantilever was constructed from a pre-hydrated PEU-1450 (24 h PBS saturation at 21 °C; thickness: ~2.1 mm; width: 5 mm; gauge length: 50 mm) and a flexible poly(tetrafluoroethylene) (PTFE) film strip, as illustrated in Scheme 6.2. The two strips were connected to each other at both ends only using an adhesive. The PTFE side was further fixed with adhesive to the centre of a screw tip, allowing both strip ends to move freely. The test was performed according to the following steps. The cantilever was first placed in cold PBS (5 °C) for 15 min (low medium temperature = PEU hydrogel swelling). The test started by adding hot PBS (95 °C), until the medium exchange resulted in a stable high temperature of ~90 °C (high medium temperature = PEU hydrogel deswelling). After 3 min cold PBS (5 °C) was added until a low temperature of ~5 °C was reached. The test was completed within 6 min.

6.2.11 Proof-of-concept preparation of PEU microspheres

PEU microspheres were prepared by an oil-in-oil solvent evaporation method [403]. Briefly, the PEU/solvent mixture (40 mL of the final reacted solution, as described in Section 6.2.3) was dispersed in pre-heated mineral oil (100 mL at 55 °C) in the presence of Span 80 surfactant (2 mL) and stirred with an overhead stirrer at 400 rpm for 5 h, allowing further crosslinking and solvent evaporation. The microspheres were collected by filtration and washed five times with hexane to remove the mineral oil. Cleaned microspheres were kept in ethanol and stored at 5 °C in a fridge until further use. SEM analysis was performed on a Camscan S2 at 5 kV on dry and gold coated PEU microspheres. The sizes of the dry microspheres were evaluated by using ImageJ software (n = 170). Only fully defined microspheres were considered for geometrical measurements.

6.2.12 Proof-of-concept preparation of PEU scaffolds

PEU-1450 scaffolds were prepared via a freeze-drying procedure, based on the previous method in Chapter 5. Briefly, the PEU/solvent mixture (40 mL of the final reacted solution, as described in Section 6.2.3) was cast into a non-sticky Teflon-coated metal baking tray (cylindrical cavities; diameter: 60 mm; purchased from a local store) and placed in a Labconco FreeZone Triad freeze-dryer for lyophilisation. The solutions were cooled during the freezing stage to -30 °C and held at the temperature for 5 h, allowing the solutions to freeze completely. During the primary drying stage the solutions were heated to -5 °C (heating rate of 1 °C min^{-1}) and sublimated for 10 h under vacuum. In the secondary drying stage, the temperature was raised to 20 °C (heating rate of 5 °C min^{-1}) and kept for 5 h. SEM analysis was performed on a Camscan S2 at 5 kV on dry and gold coated PEU scaffolds. The pore sizes of the dry scaffold microstructures were calculated by using ImageJ software (n = 315). Only fully defined pores were considered for geometrical measurements.

6.2.13 Statistics

All measurements were reported as mean ± SD with a confidence level of 95%. Statistical analysis was performed as described in Chapter 3. Two-way analysis of variance (ANOVA) was performed in addition to determine the differences in metabolic activity (see Section 6.2.8) of the *in vitro* cultured ADSCs and FIBs in respect to test time and material.

6.3 Results and discussion

6.3.1 Synthesis and characterisation of PEUs

Chemically crosslinked PEU hydrogels were synthesised using a solvent-based two-step approach with a fixed molar ratio (glycerol : NCO-terminated PEG = 1 : 0.3), according to the synthetic rout illustrated in Scheme 6.3 and 6.4. The first step involved the synthesis of NCO-terminated PEGs, by reacting PEG ($\bar{M}_n$ = 400, 1000 or 1450) with HDI in 1,4-dioxane.

In the second step, pre-synthesised pre-PGS was dissolved in 1,4-dioxane and added to the NCO-terminated PEG solution to produce PEU through the crosslinking reaction between the hydroxyl groups of the pre-PGS units and the –NCO groups from the functionalised PEG. The pre-PGS in use had a $\bar{M}_n$, $\bar{M}_w$ and PDI of 1549 g mol^{-1}, 10522 g mol^{-1} and 6.8 respectively, as determined by GPC.

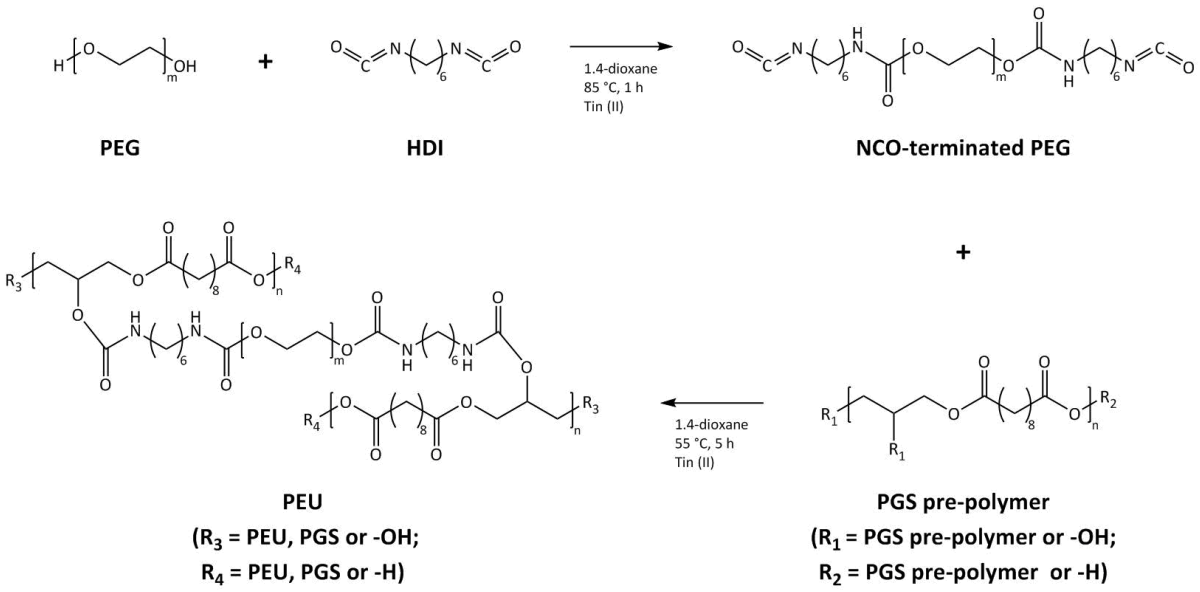

Scheme 6.3: Schematic representation of the synthetic rout of PEUs.

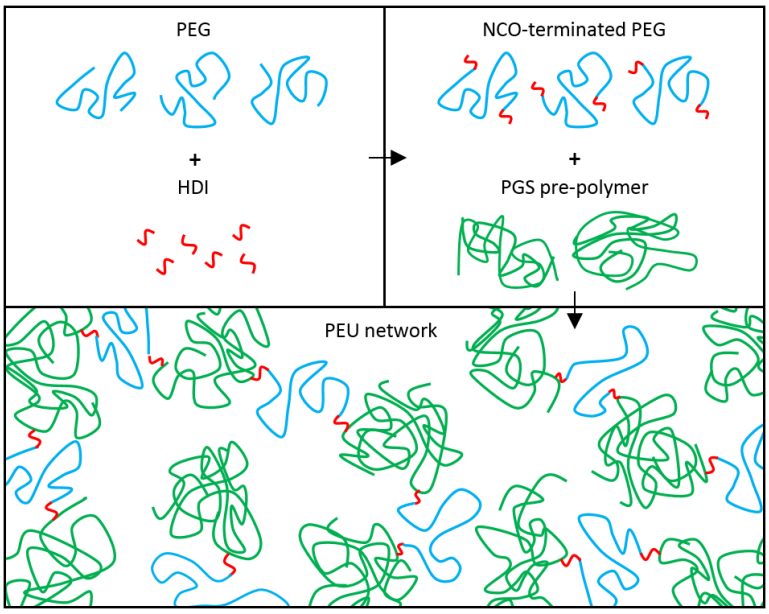

Scheme 6.4: Schematic representation of the formation of the PEU network.

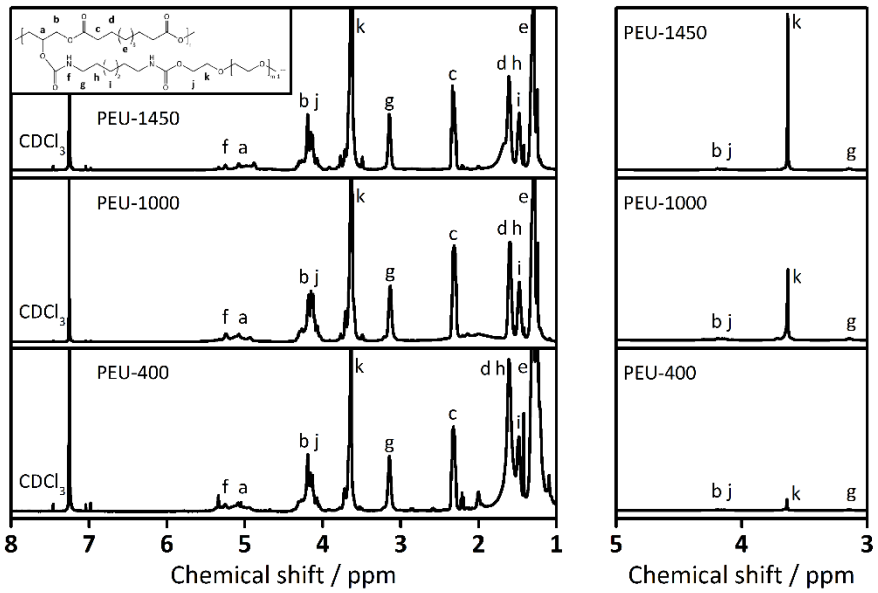

Figure 6.1: Normalised ^{1}H NMR spectra of PEU-400, PEU-1000 and PEU-1450. The figures on the right show the methylene proton related peak of PEG, "k", increases with its increasing molecular mass.

The molecular structure of the PEUs synthesised using three different molecular weights of PEG was confirmed by ^{1}H NMR spectroscopy, characterised with distinctive peaks of pre-PGS and PEGs, as well as urethane related peaks due to the reaction between pre-PGS and the NCO-terminated PEGs, as shown in Figure 6.1 and 6.2. Characteristic peaks of pre-PGS related methylene protons were assigned at 1.29, 1.61 and 2.32 ppm (position "c", "d" and "e") for sebacic acid, while peaks from 4.05-4.35 ppm and 4.92-5.24 ppm (position "b" and "a") were linked to the methylene protons of glycerol [253,302]. The methylene proton related peaks of PEG were assigned at 3.63 ppm (position "k") and 4.05-4.35 ppm (position "j", which overlaps position "b") [302]. The intensity of peak "k" increased with enhanced molecular weight of PEG, confirming the presence of a higher mass of PEG segments within the PEU. The peaks at 1.48 ppm, 1.61 ppm, 3.12 ppm and 5.34 ppm (position "i", "h", "g" and "f") were assigned to urethane and HDI related methylene protons, highlighting urethane bonds. Compared to the glycerol related peaks in the ^{1}H NMR spectra of pre-PGS, the ^{1}H NMR data of PEUs presented increased integral signals at 4.92-5.24 ppm (position "a"),

indicating that the urethane-bond formation between the NCO-terminated PEGs and the free hydroxyl groups of pre-PGS occurred preferentially with the hydroxyl groups of glycerol [253].

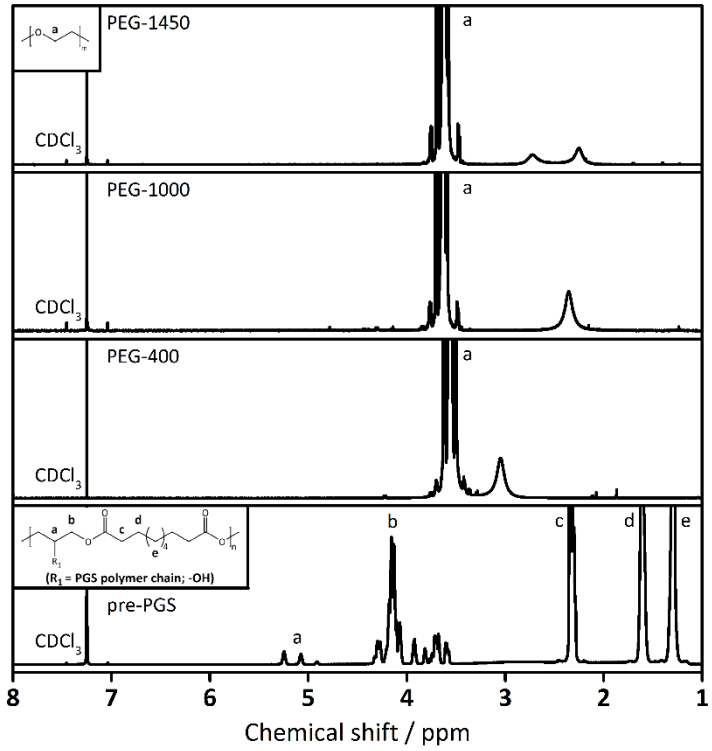

Figure 6.2: ^{1}H NMR spectra of PEG-1450, PEG-1000, PEG-400 and pre-PGS.

The analysis of FTIR spectra of PEUs, pre-PGS and PEGs supported the ^{1}H NMR results, as presented in Figure 6.3 and 6.4 (A, B). The spectra of PEUs showed the stretching vibrations of N-H at 3360 cm^{-1}, C=O at 1723 cm^{-1}, amide III at 1241 cm^{-1}, C-O at 1093 cm^{-1}, C-O-C at 948 cm^{-1}, and amide IV at 842 cm^{-1}, as well as the bending vibrations of amide II at 1532 cm^{-1}, confirming the formation of urethane linkages [16,404,405]. In contrast, FTIR spectra of NCO-terminated PEGs were characterised with the stretching vibration of HDI related –NCO end groups at 2270 cm^{-1}, the stretching and bending vibrations of urethane-bond linked C=O and amide II at 1723 cm^{-1} and 1537 cm^{-1}, and the stretching vibration of PEG associated C-O-C at 950 cm^{-1}, showing the unreacted residual –NCO groups at the chain ends and the urethane-bond formation between HDI and PEG [404,405]. The

absence of –NCO band at 2270 cm^{-1} in all the three spectra of the PEUs indicates the complete reaction of the –NCO end groups from the PEG with the hydroxyls of pre-PGS.

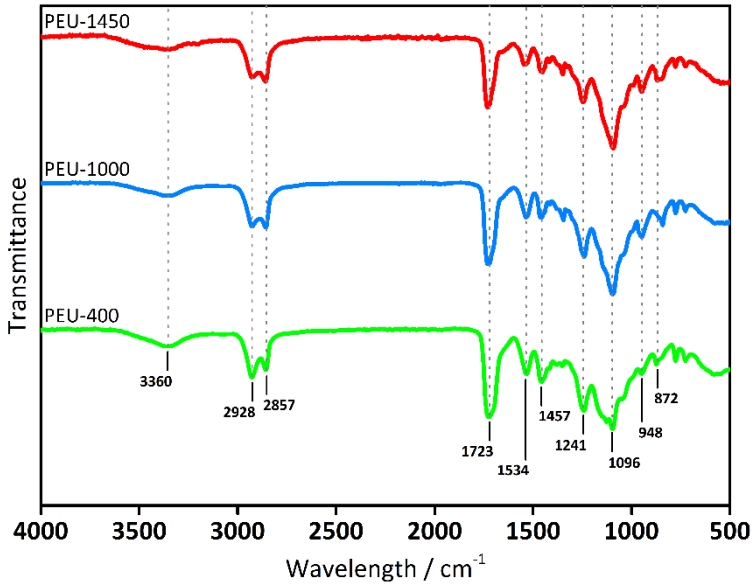

Figure 6.3: FTIR spectra of PEU-400, PEU-1000 and PEU-1450. The spectra were shifted vertically for clarity.

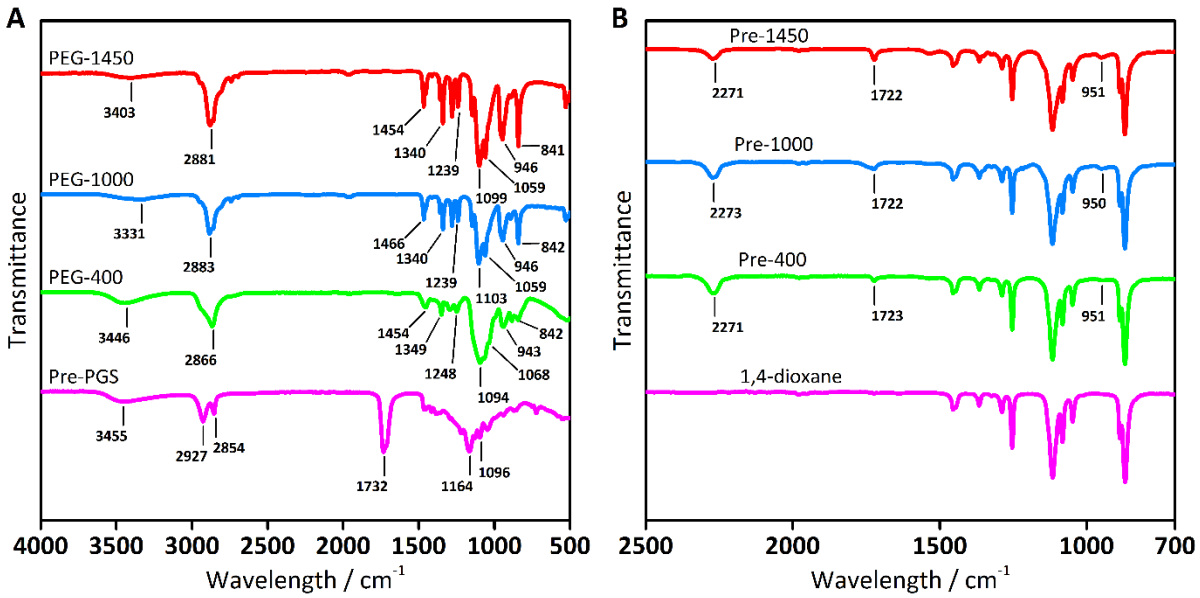

Figure 6.4: (A) FTIR spectra of pre-PGS, PEG-400, PEG-1000 and PEG-1450. (B) FTIR spectra of 1,4-dioxane, Pre-400, Pre-1000 and Pre-1450. The spectra were shifted vertically for clarity.

Raman spectra analysis of PEUs also affirmed the above ^{1}H NMR and FTIR results, as shown in Figure 6.5 (A, B). The spectra of PEUs showed the stretching vibrations of CH_2 in the range of 2700-3000 cm^{-1}, C=O at ~1731 cm^{-1}, the bending vibrations of CH_2 and CH_2-CH_2 in the range of 1200-1500 cm^{-1}, the stretching vibration of C-O at ~1140 cm^{-1} and the rocking vibration of CH_2 at 843 cm^{-1} [406–408]. Comparing the spectra of the PEUs with pre-PGS and PEGs showed a decrease of the pre-PGS related stretching vibration of C-O at 1102 cm^{-1}, as well as the disappearance of the PEG linked twisting vibration peaks of C-O-H at ~533 cm^{-1} and ~581 cm^{-1}, which are associated to the hydrogen bond reduction due to the formation of urethane bonds [406–408]. No peaks for unreacted -NCO urethane groups were detected in the spectra of PEUs, confirming the establishment of urethane linkage.

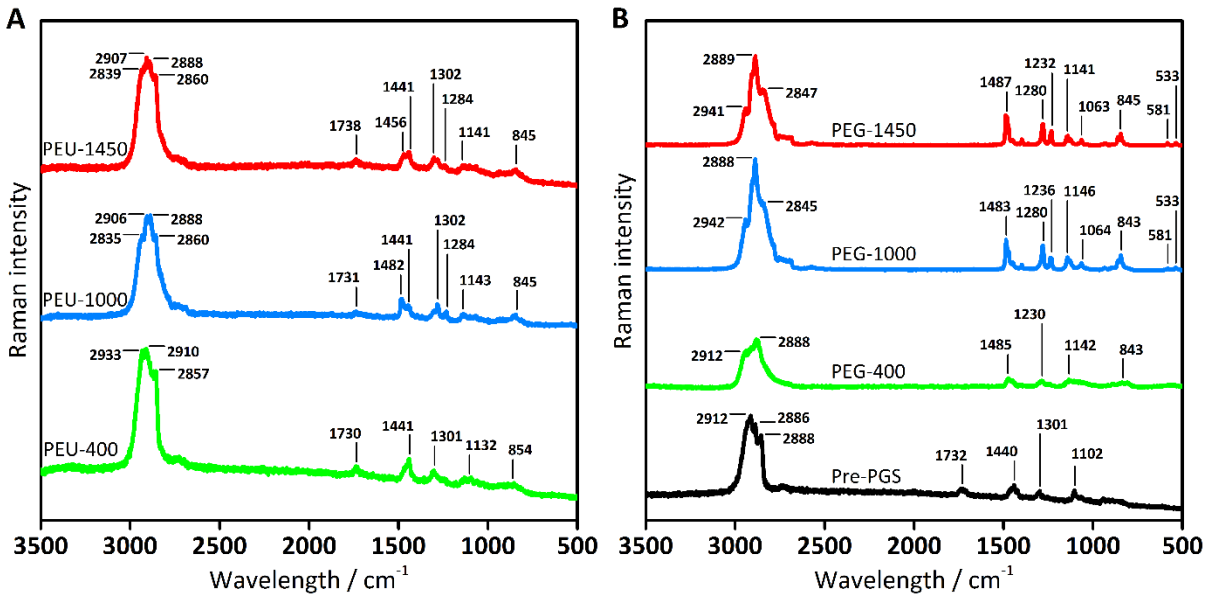

Figure 6.5: (A) Raman spectra of PEU-400, PEU-1000 and PEU-1450. (B) Raman spectra of pre-PGS, PEG-400, PEG-1000 and PEG-1450. The spectra were shifted vertically for clarity.

The thermal properties of the PEUs and their main individual components were analysed by DSC, as shown in Figure 6.6 (A, B). PEUs presented glass transition temperatures, T_g, below 0 °C, which decreased with the incorporation of longer PEG chains due to higher chain mobility (PEU-400: T_g = -27.7 °C; PEU-1000: T_g = -40.3 °C; PEU-1450: T_g = -45.2 °C). No

crystallisation temperature, T_c, or melting temperature, T_m, was detected for PEU-400 and PEU-1000 specimens within the test range, owing to the lower-molecular-weight PEG segments, which yield restricted chain mobility and no crystallisation in the PEU network [409]. However, T_c and T_m were observed in PEU-1450 specimens (T_c = -12.9 °C; T_m = 29.1 °C), owing to the presence of the semi-crystalline PEG-1450 in the network [404]. Pre-PGS presented three T_m peaks at -7.6 °C, 14.4 °C and 33.4 °C, which is typical for pre-PGS in its partially crosslinked state and related to its large PDI values, which depends on its synthesis procedure [16,252,410]. PEG-400 exhibits a low T_m of 2.1 °C, while PEG-1000 and PEG-1450 presented higher T_m values of 39.9 °C and 50.8 °C, respectively. The T_m observed for the PEU-1450 specimen was lower than that from neat PEG-1450, indicating that the chemically crosslinked network and the reduced chain mobility affected the crystallisation of the PEG-1450 segments [411]. Overall, the results reveal that the molecular weight of PEG affects the thermal transition of the PEU.

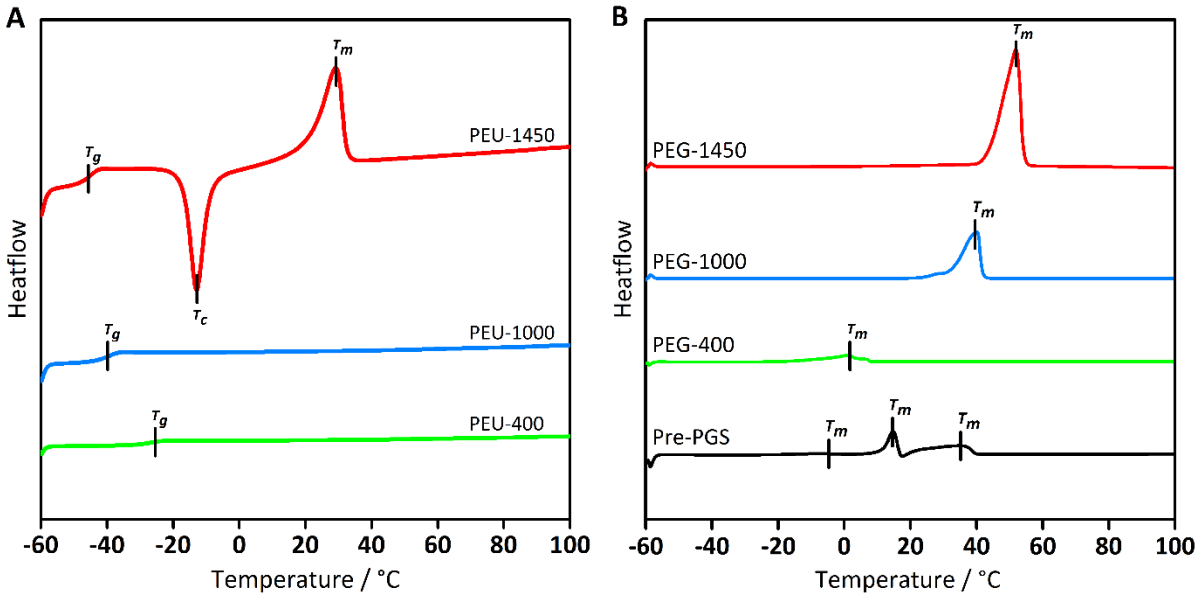

Figure 6.6: (A) DSC curves of PEU-400, PEU-1000 and PEU-1450. (B) DSC curves of pre-PGS, PEG-400, PEG-1000 and PEG-1450. The curves were shifted vertically for clarity.

All the PEUs were insoluble in various organic solvents (1,4-dioxane, dimethylformamide, diemethyl carbonate, toluene, chloroform, acetone and ethanol) and only showed strong swelling after immersion for 24 h, confirming the formation of a covalently crosslinked network. Residual analysis of PEU-400, PEU-1000 and PEU-1450 specimens gave weight losses of 23.6 ± 2.4%, 24.7 ± 0.5% and 24.5 ± 7.7% respectively, after 24 h ethanol extraction, indicating the existence of non-crosslinked components.

6.3.2 Mechanical properties of PEUs

Table 6.1: Tensile and compression properties of dry and hydrated PEUs.

		Tensile				Compression	
	Sample code	Young's modulus, E_s / MPa	UTS[a], σ_{smax} / MPa	Elongation at break, ε_{sb} / %	Energy at break, U_{sb} / MJ m^{-3}	Young's modulus, E_c / MPa	Comp.[b] stress at $\varepsilon_{c75\%}$, $\sigma_{c75\%}$ / MPa
Dry	PEU-400	0.72 ± 0.01	0.70 ± 0.02	438 ± 7	1.63 ± 0.07	1.86 ± 0.81	12.68 ± 1.01
	PEU-1000	0.71 ± 0.14	0.49 ± 0.04	400 ± 67	1.03 ± 0.17	0.80 ± 0.07	9.36 ± 2.55
	PEU-1450	13.11 ± 2.22	1.59 ± 0.25	505 ± 77	6.78 ± 0.93	17.91 ± 0.77	16.36 ± 2.86
Hydrated[c]	PEU-400	0.20 ± 0.11	0.47 ± 0.11	426 ± 44	1.09 ± 0.10	1.44 ± 0.22	10.39 ± 1.37
	PEU-1000	0.03 ± 0.01	0.05 ± 0.01	497 ± 153	0.19 ± 0.03	0.44 ± 0.17	4.60 ± 0.86
	PEU-1450	0.02 ± 0.01	0.07 ± 0.01	623 ± 193	0.23 ± 0.04	0.10 ± 0.02	0.67 ± 0.07

[a] Ultimate tensile strength; [b] Compressive; [c] 24 h saturation in PBS at 37 °C.

The mechanical properties of PEUs were determined under dry and hydrated states by quasi-static tensile and unconfined compression tests, while cyclic tensile and compressive testing were also performed for hydrated PEU hydrogels. Tensile and compression properties of dry and hydrated PEUs are listed in Table 6.1. The quasi-static mechanical properties of dry PEU-400 and PEU-1000 were similar under tensile load, while dry PEU-1450 shows significantly higher mechanical properties, with a tensile Young's modulus, E_s, ultimate tensile strength, σ_{smax}, strain at break, ε_{sb}, of 13.11 MPa, 1.59 MPa and 505%, respectively, as presented in in Figure 6.7 (A). Correspondingly, dry PEU-400 and PEU-1000 were

comparatively flexible, whereas the PEU-1450 specimens were more rigid. Moreover, dry PEUs demonstrated significant differences in the compressive Young's modulus, E_c, and in the compressive stress at 75% strain, $\sigma_{c75\%}$, with the dry PEU-1450 specimens again showing the highest stiffness, as seen in Figure 6.7 (B). This can be accounted for by the presence of the semi-crystalline PEG-1450 with the highest molecular weight in the PEU network, as previously confirmed by DSC results.

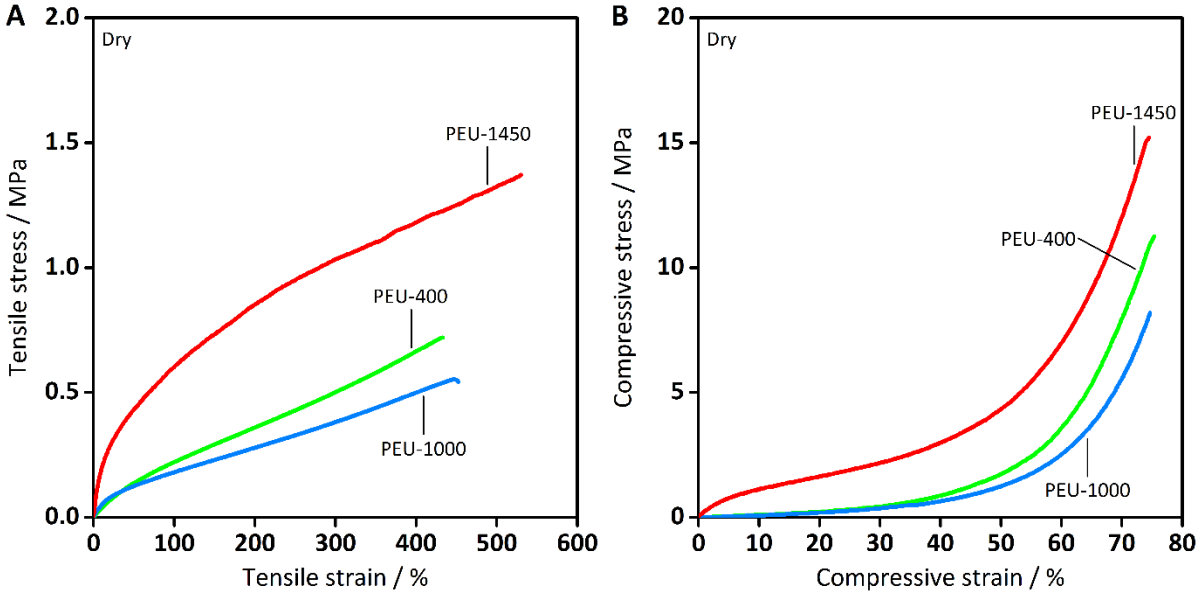

Figure 6.7 Representative quasi-static (A) tensile and (B) compression stress-strain (test terminated at a compressive strain of 75%) curves of dry PEUs.

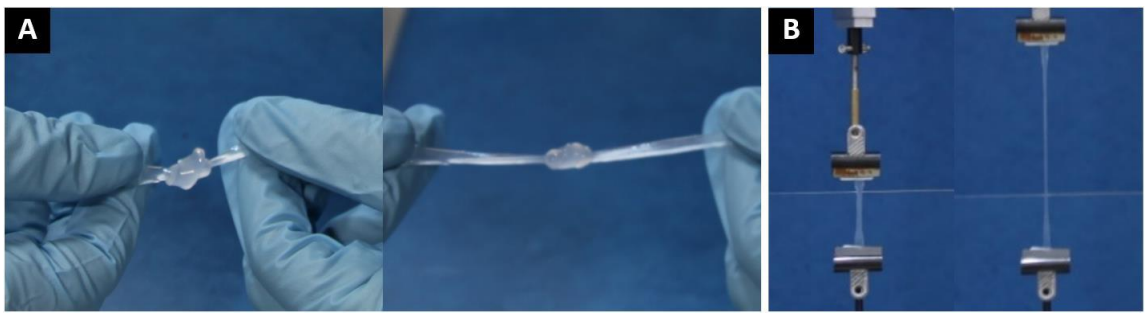

Figure 6.8: (A, B) Mechanical knotting and stretching reliability of PEU-1450 hydrogel specimens.

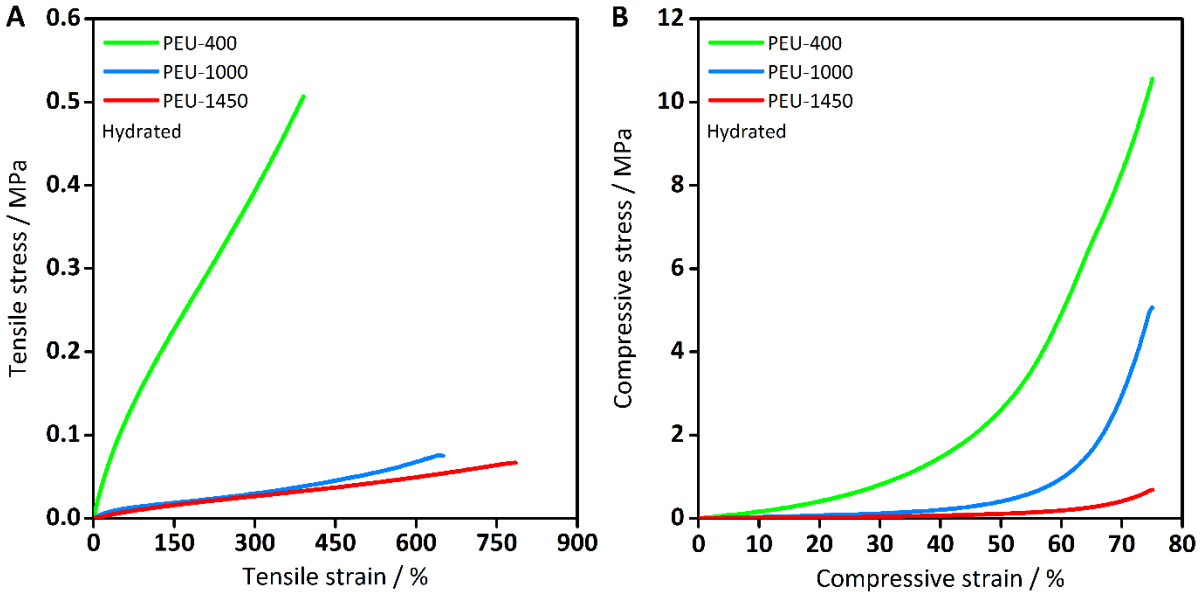

Figure 6.9: Representative quasi-static (A) tensile and (B) compression stress-strain (test terminated at a compressive strain of 75%) curve of PEU hydrogels.

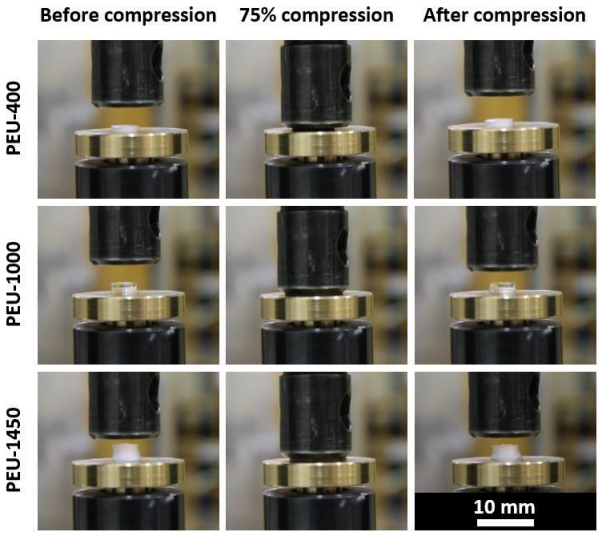

Figure 6.10: Images of the compressive behaviour of PEU hydrogels after 75% strain compression, presenting no damage and fully recovery after load is released.

With respect to the mechanical properties of hydrated PEU hydrogels, complex deformations such as knotting and stretching could be performed on all the PEU hydrogels without fracture, demonstrating excellent flexibility and stretchability, as shown in Figure 6.8 (A, B). One of the main issues with most hydrogels is their mechanical weakness [412,413]. Ideally, hydrogels for soft tissue engineering should be structurally stable and flexible to

withstand mechanical forces and deformations in demanding *in vivo* environments [412,413]. Tensile test results of PEU hydrogels indicated that an increase in PEG molecular weight from 400 to either 1000 or 1450 led to a decrease with statistical significance ($p < 0.05$) in E_s and σ_{smax}, as well as a significant increase in the energy at break, U_{sb}, of the PEU hydrogel. PEU-1450 hydrogels presented the lowest E_s of 0.02 MPa, a σ_{smax} of 0.07 MPa, and the highest ε_{sb} of 623%, as demonstrated in Figure 6.9 (A). Furthermore, all the PEU hydrogels could be compressed to a high strain (75%) without fracture and recover their original shape upon the release of the load, as seen in Figure 6.9 (B) and 6.10. The PEU hydrogels presented significant differences in E_c and $\sigma_{c75\%}$. The PEU-1450 hydrogel demonstrated the softest characteristics overall. The values of n_{eff} were calculated as 322, 64 and 11 mol m^{-3} for PEU-400, PEU-1000 and PEU-1450 hydrogels, respectively. The decrease of the tensile strength and Young's modulus, as well as the increase of elongation at break in the PEUs with higher molecular weights is a consequence of the increase in the chain length between the neighbouring crosslinks, lowering the n_{eff} in the hydrogels and improving their flexibility, which correlates with the swelling properties of the hydrogels (see Section 6.3.3) [214].

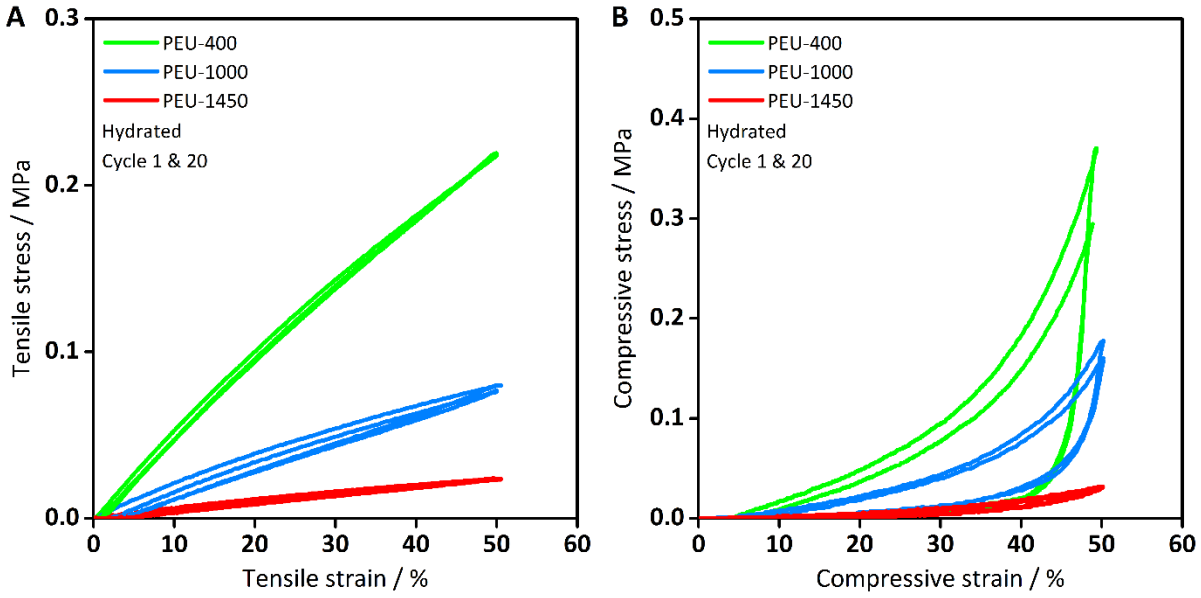

Figure 6.11: Representative cyclic (A) tensile and (B) compression stress-strain curves of PEU hydrogels.

Cyclic stress-strain curves of PEUs were characterised with a hysteresis loop during tensile and compression tests, as presented in Figure 6.11 (A, B). Under cyclic tensile testing, a minimal hysteresis loss ratio, h_r, was observed for all the PEU hydrogels. The PEU-400, PEU-1000 and PEU-1450 hydrogels were characterised with h_r values of 0.06, 0.11 and 0.15 after 20 cycles of tensile loading to 50% strain, respectively. In respect to cyclic compression testing, PEU-1450 specimens showed a h_r of 0.31, while the PEU-400 and PEU-1000 specimens presented higher degrees of h_r of 0.74 and 0.55 after 20 cycles of compression loading to 50% strain, respectively. The expelling of water from the hydrogel observed during the loading cycles presumably contributed to the higher hysteresis loss under compression.

Overall, the PEU hydrogels reported here show excellent performance under quasi-static and cyclic tensile and compressive loads. They are structurally stable, highly stretchable and suitable to engineer scaffolds for a range of soft tissues, such as human cardiac muscles (Young's modulus: 0.01-0.30 MPa) [258] or high stress adapted adipose tissue (Young's modulus: 0.02-0.18 MPa) [76] due to their similar mechanical properties. The incorporation of PEG segments with different molecular weights into the PEU hydrogel altered mechanical properties. The PEG segment with a higher molecular weight improved the flexibility and stretchability of the PEU hydrogel, while reducing their strength and modulus, mainly due to its lower crosslink density and higher water uptake (see Section 6.3.3). In comparison to the mechanical properties of PGS (see Section 3.3.1 and 4.3.1) and PGSU (see Section 5.3.1) from Chapters 3-5, the PEU hydrogels presented softer and more flexible properties, along with an enhanced toughness.

6.3.3 Swelling properties of PEUs

The hydration behaviour of the PEUs was evaluated in PBS at 5, 21 and 37 °C, as illustrated in Figure 6.12 (A, B, C, D) and 6.13. The weight swelling ratio of the PEUs increased rapidly within the first 12 h, and gradually reached a plateau after 24 h. At 5 °C, PEU-400, PEU-1000

and PEU-1450 presented the highest ratios of swelling at equilibrium of 31%, 207% and 499%, respectively, among the three test temperatures. PEU-400, PEU-1000 and PEU-1450 reached swelling ratios at equilibrium of 20%, 154% and 426% at 21 °C, and of 12%, 113% and 235% at 37 °C, respectively. The difference in the swelling ratio of the PEU hydrogels between low and high test temperatures is statistically significant ($p < 0.05$). The PEUs presented negative thermo-sensitivity, and the equilibrium ratio of swelling depended on the medium temperature as well as the hydrophilic/hydrophobic segment composition of the PEUs. The swelling capacities of the PEUs increased with higher molecular weight PEGs, due to the increased chain length between the crosslinks as discussed previously and the increased hydrophilicity of the PEGs [404]. Analysis of the dynamic swelling/deswelling behaviour of the PEU hydrogels demonstrated repeatable and reversible response to alternating medium temperatures, as shown in Figure 6.14. At lower medium temperatures the hydrogen bonding between hydrophilic PEU polymer segments and the water molecules are dominating, while at higher medium temperatures the hydrophobic interactions between the PEU polymer segments are enhanced (due to the increased intrinsic affinity of the polymer chains), causing the secretion of hydrated water molecules from the PEU network [414,415]. The PEUs presented relatively high swelling rates, while the deswelling rates were slightly lower, which can be in part associated with the alternation of the matrix permeability during the change of the medium temperature [416]. The swelling/deswelling rates depend on the specific surface area of the specimen, the composition of the hydrogel and the environmental conditions. These results also indicated that the PEUs with higher molecular weight PEGs would respond with greater swelling/deswelling rates upon minor changes of temperature, thus making these PEU hydrogels more attractive for potential thermosensitive actuation applications, such as cantilever and smart valves [417]. Also, in comparison to the water absorption capability to PGS (2.1-10.0%) [16,237] and PGSU (2.7-4.9%) from Chapters 3-5,

the PEU hydrogels presented superior water uptake properties and presumably enhanced diffusion characteristics, which should allow to engineer large-volume constructs with improved transport performance of oxygen and nutrients within the deeper compartments [397,398].

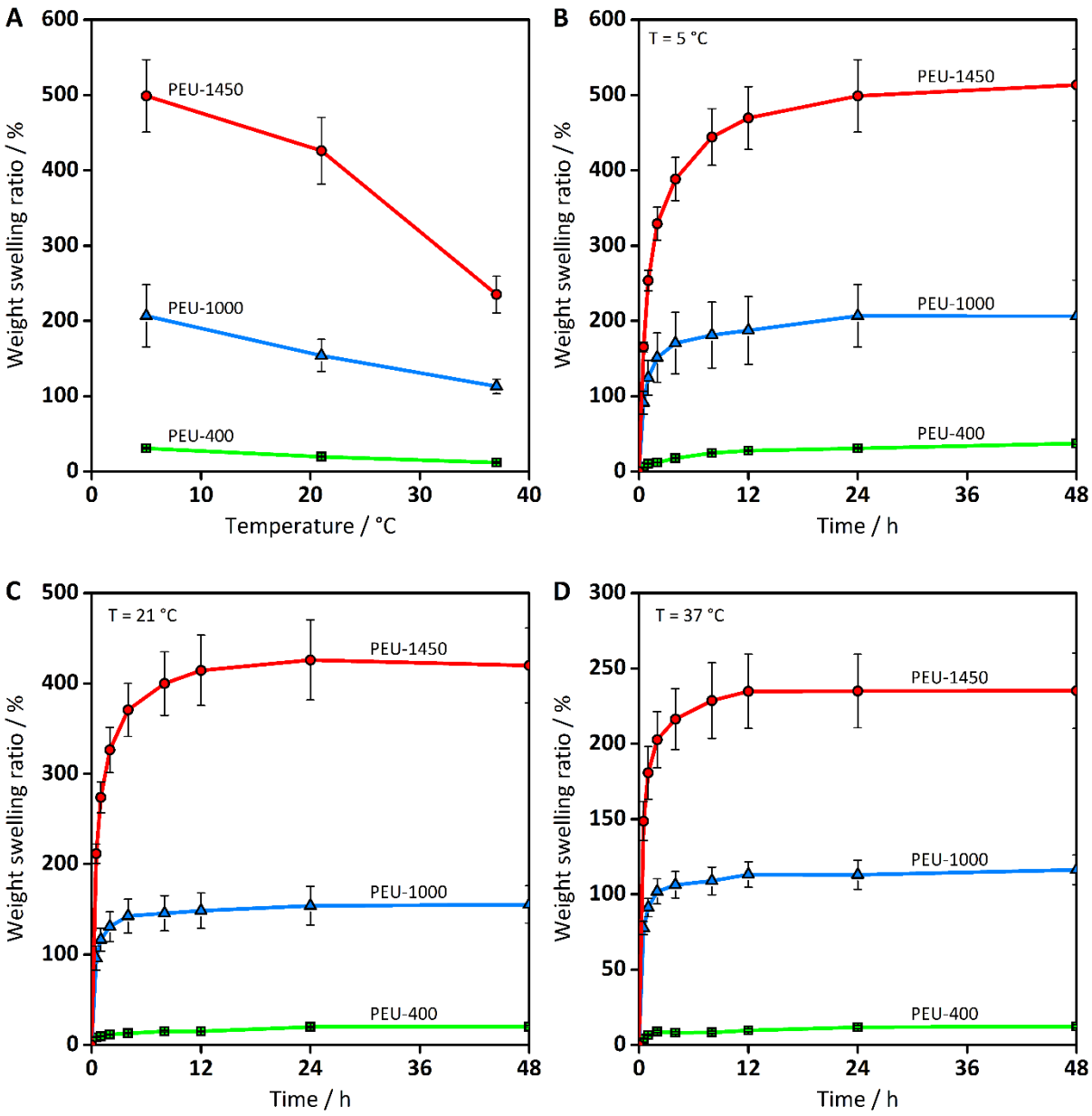

Figure 6.12: (A) Equilibrium ratio of swelling of PEU specimens in PBS solution as a function of the temperature. Hydration kinetics of PEU samples at (B) 5 °C, (C) 21 °C and (D) 37 °C for 2 days.

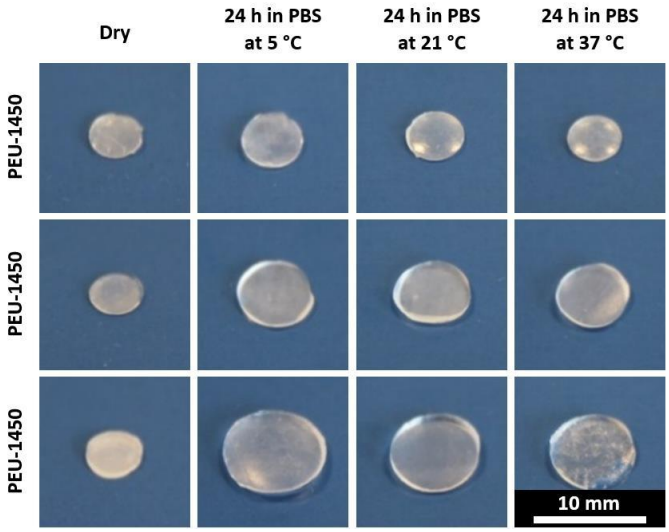

Figure 6.13: Pictures of PEU specimens in dry state and after 24 h hydration at 5 °C, 21 °C and 37 °C.

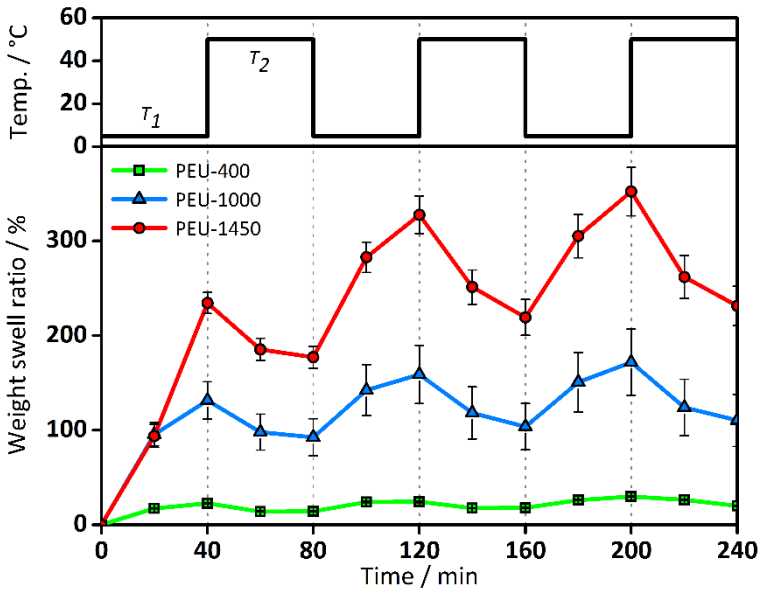

Figure 6.14: Dynamic swelling/deswelling behaviour of PEU specimens in PBS solution at alternating temperatures of 5 °C and 50 °C, at an interval of 40 min.

6.3.4 *In vitro* degradation

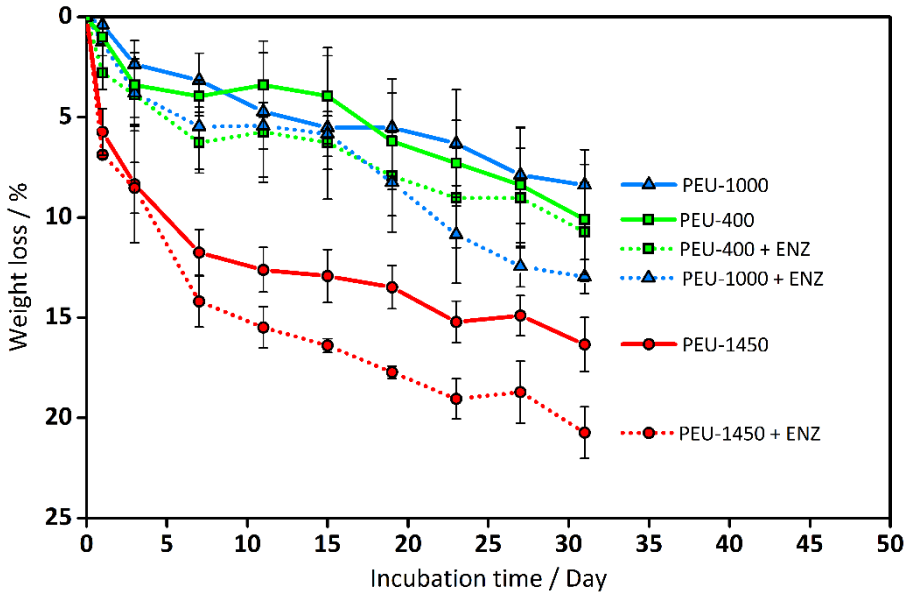

Figure 6.15: Percentage of weight loss of PEU specimens, incubated in enzyme-free or enzyme-containing PBS solutions in a shaker incubator for up to 31 days at 37 °C.

The biodegradability of thermoresponsive hydrogels is an important factor for potential biomedical applications [404,418]. *In vitro* degradation studies were performed in PBS with or without lipase for up to 31 days at 37 °C in a shaker bioincubator, as illustrated in Figure 6.15 and 6.16 (A1-3, B1-3, C1-3). The results illustrate that the rate of degradation of the PEUs can be tuned, depending on the molecular weight of the PEG segments. The higher molecular weight PEGs showed faster degradation over the 31 days studied and this was only slightly enhanced in the presence of the enzyme, which catalysed the hydrolysis process of the ester bonds of the PGS segments [356,367]. The PEUs showed bulk degradation, attributable to their high water content, in which an increase in the PEG molecular weight, as well as the presence of lipase led overall to a greater weight loss. PEU-400 underwent similar weight losses of 10.1% and 10.7% in 31 days in the enzyme-free and lipase-containing PBS solution, respectively. PEU-1000 and PEU-1450 underwent weight losses of 8.4% and 16.3%

in 31 days in the enzyme-free PBS solution, which increased to 12.9% and 20.7%, respectively, with statistical significance, in the lipase-containing solution.

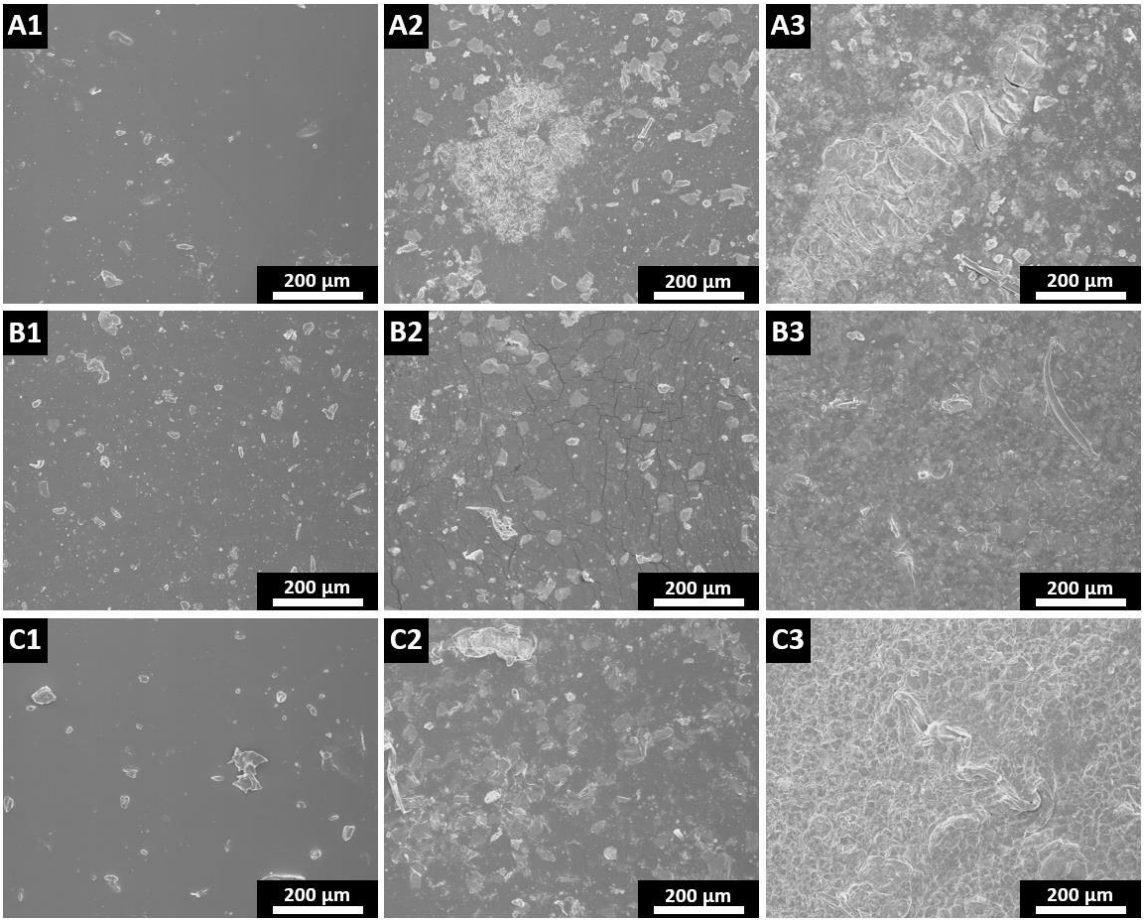

Figure 6.16: SEM micrographs of vacuum-dried (A1-3) PEU-400, (B1-3) PEU-1000 and (C1-3) PEU-1450 film surfaces: (A1, B1, C1) untreated, (A2, B2, C2) in enzyme-free PBS solution and (A3, B3, C3) in enzyme-containing PBS solution after 31 days at 37 ˚C (note that visual differences are minor).

Together with the matched mechanical properties discussed above, biodegradability enables the potential application of the PEUs in soft tissue engineering [412–414,418]. The use of thermosensitive poly(N-isopropylacrylamide) (PNIPAM)-based hydrogels and its copolymers in biomedical applications are restricted, due to PNIPAM's non-biodegradability and toxicity in its monomeric form [412,413,419]. In comparison to pristine PGS from Chapters 3 and 4, and to recently developed PGS-co-PEG block copolymers [302,310], the

PEU hydrogels presented slower degradation kinetics owing to the urethane linkages in the covalently crosslinked network. For instance, pristine PGS exhibited under the same tests conditions degradation rates of 10-18% and 29-45% after 31 days in enzyme-free and enzyme-containing PBS solution, respectively, while the PGS-co-PEG block copolymers presented weight losses of ~15-80% after 21 days under enzyme-free *in vitro* conditions [310]. PGSU scaffolds from Chapter 5 presented slower degradation rates of 3-6% and 5-9% in 35 days under enzyme-free and enzyme-containing *in vitro* conditions, respectively, due to the PGSUs higher degree of urethane linkages and low water absorption capability of PGSUs. Also, according to prior studies [302,420], the use of higher molecular weight PEGs in *in vivo* applications is preferred within the test range (< 40,000 or 60,000 g mol^{-1}) which showed that chronic high oral doses of low molecular weight PEGs (≤ 400 g mol^{-1}) led to adverse renal effects in human and animal experiments.

6.3.5 *In vitro* cell viability and proliferation

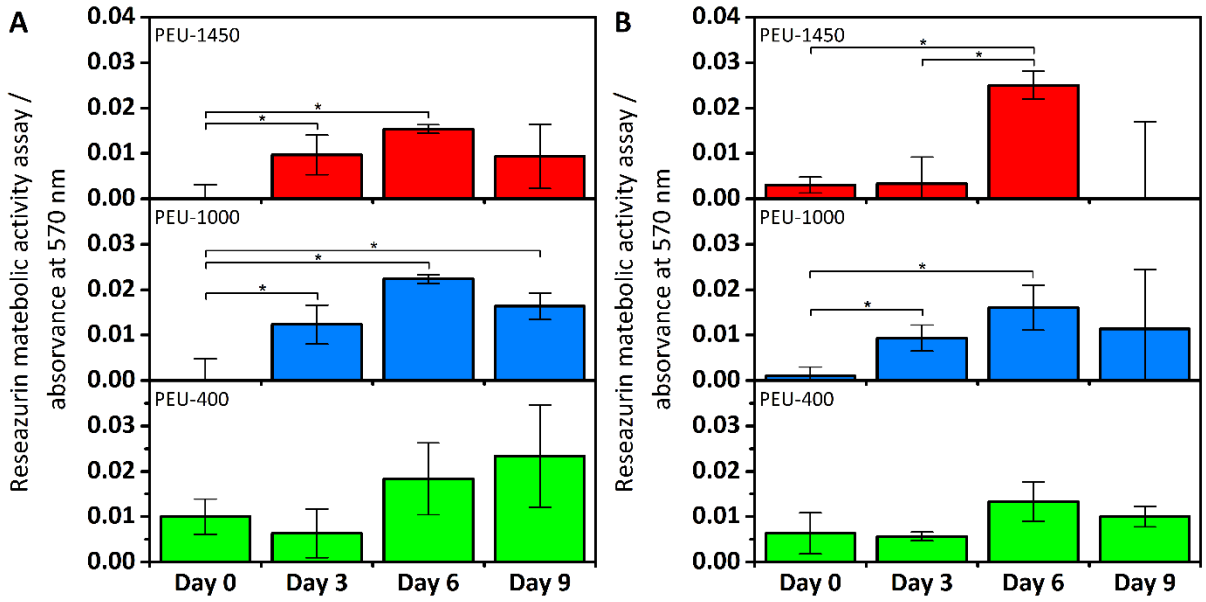

Figure 6.17: Metabolic activity assay results of (A) ADSCs and (B) FIBs cultured on PEU-400, PEU-1000 and PEU-1450 after subtracting the data for cell-free PEU controls. The data are represented as mean ± SD (n = 3; ∗ = $p < 0.05$, two-sample *t*-test).

Metabolic activity assay with resazurin was used to evaluate the *in vitro* cell viability and proliferation of ADSCs and FIBs on PEU hydrogels for up to 9 days, while confocal fluorescence microscopy was performed for cell morphology analysis, as presented in Figure 6.17 (A, B) and 6.18 (A, B). The PEU hydrogels showed no evidence of toxicity to either ADSCs or FIBs. Two-way ANOVA found significant difference between the metabolic activities of ADSCs ($p < 0.0001$) and FIBs ($p < 0.05$) with respect to the test time, while no difference in metabolic activities was found between the different PEU hydrogels. Two-sample *t*-test ($p < 0.05$) found PEU-1000 and PEU-1450 hydrogels presented a significant increase in metabolic activity for both cell types from day 0 to day 6 or 9, while both cell types showed statistically insignificant metabolic activities on the PEU-400 hydrogels. Maximum metabolic activity was achieved for both seeded cell types at day 6 without significant differences between day 6 and 9. ADSCs exhibited the highest metabolic activity on PEU-1000 hydrogels at day 6 (73% increase compared to day 0 cell-seeded specimens), while FIBs demonstrated the highest metabolic activity on PEU-1450 hydrogels at day 6 (51% increase compared to day 0 cell-seeded specimens). The colorimetric measurements were visually confirmed by the colour change of the blue resazurin dye, with a clear change to a purple colour (resorufin) for both cell types on all PEU hydrogels from day 0 to day 9 (Figure 6.S1, Appendix D). The reduction of blue resazurin to purple resorufin was only seen when living cells were present (cell-free control specimens always remained blue). In contrast, the cell-seeded area on PEU-400 and PEU-1000 hydrogels turned in a distinct pink colour, confirming the presence of cells on the surfaces and indicating similar metabolic activities between days 6 and 9. In contrast, the surfaces of the cell-seeded PEU-1450 hydrogels had less visible colour alterations for both cell types after cell seeding, as discussed below.

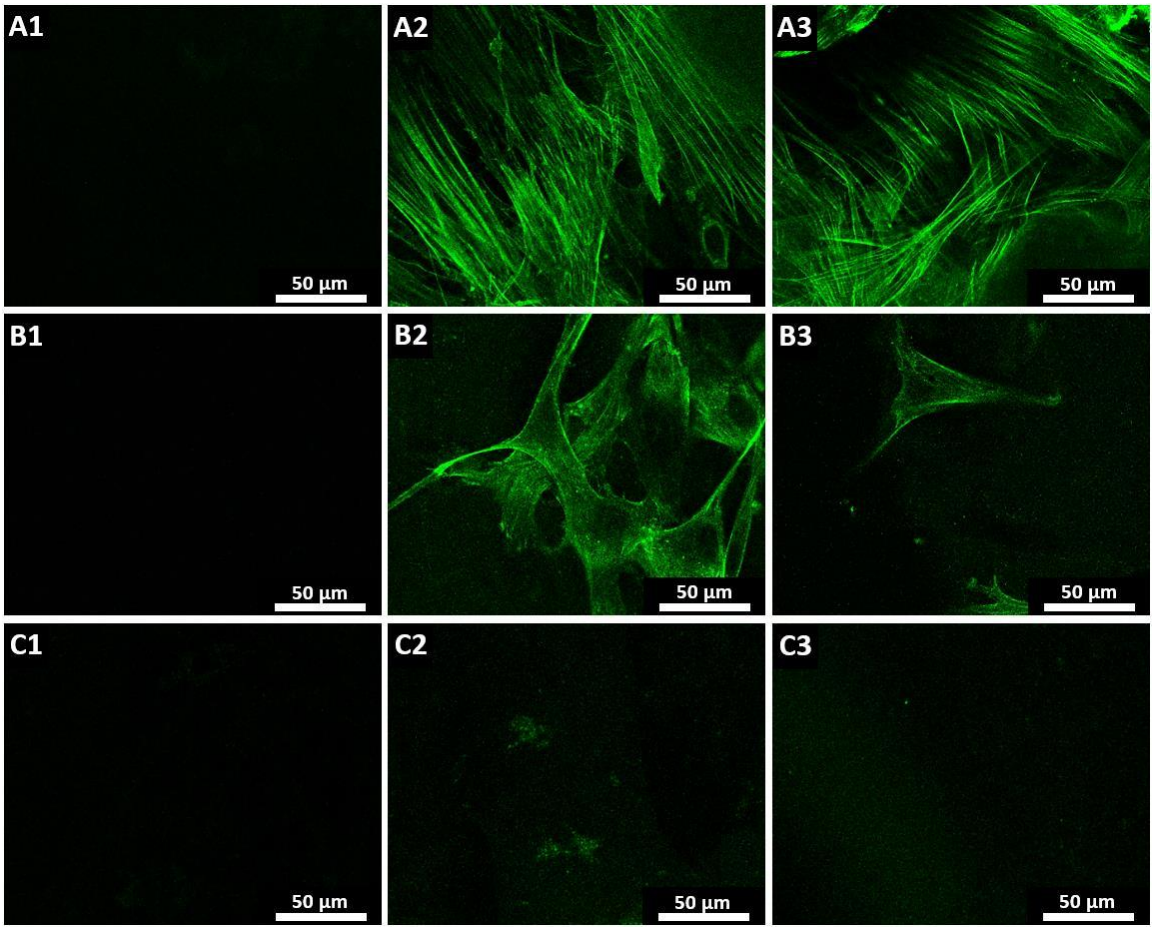

Figure 6.18 Confocal fluorescence micrographs of (A1-3) PEU-400, (B1-3) PEU-1000 and (C1-3) PEU-1450 specimens following 9 days *in vitro* cultivation: (A1, B1, C1) Cell-free PEU control samples, (A2, B2, C2) ADSCs seeded PEU samples and (A3, B3, C3) FIBs seeded PEU samples.

The confocal microscopic analysis showed elongated morphologies of the ADSCs attached to the surface of PEU-400 and PEU-1000 hydrogels and verified highly confluent cell populations, as seen in Figure 6.18 (A2, B2). FIBs also exhibited elongated morphologies on the PEU-400 and PEU-1000 hydrogel surfaces, however, the PEU-400 hydrogels facilitated a higher degree of confluence compared to the PEU-1000 hydrogels, as shown in Figure 6.18 (A3, B3). The surfaces of the PEU-1450 hydrogels showed relatively few ADSCs and FIBs in line with the colorimetric measurements, as seen in Figure 6.18 (C2, C3). This may be the result of cell detachment from the PEU hydrogels. It is likely that the temperature changes of approximately ±16 °C during the culture period (triggered by moving the samples

from the incubator to the sterile laminar flow hood for medium changes and resazurin incubations) would have resulted in volume alterations of the thermosensitive PEU specimens, causing the detachment of cells from the hydrogels [421–424]. In these experiments any detached cells would then be able to proliferate on the surrounding well plate surfaces. The swelling/deswelling rates in response to temperature changes were in the order of PEU-1450 > PEU-1000 > PEU-400, and correspondingly the degree of cell detachment was highest in PEU-1450.

Overall, the above results showed that the ADSCs and FIBs proliferated on the PEU hydrogels, indicating that the PEU hydrogels had no toxic effects on the cells within this test period of 9 days. These results are consistent with previous studies on thermoresponsive and shape-changing hydrogels where a deliberate change in temperature is then used to release cell sheets for subsequent use [421–424].

6.3.6 Drug loading and release

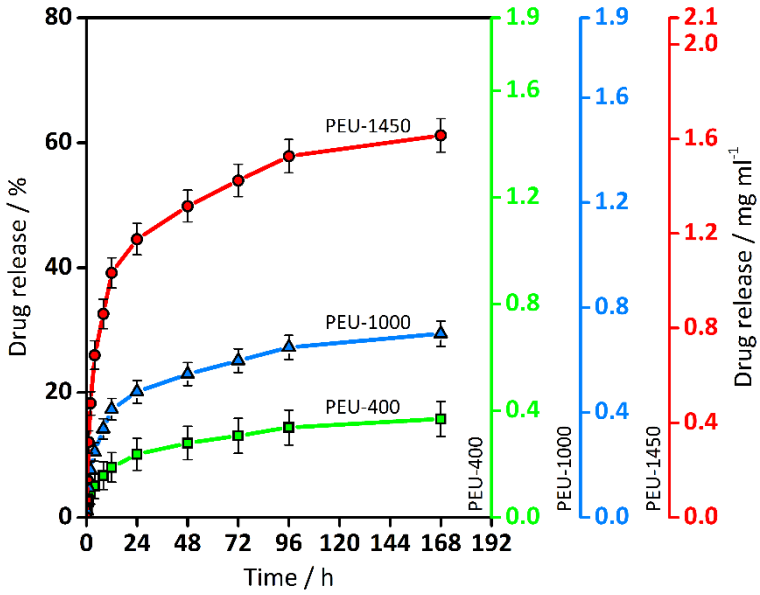

Figure 6.19: Cumulative drug release from PEUs versus swelling time at 37 °C in PBS solution in a shaker incubator.

These thermoresponsive PEU hydrogels can also be used for drug delivery applications [416]. The release of the model drug, lidocaine, from PEU hydrogels was assessed using UV-Vis spectroscopy. Dry PEU specimens were soaked in a lidocaine solution at 5 °C, to enhance the swelling ratio and thus the amount of drug loaded into the hydrogels. The swollen and lidocaine-loaded specimens were dried and then immersed in PBS at 37 °C under shaking conditions. The release profile of PEUs showed a rapid release within the first 4 h, followed by a reduced and sustained drug release in the proceeding time, as presented in Figure 6.19. PEU-400, PEU-1000 and PEU-1450 hydrogels obtained maximum drug release of 15.8% (0.37 mg ml^{-1}), 29.4% (0.70 mg ml^{-1}) and 61.2% (1.62 mg ml^{-1}) after 168 h, respectively. The initial rapid release was presumably caused by a higher drug concentration on the outer layer of the samples [425] and their shrinkage because of the higher test temperature than the drug-loading temperature. The subsequent decelerated drug release can be associated with the less permeable hydrogel matrix [416] and reduced releasable drug content over time. These results demonstrated the prospective use of the PEUs in temperature-controlled or sustained drug delivery. With a modulated volume phase transition temperature (Figure 6.S2, Appendix D), the PEU hydrogels could also potentially feature a temperature dependent on-off drug release [414,418].

6.3.7 Water-temperature activated force generation and motions

Thermoresponsive hydrogels can also be used for actuation and power generation [414,426]. PEU-1450 hydrogels at 40% strain generated temperature-induced contractile forces and stresses, as seen in Figure 6.20 (A, B). The cyclic change of water temperature from 21 °C to 37 °C and from 5 °C to 37 °C generated contractile forces of 16 ± 1 mN and 44 ± 1 mN, and stresses of 1.4 ± 0.03 kPa and 3.8 ± 0.06 kPa, respectively. Generation of the contractile forces occurred instantly upon temperature alteration and was reversible. Their values are affected by the specimen dimensions (e.g. the specific surface area), water temperature

difference, environmental conditions and swelling/deswelling capability of the PEU hydrogel. Higher contractile forces are achievable by altering these parameters, which could then be used to generate ultralow power by attaching a piezoelectric element to drive a micro- or nano-device [426]. The excellent stimuli-responsiveness of the PEU-1450 hydrogel also allowed for the design of water temperature-activated cantilevers, transducing the temperature-stimulus into reversible bending, as presented in Figure 6.21 (Movie 6.S1, Appendix D). These characteristics will enable the PEU hydrogels to be used in actuators (e.g. cantilever: transduce temperature changes into a bending motion), sensors (e.g. capacitive plate sensor: transduce temperature changes into a changing distance between the plates of a capacitor), soft robotics (e.g. shape-shifting: transduce temperature changes into a changing shape) and fluid control devices (e.g. microfluid flow regulator: transduce temperature changes into an opening or closing valve) [414].

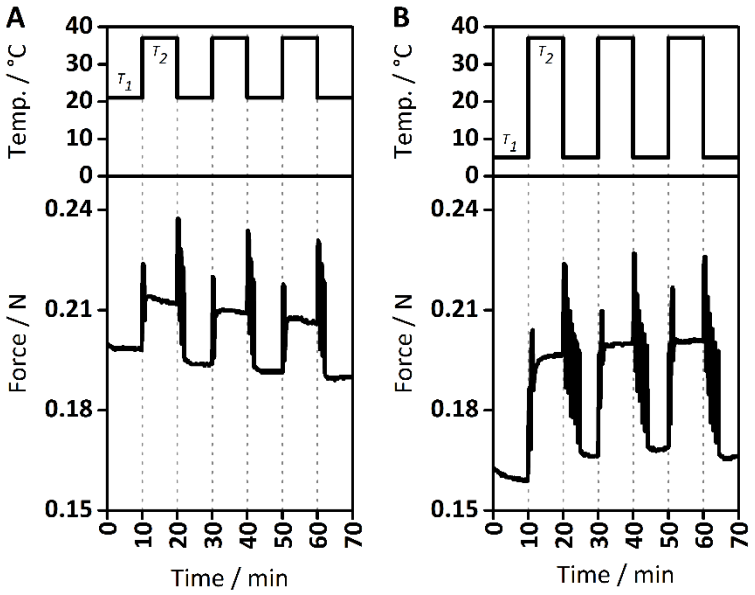

Figure 6.20: (A) Water temperature activated force generation of submerged and stretched PEU-1450 strip samples by cyclic alteration of water temperature from T_1 = 21 °C to T_2 = 37 °C, or from (B) T_1 = 5 °C to T_2 = 37 °C (sharp peaks = replacement of an equal volume of water with the pre-determined temperature to achieve the target temperature T_1 or T_2).

Figure 6.21: Water temperature responsive cantilever composed of a PEU-1450 and a PTFE film strip, transducing the water temperature dependent swelling/deswelling response into reversible bending motions.

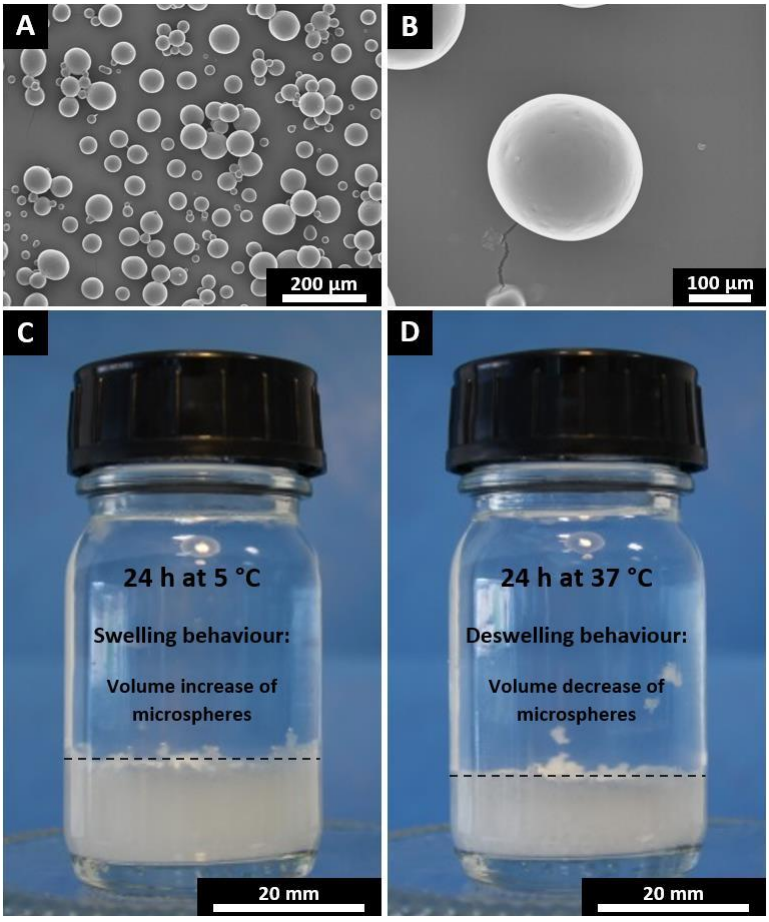

Figure 6.22: (A, B) SEM images of dry PEU-1000 microspheres, fabricated in a proof of concept study. Images of PEU-1000 microspheres immersed in PBS solution, demonstrating the microspheres swelling/deswelling behaviour after 24 h at (C) 5 °C and (D) 37 °C.

The results presented here demonstrate the successful synthesis of thermoresponsive, stretchable, biodegradable and biocompatible PEU hydrogels with tuneable physicochemical properties for a variety of possible applications. The chemically crosslinked PEU hydrogels have structurally stable and highly stretchable characteristics, which may prove useful in mechanically dynamic environments for soft tissues [412,413]. Conventional thermoresponsive PNIPAM-based hydrogels are comparably less ductile, characterised with low elongation at break values of ~50% [417,427–429], restraining their scope of potential applications in soft tissue engineering. Furthermore, the PEU hydrogels exhibited softer and/or more flexible properties in comparison to hydrated PGS-co-PEG block copolymers [310], which presented a Young's modulus, tensile strength and elongation at break in the range of 0.013-1.55 MPa, 0.012-0.30 MPa and ~25-200%, respectively [310].

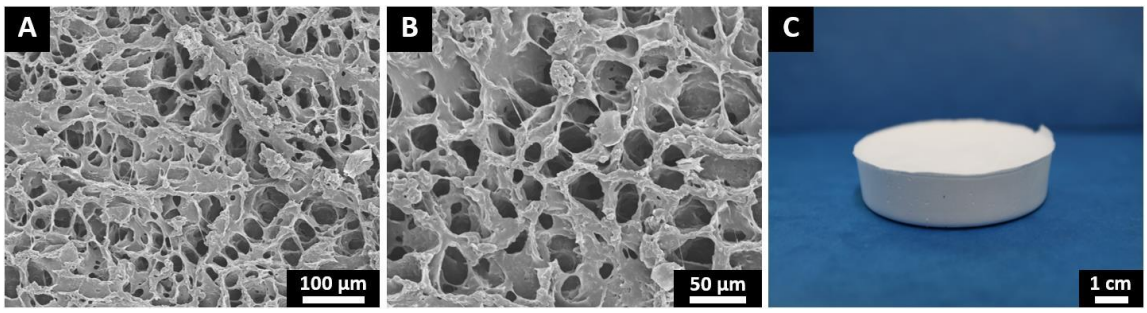

Figure 6.23: (A, B) SEM images of the microstructure dry PEU-1450 scaffold, fabricated in a proof of concept study. (C) Image of a PEU-1450 scaffold specimen.

The biodegradability and biocompatibility are critical aspects for developing thermosensitive PU-based hydrogels for biomedical applications. Further critical examination *in vivo* is needed to assess the potential for PEU hydrogels in soft tissue engineering and/or drug delivery applications, along with their prospective use in the development of bioresorbable actuators [417]. Further work can also include fabrication of the PEU hydrogels into different structures to address the needs of different applications. In a proof-of-concept study, the fabrication of the PEU into microspheres with a size range of 289 ± 42 µm was

achievable by using an oil-in-oil solvent evaporation technique [403], which also presented negative thermo-sensitivity, as seen in Figure 6.22 (A, B, C, D). Injectable microspheres are interesting for localised drug delivery and targeted soft tissue engineering applications [430]. The proof-of-concept production of large 3D scaffold constructs via freeze-drying was also realisable [356,367], producing highly porous and interconnected microstructures with pore sizes of 31 ± 5 μm, demonstrating great potential for further optimisation of the pore size and porosity for soft tissue engineering applications, as demonstrated in Figure 6.23 (A, B, C).

6.4 Conclusions

Stretchable, thermoresponsive, biodegradable and biocompatible PEU hydrogels with varying molecular weight of PEG were synthesised by a facile solvent-based two-step method. The chemical and physical characteristics of the covalently crosslinked PEU hydrogels are tuneable by changing the molecular weight of the PEG segments. PEU hydrogels were processed into films, with structurally stable and highly stretchable mechanical properties in dry and hydrated states. The PEU hydrogels were characterised with a tensile Young's modulus, ultimate tensile strength and elongation at break in the range of 0.02-0.20 MPa, 0.05-0.47 MPa and 426-623%, respectively. Compression tests showed no fracture and good recoverability after 75% axial strain. The PEU hydrogels demonstrated minimal hysteresis loss ratio during cyclic tensile tests, while cyclic compression tests showed higher hysteresis loss ratios. The PEU hydrogels were characterised with negative thermo-sensitivity, and the equilibrium ratio of swelling depended on the medium temperature and PEU composition. The PEU hydrogels demonstrate repetitive and reversible responses to changes in medium temperature from 5 ^{o}C to 37 ^{o}C with the swelling ratio at equilibrium varying from 499% to 12%. *In vitro* degradation tests of PEU hydrogels obtained weight losses of 9-16% or 11-21% in 31 days in PBS or lipase solution, respectively. *In vitro* cell test results provided clear

evidence that all the PEU hydrogels are biocompatible and suitable for the culture of ADSCs and FIBs.

The PEU hydrogels showed a rapid drug release within the first hour in PBS, followed by a sustained drug release rate in the proceeding time and reaching a maximum drug release in the range of 16-61% after 168 h. Water temperature activated force generation of submerged and stretched PEU strip samples generated contractile forces of 16 ± 1 mN and 44 ± 1 mN and stresses of 1.4 ± 0.03 kPa and 3.8 ± 0.06 kPa by cyclic water temperature changes, which occurred instantly upon temperature alteration and was reversible. The proof-of-concept fabrication of structures such as PEU microspheres and large 3D scaffolds illustrates versatility of the polymers. The high flexibility, stretchability, thermoresponsivity, biodegradability and biocompatibility show the potential of the PEU hydrogels to be applied in a variety of applications such as soft tissue engineering, temperature-controlled or sustained drug delivery as well as thermal actuation.

Chapter 7. Overall conclusions and future work

7.1 Overall conclusions

This thesis has focused on the design and development of synthetic PGS-based materials and biomimetic tissue scaffolds with similar bulk mechanical properties to those of native adipose tissue, suitable for potential application in ATE. Key findings have been discussed in each individual chapter and the research yielded several major conclusions.

Firstly, in comparison to other PGS scaffold fabrication strategies, the freeze-drying fabrication strategy utilised in this work, accompanied by the blending of pre-PGS with a minor structure-supporting biopolymer and a subsequent curing process, presented to be a more feasible and less complex method in fabricating large 3D and porous PGS-based scaffolds, whilst offering opportunities for further optimisations and modifiability for a wide variety of soft tissue engineering applications.

Secondly, large and porous PGS/PLLA scaffolds with similar mechanical properties to native low and high stress adapted adipose tissue were fabricated via the freeze-drying fabrication strategy, confirming that the fabrication method allows one to design scaffold constructs with specifically required properties. The engineered scaffolds were characterised with highly porous microstructures, as well as good cell penetration and tissue in-growth characteristics, demonstrating great potential for applications in ATE.

Thirdly, the application of isocyanate-based crosslinkers allowed the synthesis of PGS-based PU with significantly improved processability, enhanced flexibility and slower degradation kinetics. The fabrication of large and porous PGSU scaffolds was successful via the freeze-drying fabrication strategy, without the necessity of an additional minor structure-supporting biopolymer and a second curing stage. The PGSU scaffolds were characterised

with soft, flexible and more stretchable mechanical properties, as well as long-term stability and tuneable degradation kinetics.

Fourthly, the application of NCO-terminated PEGs with varying molecular weight PEGs allowed to synthesise PGS-based PU hydrogels with enhanced hydrophilicity, high flexibility, stretchability, good biodegradability and biocompatibility. The functionalities of the PEU hydrogels were evaluated for potential applications in ATE and other soft tissue engineering fields. The PEU hydrogels featured also negative thermoresponsive properties, demonstrating highly interesting properties for potential drug delivery, thermal actuation and ultralow power generation applications.

Overall, this thesis is the first step in investigating the prospective use of PGS-based materials in ATE. Several PGS related limitations in terms of scaffold fabrication, processability and physicochemical properties were overcome. The developed freeze-drying-fabrication strategy, along with the designed PGS/PLLA blends, PGSUs and PEUs, presented great potential to be developed further for ATE, as well as for other soft tissue engineering applications.

7.2 Future work

The future applications of the PGS/PLLA and PGSU scaffolds, along with the thermoresponsive PEU hydrogels are numerous, with potential uses in both biomedical and engineering applications. The materials and scaffolds need to be critically examined *in vivo* to further establish their potential utilisation in the field of tissue engineering. Furthermore, the usage of large porous scaffolds requires the application of novel vascularisation strategies. Insufficient vascularisation is still one of the major key problems in tissue engineering, which should be addressed in future work.

Future research work may also focus on the development of injectable PGS-based materials, which would be beneficial for ATE and other soft tissue engineering applications,

due to the prevention of complex surgeries. With this respect, it is assumed that the fabricated porous scaffolds (or films) can be further processed to create sheet-like and injectable particles via cryogenic grinding (working temperature of liquid nitrogen: -196 °C). For instance, the glass transition temperature, T_g, of crosslinked PGS, PGSU and PEU materials are in the range of -10 °C to -45 °C, respectively, and are therefore capable of being ground at low temperatures. This fabrication strategy could provide an opportunity to produce sheet-like and injectable particles for cell delivery strategies aimed for tissue engineering applications, but also as filler materials for designing novel polymer composites.

The freeze-drying fabrication strategy of PGS/biopolymer scaffolds could also be developed further, by using different solvents (e.g. dimethyl sulfoxide) or biopolymers (e.g. PDLA, polydioxanone) combinations, as well as by altering the freeze-drying and/or curing parameters. The biocompatibility, the biodegradability or the mechanical characteristics of these scaffolds could be modified by incorporating nanoparticles (e.g. graphene, graphene oxide, sepiolite), microfibers (e.g. PVA, chitosan) or microspheres (e.g. PVA, chitosan) into the polymer matrix, which may also enhance the structure stability of the scaffold constructs during the curing stage. The realisation of complex 3D shapes with pre-PGS/biopolymer/solvent mixtures is presumably possible via SFF by using a dispensing system connected to a cryogenic plotting plate (the usage of a support material to assist overhangs may be required) [431,432], which could be further processed through the freeze-drying and curing processing steps. Also, it is assumed that the production process of the PGS/biopolymer scaffolds could be accelerated by using a microwave-assisted curing stage [254,320], thus improving the manufacturing throughput of the freeze-drying fabrication strategy significantly.

Similarly, further developments can be performed on the PGSU scaffolds. The biocompatibility, the biodegradability and the mechanical properties of the scaffolds could be

modified by incorporating nanoparticles, microfibers or microspheres into the polymer matrix.

With respect to the chemically crosslinked PEU hydrogels, further investigation is required in respect to the scaffold and microsphere fabrication process. The modification of the PEU synthesis procedure, such as the alteration of the glycerol to NCO-terminated PEG ratio, as well as the molecular weight of the PEG segments, could modify the physicochemical properties of the PEU hydrogels further. The biocompatibility, the biodegradation and the mechanical properties of PEU hydrogels could be also modified by incorporating nanoparticles, microfibers or microspheres into the polymer matrix. In addition, further analysis is required in terms of the PEUs potential applications in drug delivery, thermal actuation and ultralow power generation.

Bibliography

[1] A.R. Golas, K.A. Hernandez, J.A. Spector, "Tissue engineering for plastic surgeons: A primer", *Aesthetic Plast. Surg.*, 2014, **38**, 207–221.

[2] F.J. O'Brien, "Biomaterials & scaffolds for tissue engineering", *Mater. Today*., 2011, **14**, 88–95.

[3] A. Persidis, "Tissue engineering", *Nat. Biotechnol.*, 1999, **17**, 508–5010.

[4] S. Bhat, A. Kumar, "Biomaterials and bioengineering tomorrow's healthcare", *Biomatter*, 2013, **3**, e24717.

[5] J.H. Choi, J.M. Gimble, K. Lee, K.G. Marra, J.P. Rubin, J.J. Yoo, G. Vunjak-Novakovic, D.L. Kaplan, "Adipose tissue engineering for soft tissue regeneration", *Tissue Eng. B*, 2010, **16**, 413–426.

[6] C.W. Patrick, "Tissue engineering strategies for adipose tissue repair", *Anat. Rec.*, 2001, **263**, 361–366.

[7] L. Flynn, K.A. Woodhouse, "Adipose tissue engineering with cells in engineered matrices", *Organogenesis*, 2008, **4**, 228–235.

[8] P. Bauer-Kreisel, A. Goepferich, T. Blunk, "Cell-delivery therapeutics for adipose tissue regeneration", *Adv. Drug Deliv. Rev.*, 2010, **62**, 798–813.

[9] Y.C. Chiu, M.H. Cheng, S. Uriel, E.M. Brey, "Materials for engineering vascularized adipose tissue", *J. Tissue Viability*., 2011, **20**, 37–48.

[10] A.R. Webb, J. Yang, G.A. Ameer, "Biodegradable polyester elastomers in tissue engineering.", *Expert Opin. Biol. Ther.*, 2004, **4**, 801–812.

[11] A.B. Brochu, S.L. Craig, W.M. Reichert, "Self-healing biomaterials", *J. Biomed. Mater. Res. A*, 2011, **96**, 492–506.

[12] N. Shoham, A. Gefen, "Mechanotransduction in adipocytes", *J. Biomech.*, 2012, **45**, 1–8.

[13] Y. Ye, Y. Yuan, F. Lu, J. Gao, "Possible role of mechanical force in regulating regeneration of the vascularized fat flap inside a tissue engineering chamber", *Med. Hypotheses*, 2015, **85**, 807-809.

[14] Y. Li, G.A. Thouas, Q.Z. Chen, "Biodegradable soft elastomers: synthesis/properties of materials and fabrication of scaffolds", *RSC Adv.*, 2012, **2**, 8229–8242.

[15] R. Shi, D. Chen, Q. Liu, Y. Wu, X. Xu, L. Zhang, W. Tian, "Recent advances in synthetic bioelastomers", *Int. J. Mol. Sci.*, 2009, **10**, 4223–4256.

[16] Y. Wang, G.A. Ameer, B.J. Sheppard, R. Langer, "A tough biodegradable elastomer", *Nat. Biotechnol.*, 2002, **20**, 602–606.

[17] R. Rai, M. Tallawi, A. Grigore, A.R. Boccaccini, "Synthesis, properties and biomedical applications of poly(glycerol sebacate) (PGS): A review", *Prog. Polym. Sci.*, 2012, **37**, 1051–1078.

[18] R. Langer, J.P. Vacanti, "Tissue engineering", *Science*, 1993, **260**, 920–926.

[19] B. Gridelli, G. Panarello, S. Gruttadauria, A. Marcos, P. Grossi, "Infections after living-donor liver transplantation", *Surg. Infect.*, 2006, **7**, 105–108.

[20] J. Weitz, M. Koch, A. Mehrabi, P. Schemmer, M. Zeier, J. Beimler, M. Büchler, J. Schmidt, "Living-donor kidney transplantation: Risks of the donor-benefits of the

recipient", *Clin. Transplant.*, 2006, **20**, 13–16.
[21] M.D. Fox, "The price is wrong: The moral cost of living donor inducements", *Am. J. Transplant.*, 2006, **6**, 2529–2530.
[22] R.S. Gaston, G.M. Danovitch, R.A. Epstein, J.P. Kahn, A.J. Matas, M.A. Schnitzler, "Limiting financial disincentives in live organ donation: A rational solution to the kidney shortage", *Am. J. Transplant.*, 2006, **6**, 2548–2555.
[23] D.L. Kaserman, "On the feasibility of resolving the organ shortage", *Inquiry*., 2006, **43**, 160–166.
[24] M. Quante, S. Wiedebusch, "Overcoming the shortage of transplantable organs: Ethical and psychological aspects", *Swiss Med. Wkly.*, 2006, **136**, 523–528.
[25] R. Langer, "Tissue engineering: A new field and its challenges", *Pharm. Res.*, 1997, **14**, 840–841.
[26] S. Liao, C.K. Chan, S. Ramakrishna, "Stem cells and biomimetic materials strategies for tissue engineering", *Mater. Sci. Eng. C*, 2008, **28**, 1189–1202.
[27] B.S. Kim, D.J. Mooney, "Development of biocompatible synthetic extracellular matrices for tissue engineering", *Trends Biotechnol.*, 1998, **16**, 224–230.
[28] T.C. Flanagan, A. Pandit, P. Taylor, S. Jockenhövel, "Living artificial heart valve alternatives: A review", *Eur. Cells Mater.*, 2003, **6**, 28–45.
[29] B. Demirbag, P.Y. Huri, G.T. Kose, A. Buyuksungur, V. Hasirci, "Advanced cell therapies with and without scaffolds", *Biotechnol. J.*, 2011, **6**, 1437–1453.
[30] E.L. Scheller, P.H. Krebsbach, D.H. Kohn, "Tissue engineering: State of the art in oral rehabilitation", *J. Oral Rehabil.*, 2009, **36**, 368–389.
[31] J.W. Nichol, A. Khademhosseini, "Modular tissue engineering: Engineering biological tissues from the bottom up", *Soft Matters*., 2010, **5**, 1312–1319.
[32] T. Lu, Y. Li, T. Chen, "Techniques for fabrication and construction of three-dimensional scaffolds for tissue engineering", *Int. J. Nanomedicine*., 2013, **8**, 337–350.
[33] D.M. Dean, A.P. Napolitano, J. Youssef, J.R. Morgan, "Rods, tori, and honeycombs: The directed self-assembly of microtissues with prescribed microscale geometries", *FASEB J.*, 2007, **21**, 4005–4012.
[34] J. Yeh, Y. Ling, J.M. Karp, J. Gantz, A. Chandawarkar, G. Eng, J. Blumling III, R. Langer, A. Khademhosseini, "Micromolding of shape-controlled, harvestable cell-laden hydrogels", *Biomaterials*, 2006, **27**, 5391–5398.
[35] N. L'Heureux, S. Pâquet, R. Labbé, L. Germain, F.A. Auger, "A completely biological tissue-engineered human blood vessel", *FASEB J.*, 1998, **12**, 47–56.
[36] V. Mironov, T. Boland, T. Trusk, G. Forgacs, R.R. Markwald, "Organ printing: Computer-aided jet-based 3D tissue engineering", *Trends Biotechnol.*, 2003, **21**, 157–161.
[37] Y. Du, E. Lo, S. Ali, A. Khademhosseini, "Directed assembly of cell-laden microgels for fabrication of 3D tissue constructs", *Proc. Natl. Acad. Sci. U. S. A.*, 2008, **105**, 9522–9527.
[38] A.P. McGuigan, M.V. Sefton, "Design and fabrication of sub-mm-sized modules containing encapsulated cells for modular tissue engineering", *Tissue Eng.*, 2007, **13**, 1069–1078.
[39] B. Dhandayuthapani, Y. Yoshida, T. Maekawa, D.S. Kumar, "Polymeric scaffolds in

tissue engineering application: A review", *Int. J. Polym. Sci.*, 2011, 290602.

[40] W. Liu, Y. Cao, "Application of scaffold materials in tissue reconstruction in immunocompetent mammals: Our experience and future requirements", *Biomaterials*, 2007, **28**, 5078–5086.

[41] J.D. Kretlow, L. Klouda, A.G. Mikos, "Injectable matrices and scaffolds for drug delivery in tissue engineering", *Adv. Drug Deliv. Rev.*, 2007, **59**, 263–273.

[42] American Society of Plastic Surgeons, "2014 American Society of Plastic Surgeons Statistics", http://www.plasticsurgery.org/Documents/news-resources/statistics/2014-statistics/reconstructive-procedure-trends-2014.pdf (accessed: 15 April 2015).

[43] L. Flynn, G.D. Prestwich, J.L. Semple, K.A. Woodhouse, "Adipose tissue engineering with naturally derived scaffolds and adipose-derived stem cells", *Biomaterials*, 2007, **28**, 3834–3842.

[44] S.R. Coleman, "Long-term survival of fat transplants: Controlled demonstrations", *Aesthetic Plast. Surg.*, 1995, **19**, 421–425.

[45] S.R. Coleman, "Facial recontouring with lipostructure", *Clin. Plast. Surg.*, 1997, **24**, 347–367.

[46] J. Smahel, "Adipose tissue engineering in plastic surgery", *Ann. Plast. Surg.*, 1986, **16**, 444–452.

[47] A. Nguyen, K.A. Pasyk, T.N. Bouvier, C.A. Hassett, L.C. Argenta, "Comparative study of survival of autologous adipose tissue taken and transplanted by different techniques", *Plast. Reconstr. Surg.*, 1990, **85**, 378–386.

[48] S.R. Coleman, A.P. Saboeiro, "Fat grafting to the breast revisited: Safty and efficacy", *Plast. Reconstr. Surg.*, 2007, **119**, 775–785.

[49] M.C. Missana, I. Laurent, L. Barreau, C. Balleyguier, "Autologous fat transfer in reconstructive breast surgery: Indications, technique and results", *Eur. J. Surg. Oncol.*, 2007, **33**, 685–90.

[50] C.T. Gomillion, K.J.L. Burg, "Stem cells and adipose tissue engineering", *Biomaterials*, 2006, **27**, 6052–6063.

[51] A.L. Albright, J.S. Stern, "Adipose tissue", *Encycl. Sport. Med. Sci.*, 1998, http://www.sportsci.org/encyc/adipose/adipose.html (accessed: 23 Janurary 2015).

[52] S.R. Farmer, "Molecular determinants of brown adipocyte formation and function", *Genes Dev.*, 2008, **22**, 1269–1275.

[53] H.N. Langstein, G.L. Robb, "Reconstructive approaches in a soft tissue sarcoma", *Semin. Surg. Oncol.*, 1999, **17**, 52–65.

[54] D.T. Lindsay, Functional human anatomy, St. Louis: Mosby, 1996, 1–976.

[55] H. Tilg, A.R. Moschen, "Adipocytokines: Mediators linking adipose tissue, inflammation and immunity", *Nat. Rev. Immunol.*, 2006, **6**, 772–783.

[56] G. Rajashekhar, D.O. Traktuev, W.C. Roell, B.H. Johnstone, S. Merfeld-Clauss, B. Van Natta, E.D. Rosen, K.L. March, M. Clauss, "IFATS collection: Adipose stromal cell differentiation is reduced by endothelial cell contact and paracrine communication: Role of canonical Wnt signaling", *Stem Cells.*, 2008, **26**, 2674–2681.

[57] K. Yoshimura, K. Sato, N. Aoi, M. Kurita, T. Hirohi, K. Harii, "Cell-assisted lipotransfer for cosmetic breast augmentation: Supportive use of adipose-derived stem/stromal cells", *Aesthetic Plast. Surg.*, 2008, **32**, 48–55.

[58] S. Cinti, "The adipose organ", *Prostaglandins Leukot. Essent. Fat. Acids*., 2005, **73**, 9–15.
[59] S. Gesta, Y.H. Tseng, C.R. Kahn, "Developmental Origin of Fat: Tracking Obesity to Its Source", *Cell*., 2007, **131**, 242–256.
[60] A. Rigamonti, K. Brennand, F. Lau, C.A. Cowan, "Rapid cellular turnover in adipose tissue", *PLoS One*., 2011, **6**, e17637.
[61] W.T. Branch, R.W. Alexander, R.C. Schlant, J. Hurst, Cardiology in Primary Care, New York: McGraw-Hill Medical Publishing Division, 2000, 1–940.
[62] K. Comley, N.A. Fleck, "The toughness of adipose tissue: Measurements and physical basis", *J. Biomech.*, 2010, **43**, 1823–1826.
[63] C.G. Brook, J.K. Lloyd, O.H. Wolf, "Relation between age of onset of obesity and size and number of adipose cells.", *Br. Med. J.*, 1972, **2**, 25–27.
[64] P. Trayhurn, C. Bing, I.S. Wood, "Adipose tissue and adipokines - energy regulation from the human perspective", *J. Nutr.*, 2006, **136**, 1935S–1939S.
[65] K. Comley, N.A. Fleck, "A micromechanical model for the Young's modulus of adipose tissue", *Int. J. Solids Struct.*, 2010, **47**, 2982–2990.
[66] L. Flynn, J.L. Semple, K.A. Woodhouse, "Decellularized placental matrices for adipose tissue engineering", *J. Biomed. Mater. Res. A.*, 2006, **79**, 359–369.
[67] G. Sommer, M. Eder, L. Kovacs, H. Pathak, L. Bonitz, C. Mueller, P. Regitnig, G.A. Holzapfer, "Multiaxial mechanical properties and constitutive modeling of human adipose tissue: A basis for preoperative simulations in plastic and reconstructive surgery", *Acta Biomater*., 2013, **9**, 9036–9048.
[68] S. Cinti, "Transdifferentiation properties of adipocytes in the adipose organ", *AJP Endocrinol. Metab.*, 2009, **297**, E977–E986.
[69] W.J.F.M. Jurgens, M.J. Oedayrajsingh-Varma, M.N. Helder, B. ZandiehDoulabi, T.E. Schouten, D.J. Kuik, M.J.P.F. Ritt, F.J. Van Milligen, "Effect of tissue-harvesting site on yield of stem cells derived from adipose tissue: Implications for cell-based therapies", *Cell Tissue Res.*, 2008, **332**, 415–426.
[70] E. Linder-Ganz, N. Shabshin, Y. Itzchak, A. Gefen, "Assessment of mechanical conditions in sub-dermal tissues during sitting: A combined experimental-MRI and finite element approach", *J. Biomech.*, 2007, **40**, 1443–1454.
[71] E. Linder-Ganz, N. Shabshin, Y. Itzchak, Z. Yizhar, I. Siev-Ner, A. Gefen, "Strains and stresses in sub-dermal tissues of the buttocks are greater in paraplegics than in healthy during sitting", *J. Biomech.*, 2008, **41**, 567–580.
[72] H Zhao, N.A. Fleck, IUTAM Symposium on Mechanical Properties of Cellular Materials, Cachan: Springer Science & Business Media, 2008, 1-240.
[73] N. Alkhouli, J. Mansfield, E. Green, J. Bell, B. Knight, N. Liversedge, J.C. Tham, R. Welbourn, A.C. Shore, K. Kos, C.P. Winlove, "The mechanical properties of human adipose tissues and their relationships to the structure and composition of the extracellular matrix.", *Am. J. Physiol. Endocrinol. Metab.*, 2013, **305**, E1427–1435.
[74] K. Chen, J.D. Weiland, "Mechanical properties of orbital fat and its encapsulating connective tissue", *J. Biomech. Eng.*, 2011, **133**, 064505.
[75] J.E. Miller-Young, N.A. Duncan, G. Baroud, "Material properties of the human calcaneal fat pad in compression experiment and theory", *J. Biomech.*, 2002,

35, 1523–1531.

[76] A. Gefen, E. Haberman, "Viscoelastic properties of ovine adipose tissue covering the gluteus muscles", *J. Biomech. Eng.*, 2007, **129**, 924–930.

[77] A. Samani, D. Plewes, "A method to measure the hyperelastic parameters of ex vivo breast tissue samples", *Phys. Med. Biol.*, 2004, **49**, 4395–4405.

[78] A. Samani, J. Zubovits, D. Plewes, "Elastic moduli of normal and pathological human breast tissues: An inversion-technique-based investigation of 169 samples", *Phys. Med. Biol.*, 2007, **52**, 1565–1576.

[79] R. Sinkus, M. Tanterb, T. Xydeasc, S. Cathelineb, J. Bercoffb, M. Fink, "Viscoelastic shear properties of in vivo breast lesions measured by MR elastography", *Magn. Reson. Imaging*., 2005, **23**, 159–165.

[80] J.B. Weaver, M. Doyley, Y. Cheung, F. Kennedy, E.L. Madsen, E.E.W. Van Houten, K. Paulsen, "Imaging the shear modulus of the heel fat pads", *Clin. Biomech.*, 2005, **20**, 312–319.

[81] K. Comley, N. Fleck, "The mechanical response of porcine adipose tissue", *J. Biomech. Eng.*, 2009, 1–30.

[82] N. Shoham, A.L. Sasson, F.H. Lin, D. Benayahu, R. Haj-Ali, A. Gefen, "The mechanics of hyaluronic acid/adipic acid dihydrazide hydrogel: Towards developing a vessel for delivery of preadipocytes to native tissues", *J. Mech. Behav. Biomed. Mater.*, 2013, **28**, 320–331.

[83] D.E. Jaalouk, J. Lammerding, "Mechanotransduction gone awry", *Nat. Rev. Mol. Cell Biol.*, 2009, **10**, 63–73.

[84] P.N. Patel, C.K. Smith, C.W. Patrick, "Rheological and recovery properties of poly(ethylene glycol) diacrylate hydrogels and human adipose tissue", *J. Biomed. Mater. Res. A.*, 2005, **73**, 313–319.

[85] E.E.W. Van Houten, M.M. Doyley, F.E. Kennedy, J.B. Weaver, K.D. Paulsen, "Initial in vivo experience with steady-state subzone-based MR elastography of the human breast", *J. Magn. Reson. Imaging*., 2003, **17**, 72–85.

[86] A. Gefen, M. Megido-Ravid, Y. Itzchak, "In vivo biomechanical behavior of the human heel pad during the stance phase of gait", *J. Biomech.*, 2001, **34**, 1661–1665.

[87] M. Geerligs, G.W.M. Peters, P.A.J. Ackermans, C.W.J. Oomens, F.P.T. Baaijens, "Linear viscoelastic behavior of subcutaneous adipose tissue", *Biorheology*, 2008, **45**, 677–688.

[88] I. Schoemaker, P.P.W. Hoefnagel, T.J. Mastenbroek, C.F. Kolff, S. Schutte, F.C.T. Van Der Helm, S.J. Picken, A.F.C. Gerritsen, P.A. Wielopolski, H. Spekreijse, H.J. Simonsz, "Elasticity, viscosity, and deformation of orbital fat", *Investig. Ophthalmol. Vis. Sci.*, 2006, **47**, 4819–4826.

[89] C.W. Patrick, "Adipose tissue engineering : The future of breast and soft tissue reconstruction following tumor resection", *Semin. Surg. Oncol.*, 2000, **19**, 302–311.

[90] L.P. Bucky, I. Percec, "The Science of Autologous Fat Grafting : Views on Current and Future Approaches", *Aesthetic Surg. J.*, 2008, **28**, 313–321.

[91] C.W. Patrick, P.B. Chauvin, J. Hobley, G.P. Reece, "Preadipocyte seeded PLGA scaffolds for adipose tissue engineering", *Tissue Eng.*, 1999, **5**, 139–151.

[92] C.W. Patrick, "Engineering Adipose Tissue for Regenerative and Reparative

Therapies", *Semin. Plast. Surg.*, 2005, **19**, 207–215.
[93] D.A. De Ugarte, K. Morizono, A. Elbarbary, Z. Alfonso, P.A. Zuk, M. Zhu, J.L. Dragoo, P. Ashjian, B. Thomas, P. Benhaim, I. Chen, J. Fraser, M.H. Hedrick, "Comparison of Multi-Lineage Cells from Human Adipose Tissue and Bone Marrow", *Cells Tissues Organs*., 2003, **174**, 101–109.
[94] F.P. Barry, J.M. Murphy, "Mesenchymal stem cells: clinical applications and biological characterization", *Int. J. Biochem. Cell Biol.*, 2004, **36**, 568–584.
[95] J. Ringe, C. Kaps, G.R. Burmester, M. Sittinger, "Stem cells for regenerative medicine: advances in the engineering of tissues and organs", *Naturwissenschaften*, 2002, **89**, 338–351.
[96] D.A. De Ugarte, P.H. Ashjian, A. Elbarbary, M.H. Hedrick, "Future of fat as raw material for tissue regeneration", *Ann. Plast. Surg.*, 2003, **50**, 215–219.
[97] S.S. Tholpady, R. Llull, R.C. Ogle, J.P. Rubin, J.W. Futrell, A.J. Katz, "Adipose tissue: stem cells and beyond", *Clin. Plast. Surg.*, 2006, **33**, 55–62.
[98] T.M. Liu, M. Martina, D.W. Hutmacher, J.H.P. Hui, E.H. Lee, B. Lim, "Identification of common pathways mediating differentiation of bone marrow- and adipose tissue-derived human mesenchymal stem cells into three mesenchymal lineages.", *Stem Cells*., 2007, **25**, 750–760.
[99] F. Giorgino, L. Laviola, J.W. Eriksson, "Regional differences of insulin action in adipose tissue: insights from in vivo and in vitro studies", *Acta Physiol. Scand.*, 2005, **183**, 13–30.
[100] K.J. Burg, T. Boland, "Minimally invasive tissue engineering composites and cell printing", *IEEE Eng. Med. Bilogy Mag.*, 2003, **22**, 84–91.
[101] C.T. Gomillion, A.N. Cavin, S.E. Ellis, K.J.L. Burg, “Evaluation of tissue engineered injectable devices for breast tissue engineering”, in: Transactions of the 30th annual meeting of the Society for Biomaterials, Memphis, Texas. 2005.
[102] K. Hemmrich, K. Van de Sijpe, N.P. Rhodes, J.A. Hunt, C. Di Bartolo, N. Pallua, P. Blondeel, D. von Heimburg, "Autologous in vivo adipose tissue engineering in hyaluronan-based gels - A pilot study", *J. Surg. Res.*, 2008, **144**, 82–88.
[103] K.J.L. Burg, C.E. Austin, C.R. Culberson, K.G. Greene, C.R. Halberstadt, W.D. Holder Jr., E. Al., “A novel approach to tissue engineering: injectable composites”, in: Transactions of the 2000 world biomaterials congress, Kona, Hawaii, 2000.
[104] Y.S. Choi, S.N. Park, H. Suh, "Adipose tissue engineering using mesenchymal stem cells attached to injectable PLGA spheres", *Biomaterials*, 2005, **26**, 5855–5863.
[105] Y.S. Choi, S.M. Cha, Y.Y. Lee, S.W. Kwon, C.J. Park, M. Kim, "Adipogenic differentiation of adipose tissue derived adult stem cells in nude mouse", *Biochem. Biophys. Res. Commun.*, 2006, **345**, 631–637.
[106] J.P. Rubin, J.M. Bennett, J.S. Doctor, B.M. Tebbets, K.G. Marra, "Collagenous microbeads as a scaffold for tissue engineering with adipose-derived stem cells", *Plast. Reconstr. Surg.*, 2007, **120**, 414–424.
[107] S. Natesan, D.G. Baer, T.J. Walters, M. Babu, R.J. Christy, "Adipose-derived stem cell delivery into collagen gels using chitosan microspheres", *Tissue Eng. A*, 2010, **16**, 1369–1384.
[108] M.L. Moya, M.H. Cheng, J.J. Huang, M.E. Francis-Sedlak, S.W. Kao, E.C. Opara,

E.M. Brey, "The effect of FGF-1 loaded alginate microbeads on neovascularization and adipogenesis in a vascular pedicle model of adipose tissue engineering", *Biomaterials*, 2010, **31**, 2816–2826.

[109] Y. Kimura, M. Ozeki, T. Inamoto, Y. Tabata, "Time course of de novo adipogenesis in matrigel by gelatin microspheres incorporating basic fibroblast growth factor", *Tissue Eng.*, 2002, **8**, 603–613.

[110] T. Masuda, M. Furue, T. Matsuda, "Novel strategy for soft tissue augmentation based on transplantation of fragmented omentum and preadipocytes", *Tissue Eng.*, 2004, **10**, 1672–1683.

[111] N. Kawaguchi, K. Toriyama, E. Nicodemou-Lena, K. Inou, S. Torii, Y. Kitagawa, "De novo adipogenesis in mice at the site of injection of basement membrane and basic fibroblast growth factor", *Proc. Natl. Acad. Sci. U. S. A.*, 1998, **95**, 1062–1066.

[112] Y. Tabata, M. Miyao, T. Inamoto, T. Ishii, Y. Hirano, Y. Yamaoki, Y. Ikada, "De novo formation of adipose tissue by controlled release of basic fibroblast growth factor", *Tissue Eng.*, 2000, **6**, 279–89.

[113] K. Toriyama, N. Kawaguchi, J. Kitoh, R. Tajima, K. Inou, Y. Kitagawa, S. Torii, "Endogenous adipocyte precursor cells for regenerative soft-tissue engineering", *Tissue Eng.*, 2002, **8**, 157–165.

[114] T. Masuda, M. Furue, T. Matsuda, "Photocured, styrenated gelatin-based microspheres for de novo adipogenesis through corelease of basic fibroblast growth factor, insulin, and insulin-like growth factor I", *Tissue Eng.*, 2004, **10**, 523–535.

[115] E. Yuksel, A.B. Weinfeld, R. Cleek, J.M. Waugh, J. Jensen, S. Boutros, S.M. Shenaq, M. Spira, "De novo adipose tissue generation through long-term, local delivery of insulin and insulin-like growth factor-1 by PLGA/PEG microshperes in an in vivo rat model: a novel concept and capability", *Plast. Reconstr. Surg.*, 2000, **105**, 1721–1729.

[116] A.V. Vashi, K.M. Abberton, G.P. Thomas, W.A. Morrison, A.J. O'Connor, J.J. Cooper-White, E.W. Thompson, "Adipose tissue engineering based on the controlled release of fibroblast growth factor-2 in a collagen matrix", *Tissue Eng.*, 2006, **12**, 3035–3043.

[117] R.L. Walton, E.K. Beahm, L. Wu, "De novo adipose formation in a vascularized engineered construct", *Microsurgery*, 2004, **24**, 378–384.

[118] J.H. Dolderer, K.M. Abberton, E.W. Thompson, J.L. Slavin, G.W. Stevens, A.J. Penington, W.A. Morrison, "Spontaneous large volume adipose tissue generation from a vascularized pedicled fat flap inside a chamber space", *Tissue Eng.*, 2007, **13**, 673–681.

[119] K.J. Cronin, A. Messina, K.R. Knight, J.J. Cooper-White, G.W. Stevens, A.J. Penington, W.A. Morrison, "New murine model of spontaneous autologous tissue engineering, combining an arteriovenous pedicle with matrix materials", *Plast. Reconstr. Surg.*, 2004, **113**, 260–269.

[120] P.S. Wiggenhauser, D.F. Müller, F.P. Melchels, J.T. Egaña, K. Storck, H. Mayer, P. Leuthner, D. Skodacek, U. Hopfner, H.G. Machens, R. Staudenmaier, J.T. Schantz, "Engineering of vascularized adipose constructs", *Cell Tissue Res.*, 2012, **347**, 747–757.

[121] B. Weiser, L. Prantl, T.E.O. Schubert, J. Zellner, C. Fischbach-Teschl, T. Spruss, A.K.

Seitz, J. Tessmar, A. Goepferich, T. Blunk, "In vivo development and long-term survival of engineered adipose tissue depend on in vitro precultivation strategy", *Tissue Eng. A*, 2008, **14**, 275–284.

[122] D.A. Young, K.L. Christman, "Injectable biomaterials for adipose tissue engineering", *Biomed. Mater.*, 2012, **7**, 024104.

[123] A.K.L. Chen, S. Reuveny, S.K.W. Oh, "Application of human mesenchymal and pluripotent stem cell microcarrier cultures in cellular therapy: Achievements and future direction.", *Biotechnol. Adv.*, 2013, **31**, 1032–46.

[124] G.E. Wnek, G.L. Bowlin, Encyclopedia of Biomaterials and Biomedical Engineering, 4 Volume Set, Second Edition, New York: CRC Press, 2008, 1–3552.

[125] E. Lavik, R. Langer, "Tissue engineering: current state and perspectives", *Appl. Microbiol. Biotechnol.*, 2004, **65**, 1–8.

[126] A.V. Vashi, E. Keramidaris, K.M. Abberton, W.A. Morrison, J.L. Wilson, A.J. O'Connor, J.J. Cooper-White, E.W. Thompson, "Adipose differentiation of bone marrow-derived mesenchymal stem cells using Pluronic F-127 hydrogel in vitro", *Biomaterials*, 2008, **29**, 573–579.

[127] J.R. Mauney, T. Nguyen, K. Gillen, C. Kirker-Head, J.M. Gimble, D.L. Kaplan, "Engineering adipose-like tissue in vitro and in vivo utilizing human bone marrow and adipose-derived mesenchymal stem cells with silk fibroin 3D scaffolds", *Biomaterials*, 2007, **28**, 5280–5290.

[128] Y. Hiraoka, H. Yamashiro, K. Yasuda, Y. Kimura, T. Inamoto, Y. Tabata, "In situ regeneration of adipose tissue in rat fat pad by combining a collagen scaffold with gelatin microspheres containing basic fibroblast growth factor", *Tissue Eng.*, 2006, **12**, 1475–1487.

[129] Y. Kimura, M. Ozeki, T. Inamoto, Y. Tabata, "Adipose tissue engineering based on human preadipocytes combined with gelatin microspheres containing basic fibroblast growth factor", *Biomaterials*, 2003, **24**, 2513–2521.

[130] K.C. O'Connor, H. Song, N. Rosenzweig, D.A. Jansen, "Extracellular matrix substrata alter adipocyte yield and lipogenesis in primary cultures of stromal-vascular cells from human adipose", *Biotechnol. Lett.*, 2003, **25**, 1967–1972.

[131] S. Neuss, R. Stainforth, J. Salber, P. Schenck, M. Bovi, R. Knüchel, a. Perez-Bouza, "Long-term survival and bipotent terminal differentiation of human mesenchymal stem cells (hMSC) in combination with a commercially available three-dimensional collagen scaffold", *Cell Transplant.*, 2008, **17**, 977–986.

[132] E. Gentleman, E.A. Nauman, G.A. Livesay, K.C. Dee, "Collagen composite biomaterials resist contraction while allowing development of adipocytic soft tissue in vitro", *Tissue Eng.*, 2006, **12**, 1639–49.

[133] W. Tsuji, T. Inamoto, H. Yamashiro, T. Ueno, H. Kato, Y. Kimura, Y. Tabata, M. Toi, "Adipogenesis induced by human adipose tissue-derived stem cells", *Tissue Eng. A*, 2009, **15**, 83–93.

[134] X. Wu, L. Black, G. Santacana-Laffitte, C.W. Patrick, "Preparation and assessment of glutaraldehyde-crosslinked collagen-chitosan hydrogels for adipose tissue engineering", *J. Biomed. Mater. Res. A*, 2007, **81**, 59–65.

[135] D. Von Heimburg, S. Zachariah, H. Kühling, I. Heschel, H. Schoof, B. Hafemann, N.

Pallua, "Human preadipocytes seeded on freeze-dried collagen scaffolds investigated in vitro and in vivo", *Biomaterials*, 2001, **22**, 429–438.

[136] S.D. Lin, S.H. Huang, Y.N. Lin, S.H. Wu, H.W. Chang, T.M. Lin, C.Y. Chai, C.S. Lai, "Engineering adipose tissue from uncultured human adipose stromal vascular fraction on collagen matrix and gelatin sponge scaffolds", *Tissue Eng. A*, 2011, **17**, 1489–1498.

[137] Y. Itoi, M. Takatori, H. Hyakusoku, H. Mizuno, "Comparison of readily available scaffolds for adipose tissue engineering using adipose-derived stem cells", *J. Plast. Reconstr. Asthetic Surg. JPRAS.*, 2010, **63**, 858–864.

[138] L.E. Flynn, G.D. Prestwich, J.L. Semple, K.A. Woodhouse, "Proliferation and differentiation of adipose-derived stem cells on naturally derived scaffolds", *Biomaterials*, 2008, **29**, 1862–1871.

[139] L. Flynn, G.D. Prestwich, J.L. Semple, K.A. Woodhouse, "Adipose tissue engineering in vivo with adipose-derived stem cells on naturally derived scaffolds", *J. Biomed. Mater. Res. A*, 2009, **89**, 929–941.

[140] A. Borzacchiello, L. Mayol, P.A. Ramires, A. Pastorello, C.D. Bartolo, L. Ambrosio, E. Milella, "Structural and rheological characterization of hyaluronic acid-based scaffolds for adipose tissue engineering", *Biomaterials*, 2007, **28**, 4399–4408.

[141] M. Halbleib, T. Skurk, C. De Luca, D. Von Heimburg, H. Hauner, "Tissue engineering of white adipose tissue using hyaluronic acid-based scaffolds. I: In vitro differentiation of human adipocyte precursor cells on scaffolds", *Biomaterials*, 2003, **24**, 3125–3132.

[142] K. Hemmrich, D. Von Heimburg, R. Rendchen, C. Di Bartolo, E. Milella, N. Pallua, "Implantation of preadipocyte-loaded hyaluronic acid-based scaffolds into nude mice to evaluate potential for soft tissue engineering", *Biomaterials*, 2005, **26**, 7025–7037.

[143] N.P. Rhodes, "Inflammatory signals in the development of tissue-engineered soft tissue", *Biomaterials*, 2007, **28**, 5131–5136.

[144] F.B. Stillaert, C. Di Bartolo, J.A. Hunt, N.P. Rhodes, E. Tognana, S. Monstrey, P.N. Blondeel, "Human clinical experience with adipose precursor cells seeded on hyaluronic acid-based spongy scaffolds", *Biomaterials*, 2008, **29**, 3953–3959.

[145] D. von Heimburg, S. Zachariah, A. Low, N. Pallua, "Influence of differerent biodegradable carriers on the in vivo behavior of adipose precursors cells", *Plast. Reconstr. Surg.*, 2001, **108**, 411–420.

[146] S. Uriel, J.J. Huang, M.L. Moya, M.E. Francis, R. Wang, S.Y. Chang, M.H. Cheng, E.M. Brey, "The role of adipose protein derived hydrogels in adipogenesis", *Biomaterials*, 2008, **29**, 3712–3719.

[147] K. Hemmrich, G.P.L. Thomas, K.M. Abberton, E.W. Thompson, J.A. Rophael, A.J. Penington, W.A. Morrison, "Monocyte chemoattractant protein-1 and nitric oxide promote adipogenesis in a model that mimics obesity", *Obesity*, 2007, **15**, 2951–2957.

[148] J.H. Piasecki, K.A. Gutowski, G.P. Lahvis, K.I. Moreno, "An Experimental Model for Improving Fat Graft Viability and Purity", *Plast. Reconstr. Surg.*, 2007, **119**, 1571–1583.

[149] J.A. Rophael, R.O. Craft, J.A. Palmer, A.J. Hussey, G.P.L. Thomas, W.A. Morrison, A.J. Penington, G.M. Mitchell, "Angiogenic growth factor synergism in a murine tissue engineering model of angiogenesis and adipogenesis", *Am. J. Pathol.*, 2007, **171**, 2048–2057.

[150] M.H. Cheng, S. Uriel, M.L. Moya, M. Francis-Sedlak, R. Wang, J.J. Huang, S.Y. Chang, E.M. Brey, "Dermis-derived hydrogels support adipogenesis in vivo.", *J. Biomed. Mater. Res. A*, 2010, **92**, 852–858.

[151] N. Kawaguchi, K. Toriyama, E. Nicodemou-Lena, K. Inou, S. Torii, Y. Kitagawa, "Reconstituted basement membrane potentiates in vivo adipogenesis of 3T3-F442A cells.", *Cytotechnology*, 1999, **31**, 215–220.

[152] K.J. Cronin, A. Messina, E.W. Thompson, W.A. Morrison, G.W. Stevens, K.R. Knight, "The role of biological extracellular matrix scaffolds in vascularized three-dimensional tissue growth in vivo", *J. Biomed. Mater. Res. B*, 2007, **82**, 122–128.

[153] J.J. Marler, A. Guha, J. Rowley, R. Koka, D. Mooney, J. Upton, J.P. Vacanti, "Soft-tissue augmentation with injectable alginate and syngeneic fibroblasts", *Plast. Reconstr. Surg.*, 2000, **105**, 2049–2058.

[154] W.S. Kim, D.J. Mooney, P.R. Arany, K. Lee, N. Huebsch, J. Kim, "Adipose tissue engineering using injectable, oxidized alginate hydrogels", *Tissue Eng. A*, 2012, **18**, 737–743.

[155] R. Yao, R. Zhang, F. Lin, J. Luan, "Biomimetic injectable HUVEC-adipocytes/collagen/alginate microsphere co-cultures for adipose tissue engineering", *Biotechnol. Bioeng.*, 2013, **110**, 1430–1443.

[156] D. Jaikumar, K.M. Sajesh, S. Soumya, T.R. Nimal, K.P. Chennazhi, S.V. Nair, R. Jayakumar, "Injectable alginate-O-carboxymethyl chitosan/nano fibrin composite hydrogels for adipose tissue engineering", *Int. J. Biol. Macromol.*, 2015, **74**, 318–326.

[157] S.W. Cho, K.W. Song, J.W. Rhie, M.H. Park, C.Y. Choi, B.-S. Kim, "Engineered adipose tissue formation enhanced by basic fibroblast growth factor and a mechanically stable environment", *Cell Transplant.*, 2007, **16**, 421–434.

[158] S.W. Cho, S.S. Kim, J. Won Rhie, H. Mi Cho, C. Yong Choi, B.S. Kim, "Engineering of volume-stable adipose tissues", *Biomaterials*, 2005, **26**, 3577–3585.

[159] J. Borges, M.C. Mueller, N.T. Padron, F. Tegtmeier, E.M. Lang, G.B. Stark, "Engineered adipose tissue supplied by functional microvessels", *Tissue Eng.*, 2003, **9**, 1263–1270.

[160] S.W. Cho, I. Kim, S.H. Kim, J.W. Rhie, C.Y. Choi, B.S. Kim, "Enhancement of adipose tissue formation by implantation of adipogenic-differentiated preadipocytes", *Biochem. Biophys. Res. Commun.*, 2006, **345**, 588–594.

[161] N. Torio-Padron, N. Baerlecken, A. Momeni, G.B. Stark, J. Borges, "Engineering of adipose tissue by injection of human preadipocytes in fibrin", *Aesthetic Plast. Surg.*, 2007, **31**, 285–293.

[162] S.D. Lin, K.-H. Wang, A.P. Kao, "Engineered adipose tissue of predefined shape and dimensions from human adipose-derived mesenchymal stem cells", *Tissue Eng. A*, 2008, **14**, 571–581.

[163] L. Hong, I. Peptan, P. Clark, J.J. Mao, "Ex vivo adipose tissue engineering by human marrow stromal cell seeded gelatin sponge", *Ann. Biomed. Eng.*, 2005, **33**, 511–517.

[164] J.H. Choi, E. Bellas, G. Vunjak-Novakovic, D.L. Kaplan, "Adipogenic Differentiation of Human Adipose-Derived Stem Cells on 3D Silk Scaffolds", *Methods Mol. Biol.*, 2011, **702**, 319–330.

[165] E. Bellas, K.G. Marra, D.L. Kaplan, "Sustainable three-dimensional tissue model of

human adipose tissue", *Tissue Eng. C*, 2013, **19**, 745–754.
[166] J.H. Kang, J.M. Gimble, D.L. Kaplan, "In vitro 3D model for human vascularized adipose tissue", *Tissue Eng. A*, 2009, **15**, 2227–2236.
[167] M. Vermette, V. Trottier, V. Ménard, L. Saint-Pierre, A. Roy, J. Fradette, "Production of a new tissue-engineered adipose substitute from human adipose-derived stromal cells", *Biomaterials*, 2007, **28**, 2850–2860.
[168] M. Vallée, J.F. Côté, J. Fradette, "Adipose-tissue engineering: Taking advantage of the properties of human adipose-derived stem/stromal cells", *Pathol. Biol.*, 2009, **57**, 309–317.
[169] M.E. Nimni, D. Cheung, B. Strates, M. Kodama, K. Sheikh, "Chemically modified collagen: a natural biomaterial for tissue replacement", *J. Biomed. Mater. Res.*, 1987, **21**, 741–771.
[170] B.S. Kim, C.E. Baez, A. Atala, "Biomaterials for tissue engineering", *World J. Urol.*, 2000, **18**, 2–9.
[171] R. Parenteau-Bareil, R. Gauvin, F. Berthod, "Collagen-based biomaterials for tissue engineering applications", *Materials*, 2010, **3**, 1863–1887.
[172] V. Vindigni, R. Cortivo, L. Iacobellis, G. Abatangelo, B. Zavan, "Hyaluronan benzyl ester as a scaffold for tissue engineering", *Int. J. Mol. Sci.*, 2009, **10**, 2972–2985.
[173] J.A. Burdick, G.D. Prestwich, "Hyaluronic acid hydrogels for biomedical applications", *Adv. Healthc. Mater.*, 2011, **23**, H41–H56.
[174] M.N. Collins, C. Birkinshaw, "Hyaluronic acid based scaffolds for tissue engineering-a review", *Carbohydr. Polym.*, 2013, **92**, 1262–1279.
[175] S.K. Seidlits, Z.Z. Khaing, R.R. Petersen, J.D. Nickels, J.E. Vanscoy, J.B. Shear, C.E. Schmidt, "The effects of hyaluronic acid hydrogels with tunable mechanical properties on neural progenitor cell differentiation", *Biomaterials*, 2010, **31**, 3930–3940.
[176] J.M. Cloyd, N.R. Malhotra, L. Weng, W. Chen, R.L. Mauck, D.M. Elliott, "Material properties in unconfined compression of human nucleus pulposus, injectable hyaluronic acid-based hydrogels and tissue engineering scaffolds", *Eur. Spine J.*, 2007, **16**, 1892–1898.
[177] A. Casadei, R. Epis, L. Ferroni, I. Tocco, C. Gardin, E. Bressan, S. Sivolella, V. Vindigni, P. Pinton, G. Mucci, B. Zavan, "Adipose tissue regeneration: A state of the art", *J. Biomed. Biotechnol.*, 2012, **2012**, 462543.
[178] H.K. Kleinman, G.R. Martin, "Matrigel: basement membrane matrix with biological activity", *Semin. Cancer Biol.*, 2005, **15**, 378–386.
[179] J. Alcaraz, R. Xu, H. Mori, C.M. Nelson, R. Mroue, V.A. Spencer, D. Brownfield, D.C. Radisky, C. Bustamante, M.J. Bissell, "Laminin and biomimetic extracellular elasticity enhance functional differentiation in mammary epithelia", *EMBO J.*, 2008, **27**, 2829–2838.
[180] J. Reed, W.J. Walczak, O.N. Petzold, J.K. Gimzewski, "In situ mechanical interferometry of Matrigel™ films", *Langmuir*, 2009, **25**, 36–39.
[181] S.S. Soofi, J.A. Last, S.J. Liliensiek, P.F. Nealey, C.J. Murphy, "The elastic modulus of Matrigel as determined by atomic force microscopy", *J. Struct. Biol.*, 2009, **167**, 216–219.
[182] J.A. Wood, S.J. Liliensiek, P. Russell, P.F. Nealey, C.J. Murphy, "Biophysical cueing

and vascular endothelial cell behavior", *Materials*, 2010, **3**, 1620–1639.
[183] J.H. Piasecki, K.A. Gutowski, K.M. Moreno, G.L. Lahvis, "Purified viable fat suspended in matrigel improves volume longevity", *Asthetic Surg. J.*, 2008, **28**, 24–32.
[184] K. Hemmrich, D. von Heimburg, "Biomaterials for adipose tissue engineering", *Expert Rev. Med. Devices*., 2006, **3**, 635–645.
[185] R.M. Shanti, S. Janjanin, W.-J. Li, L.J. Nesti, M.B. Mueller, M.B. Tzeng, R.S. Tuan, "In vitro adipose tissue engineering using an electrospun nanofibrous scaffold", *Ann. Plast. Surg.*, 2008, **61**, 566–571.
[186] A. Chaubey, K.J. Ross, R.M. Leadbetter, K.J. Burg, "Surface patterning: tool to modulate stem cell differentiation in an adipose system", *J. Biomed. Mater. Res. B*, 2008, **84**, 70–78.
[187] C. Fischbach, T. Spruß, B. Weiser, M. Neubauer, C. Becker, M. Hacker, A. Göpferich, T. Blunk, "Generation of mature fat pads in vitro and in vivo utilizing 3-D long-term culture of 3T3-L1 preadipocytes", *Exp. Cell Res.*, 2004, **300**, 54–64.
[188] S.W. Kang, S.W. Seo, C.Y. Choi, B.S. Kim, "Porous poly(lactic-co-glycolic acid) microsphere as cell culture substrate and cell transplantation vehicle for adipose tissue engineering", *Tissue Eng. C*, 2008, **14**, 25–34.
[189] M. Neubauer, M. Hacker, P. Bauer-Kreisel, B. Weiser, C. Fischbach, M.B. Schulz, A. Goepferich, T. Blunk, "Adipose tissue engineering based on mesenchymal stem cells and basic fibroblast growth factor in vitro", *Tissue Eng.*, 2005, **11**, 1840–1851.
[190] C.W. Patrick, B. Zheng, C. Johnston, G.P. Reece, "Long-term implantation of preadipocyte-seeded PLGA scaffolds", *Tissue Eng.*, 2002, **8**, 283–293.
[191] S.M. Morgan, B.J. Ainsworth, J.M. Kanczler, J.C. Babister, J.B. Chaudhuri, R.O.C. Oreffo, "Formation of a human-derived fat tissue layer in PDLLGA hollow fibre scaffolds for adipocyte tissue engineering", *Biomaterials*, 2009, **30**, 1910–1917.
[192] Y.S. Choi, S.N. Park, H. Suh, "The effect of PLGA sphere diameter on rabbit mesenchymal stem cells in adipose tissue engineering", *J. Mater. Sci. Mater. Med.*, 2008, **19**, 2165–2171.
[193] H.J. Chung, T.G. Park, "Injectable cellular aggregates prepared from biodegradable porous microspheres for adipose tissue engineering", *Tissue Eng. A*, 2009, **15**, 1391–400.
[194] K.G. Marra, A.J. Defail, J.A. Clavijo-Alvarez, S.F. Badylak, A. Taieb, B. Schipper, J. Bennett, J.P. Rubin, "FGF-2 enhances vascularization for adipose tissue engineering", *Plast. Reconstr. Surg.*, 2008, **121**, 1153–1164.
[195] X. Kang, Y. Xie, H.M. Powell, L. James Lee, M.A. Belury, J.J. Lannutti, D.A. Kniss, "Adipogenesis of murine embryonic stem cells in a three-dimensional culture system using electrospun polymer scaffolds", *Biomaterials*, 2007, **28**, 450–458.
[196] A. Alhadlaq, M. Tang, J.J. Mao, "Engineered adipose tissue from human mesenchymal stem cells maintains predefined shape and dimension: Implications in soft tissue augmentation and reconstruction.", *Tissue Eng.*, 2005, **11**, 556–566.
[197] E.N. Lamme, D. Druecke, J. Pieper, P.S. May, P. Kaim, F. Jacobsen, H.-U. Steinau, L. Steinstraesser, "Long-term evaluation of porous PEGT/PBT implants for soft tissue augmentation", *J. Biomater. Appl.*, 2008, **22**, 309–335.
[198] F.P. Brandl, A.K. Seitz, J.K.V. Teßmar, T. Blunk, A.M. Göpferich, "Enzymatically

degradable poly(ethylene glycol) based hydrogels for adipose tissue engineering", *Biomaterials*, 2010, **31**, 3957–3966.

[199] M.S. Stosich, J.J. Mao, "Adipose tissue engineering from human adult stem cells: Clinical implications in plastic and reconstructive surgery", *Plast. Reconstr. Surg.*, 2007, **119**, 71–85.

[200] A.T. Hillel, S. Varghese, J. Petsche, M.J. Shamblott, J.H. Elisseeff, "Embryonic germ cells are capable of adipogenic differentiation in vitro and in vivo", *Tissue Eng. A*, 2009, **15**, 479–486.

[201] P.N. Patel, A.S. Gobin, J.L. West, C.W.J. Patrick, "Poly(ethylene glycol) hydrogel system supports preadipocyte viability, adhesion, and proliferation", *Tissue Eng.*, 2005, **11**, 1498–1505.

[202] D.H. Stacey, S.E. Hanson, G. Lahvis, K.A. Gutowski, K.S. Masters, "In vitro adipogenic differentiation of preadipocytes varies with differentiation stimulus, culture dimensionality, and scaffold composition", *Tissue Eng. A*, 2009, **15**, 3389–3399.

[203] A. Gugerell, J. Kober, T. Laube, T. Walter, S. Nürnberger, E. Grönniger, S. Brönneke, R. Wyrwa, M. Schnabelrauch, M. Keck, "Electrospun poly(ester-urethane)- and poly(ester-urethane-urea) fleeces as promising tissue engineering scaffolds for adipose-derived stem cells", *PLoS One*., 2014, **9**, e90676.

[204] X. Kang, Y. Xie, D.A. Kniss, "Adipose tissue model using three-dimensional cultivation of preadipocytes seeded onto fibrous polymer scaffolds", *Tissue Eng.*, 2005, **11**, 458–468.

[205] J.A. Clavijo-Alvarez, J.P. Rubin, J. Bennett, V.T. Nguyen, J. Dudas, C. Underwood, K.G. Marra, "A novel perfluoroelastomer seeded with adipose-derived stem cells for soft-tissue repair", *Plast. Reconstr. Surg.*, 2006, **118**, 1132–1142.

[206] J.G. Kral, D.L. Crandall, "Development of a human adipocyte synthetic polymer scaffold", *Plast. Reconstr. Surg.*, 1999, **104**, 1732–1738.

[207] M.I. Sabir, X. Xu, L. Li, "A review on biodegradable polymeric materials for bone tissue engineering applications", *J. Mater. Sci.*, 2009, **44**, 5713–5724.

[208] I. Vroman, L. Tighzert, "Biodegradable Polymers", *Materials (Basel).*, 2009, **2**, 307–344.

[209] ASM International, Materials and Coatings for Medical Devices: Cardiovascular, Ohio: ASM International, 2009, 1–444.

[210] A.J.R. Lasprilla, G.A.R. Martinez, B.H. Lunelli, A.L. Jardini, R.M. Filho, "Poly-lactic acid synthesis for application in biomedical devices - A review", *Biotechnol. Adv.*, 2012, **30**, 321–328.

[211] M.A. Woodruff, D.W. Hutmacher, "The return of a forgotten polymer - Polycaprolactone in the 21st century", *Prog. Polym. Sci.*, 2010, **35**, 1217–1256.

[212] C. Bastioli, Handbook of Biodegradable Polymers, Shropshire: Rapra Technology Limted, 2005, 1–552.

[213] S. Eshraghi, S. Das, "Mechanical and microstructural properties of polycaprolactone scaffolds with 1-D, 2-D, and 3-D orthogonally oriented porous architectures produced by selective laser sintering", *Acta Biomater.*, 2010, **6**, 2467–2476.

[214] J. Zhu, R.E. Marchant, "Design properties of hydrogel tissue-engineering scaffolds", *Expert Rev. Med. Devices*., 2011, **8**, 607–626.

[215] J.P. Mazzoccoli, D.L. Feke, H. Baskaran, P.N. Pintauro, "Mechanical and cell viability properties of crosslinked low- and high-molecular weight poly(ethylene glycol) diacrylate blends", *J. Biomed. Mater. Res. A*, 2010, **93**, 558–566.

[216] J. Malda, T.B. Woodfield, F. van der Vloodt, C. Wilson, D.E. Martens, J. Tramper, C.A. van Blitterswijk, J. Riesle, "The effect of PEGT/PBT scaffold architecture on the composition of tissue engineered cartilage", *Biomaterials*, 2005, **26**, 63–72.

[217] A. El-Ghalbzouri, E.N. Lamme, C. van Blitterswijk, J. Koopman, M. Ponec, "The use of PEGT/PBT as a dermal scaffold for skin tissue engineerin", *Biomaterials*, 2004, **25**, 2978–2996.

[218] J. Malda, T.B. Woodfield, F. van der Vloodt, F.K. Kooy, D.E. Martens, J. Tramper, C.A. van Blitterswijk, J. Riesle, "The effect of PEGT/PBT scaffold architecture on oxygen gradients in tissue engineered cartilaginous constructs", *Biomaterials*, 2004, **25**, 5773–5780.

[219] S.A. Guelcher, "Biodegradable polyurethanes: synthesis and applications in regenerative medicine", *Tissue Eng. B*, 2008, **14**, 3–17.

[220] H. Janik, M. Marzec, "A review: Fabrication of porous polyurethane scaffolds", *Mater. Sci. Eng. C*., 2015, **48**, 586–591.

[221] B. Ellis, R. Smith, Polymers: A property database, Second edition, Boca Raton: CRC Press - Taylor & Francis Group, 2009, 1–1052.

[222] J.E. Mark, Polymer Data Handbook, Oxford: Oxford Press, 1999, 1–1018.

[223] C.A. Harper, Handbook of Plastics, Elastomers, and Composites, Second Edition, New York: MacGraw-Hill, 1992, 1–768.

[224] K. Modjarrad, S. Ebnesajjad, Handbook of Polymer Applications in Medicine and Medical Devices, Oxford: Elsevier, 2014, 1–278.

[225] C. Legnani, A. Ventura, C. Terzaghi, E. Borgo, W. Albisetti, "Anterior cruciate ligament reconstruction with synthetic grafts. A review of literature", *Int. Orthop.*, 2010, **34**, 465–471.

[226] B. Veleirinho, D.S. Coelho, P.F. Dias, M. Maraschin, R. Pinto, E. Cargnin-Ferreira, A. Peixoto, J.A. Souza, R.M. Ribeiro-do-Valle, J.A. Lopes-da-Silva, "Foreign body reaction associated with PET and PET/chitosan electrospun nanofibrous abdominal meshes", *PLoS One*., 2014, **9**, e95293.

[227] Y. Bilsel, I. Abci, "The search for ideal hernia repair; mesh materials and types", *Int. J. Surg.*, 2012, **10**, 317–321.

[228] S. Ravi, E.L. Chaikof, "Biomaterials for vascular tissue engineering", *Regen. Med.*, 2010, **5**, 107–120.

[229] Y. Kinoshita, H. Maeda, "Recent developments of functional scaffolds for craniomaxillofacial bone tissue engineering applications", *Sci. World J.*, 2013, **2013**, 863157.

[230] A.U. Daniels, "Silicone breast implant materials", *Swiss Med. Wkly.*, 2012, **142**, w13614.

[231] T.J. Gampper, H. Khoury, W. Gottlieb, R.F. Morgan, "Silicone gel implants in breast augmentation and reconstruction", *Ann. Plast. Surg.*, 2007, **59**, 581–590.

[232] K. Gerszten, P.C. Gerszten, "Silicone Breast Implants: An Oncologic Perspective", *Oncology*, 1998, **12**, 1439–1443.

[233] C.A. Sundback, J.Y. Shyu, Y. Wang, W.C. Faquin, R.S. Langer, J.P. Vacanti, T.A. Hadlock, "Biocompatibility analysis of poly(glycerol sebacate) as a nerve guide material", *Biomaterials*, 2005, **26**, 5454–5464.

[234] H. Park, B.L. Larson, M.D. Guillemette, S.R. Jain, C. Hua, G.C. Engelmayr, L.E. Freed, "The significance of pore microarchitecture in a multi-layered elastomeric scaffold for contractile cardiac muscle constructs", *Biomaterials*, 2011, **32**, 1856–1864.

[235] R. Maidhof, A. Marsano, E.J. Lee, G. Vunjak-Novakovic, "Perfusion seeding of channeled elastomeric scaffolds with myocytes and endothelial cells for cardiac tissue engineering", *Biotechnol. Prog.*, 2010, **26**, 565–572.

[236] M. Radisic, H. Park, T.P. Martens, J.E. Salazar-Lazaro, W. Geng, Y. Wang, R. Langer, L.E. Freed, G. Vunjak-Novakovic, "Pre-treatment of synthetic elastomeric scaffolds by cardiac fibroblasts improves engineered heart tissue", *J. Biomed. Mater. Res. A*, 2008, **86**, 713–724.

[237] Q.Z. Chen, A. Bismarck, U. Hansen, S. Junaid, M.Q. Tran, S.E. Harding, N.N. Ali, A.R. Boccaccini, "Characterisation of a soft elastomer poly(glycerol sebacate) designed to match the mechanical properties of myocardial tissue", *Biomaterials*, 2008, **29**, 47–57.

[238] W.L. Neeley, S. Redenti, H. Klassen, S. Tao, T. Desai, M.J. Young, R. Langer, "A microfabricated scaffold for retinal progenitor cell grafting", *Biomaterials*, 2008, **29**, 418–426.

[239] S. Redenti, W.L. Neeley, S. Rompani, S. Saigal, J. Yang, H. Klassen, R. Langer, M.J. Young, "Engineering retinal progenitor cell and scrollable poly(glycerol-sebacate) composites for expansion and subretinal transplantation", *Biomaterials*, 2009, **30**, 3405–3414.

[240] D. Motlagh, J. Yang, K.Y. Lui, A.R. Webb, G.A. Ameer, "Hemocompatibility evaluation of poly(glycerol-sebacate) in vitro for vascular tissue engineering", *Biomaterials*, 2006, **27**, 4315–4324.

[241] J. Gao, A.E. Ensley, R.M. Nerem, Y. Wang, "Poly(glycerol sebacate) supports the proliferation and phenotypic protein expression of primary baboon vascular cells", *J. Biomed. Mater. Res. A*, 2007, **83**, 1070–1075.

[242] J.M. Kemppainen, S.J. Hollister, "Tailoring the mechanical properties of 3D-designed poly(glycerol sebacate) scaffolds for cartilage applications", *J. Biomed. Mater. Res. A*, 2010, **94**, 9–18.

[243] X. Zhao, Y. Wu, Y. Du, X. Chen, B. Lei, Y. Xue, P.X. Ma, "A highly bioactive and biodegradable poly(glycerol sebacate)–silica glass hybrid elastomer with tailored mechanical properties for bone tissue regeneration", *J. Mater. Chem. B*, 2015, **3**, 3222–3233.

[244] Z.J. Sun, C. Chen, M.Z. Sun, C.H. Ai, X.L. Lu, Y.F. Zheng, B.F. Yang, D.L. Dong, "The application of poly (glycerol-sebacate) as biodegradable drug carrier", *Biomaterials*, 2009, **30**, 5209–5214.

[245] Q.Z. Chen, S. Liang, G.A. Thouas, "Synthesis and characterisation of poly(glycerol sebacate)-co-lactic acid as surgical sealants", *Soft Matter*., 2011, **7**, 6484.

[246] A. Mahdavi, L. Ferreira, C. Sundback, J.W. Nichol, E.P. Chan, D.J.D. Carter, C.J. Bettinger, S. Patanavanich, L. Chignozha, E. Ben-Joseph, A. Galakatos, H. Pryor, I.

Pomerantseva, P.T. Masiakos, W. Faquin, A. Zumbuehl, S. Hong, J. Borenstein, J. Vacanti, R. Langer, J.M. Karp, “A biodegradable and biocompatible gecko-inspired tissue adhesive", *Proc. Natl. Acad. Sci. U. S. A.*, 2008, **105**, 2307–2312.

[247] M.F. Yanik, "Towards gecko-feet-inspired bandages", *Trends Biotechnol.*, 2009, **27**, 1–2.

[248] D. Lin, K. Yang, W. Tang, Y. Liu, Y. Yuan, C. Liu, "A poly(glycerol sebacate)-coated mesoporous bioactive glass scaffold with adjustable mechanical strength, degradation rate, controlled-release and cell behavior for bone tissue engineering", *Colloids Surfaces B*, 2015, **131**, 1–11.

[249] M.J. Kim, M.Y. Hwang, J. Kim, D.J. Chung, "Biodegradable and Elastomeric Poly (glycerol sebacate) as a Coating Material for Nitinol Bare Stent", *Biomed Res. Int.*, 2014, **2014**, 956952.

[250] H. Shi, Q. Gan, X. Liu, Y. Ma, J. Hu, Y. Yuan, C. Liu, "Poly(glycerol sebacate)-modified polylactic acid scaffolds with improved hydrophilicity, mechanical strength and bioactivity for bone tissue regeneration", *RSC Adv.*, 2015, **5**, 79703–79714.

[251] I. Pomerantseva, N. Krebs, A. Hart, C.M. Neville, A.Y. Huang, C.A. Sundback, "Degradation behavior of poly(glycerol sebacate)", *J. Biomed. Mater. Res. A*, 2009, **91**, 1038–1047.

[252] I.H. Jaafar, M.M. Ammar, S.S. Jedlicka, R.A. Pearson, J.P. Coulter, "Spectroscopic evaluation, thermal, and thermomechanical characterization of poly(glycerol-sebacate) with variations in curing temperatures and durations", *J. Mater. Sci.*, 2010, **45**, 2525–2529.

[253] C.L.E. Nijst, J.P. Bruggeman, J.M. Karp, L. Ferreira, A. Zumbuehl, C.J. Bettinger, R. Langer, "Synthesis and characterization of photocurable elastomers from poly(glycerol-co-sebacate)", *Biomacromolecules*, 2007, **8**, 3067–3073.

[254] H.M. Aydin, K. Salimi, Z.M.O. Rzayevc, E. Pişkin, "Microwave-assisted rapid synthesis of poly(glycerol-sebacate) elastomers", *Biomater. Sci.*, 2013, **1**, 503–509.

[255] G.C. Engelmayr, M. Cheng, C.J. Bettinger, J.T. Borenstein, R. Langer, L.E. Freed, "Accordion-like honeycombs for tissue engineering of cardiac anisotropy", *Nat. Mater.*, 2008, **7**, 1003–1010.

[256] S.L. Liang, W.D. Cook, G.A. Thouas, Q.Z. Chen, "The mechanical characteristics and in vitro biocompatibility of poly(glycerol sebacate)-Bioglass elastomeric composites", *Biomaterials*, 2010, **31**, 8516–8529.

[257] Q.Z. Chen, S.L. Liang, J. Wang, G.P. Simon, "Manipulation of mechanical compliance of elastomeric PGS by incorporation of halloysite nanotubes for soft tissue engineering applications", *J. Mech. Behav. Biomed. Mater.*, 2011, **4**, 1805–1818.

[258] Q.Z. Chen, S.E. Harding, N.N. Ali, A.R. Lyon, A.R. Boccaccini, "Biomaterials in cardiac tissue engineering : Ten years of research survey", *Mater. Sci. Eng. R.*, 2008, **59**, 1–37.

[259] S.L. Liang, X.Y. Yang, X.Y. Fang, W.D. Cook, G.A. Thouas, Q.Z. Chen, "In Vitro enzymatic degradation of poly(glycerol sebacate)-based materials", *Biomaterials*, 2011, **32**, 8486–8496.

[260] Y. Wang, Y.M. Kim, R. Langer, "In vivo degradation characteristics of poly(glycerol sebacate)", *J. Biomed. Mater. Res. A*, 2003, **66**, 192–197.

[261] Q.Z. Chen, L. Jin, W.D. Cook, D. Mohn, E.L. Lagerqvist, D.A. Elliott, J.M. Haynes, N. Boyd, W.J. Stark, C.W. Pouton, E.G. Stanleye, A.G. Elefanty, "Elastomeric nanocomposites as cell delivery vehicles and cardiac support devices", *Soft Matter.*, 2010, **6**, 4715–4726.

[262] Q.Z. Chen, H. Ishii, G.A. Thouas, A.R. Lyon, J.S. Wright, J.J. Blaker, W. Chrzanowski, A.R. Boccaccini, N.N. Ali, J.C. Knowles, S.E. Harding, "An elastomeric patch derived from poly(glycerol sebacate) for delivery of embryonic stem cells to the heart", *Biomaterials*, 2010, **31**, 3885–3893.

[263] P.M. Crapo, J. Gao, Y. Wang, "Seamless tubular poly(glycerol sebacate) scaffolds: High-yield fabrication and potential applications", *J. Biomed. Mater. Res. A*, 2008, **86**, 354–363.

[264] P.M. Crapo, Y. Wang, "Physiologic compliance in engineered small-diameter arterial constructs based on an elastomeric substrate", *Biomaterials*, 2010, **31**, 1626–1635.

[265] C.J. Bettinger, E.J. Weinberg, K.M. Kulig, J.P. Vacanti, Y. Wang, J.T. Borenstein, R. Langer, "Three-dimensional microfluidic tissue-engineering scaffolds using a flexible biodegradable polymer", *Adv. Mater.*, 2006, **18**, 165–169.

[266] S. Sant, C.M. Hwang, S.H. Lee, A. Khademhosseini, "Hybrid PGS-PCL microfibrous scaffolds with improved mechanical and biological properties", *J. Tissue Eng. Regen. Med.*, 2011, **5**, 283–291.

[267] C.J. Bettinger, B. Orrick, A. Misra, R. Langer, J.T. Borenstein, "Microfabrication of poly (glycerol-sebacate) for contact guidance applications", *Biomaterials*, 2006, **27**, 2558–2565.

[268] F. Yi, D.A. La Van, "Poly(glycerol sebacate) nanofiber scaffolds by core/shell electrospinning", *Macromol. Biosci.*, 2008, **8**, 803–806.

[269] C. Fidkowski, M.R. Kaazempur-Mofrad, J. Borenstein, J.P. Vacanti, R. Langer, Y. Wang, "Endothelialized microvasculature based on a biodegradable elastomer", *Tissue Eng.*, 2005, **11**, 302–309.

[270] N. Masoumi, N. Annabi, A. Assmann, B.L. Larson, J. Hjortnaes, N. Alemdar, M. Kharaziha, K.B. Manning, J.E. Mayer, A. Khademhosseini, "Tri-layered elastomeric scaffolds for engineering heart valve leaflets", *Biomaterials*, 2014, **35**, 7774–7785.

[271] N. Masoumi, K.L. Johnson, M.C. Howell, G.C. Engelmayr, "Valvular interstitial cell seeded poly(glycerol sebacate) scaffolds: Toward a biomimetic in vitro model for heart valve tissue engineering", *Acta Biomater.*, 2013, **9**, 5974–5988.

[272] A. Jean, G.C. Engelmayr, "Finite element analysis of an accordion-like honeycomb scaffold for cardiac tissue engineering", *J. Biomech.*, 2010, **43**, 3035–3043.

[273] N. Masoumi, A. Jean, J.T. Zugates, K.L. Johnson, G.C. Engelmayr, "Laser microfabricated poly(glycerol sebacate) scaffolds for heart valve tissue engineering", *J. Biomed. Mater. Res. A*, 2013, **101**, 104–114.

[274] S. Sant, D. Iyer, A.K. Gaharwar, A. Patel, A. Khademhosseini, "Effect of biodegradation and de novo matrix synthesis on the mechanical properties of valvular interstitial cell-seeded polyglycerol sebacate-polycaprolactone scaffolds", *Acta Biomater.*, 2013, **9**, 5963–5973.

[275] S. Salehi, M. Fathi, S.H. Javanmard, T. Bahners, J.S. Gutmann, S. Ergün, K.P. Steuhl, T.A. Fuchsluger, "Generation of PGS/PCL blend nanofibrous scaffolds mimicking

corneal stroma structure", *Macromol. Mater. Eng.*, 2014, **299**, 455–469.

[276] M. Kharaziha, M. Nikkhah, S.R. Shin, N. Annabi, N. Masoumi, A.K. Gaharwar, G. Camci-Unal, A. Khademhosseini, "PGS:Gelatin nanofibrous scaffolds with tunable mechanical and structural properties for engineering cardiac tissues", *Biomaterials*, 2013, **34**, 6355–6366.

[277] E.M. Jeffries, R.A. Allen, J. Gao, M. Pesce, Y. Wang, "Highly elastic and suturable electrospun poly(glycerol sebacate) fibrous scaffolds", *Acta Biomater.*, 2015, **18**, 30–39.

[278] B. Xu, B. Rollo, L.A. Stamp, D. Zhang, X. Fang, D.F. Newgreen, Q.Z. Chen, "Non-linear elasticity of core/shell spun PGS/PLLA fibres and their effect on cell proliferation", *Biomaterials*, 2013, **34**, 6306–6317.

[279] H. Kenar, G.T. Kose, V. Hasirci, "Design of a 3D aligned myocardial tissue construct from biodegradable polyesters", *J. Mater. Sci. Mater. Med.*, 2010, **21**, 989–997.

[280] M. Tallawi, D.C. Zebrowski, R. Rai, J.A. Roether, D.W. Schubert, M. El Fray, F.B. Engel, K.E. Aifantis, A.R. Boccaccini, "Poly(Glycerol Sebacate)/poly(butylene succinate-butylene dilinoleate) fibrous scaffolds for cardiac tissue engineering", *Tissue Eng. C*, 2015, **21**, 585–596.

[281] R. Rai, M. Tallawi, C. Frati, A. Falco, A. Gervasi, F. Quaini, J.A. Roether, T. Hochburger, D.W. Schubert, L. Seik, N. Barbani, L. Lazzeri, E. Rosellini, A.R. Boccaccini, "Bioactive electrospun fibers of poly(glycerol sebacate) and poly(ε-caprolactone) for cardiac patch application", *Adv. Healthc. Mater.*, 2015, **4**, 2012–2025.

[282] R. Ravichandran, J.R. Venugopal, S. Sundarrajan, S. Mukherjee, R. Sridhar, S. Ramakrishna, "Minimally invasive injectable short nanofibers of poly(glycerol sebacate) for cardiac tissue engineering", *Nanotechnology*, 2012, **23**, 385102.

[283] R. Ravichandran, J.R. Venugopal, S. Sundarrajan, S. Mukherjee, S. Ramakrishna, "Poly(glycerol sebacate)/gelatin core/shell fibrous structure for regeneration of myocardial infarction", *Tissue Eng. A*, 2011, **17**, 1363–1373.

[284] R. Ravichandran, J.R. Venugopal, S. Sundarrajan, S. Mukherjee, S. Ramakrishna, "Cardiogenic differentiation of mesenchymal stem cells on elastomeric poly (glycerol sebacate)/collagen core/shell fibers", *World J. Cardiol.*, 2013, **5**, 28–41.

[285] R. Ravichandran, J.R. Venugopal, S. Sundarrajan, S. Mukherjee, R. Sridhar, S. Ramakrishna, "Expression of cardiac proteins in neonatal cardiomyocytes on PGS/fibrinogen core/shell substrate for Cardiac tissue engineering", *Int. J. Cardiol.*, 2013, **167**, 1461–1468.

[286] B. Xu, Y. Li, C. Zhu, W.D. Cook, J. Forsythe, Q.Z. Chen, "Fabrication, mechanical properties and cytocompatibility of elastomeric nanofibrous mats of poly(glycerol sebacate)", *Eur. Polym. J.*, 2015, **64**, 79–92.

[287] M. Radisic, A. Marsano, R. Maidhof, Y. Wang, G. Vunjak-Novakovic, "Cardiac tissue engineering using perfusion bioreactor systems", *Nat. Protoc.*, 2008, **3**, 719–738.

[288] J. Gao, P.M. Crapo, Y. Wang, "Macroporous elastomeric scaffolds with extensive micropores for soft tissue engineering", *Tissue Eng.*, 2006, **12**, 917–925.

[289] R. Rai, M. Tallawi, N. Barbani, C. Frati, D. Madeddu, S. Cavalli, G. Graiani, F. Quaini, J.A. Roether, D.W. Schubert, E. Rosellini, A.R. Boccaccini, "Biomimetic

poly(glycerol sebacate) (PGS) membranes for cardiac patch application", *Mater. Sci. Eng. C*, 2013, **33**, 3677–3687.

[290] J. Folkman, M. Hochberg, "Self-regulation of growth in three dimesnions", *J. Exp. Med.*, 1973, **138**, 745–753.

[291] C.K. Colton, "Implantable biohybrid artificial organs", *Cell Transplant.*, 1995, **4**, 415–436.

[292] H. Ye, C. Owh, X.J. Loh, "A thixotropic polyglycerol sebacate-based supramolecular hydrogel showing UCST behavior", *RSC Adv.*, 2015, **5**, 48720–48728.

[293] T. Dvir, B.P. Timko, D.S. Kohane, R. Langer, "Nanotechnological strategies for engineering complex tissues", *Nat. Nanotechnol.*, 2011, **6**, 13–22.

[294] J.J. Stankus, J. Guanc, K. Fujimoto, W.R. Wagner, "Microintegrating smooth muscle cells into a biodegradable, elastomeric fiber matrix", *Biomaterials*, 2006, **27**, 735–744.

[295] C. Vaquette, J. Cooper-White, "The use of an electrostatic lens to enhance the efficiency of the electrospinning process", *Cell Tissue Res.*, 2012, **347**, 815–826.

[296] R. Kessick, J. Fenn, G. Tepper, "The use of AC potentials in electrospraying and electrospinning processes", *Polymer*, 2004, **45**, 2981–2984.

[297] S. Thandavamoorthy, N. Gopinath, S.S. Ramkumar, "Self-assembled honeycomb polyurethane nanofibers", *J. Appl. Polym. Sci.*, 2006, **101**, 3121–3124.

[298] J.L. Ifkovits, J.J. Devlin, G. Eng, T.P. Martens, G. Vunjak-Novakovic, J.A. Burdick, "Biodegradable fibrous scaffolds with tunable properties formed from photo-cross-linkable poly(glycerol sebacate)", *ACS Appl. Mater. Interfaces*., 2009, **1**, 1878–1886.

[299] J.L. Ifkovits, K. Wu, R.L. Mauck, J.A. Burdick, "The influence of fibrous elastomer structure and porosity on matrix organization", *PLoS One*., 2010, **5**, e15717.

[300] W.L. Murphy, R.G. Dennis, J.L. Kileny, D.J. Mooney, "Salt fusion: An approach to improve pore interconnectivity within tissue engineering scaffolds", *Tissue Eng.*, 2002, **8**, 43–52.

[301] S. Gerecht, S.A. Townsend, H. Pressler, H. Zhu, C.L.E. Nijst, J.P. Bruggeman, J.W. Nichol, R. Langer, "A porous photocurable elastomer for cell encapsulation and culture", *Biomaterials*, 2007, **28**, 4826–4835.

[302] Y. Wu, L. Wang, B. Guo, P. X Ma, "Injectable biodegradable hydrogels and microgels based on methacrylated poly(ethylene glycol)-co-poly(glycerol sebacate) multi-block copolymers: synthesis, characterization, and cell encapsulation", *J. Mater. Chem. B*, 2014, **2**, 3674-3685.

[303] C. Zhu, S.R. Kustra, C.J. Bettinger, "Photocrosslinkable biodegradable elastomers based on cinnamate- functionalized polyesters", *Acta Biomater.*, 2013, **9**, 7362–7370.

[304] Z.J. Sun, L. Wu, W. Huang, C. Chen, Y. Chen, X.L. Lu, X.L. Zhang, B.F. Yang, D.L. Dong, "Glycolic acid modulates the mechanical property and degradation of poly(glycerol, sebacate, glycolic acid)", *J. Biomed. Mater. Res. A*, 2010, **92**, 332–339.

[305] Z.J. Sun, L. Wu, W. Huang, X.L. Zhang, X.L. Lu, Y.F. Zheng, B.F. Yang, D.L. Dong, "The influence of lactic on the properties of poly(glycerol-sebacate-lactic acid)", *Mater. Sci. Eng. C*, 2009, **29**, 178–182.

[306] Z.J. Sun, L. Wu, X.L. Lu, Z.X. Meng, Y.F. Zheng, D.L. Dong, "The characterization of mechanical and surface properties of poly(glycerol-sebacate-lactic acid) during degradation in phosphate buffered saline", *Appl. Surf. Sci.*, 2008, **255**, 350–352.

[307] Y. Wu, R. Shi, D. Chen, L. Zhang, W. Tian, "Nanosilica filled poly(glycerol-sebacate-citrate) elastomers with improved mechanical properties, adjustable degradability, and better biocompatibility", *J. Appl. Polym. Sci.*, 2012, **123**, 1612–1620.

[308] Q. Liu, T. Tan, J. Weng, L. Zhang, "Study on the control of the compositions and properties of a biodegradable polyester elastomer", *Biomed. Mater.*, 2009, **4**, 025015.

[309] Q. Liu, J. Wu, T. Tan, L. Zhang, D. Chen, W. Tian, "Preparation, properties and cytotoxicity evaluation of a biodegradable polyester elastomer composite", *Polym. Degrad. Stab.*, 2009, **94**, 1427–1435.

[310] A. Patel, A.K. Gaharwar, G. Iviglia, H. Zhang, S. Mukundan, S.M. Mihaila, D. Demarchi, A. Khademhosseini, "Highly elastomeric poly(glycerol sebacate)-co-poly(ethylene glycol) amphiphilic block copolymers", *Biomaterials*, 2013, **34**, 3970–3983.

[311] S. Cheng, L. Yang, F. Gong, "Novel branched poly(L-lactide) with poly(glycerol-co-sebacate) core", *Polym. Bull.*, 2010, **65**, 643–655.

[312] M.J.N. Pereira, B. Ouyang, C.A. Sundback, N. Lang, I. Friehs, S. Mureli, I. Pomerantseva, J. McFadden, M.C. Mochel, O. Mwizerwa, P. Del Nido, D. Sarkar, P.T. Masiakos, R. Langer, L.S. Ferreira, J.M. Karp, "A highly tunable biocompatible and multifunctional biodegradable elastomer", *Adv. Mater.*, 2013, **25**, 1209–1215.

[313] S. Liang, W.D. Cook, Q.Z. Chen, "Physical characterization of poly(glycerol sebacate)/Bioglass composites", *Polym. Int.*, 2012, **61**, 17–22.

[314] T.N. Rosenbalm, M. Teruel, C.S. Day, G.L. Donati, M. Morykwas, L. Argenta, N. Kuthirummal, N. Levi-Polyachenko, "Structural and mechanical characterization of bioresorbable, elastomeric nanocomposites from poly(glycerol sebacate)/nanohydroxyapatite for tissue transport applications", *J. Biomed. Mater. Res. B.*, 2015, DOI: 10.1002/jbm.b.33467.

[315] L. Zhou, H. He, C. Jiang, S. He, "Preparation and characterization of poly(glycerol sebacate)/cellulose nanocrystals elastomeric composites", *J. Appl. Polym. Sci.*, 2015, **132**, DOI: 10.1002/app.42196.

[316] A.K. Gaharwar, A. Patel, A. Dolatshahi-Pirouz, "Biomaterials Science poly(glycerol sebacate) chemically crosslinked with carbon nanotubes", *Biomater. Sci.*, 2014, **3**, 46–58.

[317] P. Kerativitayanan, A.K. Gaharwar, "Elastomeric and mechanically stiff nanocomposites from poly(glycerol sebacate) and bioactive nanosilicates", *Acta Biomater.*, 2015, **26**, 34–44.

[318] S. Bodakhe, S. Verma, K. Garkhal, S.K. Samal, S.S. Sharma, N. Kumar, "Injectable photocrosslinkable nanocomposite based on poly(glycerol sebacate) fumarate and hydroxyapatite: development, biocompatibility and bone regeneration in a rat calvarial bone defect model", *Nanomedicine*, 2013, **8**, 1777–1795.

[319] H.M. Aydin, K. Salimi, M. Yilmaz, M. Turk, Z.M. Rzayev, E. Pişkin, "Synthesis and characterization of poly(glycerol-co-sebacate-co-ε-caprolactone) elastomers", *J. Tissue Eng. Regen. Med.*, 2013, DOI: 10.1002/term.1759.

[320] X. Li, A.T.L. Hong, N. Naskar, H.J. Chung, "Criteria for quick and consistent synthesis of poly(glycerol sebacate) for tailored mechanical properties", *Biomacromolecules*, 2015, **16**, 1525–1533.

[321] E.L. Petsonk, M.L. Wang, D.M. Lewis, P.D. Siegel, B.J. Husberg, "Asthma-like symptoms in wood product plant workers exposed to methylene diphenyl diisocyanate", *Chest*., 2000, **118**, 1183–1193.
[322] L. Yu, K. Dean, L. Lin, "Polymer blends and composites from renewable resources", *Prog. Polym. Sci.*, 2006, **31**, 576–602.
[323] M. Tallawi, R. Rai, M. R-Gleixner, O. Roerick, M. Weyand, J. a. Roether, D.W. Schubert, A. Kozlowska, M.E. Fray, B. Merle, M. Göken, K. Aifantis, A.R. Boccaccini, "Poly(glycerol sebacate)\poly(butylene succinate-dilinoleate) blends as candidate materials for cardiac tissue engineering", *Macromol. Symp.*, 2013, **334**, 57–67.
[324] J.A. Roether, R. Rai, R. Wolf, M. Tallawi, A.R. Boccaccini, "Biodegradable poly(glycerol sebacate)/poly(3-hydroxybutyrate)-TiO 2 nanocomposites: fabrication and characterisation", *Mater. Sci. Technol.*, 2014, **30**, 574–581.
[325] T.H. Qazi, R. Rai, D. Dippold, J.E. Roether, D.W. Schubert, E. Rosellini, N. Barbani, A.R. Boccaccini, "Development and characterization of novel electrically conductive PANI-PGS composites for cardiac tissue engineering applications", *Acta Biomater.*, 2014, **10**, 2434–2445.
[326] T. Wu, M. Frydrych, K.O. Kelly, B. Chen, "Poly(glycerol sebacate urethane) − Cellulose nanocomposites with water-active shape-memory effects", *Biomacromolecules*, 2014, **15**, 2663–2671.
[327] G.W. Oetien, P. Haseley, Freeze-Drying, Weinheim: Wiley-VCH GmbH & Co. KGaA, 2004, 1–407.
[328] F. Franks, "Freeze-drying of bioproducts: putting principles into practice", *Eur. J. Pharm. Biopharm.*, 1998, **45**, 221–229.
[329] E. Landi, F. Valentini, A. Tampieri, "Porous hydroxyapatite/gelatine scaffolds with ice-designed channel-like porosity for biomedical applications", *Acta Biomater.*, 2008, **4**, 1620–1626.
[330] I. Aranaz, M.C. Gutiérrez, M.L. Ferrer, F. del Monte, "Preparation of chitosan nanocomposites with a macroporous structure by unidirectional freezing and subsequent freeze-drying", *Mar. Drugs*., 2014, **12**, 5619–5642.
[331] Labconco Corporation, "User's Manual - FreeZone® Triad™ Freeze Dry System", 2007, 1–59.
[332] M.J. Pikal, S. Shah, M.L. Roy, R. Putman, "The secondary drying stage of freeze-drying kinetics as a function of temperature and chamber pressure", *Int. J. Pharm.*, 1990, **60**, 203–217.
[333] L. Rey, J.C. May, Freeze Drying/Lyopilization of Pharmaceutical and Biological Products, Third Edition, London: CRC Press, 2010, 1–584.
[334] Q. Hou, D.W. Grijpma, J. Feijen, "Preparation of interconnected highly porous polymeric structures by a replication and freeze-drying process", *J. Biomed. Mater. Res. B*, 2003, **67**, 732–740.
[335] F.J. O'Brien, B.A. Harley, I.V. Yannas, L. Gibson, "Influence of freezing rate on pore structure in freeze-dried collagen-GAG scaffolds", *Biomaterials*, 2004, **25**, 1077–1086.
[336] L.H. Sperling, Introduction to Physical Polymer Science, Fourth Edition, Hoboken: Wiley, 2005, 1–845.

[337] C. Wan, B. Chen, "Reinforcement and interphase of polymer/graphene oxide nanocomposites", *J. Mater. Chem.*, 2012, **22**, 3637–3646.
[338] J.S. Chawla, M.M. Amiji, "Biodegradable poly(ε-caprolactone) nanoparticles for tumor-targeted delivery of tamoxifen", *Int. J. Pharm.*, 2002, **249**, 127–138.
[339] W. Cai, L. Liu, "Shape-memory effect of poly (glycerol-sebacate) elastomer", *Mater. Lett.*, 2008, **62**, 2175–2177.
[340] V. Maquet, A.R. Boccaccini, L. Pravata, I. Notingher, R. Jérôme, "Porous poly(alpha-hydroxyacid)/Bioglass composite scaffolds for bone tissue engineering. I: Preparation and in vitro characterisation.", *Biomaterials*, 2004, **25**, 4185–4194.
[341] S.P. Khan, G.G. Auner, G.M. Newaz, "Influence of nanoscale surface roughness on neural cell attachment on silicon", *Nanomed. Nanotechnol.*, 2005, **1**, 125–129.
[342] J.Y. Lim, A.D. Dreiss, Z. Zhou, J.C. Hansen, C.A. Siedlecki, R.W. Hengstebeck, J. Cheng, N. Winograd, H.J. Donahue, "The regulation of integrin-mediated osteoblast focal adhesion and focal adhesion kinase expression by nanoscale topography", *Biomaterials*, 2007, **28**, 1787–1797.
[343] J.E. Nichols, J.A. Niles, J. Cortiella, "Production and utilization of acellular lung scaffolds in tissue engineering", *J. Cell. Biochem.*, 2012, **113**, 2185–2192.
[344] X. Gu, F. Ding, Y. Yang, J. Liu, "Construction of tissue engineered nerve grafts and their application in peripheral nerve regeneration", *Prog. Neurobiol.*, 2011, **93**, 204–230.
[345] J. Tang, Z. Zhang, Z. Song, L. Chen, X. Hou, K. Yao, "Synthesis and characterization of elastic aliphatic polyesters from sebacic acid, glycol and glycerol", *Eur. Polym. J.*, 2006, **42**, 3360–3366.
[346] L. Lu, S.J. Peter, M.D. Lyman, H.L. Lai, S.M. Leite, J.A. Tamada, J.P. Vacanti, R. Langer, A.G. Mikos, "In vitro degradation of porous poly(L-lactic acid) foams", *Biomaterials*, 2000, **21**, 1595–1605.
[347] H. Tsuji, A. Mizuno, Y. Ikada, "Properties and morphology of poly(L-lactide). III. Effects of initial crystallinity on long-term in vitro hydrolysis of high molecular weight poly(L-lactide) film in phosphate-buffered solution", *J. Appl. Polym. Sci.*, 2000, **77**, 1452–1464.
[348] H. Tsuji, T. Ishizaka, "Blends of aliphatic polyesters. VI. Lipase-catalyzed hydrolysis and visualized phase structure of biodegradable blends from poly(ε-caprolactone) and poly(L-lactide)", *Int. J. Biol. Macromol.*, 2001, **29**, 83–89.
[349] M. Frydrych, C. Wan, R. Stengler, K.U. O'Kelly, B. Chen, "Structure and mechanical properties of gelatin/sepiolite nanocomposite foams", *J. Mater. Chem.*, 2011, **21**, 9103–9111.
[350] Y. Gong, Q. Zhou, C. Gao, J. Shen, "In vitro and in vivo degradability and cytocompatibility of poly(L-lactic acid) scaffold fabricated by a gelatin particle leaching method", *Acta Biomater.*, 2007, **3**, 531–540.
[351] Y. Cao, T.I. Croll, A.J. Oconnor, G.W. Stevens, J.J. Cooper-White, "Systematic selection of solvents for the fabrication of 3D combined macro- and microporous polymeric scaffolds for soft tissue engineering.", *J. Biomater. Sci. Polym. Ed.*, 2006, **17**, 369–402.
[352] M. J. Radford, J. Noakes, J. Read, D.G. Wood, "The natural history of a bioabsorbable

interference screw used for anterior cruciate ligament reconstruction with a 4-strand hamstring technique", *Arthrosc. J. Arthrosc. Relat. Surg.*, 2005, **21**, 707–710.

[353] V.J. Chen, P.X. Ma, "Nano-fibrous poly(L-lactic acid) scaffolds with interconnected spherical macropores", *Biomaterials*, 2004, **25**, 2065–2073.

[354] J. Zhang, L. Wu, D. Jing, J. Ding, "A comparative study of porous scaffolds with cubic and spherical macropores", *Polymer*, 2005, **46**, 4979–4985.

[355] S. Román, A. Mangera, N.I. Osman, A.J. Bullock, C.R. Chapple, S. MacNeil, "Developing a tissue engineered repair material for treatment of stress urinary incontinence and pelvic organ prolapse-which cell source?", *Neurourol. Urodyn.*, 2014, **33**, 531–537.

[356] M. Frydrych, B. Chen, "Large three-dimensional poly(glycerol sebacate)-based scaffolds – a freeze-drying preparation approach", *J. Mater. Chem. B*, 2013, **1**, 6650–6661.

[357] A. Montesi, M. Pasquali, F.C. MacKintosh, "Collapse of a semiflexible polymer in poor solvent", *Phys. Rev. E Stat. Nonlin. Soft Mattern Phys.*, 2004, **69**, 021916.

[358] L.J. Gibson, "Biomechanics of cellular solids", *J. Biomech.*, 2005, **38**, 377–399.

[359] S.H. Oh, J.H. Lee, "Hydrophilization of synthetic biodegradable polymer scaffolds for improved cell/tissue compatibility", *Biomed. Mater.*, 2013, **8**, 014101.

[360] K. Wittmann, S. Dietl, N. Ludwig, O. Berberich, C. Hoefner, K. Storck, T. Blunk, P. Bauer-Kreisel, "Engineering vascularized adipose tissue using the stromal-vascular fraction and fibrin hydrogels", *Tissue Eng. A*, 2015, **21**, 1343–1353.

[361] R.P. Lanza, R. Langer, J. Vacanti, *Principles of Tissue Engineering*, San Diego: Academic Press, 2000, 1-995.

[362] L. Li, S. Pan, B. Ni, Y. Lin, "Improvement in autologous human fat transplant survival with SVF plus VEGF-PLA nano-sustained release microspheres", *Cell Biol. Int.*, 2014, **38**, 962–970.

[363] A.J. Kinloch, R.J. Young, *Fracture Behaviour of Polymers*, London and New York: Applied Science Publisher, 1983, 1–496.

[364] H. Cheng, P.S. Hill, D.J. Siegwart, N. Vacanti, A.K.R. Lytton-Jean, S.W. Cho, A. Ye, R. Langer, D.G. Anderson, "A Novel Family of Biodegradable Poly(ester amide) Elastomers", *Adv. Mater.*, 2011, **23**, H95–H100.

[365] Q. Liu, L. Jiang, R. Shi, L. Zhang, "Synthesis, preparation, in vitro degradation, and application of novel degradable bioelastomers - A review", *Prog. Polym. Sci.*, 2012, **37**, 715–765.

[366] F.S. Yen, J.L. Hong, "Hydrogen-bond interactions between ester and urethane linkages in small model compounds and polyurethanes", *Macromolecules*, 1997, **30**, 7927–7938.

[367] M. Frydrych, S. Román, S. MacNeil, B. Chen, "Biomimetic poly(glycerol sebacate)/poly(L-lactic acid) blend scaffolds for adipose tissue engineering", *Acta Biomater.*, 2015, **18**, 40–49.

[368] H. Shearer, M.J. Ellis, S.P. Perera, J.B. Chaudhuri, "Effects of common sterilization methods on the structure and properties of poly(D,L lactic-co-glycolic acid) scaffolds", *Tissue Eng.*, 2006, **12**, 2717–2727.

[369] Z. Pan, J. Ding, "Poly(lactide-co-glycolide) porous scaffolds for tissue engineering and

regenerative medicine", *Interface Focus.*, 2012, **2**, 366–377.
[370] T. Siritientong, T. Srichana, P. Aramwit, "The Effect of Sterilization Methods on the Physical Properties of Silk Sericin Scaffolds", *AAPS PharmSciTech.*, 2011, **12**, 771–781.
[371] S.B.G. Blanquer, S.P. Haimi, A.A. Poot, D.W. Grijpma, "Effect of pore characteristics on mechanical properties and annulus fibrosus cell seeding and proliferation in designed PTMC tissue engineering scaffolds", *Macromol. Symp.*, 2013, **334**, 75–81.
[372] M. Frydrych, S. Román, N.H. Green, S. MacNeil, B. Chen, "Thermoresponsive, stretchable, biodegradable and biocompatible poly(glycerol sebacate)-based polyurethane hydrogels", *Polym. Chem.*, 2015, **6**, 7974–7987.
[373] L. Budyanto, Y.Q. Goh, C.P. Ooi, "Fabrication of porous poly(L-lactide) (PLLA) scaffolds for tissue engineering using liquid-liquid phase separation and freeze extraction", *J. Mater. Sci. Mater. Med.*, 2009, **20**, 105–111.
[374] R. Zhang, P.X. Ma, "Poly(α-hydroxyl acids)/hydroxyapatite porous composites for bone-tissue engineering", *J. Biomed. Mater. Res.*, 1999, **44**, 446–455.
[375] C. Tu, Q. Cai, J. Yang, Y. Wan, J. Bei, S. Wang, "The fabrication and characterization of poly(lactic acid) scaffolds for tissue engineering by improved solid–liquid phase separation", *Polym. Adv. Technol.*, 2003, **14**, 565–573.
[376] E. Nejati, V. Firouzdor, M.B. Eslaminejad, F. Bagheri, "Needle-like nano hydroxyapatite/poly(L-lactide acid) composite scaffold for bone tissue engineering application", *Mater. Sci. Eng. C*, 2009, **29**, 942–949.
[377] G. Wei, P.X. Ma, "Structure and properties of nano-hydroxyapatite/polymer composite scaffolds for bone tissue engineering", *Biomaterials*, 2004, **25**, 4749–4757.
[378] P.X. Ma, J.W. Choi, "Biodegradable polymer scaffolds with well-defined interconnected spherical pore network", *Tissue Eng.*, 2001, **7**, 23–33.
[379] D. Jing, L. Wu, J. Ding, "Solvent-assisted room-temperature compression molding approach to fabricate porous scaffolds for tissue engineering", *Macromol. Biosci.*, 2006, **6**, 747–757.
[380] J.J. Blaker, V. Maquet, R. Jérôme, A.R. Boccaccini, S.N. Nazhat, "Mechanical properties of highly porous PDLLA/Bioglass® composite foams as scaffolds for bone tissue engineering", *Acta Biomater.*, 2005, **1**, 643–652.
[381] L. Wu, H. Zhang, J. Zhang, J. Ding, "Fabrication of three-dimensional porous scaffolds of complicated shape for tissue engineering. I. Compression molding based on flexible-rigid combined mold", *Tissue Eng.*, 2005, **11**, 1105–1114.
[382] L.D. Harris, B.S. Kim, D.J. Mooney, "Open pore biodegradable matrices formed with gas foaming", *J. Biomed. Mater. Res.*, 1998, **42**, 396–402.
[383] J. Zhang, H. Zhang, L. Wu, J. Ding, "Fabrication of three dimensional polymeric scaffolds with spherical pores", *J. Mater. Sci.*, 2006, **41**, 1725–1731.
[384] L. Wu, J. Zhang, D. Jing, J. Ding, "“Wet-state” mechanical properties of three-dimensional polyester porous scaffolds", *J. Biomed. Mater. Res.*, 2006, **76**, 264–271.
[385] H.M. Wong, P.K. Chu, F.K.L. Leung, K.M.C. Cheung, K.D.K. Luk, K.W.K. Yeung, "Engineered polycaprolactone–magnesium hybrid biodegradable porous scaffold for bone tissue engineering", *Prog. Nat. Sci. Mater. Int.*, 2014, **24**, 561–567.
[386] M.J. Chern, L.Y. Yang, Y.K. Shen, J.H. Hung, "3D scaffold with PCL combined

biomedical ceramic materials for bone tissue regeneration", *Int. J. Precis. Eng. Manuf.*, 2013, **14**, 2201–2207.

[387] F. Naghizadeh, N. Sultana, M.R.A. Kadir, T.M.T.M. Shihabudin, R. Hussain, T. Kamarul, "The fabrication and characterization of PCL/rice husk derived bioactive glass-ceramic composite scaffolds", *J. Nanomater.*, 2014, **2014**, 253185.

[388] F. Wu, C. Liu, B. O'Neill, J. Wei, Y. Ngothai, "Fabrication and properties of porous scaffold of magnesium phosphate/polycaprolactone biocomposite for bone tissue engineering", *Appl. Surf. Sci.*, 2012, **258**, 7589–7595.

[389] M. Diba, M. Kharaziha, M.H. Fathi, M. Gholipourmalekabadi, A. Samadikuchaksaraei, "Preparation and characterization of polycaprolactone/forsterite nanocomposite porous scaffolds designed for bone tissue regeneration", *Compos. Sci. Technol.*, 2012, **72**, 716–723.

[390] J.J. Kim, R.K. Singh, S.J. Seo, T.H. Kim, J.H. Kim, E.J. Lee, H.W. Kim, "Magnetic scaffolds of polycaprolactone with functionalized magnetite nanoparticles: physicochemical, mechanical, and biological properties effective for bone regeneration", *RSC Adv.*, 2014, **4**, 17325–17336.

[391] P. Fabbri, V. Cannillo, A. Sola, A. Dorigato, F. Chiellini, "Highly porous polycaprolactone-45S5 Bioglass® scaffolds for bone tissue engineering", *Compos. Sci. Technol.*, 2010, **70**, 1869–1878.

[392] H. Zhang, A.I. Cooper, "Aligned porous structures by directional freezing", *Adv. Mater.*, 2007, **19**, 1529–1533.

[393] Z. Tong, X. Jia, "Biomaterials-based strategies for the engineering of mechanically active soft tissues", *MRS Commun.*, 2012, **2**, 31–39.

[394] S. Mitragotri, J. Lahann, "Physical approaches to biomaterial design", *Nat. Mater.*, 2009, **8**, 15–23.

[395] C.J. Bettinger, "Synthesis and microfabrication of biomaterials for soft-tissue engineering", *Pure Appl. Chem.*, 2009, **81**, 2183–2201.

[396] J. Yang, D. Motlagh, A.R. Webb, G.A. Ameer, "Novel biphasic elastomeric scaffold for small-diameter blood vessel tissue engineering", *Tissue Eng.*, 2005, **11**, 1876–1886.

[397] N. Annabi, J.W. Nichol, X. Zhong, C. Ji, S. Koshy, F. Khademhosseini, A. Dehghani, "Controlling the porosity and microarchitecture of hydrogels for tissue engineering", *Tissue Eng. B*, 2010, **16**, 371–383.

[398] A. Khademhosseinia, R. Langer, "Microengineered hydrogels for tissue engineering", *Biomaterials*, 2007, **28**, 5087–5092.

[399] J. Tuominen, J. Kylma, A. Kapanen, O. Venelampi, M. Itävaara, J. Seppälä, "Biodegradation of lactic acid based polymers under controlled composting conditions and evaluation of the ecotoxicological impact", *Biomacromolecules*, 2002, **3**, 445–455.

[400] K. Park, W.S.W. Shalby, H. Park, *Biodegradable Hydrogels for Drug Delivery*, Lancaster: CRC Press, 1993, 1–262.

[401] J. Ruiz, A. Mantecón, V. Cádiz, "Synthesis and properties of hydrogels from poly(vinyl alcohol) and ethylenediaminetetraacetic dianhydride", *Polymer*, 2001, **42**, 6347–6354.

[402] D.R. Ralston, C. Layton, A.J. Dalley, S.G. Boyce, E. Freedlander, S. MacNeil, "Keratinocytes contract human dermal extracellular matrix and reduce soluble fibronectin production by fibroblasts in a skin composite model", *Br. J. Plast. Surg.*,

1997, **50**, 408–415.
[403] M. Li, O. Rouaud, D. Poncelet, "Microencapsulation by solvent evaporation: State of the art for process engineering approaches", *Int. J. Pharm.*, 2008, **363**, 26–39.
[404] R. París, Á. Marcos-Fernández, I. Quijada-Garrido, "Synthesis and characterization of poly(ethylene glycol)-based thermo-responsive polyurethane hydrogels for controlled drug release", *Polym. Adv. Technol.*, 2013, **24**, 1062–1067.
[405] M.W. Urban, C.L. Allison, "Interfacial studies of crosslinked urethanes: Part IV. Substrate effect on film formation in polyester waterborne polyurethanes", *J. Coatings Technol.*, 1999, **71**, 73–78.
[406] R. Maliger, P.J. Halley, J.J. Cooper-White, "Poly(glycerol-sebacate) bioelastomers-kinetics of step-growth reactions using Fourier Transform (FT)-Raman spectroscopy", *J. Appl. Polym. Sci.*, 2013, **127**, 3980–3986.
[407] D. Yamini, G. Devanand Venkatasubbu, J. Kumar, V. Ramakrishnan, "Raman scattering studies on PEG functionalized hydroxyapatite nanoparticles", *Spectrochim. Acta A Mol. Biomol. Spectrosc.*, 2014, **117**, 299–303.
[408] Y. Jin, M. Sun, D. Mu, X. Ren, Q. Wang, L. Wen, "Investigation of PEG adsorption on copper in Cu 2+ -free solution by SERS and AFM", *Electrochim. Acta.*, 2012, **78**, 459–465.
[409] S.Y. Moon, Y.D. Park, C.J. Kim, C.H. Won, Y.S. Lee, "Effect of chain extenders on polyurethanes containing both poly(butylene succinate) and poly(ethylene glycol) as soft segments", *Bull. Korean Chem. Soc.*, 2003, **24**, 1361–1364.
[410] Z. You, H. Cao, J. Gao, P.H. Shin, B.W. Day, Y. Wang, "A functionalizable polyester with free hydroxyl groups and tunable physiochemical and biological properties", *Biomaterials*, 2010, **31**, 3129–3138.
[411] Y. Li, Q. Ma, C. Huang, G. Liu, "Crystallization of poly(ethylene glycol) in poly(methyl methacrylate) networks", *Mater. Sci. Medzg.*, 2013, **19**, 147–151.
[412] H.L. Lim, Y. Hwang, M. Kar, S. Varghese, "Smart hydrogels as functional biomimetic systems", *Biomater. Sci.*, 2014, **2**, 603–618.
[413] A.B. Imran, T. Seki, Y. Takeoka, "Recent advances in hydrogels in terms of fast stimuli responsiveness and superior mechanical performance", *Polym. J.*, 2010, **42**, 839–851.
[414] K. Deligkaris, T.S. Tadele, W. Olthuis, A. van den Berg, "Hydrogel-based devices for biomedical applications", *Sensor. Actuat. B Chem.*, 2010, **147**, 765–774.
[415] A.K. Bajpai, S.K. Shukla, S. Bhanu, S. Kankane, "Responsive polymers in controlled drug delivery", *Prog. Polym. Sci.*, 2008, **33**, 1088–1118.
[416] Y. Qiu, K. Park, "Environment-sensitive hydrogels for drug delivery", *Adv. Drug Deliv. Rev.*, 2012, **64**, 49–60.
[417] L. Ionov, "Hydrogel-based actuators: Possibilities and limitations", *Mater. Today.*, 2014, **17**, 494–503.
[418] L. Klouda, A.G. Mikos, "Thermoresponsive hydrogels in biomedical applications", *Eur. J. Pharm. Biopharm.*, 2008, **68**, 34–45.
[419] H.G. Schild, "Poly(N-isopropylacrylamide): Experiment, theory and application", *Prog. Polym. Sci.*, 1992, **17**, 163–249.
[420] K. Knop, R. Hoogenboom, D. Fischer, U.S. Schubert, "Poly(ethylene glycol) in drug

delivery: Pros and cons as well as potential alternatives", *Angew. Chem. Int. Ed.*, 2010, **49**, 6288–6308.

[421] S.J. Kim, I. Jun, D.W. Kim, Y.B. Lee, Y.J. Lee, J.H. Lee, K.D. Park, H. Park, H. Shin, "Rapid transfer of endothelial cell sheet using a thermosensitive hydrogel and its effect on therapeutic angiogenesis", *Biomacromolecules*, 2013, **14**, 4309–4319.

[422] I. Jun, Y.B. Lee, Y.S. Choi, A.J. Engler, H. Park, H. Shin, "Transfer stamping of human mesenchymal stem cell patches using thermally expandable hydrogels with tunable cell-adhesive properties", *Biomaterials*, 2015, **54**, 44–54.

[423] O.O. Akintewe, S.J. DuPont, K.K. Elineni, M.C. Cross, R.G. Toomey, N.D. Gallant, "Shape-changing hydrogel surfaces trigger rapid release of patterned tissue modules", *Acta Biomater.*, 2015, **11**, 96–103.

[424] A. Kikuchi, T. Okano, "Nanostructured designs of biomedical materials: Applications of cell sheet engineering to functional regenerative tissues and organs", *J. Control. Release.*, 2005, **101**, 69–84.

[425] X. Huang, C.S. Brazel, "On the importance and mechanisms of burst release in matrix-controlled drug delivery systems", *J. Control. Release.*, 2001, **73**, 121–136.

[426] M. Ma, L. Guo, D.G. Anderson, R. Langer, "Bio-inspired polymer composite actuator and generator driven by water gradients", *Science*, 2012, **339**, 9–12.

[427] Y. Tan, K. Xu, P. Wang, W. Li, S. Sun, L.S. Dong, "High mechanical strength and rapid response rate of poly(N-isopropyl acrylamide) hydrogel crosslinked by starch-based nanospheres", *Soft Matter.*, 2010, **6**, 1467-1471.

[428] Z. Li, J. Shen, H. Ma, X. Lu, M. Shi, N. Li, M. Ye, "Preparation and characterization of pH- and temperature-responsive nanocomposite double network hydrogels", *Mater. Sci. Eng. C*, 2013, **33**, 1951–1957.

[429] K. Haraguchi, T. Takehisa, S. Fan, "Effects of clay content on the properties of nanocomposite hydrogels composed of poly(N-isopropylacrylamide) and clay", *Macromolecules*, 2002, **35**, 10162–10171.

[430] N.K. Varde, D.W. Pack, "Microspheres for controlled release drug delivery", *Expert Opin. Biol. Ther.*, 2004, **4**, 35–51.

[431] Y.B. Kim, G.H. Kim, "Rapid-prototyped collagen scaffolds reinforced with PCL/β-TCP nanofibres to obtain high cell seeding efficiency and enhanced mechanical properties for bone tissue regeneration", *J. Mater. Chem.*, 2012, **22**, 16880–16889.

[432] S.H. Ahn, Y.B. Kim, H.J. Lee, G.H. Kim, "A new hybrid scaffold constructed of solid freeform-fabricated PCL struts and collagen struts for bone tissue regeneration: fabrication, mechanical properties, and cellular activity", *J. Mater. Chem. Chem.*, 2012, **22**, 15901–15909.

Appendix A - Supplementary information for Chapter 3

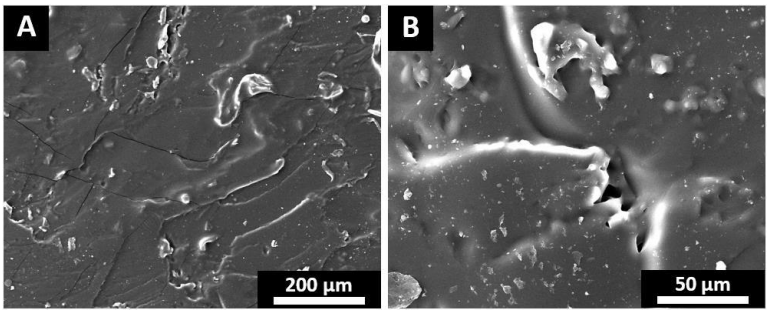

Figure 3.S1: (A, B) SEM micrographs of the cured PGS (24 h at 150 °C) film surface, after 24 h ethanol extraction.

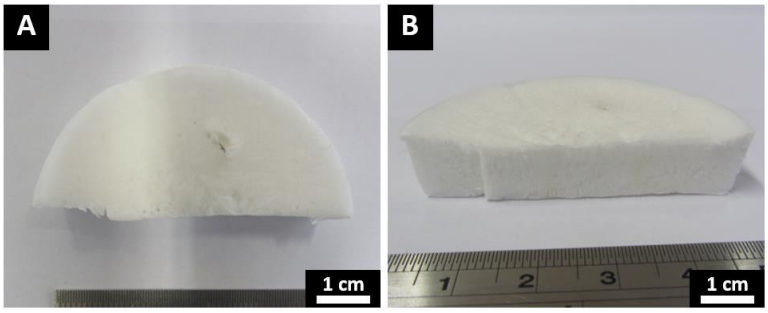

Figure 3.S2: (A) Top and (B) side view (cross section) of non-cured freeze-dried PLLA scaffold, produced with 2 g PLLA and 40 mL 1,4-dioxane.

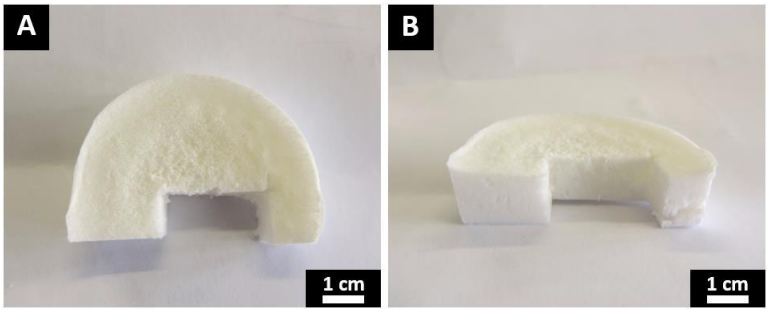

Figure 3.S3: (A) Top and (B) side view of cured PGS/PLLA blend scaffold with a weight ratios of 2.5:1.

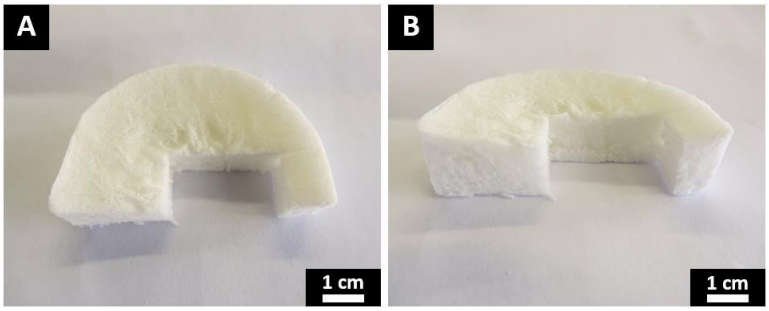

Figure 3.S4: (A) Top and (B) side view of cured PGS/PLLA blend scaffold with a weight ratios of 3:1.

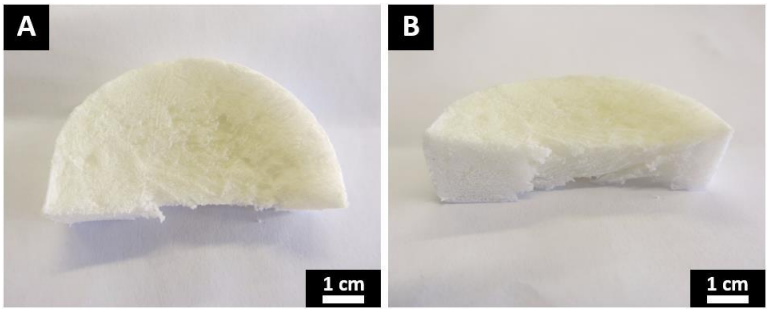

Figure 3.S5: (A) Top and (B) side view of cured PGS/PLLA blend scaffold with a weight ratios of 3.5:1.

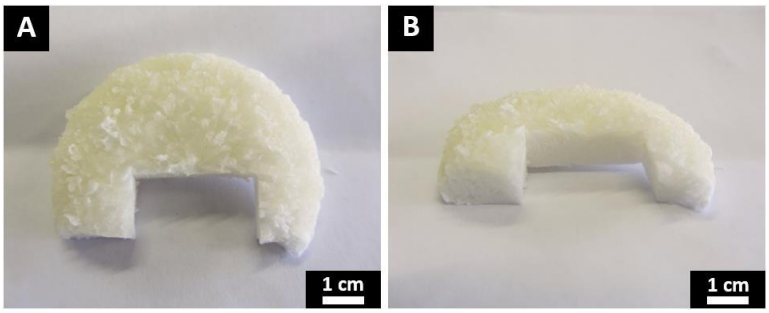

Figure 3.S6: (A) Top and (B) side view of cured PGS/PLLA blend scaffold with a weight ratios of 4:1.

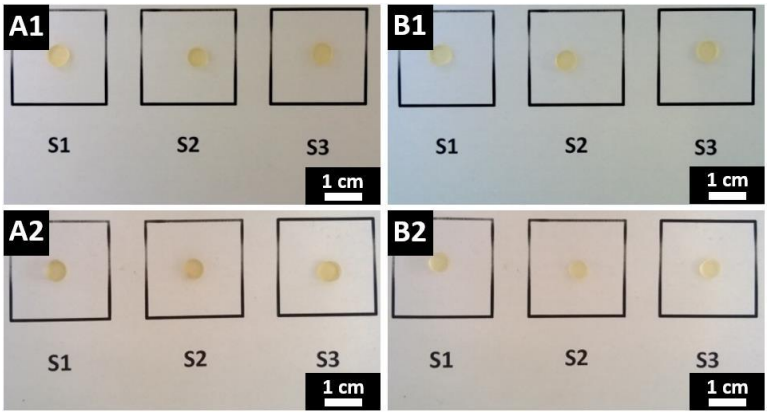

Figure 3.S7: Pictures of cured PGS film (24 h for 150 °C) samples, (A1, B1) before and (A2, B2) after 31 days *in vitro* biodegradation tests in (A1-2) enzyme-free and in (B1-2) enzyme-containing PBS solution.

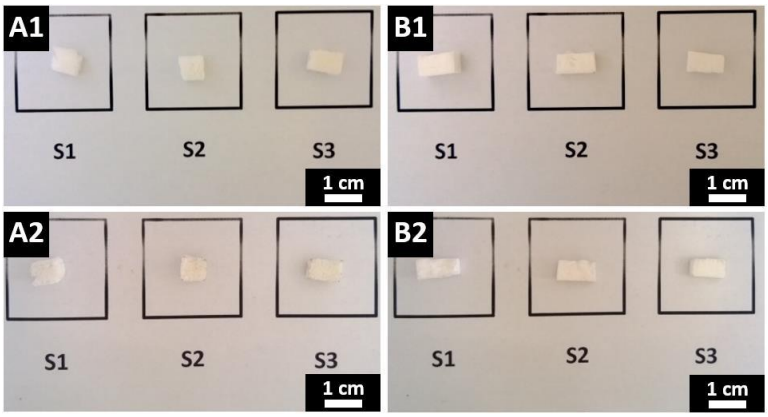

Figure 3.S8: Pictures of PLLA scaffold samples, (A1, B1) before and (A2, B2) after 31 days *in vitro* biodegradation tests in (A1-2) enzyme-free and in (B1-2) enzyme-containing PBS solution.

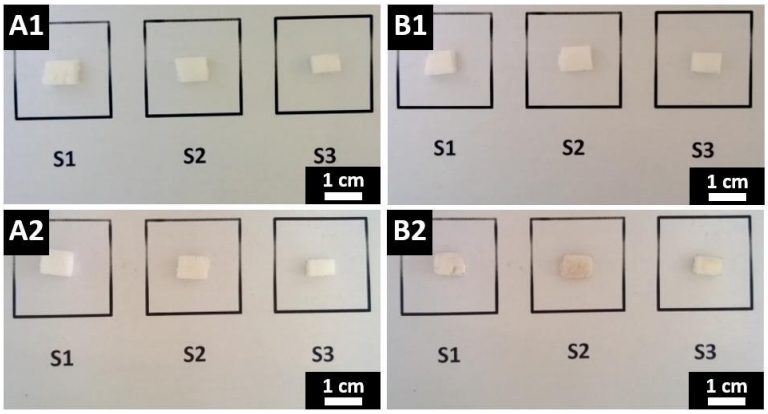

Figure 3.S9: Pictures of PGS/PLLA scaffold samples with a weight ratio of 2.5:1, (A1, B1) before and (A2, B2) after 31 days *in vitro* biodegradation tests in (A1-2) enzyme-free and in (B1-2) enzyme-containing PBS solution.

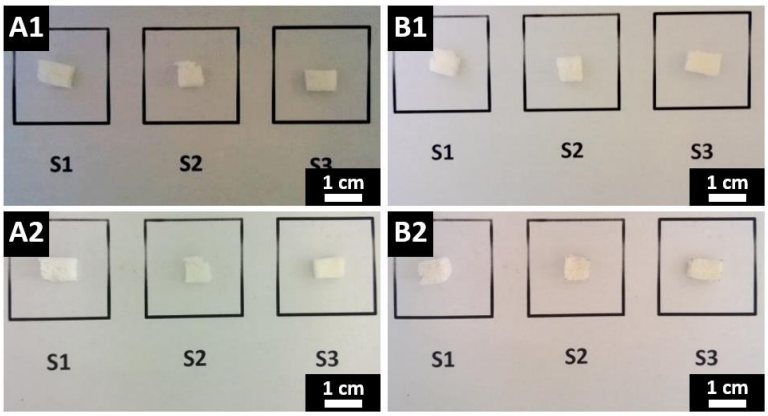

Figure 3.S10: Pictures of PGS/PLLA scaffold samples with a weight ratio of 3:1, (A1, B1) before and (A2, B2) after 31 days *in vitro* biodegradation tests in (A1-2) enzyme-free and in (B1-2) enzyme-containing PBS solution.

Appendix B - Supplementary information for Chapter 4

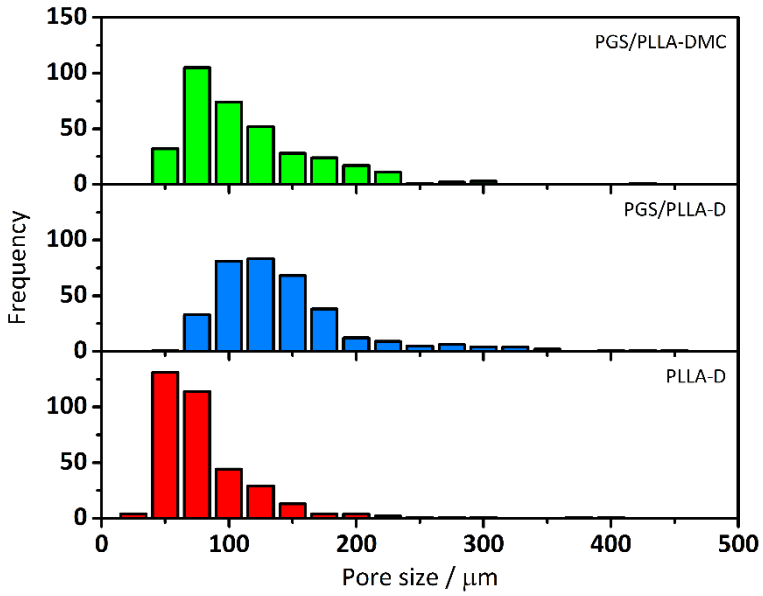

Figure 4.S1: Histograms of the pore size distribution of PLLA-D (narrow distribution: 50 µm - 100 µm), PGS/PLLA-D (wide distribution: 75 µm - 175 µm) and PGS/PLLA-DMC (wide distribution: 50 µm - 175 µm) scaffold samples (n = 350).

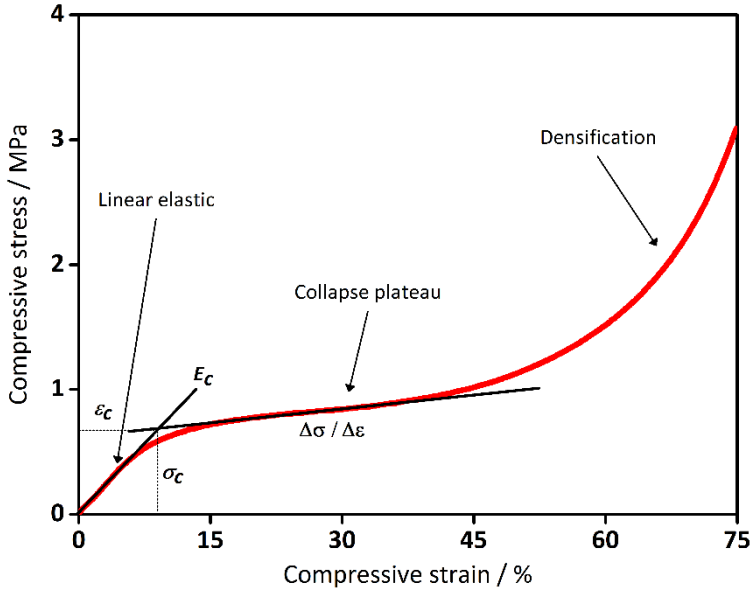

Figure 4.S2: Compressive stress-strain curve for PLLA-D scaffold. E_c is the Young's modulus, σ_c and ε_c are the collapse stress and strain. $\Delta\sigma/\Delta\varepsilon$ is the linear regression of the collapse plateau regime. The compressive stress-strain curve is characterised with a distinct linear elastic, collapse plateau and densification regime.

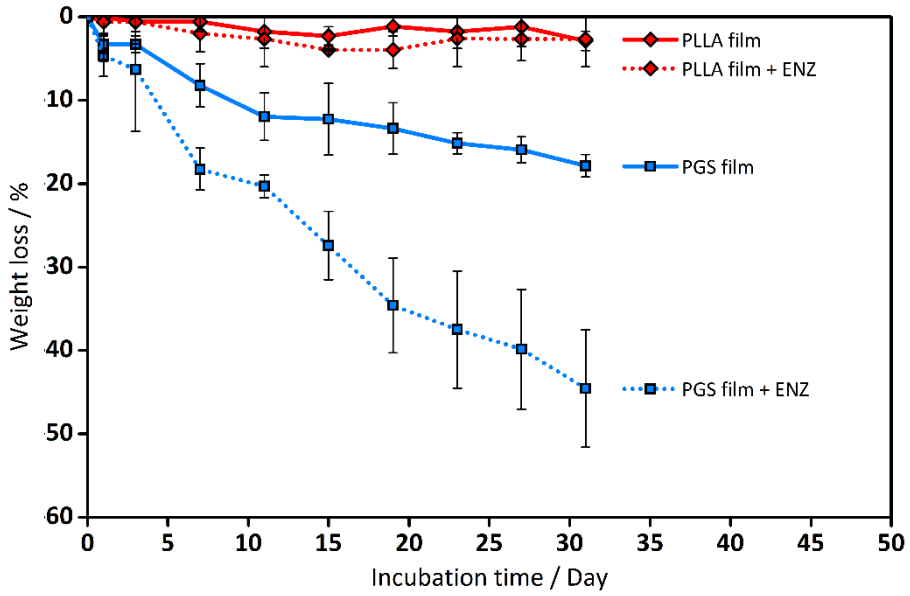

Figure 4.S3: Percentage of weight loss of PLLA and PGS (cured at 120 °C for 36 h) films, incubated in PBS for up to 31 days in a shaker incubator at 37 °C and 100 rpm (n = 3; Diameter: 6 mm and thickness: 0.44 ± 0.12 mm). The PLLA specimens maintained in the enzyme-free and lipase enzyme-containing PBS solution a constant weight and obtained in both cases a negligible weight loss of less than 3% in 31 days. During the test period PGS presented in the enzymatic-free PBS solution a weight loss of 18%, while in the lipase enzyme-containing PBS solution PGS obtained an increased weight loss of 45%.

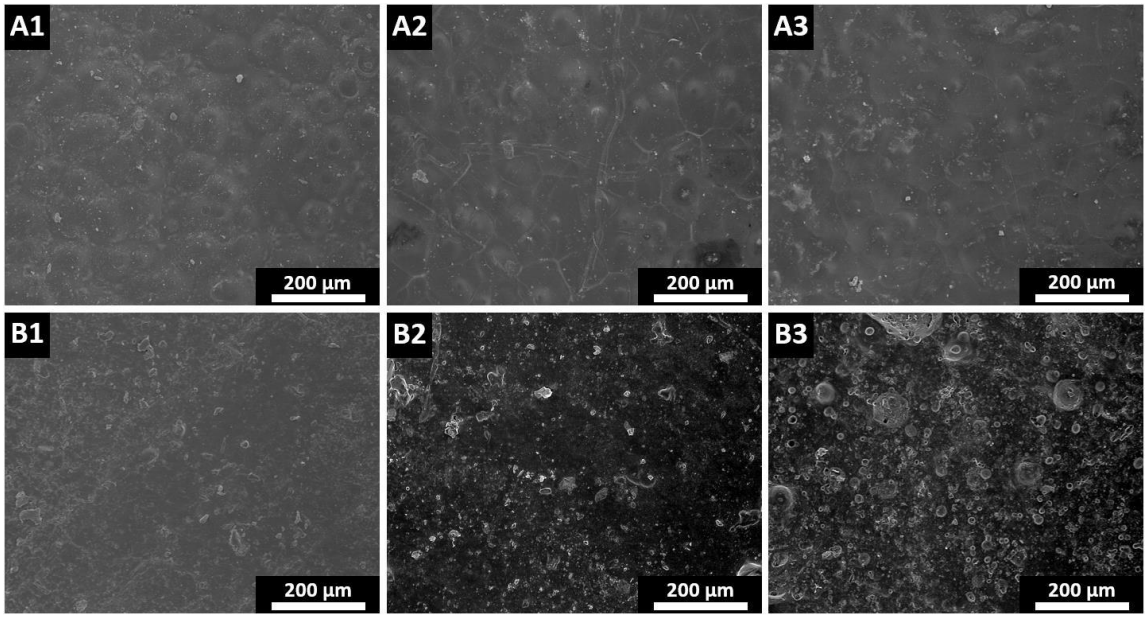

Figure 4.S4: SEM micrographs of the (A1-3) PLLA and (B1-3) PGS film surface: (A1, B1) untreated (36 h at 120 ˚C), after 31 days at 37 ˚C in (A2, B2) enzyme-free PBS solution and (A3, B3) in lipase enzyme-containing PBS solution.

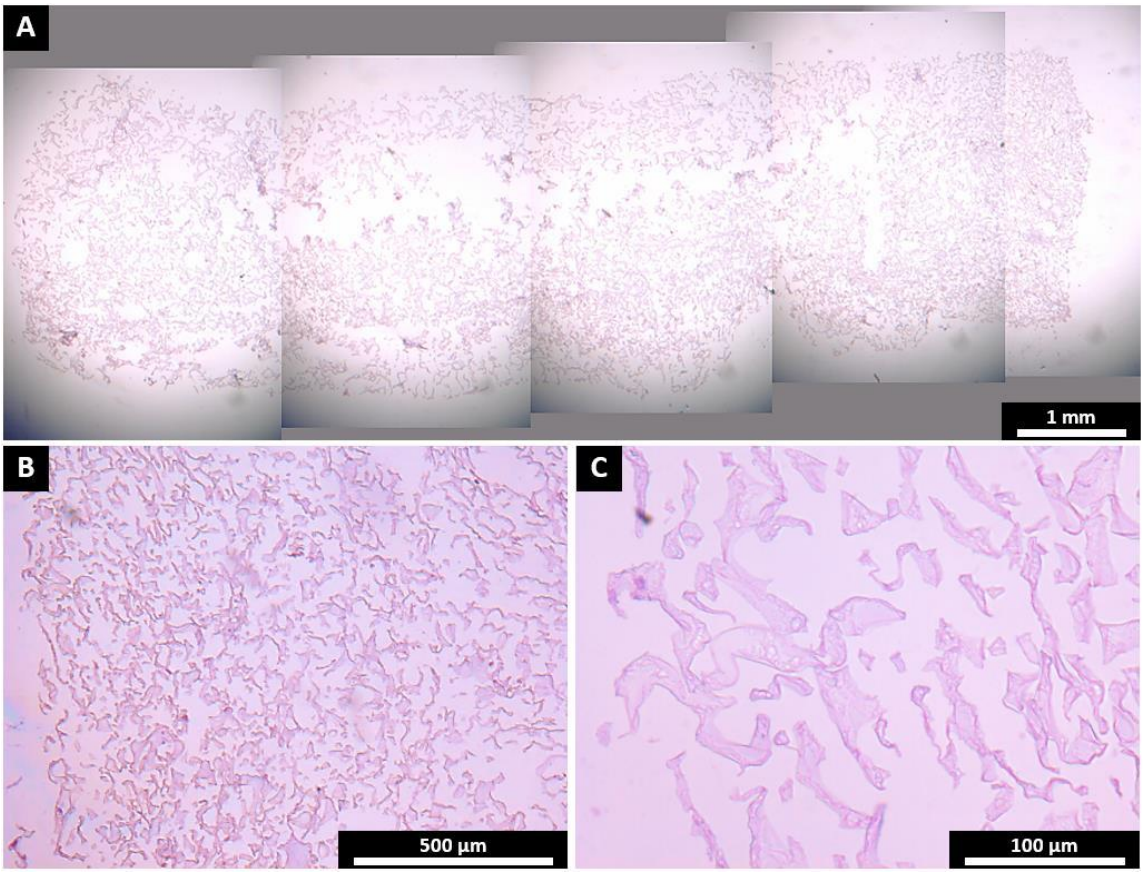

Figure 4.S5: (A, B, C) Histological section of a PGS/PLLA-D scaffold control sample (without cells), stained with haematoxylin and eosin after 21 days in DMEM. The results present a relatively porous scaffold microstructure with large pore sizes.

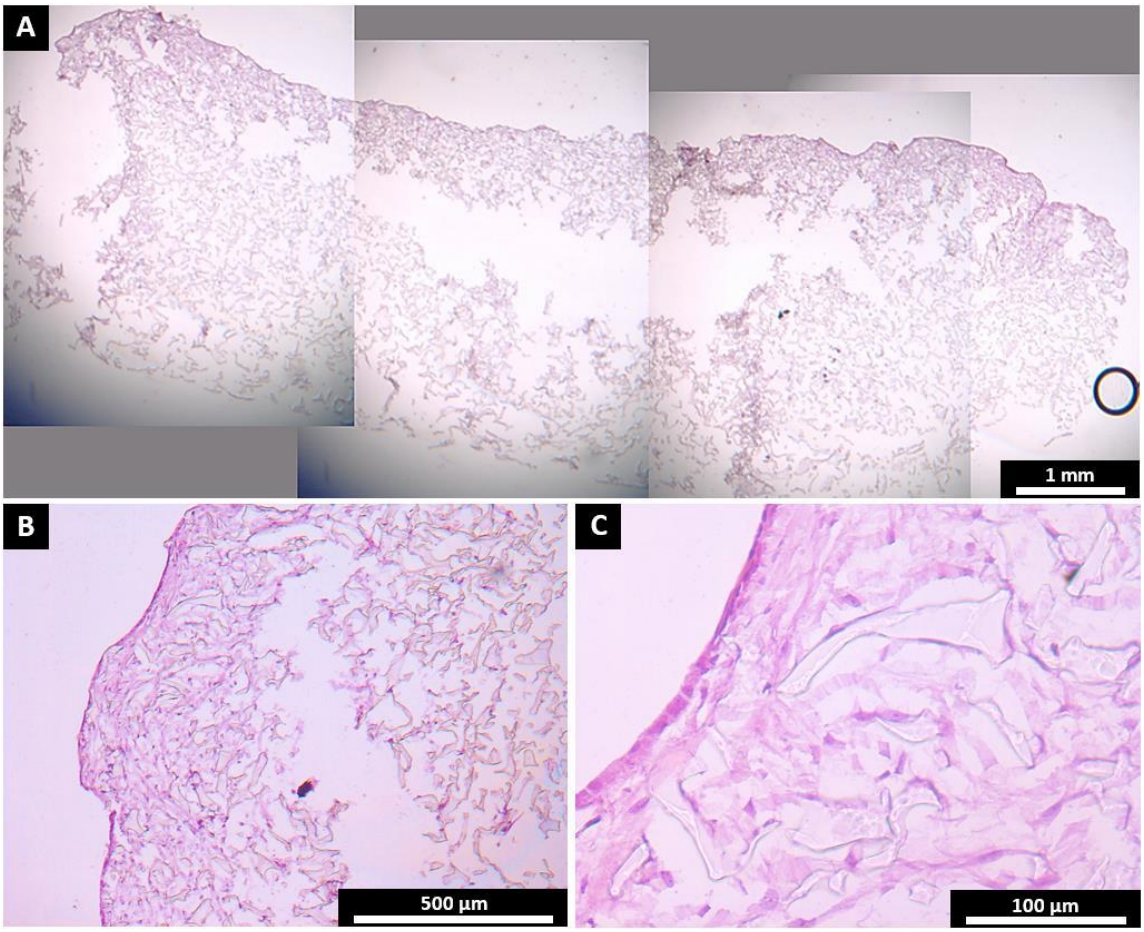

Figure 4.S6: (A, B, C) Histological section of an ADSC-seeded PGS/PLLA-D scaffold sample, stained with haematoxylin and eosin after cultured for 21 days in DMEM. The results present a high density of structural integrated cells and ECM within the cell-seeded scaffold surface, overall improving the structure integrity of the scaffold.

Appendix C - Supplementary information for Chapter 5

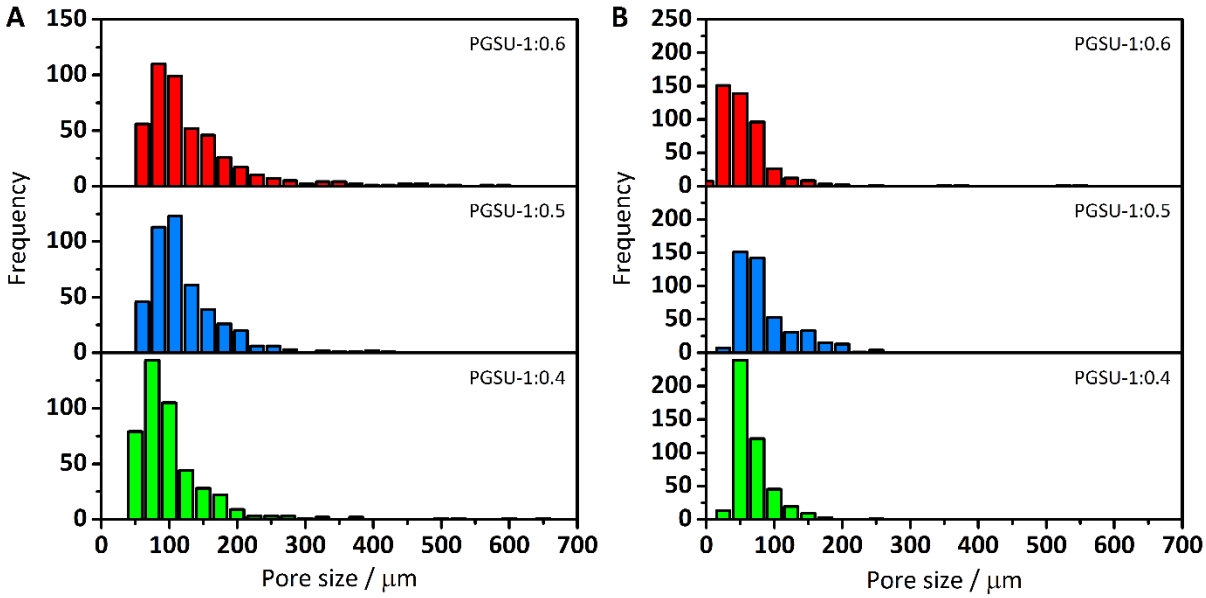

Figure 5.S1: Histograms of the pore size distribution of (A) "as-prepared" and (B) cleaned and dry PGSU scaffold samples (n = 450).

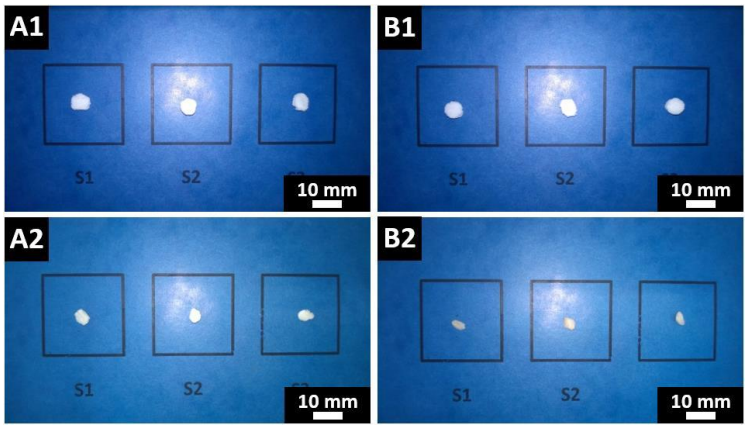

Figure 5.S2: Pictures of PGSU-1:0.4 scaffold samples, (A1, B1) before and (A2, B2) after 112 days *in vitro* biodegradation tests in (A1-2) enzyme-free and in (B1-2) enzyme-containing PBS solution.

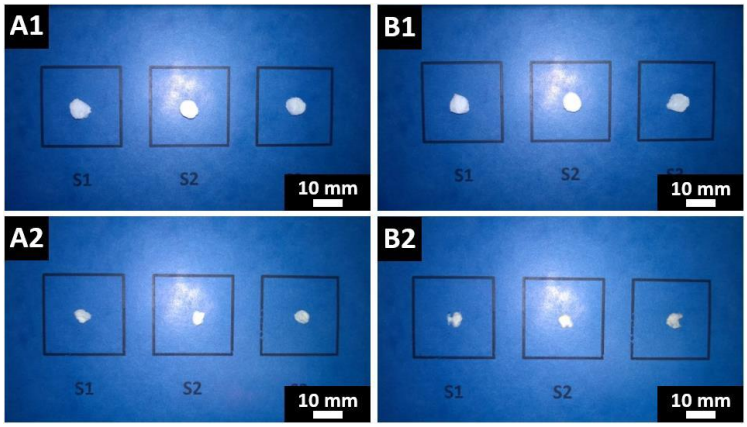

Figure 5.S3: Pictures of PGSU-1:0.5 scaffold samples, (A1, B1) before and (A2, B2) after 112 days *in vitro* biodegradation tests in (A1-2) enzyme-free and in (B1-2) enzyme-containing PBS solution.

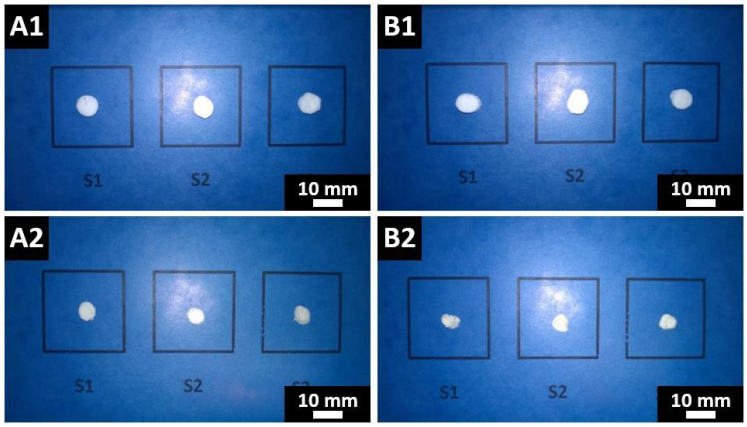

Figure 5.S4: Pictures of PGSU-1:0.6 scaffold samples, (A1, B1) before and (A2, B2) after 112 days *in vitro* biodegradation tests in (A1-2) enzyme-free and in (B1-2) enzyme-containing PBS solution.

Table 5.S1. Selected physical properties of polymer scaffolds reported in the literature.

Polymer	Fabrication Method	Porosity, P_f / %	Relative density, ρ_r / (1-P_f)	Compressive modulus, E_c / MPa	Reference
PLLA	TIPS[b]	82.4	0.176	4.40	[373]
PLLA	TIPS[b]	81.3	0.187	7.50	[373]
PLLA	TIPS[b]	92.7	0.073	6.00	[374]
PLLA	SC/PL[c]	93.5	0.065	3.60	[375]
PLLA	SC/PL[c]	95.5	0.045	3.10	[375]
PLLA	SC/PL[c]	96.4	0.036	2.30	[375]
PLLA	SC/PL[c]	98.5	0.015	2.10	[375]
PLLA	TIPS[b]	87.0	0.130	1.79	[376]
PLLA	TIPS[b]	93.0	0.070	4.30	[377]
PLLA	SC/PL[c]	94.5	0.055	0.30	[378]
PLLA	SC/PL[c]	96.8	0.032	0.02	[378]
PLLA	SC/PL[c]	95.2	0.048	0.05	[378]
PLLA	SC/PL[c]	95.8	0.042	0.05	[378]
PLLA	SC/PL[c]	96.1	0.039	0.08	[378]
PDLLA	RM/PL	90.0	0.100	5.20	[379]
PDLLA	RM/PL	92.6	0.074	1.70	[379]
PDLLA	TIPS[b]	94.0	0.06	0.89	[380]
PDLLA	SC/PL[c]	93.0	0.070	2.40	[381]
PLGA	SC/PL	90.0	0.100	0.16	[382]
PLGA	GF/PL	90.0	0.100	0.29	[382]
PLGA	SC/PL[c]	97.0	0.030	0.25	[383]
PLGA	SC/PL[c]	93.0	0.070	2.00	[383]
PLGA	SC/PL[c]	92.0	0.080	3.00	[383]
PLGA	SC/PL[c]	91.5	0.085	3.50	[383]
PLGA	SC/PL[c]	87.0	0.130	7.50	[383]
PLGA	SC/PL[c]	80.0	0.200	12.00	[383]
PLGA	RM/PL	88.0	0.120	14.80	[384]
PLGA	RM/PL	88.0	0.120	7.50	[384]
PLGA	RM/PL	88.0	0.120	7.00	[384]
PLGA	RM/PL	88.0	0.120	5.50	[384]
PLGA	RM/PL	88.0	0.120	4.50	[384]
PCL	SC/PL[c]	74.0	0.260	0.40	[385]

PCL	SC/PL[c]	88.1	0.119	0.22	[386]
PCL	TIPS[b]	80.0	0.200	0.38	[387]
PCL	SC/PL[c]	76.0	0.240	4.32	[388]
PCL	SC/PL[c]	93.0	0.070	3.10	[389]
PCL	SC/PL[c]	65.0	0.350	1.20	[390]
PCL	TIPS[b]	89.0	0.110	0.08	[391]
PCL	TIPS[b]	88.0	0.120	0.19	[391]

[a] Freeze-drying; [b] Thermally induced phase separation; [c] Solvent casting / particulate leaching; RM/PL = Room temperature compression moulding / particular leaching; GF/PL = Gas foamed / particular leaching.

Appendix D - Supplementary information for Chapter 6

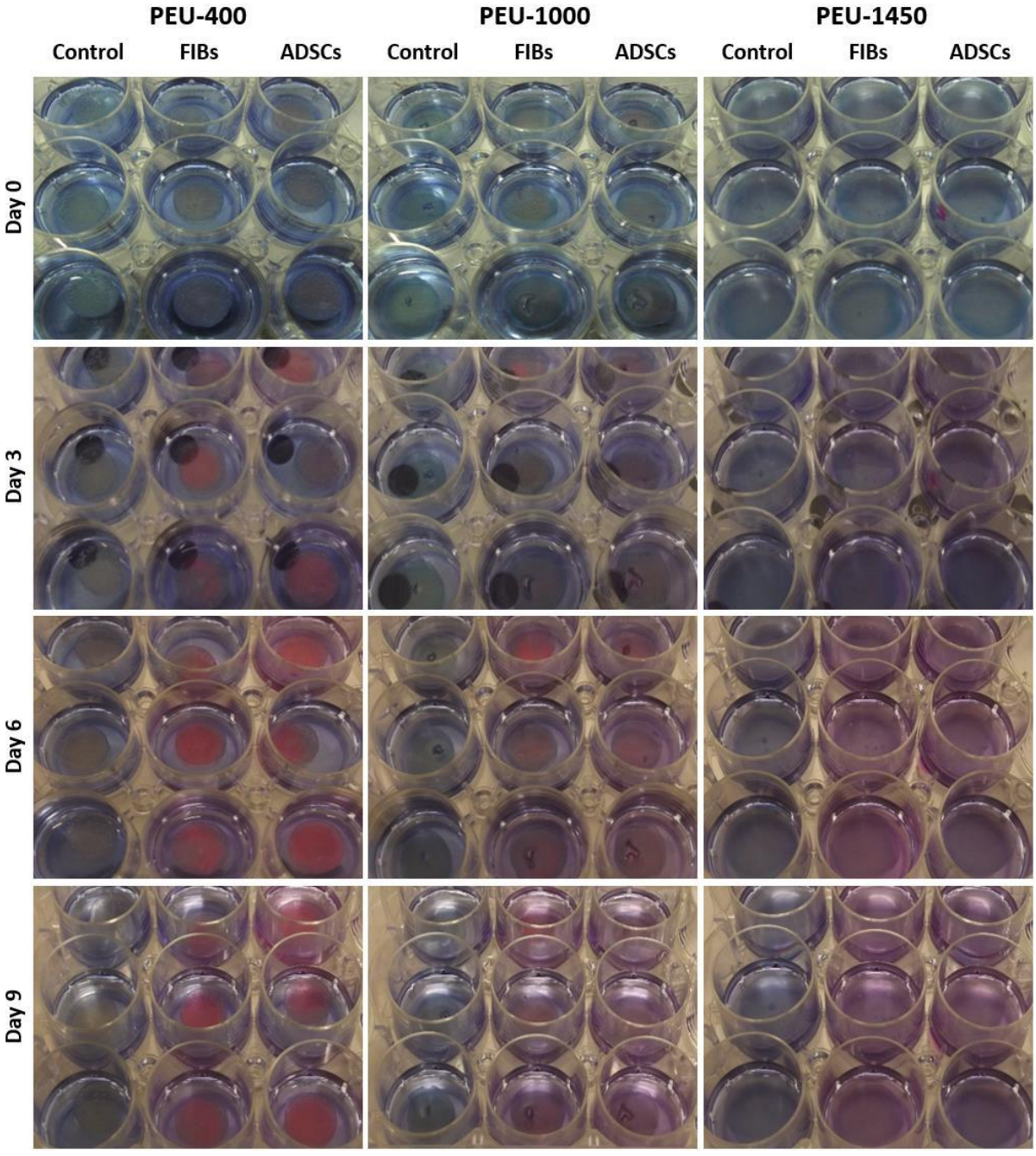

Figure 6.S1: Images of performed metabolic activity assay tests (at days 0, 3, 6 and 9), illustrating the resazurin color change for FIBs and ADSCs cultured PEUs in comparison to cell-free PEU control specimens. Briefly, the assay is based on the mechanism that blue resazurin can only be reduced to pink resorufin by proliferating cells. Thus, the production of pink resorufin correlates confidently with cell viability and proliferation.

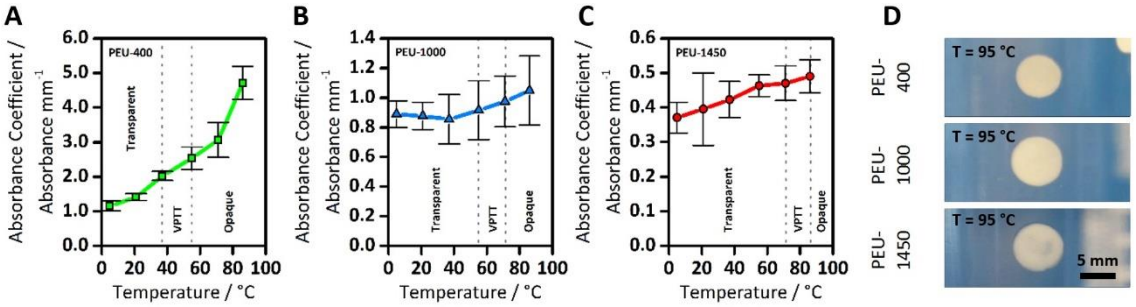

Figure 6.S2: Estimation of the volume phase transition temperature (VPTT) of (A) PEU-400, (B) PEU-1000 and (C) PEU-1450 films by the cloud point method and defined in a temperature range at the onset of cloudiness by optical conformation. Briefly, the absorbance coefficient (absorbance/sample thickness) at 600 nm was measured as a function of the PBS solution temperature (monitored at 5, 21, 37, 55, 71 and 86 °C) with a UV-Vis spectrometer (Perkin Elmer Lambda 900. Pre-hydrated samples (n = 5; 24 h saturation in PBS solution at 21 °C) were submerged for 2 h in the temperature monitored PBS solution, and the absorbance of the individual swollen specimens and the sample thickness were measured. No sharp VPTT transitions were observed in the figure; PEU-400, PEU-1000 and PEU-1450 specimens presented a VPTT within the range of 37-55 °C, 55-71 °C and 71-86 °C, respectively. The VPTT can be defined as the critical temperature below which the hydrogel swells (hydrophilic characteristics) and above which the hydrogel contracts (hydrophobic characteristics). The results imply that the VPTT is adjustable and that the incorporation of higher molecular weight PEG increased the VPTT, due to its enhanced hydrophilicity. (D) Swollen PEUs were transparent at low medium temperatures but changed to opaque at higher temperatures, which is associated with temperature-dependent phase separation of the hydrogels from the aqueous solution.

Movie 6.S1: Water temperature responsive cantilever tests (see Section 6.2.10 and Scheme 6.2). The supplemental movie is in MP4 format included on the enclosed CD-ROM.